The Dissertation Committee for Sarah Joy Moench Certifies that this is the approved version of the following dissertation:

Synthesis and Characterization of Functional Polymeric Materials for Use in Organic Photovoltaics

Committee:

Carlton Grant Willson, Supervisor

Christopher J. Ellison

David A. Vanden Bout

Guangbin Dong

Synthesis and Characterization of Functional Polymeric Materials for Use in Organic Photovoltaics

by

Sarah Joy Moench, B.A.

Dissertation

Presented to the Faculty of the Graduate School of

The University of Texas at Austin

in Partial Fulfillment

of the Requirements

for the Degree of

Doctor of Philosophy

The University of Texas at Austin

May 2016

Dedication

To my mom, dad and sister. I would not be who I am today without your unconditional love and encouragement. Everything I have achieved is because of you. Thank you for never letting me think I couldn't and for supporting me even through you're not sure what I'm doing. I love you, always.

Acknowledgements

First, I would also like to thank my advisor, Dr. Bradley J. Holliday for giving me the opportunity to learn and grow as a research scientist in his group.

I would also like to thank Professor Carlton Grant Willson for his support, advice, and advisement. His enthusiasm for science and teaching is inspiring.

Furthermore, I would like to thank my dissertation committee, Professor Guangbin Dong, Professor Christopher J. Ellison, and Professor David A. Vanden Bout, for their help and support.

I would also like to thank the Willson and Ellison group members for continuously answering my questions about block copolymers, thin film preparation, imaging techniques, directed self-assembly, and polymer characterization methods. Especially Michael Maher, Austin Lane, Sunshine Zhou, and Yichen Fang, thank you for always being willing to take time out of your day to teach me new techniques or help me with SAXS and DSC.

Additionally, I would like to thank my mentor Guy D. Joly. Thank you for seeing something in me when I was just an undergraduate chemistry major who had never been in a lab. Working with you at 3M inspired my love of chemistry. You believed in me before I did and you taught me how to be the chemist that I am. You've been my inspiration, my motivator, and my supporter whenever I needed encouragement or advice. I would not be where I am today without you. I cannot express what your mentorship has meant to me. Thank you from the bottom of my heart for your kindness and your continued support.

I would also like to thank the Holliday group. I have had the chance to work with some of the most wonderful, intelligent, and generous people I have ever met. I would

not have gotten to this point without their constant and unwavering support and, more importantly, friendship. Thank you to Trang Nguyen, Yawei Liang, Minh Nguyen, Rob Fimognari, Matthew Moore, Lauren Lytwak, Matthew Raiford, Weiran Wang, Tyler Davis, Eric Sikma, and Dan Strohecker for always listening to me (even when you didn't want to), for never failing to make me smile, for all of your edits on the following thesis, for your advice, and for being some of the most amazing people I know.

Jordan A. Dinser, I am so grateful for the day that Brad decided to put me in your office. He knew before we did how perfect we were together. You taught me how to do air-free chemistry (over and over), and from that first day I met you, you've inspired me, supported me, and believed in me. There are not enough synonyms to describe how brilliant, kind, and beautiful you are. Thank you for showing me what true friendship is. I love all of our adventures and I can't wait for so many more to come. I'm so lucky to have you as a best friend. I love you.

Kory M. Mueller, you inspire me daily to be a better chemist and a better person. I have so much respect for you. You have a passion for chemistry that is so rare and wonderful, and I admire your curiosity and ingenuity. You are also the kindest, most generous man I know and it is no surprise that everyone comes to you for advice. I cannot express how grateful I am that you are my year-mate and that I've gotten to share this whole journey with you. You have been my supporter, my shoulder to cry on, and the person I go to daily for scientific postulating. Thank you for your endless enthusiasm, for your good humor, for laughing with (and at) me, and for always having time to talk. Most importantly, thank you for your friendship.

Lauren A. Mitchell, Kristin J. Suhr, and Claudina X. Cammack, you are three of the most amazing women I know and I am so grateful for your friendships. Lauren: thank you for helping me with all of my polymer related woes, for your unwavering excitement

about chemistry, and for your constant encouragement. Kristin: I have loved sharing the last five years with you. You are such a caring, big-hearted person. Thank you for always being there for me through grad school hardships and life changes, and for always showing me unconditional love. Claudina: Thank you for being the amazing, silly, good-natured person you are. Thank you for always listening to me, laughing with me, and knowing when I just need a hug. Thank you for Raleigh, for being my Tabata partner-in-crime, and for binge-watching Netflix with me. I love you and I am so glad you moved in to our house so that we could spend 24/7 together.

Leander Cinninger, thank you for being the best hood-mate ever. I wouldn't want to work next to anybody else. You have always supported me, stood up for me, and helped me in any way you could. Thank you for always listening to me, for letting me play my music (and sing along) as loudly as I wanted, and for letting me run columns in your hood. You are a kind-hearted and amazing man, a great teacher, and a wonderful friend.

I also want to thank all of the other incredible people I have met during my time at the University of Texas at Austin. Brette Chapin, Leo Joyce, Sarah Swingle, Kate Biberdorf, Stephany Garcia, Nelly Membreno, John Lin, John Thompson, Sarah Ross Thompson, Brandon Reinus, Liz Gratton, Nolan Waggoner, and Graham Piburn, you have all helped me in so many different ways and I am grateful to know each of you.

Additionally, Shannon Briggs, thank you for Tabata, for making me smile, and for being the best part of my day two times a week for the last three years. Seeing you always brightens my day and reduces my stress levels. I'm grateful for that first day I walked into your Tabata class and you kicked my butt, and every day since.

Finally, thank you to my family. To my mom and dad for making everything I have accomplished possible. Thank you for always believing in me and for making me

believe I could achieve anything I set my mind to. Thank you for endlessly supporting me. I love you more than words can express. You are my constant inspiration and I hope that I've made you proud. Also, thank you to my beautiful, brilliant sister. I miss you every day that I'm not there to share adventures with you. You are my best friend and my better half, no matter how many miles separate us. Also, thank you Shawn Stender, for keeping my sister company in my absence.

Synthesis and Characterization of Functional Polymeric Materials for Use in Organic Photovoltaics

Sarah Joy Moench, Ph.D.

The University of Texas at Austin, 2016

Supervisor: Carlton Grant Willson

Norbornene-type monomers with pendant oligothiophene donor and perylene diimide acceptor groups were synthesized and polymerized using ring-opening metathesis polymerization (ROMP) to yield donor and acceptor homopolymers. These semiconducting homopolymers were characterized by UV-Vis and fluorescence spectroscopy to determine absorbance maxima, emission and excitation profiles, optical bandgaps, molar absorbtivities, and quantum yields. The electrochemical behavior of the donor and acceptor materials was characterized by cyclic voltammetry to determine the highest occupied molecular orbital (HOMO) and lowest unoccupied molecular orbital (LUMO) energy levels of the organic semiconductors. Donor-acceptor diblock copolymers were synthesized using ROMP. Fluorescence spectroscopy demonstrated increased donor emission quenching with decreasing block length. Random donor-acceptor copolymers demonstrated almost complete quenching of the donor emission, likely due to increased donor-acceptor interfaces for charge transfer. Electron paramagnetic resonance spectroscopy (EPR) confirmed the formation of persistent donor radical cations and acceptor radical anions in the block copolymers. Small-angle X-ray scattering (SAXS) demonstrated bulk microphase separation with domain sizes between 24-28 nm. Furthermore, the formation of crystalline structure within the ordered

microdomains was also observed. All of these studies indicate that the designed materials may be useful as the active layer in organic photovoltaic applications.

As a route to functional hybrid materials, block copolymers containing a donor-segment and a Lewis-basic oligoethylene glycol segment, for preferential ZnO nanoparticle growth, were synthesized by ROMP. Photophysical and electrochemical characterization demonstrated that the donor electronic properties were maintained upon incorporation into the copolymer. SAXS was used to demonstrate lamellar morphology in bulk films of the symmetric block copolymers. ZnO nanoparticles were synthesized and incorporated into composite thin films with the block copolymers. These composite films demonstrated high photoluminescence quenching, which increased upon thermal annealing, as a result of favorable charge transfer from the photo-excited donor to the ZnO nanoparticles. These studies demonstrate that improved morphology control and self-assembly can increase charge transfer in hybrid materials through increased interfacial area. As an alternative route to directed ZnO nanoparticle growth, a copolymer containing pendant dipicolylamine moieties was synthesized and characterized by photophysical and electrochemical methods.

Table of Contents

List of Tables

List of Figures

List of Schemes

ORGANIC DONOR-ACCEPTOR BLOCK COPOLYMERS

Chapter 1: Block Copolymers as Functional Materials for OPV Applications

INTRODUCTION

Currently, global energy consumption is approximately 18 terawatts (TW) of energy annually. This number that is projected to reach 30 TW by the year 2050.[1,2] The development of alternative energy sources is, consequently, one of the most important challenges facing modern society—not only due to the limited reserve of traditional fossil fuel sources, but also because of the need for energy independence, global security, and perhaps most significantly, climate stability.[2,3] Beyond fossil fuels and nuclear energy, the only other viable energy sources available are renewable energy sources such as hydropower, wind, geothermal, biomass, and solar. While a diverse mix of energy sources is a practical necessity, solar energy has the largest capacity for energy generation and is, perhaps, the most obvious source of renewable energy. A vast amount of energy from the sun reaches the Earth each year and harnessing even a small percentage of this would more than meet the total global energy demand.[2–4] For example, if solar panels having an average power conversion efficiency (PCE) of 12% were deployed evenly over 2% of Earth's land area, the feasible generated solar energy supply would be approximately 67 TW—more than twice the projected energy demand for 2050.[2]

HISTORY OF THE SOLAR CELL

In 1954, Daryl Chapin, Gerald Pearson, and Calvin Fuller at Bell Laboratories invented the first modern-day solar cell based on single-crystal silicon negatively doped with arsenic and coated with a thin layer of boron to make a p-n junction.[5] While

previous photovoltaic cells were based on solid selenium and demonstrated PCEs less than 1%, this first silicon solar cell had an efficiency of 6%. This led *The New York Times* to write that this discovery marked "the beginning of a new era, leading eventually to the realization of one of mankind's most cherished dreams—the harnessing of the almost limitless energy of the sun for the use of civilization."[5–7] By 1958, small-area silicon solar cells had reached 14% efficiencies under terrestrial light, and on March 17, 1958, the world's first solar powered satellite, Vanguard I, was launched. This satellite carried two separate radios: a battery-powered transmitter, which operated for 20 days; and a solar cell-powered transmitter, which operated until 1964, when it is believed that the circuitry failed.[7,8] Since then, there have been tremendous advances in solar cell technology. With the use of improved materials and device architectures, PCEs have steadily increased from 6% to 44% for state-of-the-art technologies.[9,10] In 2014, the U.S. Energy Information Administration reported that renewable energy sources accounted for 10% of the total energy consumption in the United States, with solar energy accounting for 4% of this renewable energy expenditure, up from 2% in 2011.[11]

Currently, inorganic-based solar cells dominate the market, with typical module efficiencies of 15-20% and device lifetimes on the order of 20 years for silicon technologies.[2,10] Silicon solar panels come in three basic types: monocrystalline silicon, polycrystalline silicon, and amorphous silicon. Monocrystalline silicon is the leader in module efficiency, with the best lab devices demonstrating efficiencies just below 28% and commercial modules reaching 20% efficiency. Polycrystalline silicon solar cells are next, with lab efficiencies reaching 20% and commercial module efficiencies reaching 15%. While amorphous silicon solar cells are less efficient, reaching 10% in lab settings and 5% in commercial modules, these thin-film devices offer the advantage of mechanical flexibility.[2,9] Despite the high performance of silicon solar cells, as well as

devices based on other inorganic materials such as cadmium telluride (CdTe), copper indium gallium diselenide (CIGS), and gallium arsenide (GaAs), the high costs and processing difficulties associated with these materials have slowed large-scale commercial development. Furthermore, costs associated with the installation of inorganic solar panels, as well as the inherent rigidity of the materials themselves, has limited the scope of solar technology applications.[8]

ORGANIC PHOTOVOLATICS

Organic photovoltaic devices (OPVs), made by combining electron-donating (donor, p-type) and electron-accepting (acceptor, n-type) semiconducting materials, offer a promising option for advancing solar technology due to reduced material and fabrication costs, as well as the ability to make light-weight, flexible devices from solution-based processing methods.[12–17] Furthermore, the electronic and optical properties of organic semiconductors can be tuned to a large extent with synthetic structural modifications, allowing tailoring for specialized applications. With the use of low-cost materials and processing procedures, some statistics show that OPVs are expected to have a much lower energy payback time and better environmental sustainability than inorganic photovoltaic technologies.[2,9]

The first efficient organic solar cell was reported in 1986, achieving a PCE of approximately 1%.[18] Since then, there have been remarkable improvements in OPV PCEs, with record efficiencies now surpassing the 10% benchmark in laboratory settings.[10,19–21] Still, there are several challenges remaining that hinder the commercial viability of OPV technologies. Not only are the PCEs lower for OPVs than for commercially available inorganic competitors, but the differences between lab-scale cell records and commercial module efficiencies are also far larger for OPV technologies. For

example, OPVs demonstrate up to an 85% decrease from lab-scale performance to large-area module performance compared to a 20% decrease for monocrystalline silicon devices and a 28% decrease for polycrystalline silicon devices.[2] Additionally, operational lifetimes lag behind their inorganic counterparts due, in part, to the high susceptibility of the organic semiconductors to both photodegradation and nanomorphology degradation over time.[22] Finally, batch-to-batch inconsistencies in organic source materials, especially in the case of polymer-based devices, make consistent device performance difficult.[2,10] The development of OPVs that exhibit lifetimes on the order of 10 years and module PCEs greater than 10% is considered an important benchmark for widespread utilization,[23] although it has been suggested that OPV market competitiveness could be achieved if large-area module efficiencies could reach 7% with a 5-year device lifetime.[24]

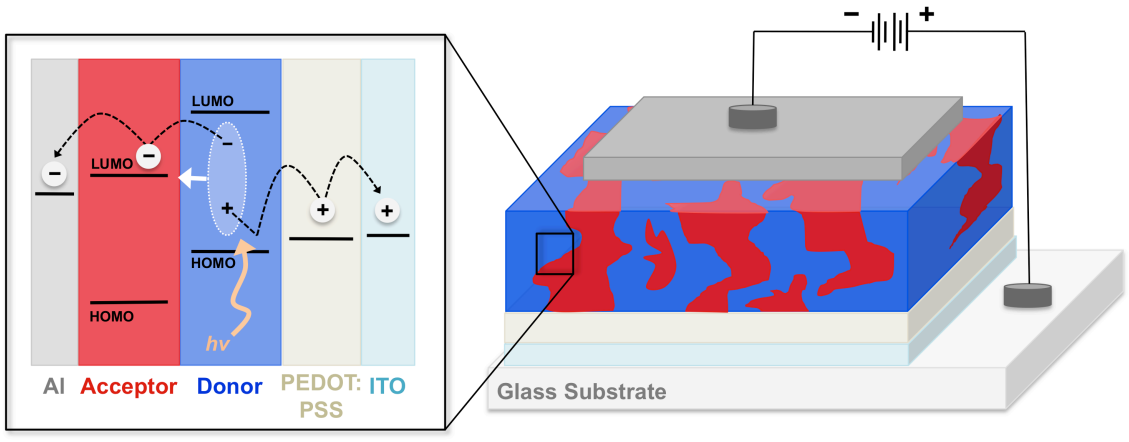

Figure 1.1. Schematic representation of an OPV device and the proposed mechanism of photocurrent generation.

The basic mechanism of photocurrent generation in OPVs is illustrated in **Figure 1.1**. First, photoexcitation results in the formation of a Coulombically-bound electron-hole pair. Diffusion of this electron-hole pair to the donor-acceptor interface results in dissociation, generating free charge carriers. These free charge carriers are then

transported to the appropriate electrodes, where they can be collected to generate photocurrent. The fundamental difference between inorganic and organic photovoltaics is the creation of these strongly-bound electron-hole pairs, known as Frenkel excitons, upon photoexcitation of organic semiconductors. These excitons have typical binding energies on the order of 0.3-1.0 eV, and are formed as a result of the low dielectric constants of organic semiconductor materials.[3,4,14,16,25–27] Since this binding energy is much greater than the thermal energy (kT) at room temperature (~0.025 eV), the driving force for exciton dissociation is almost exclusively represented by the energetic offset found at the interface of the donor and acceptor materials. This energetic offset results from the differences in ionization potential and electron affinity of the two materials.[23,27–32] Consequently, a donor-acceptor interface must exist within the exciton diffusion length (≤10 nm, based on the typical lifetimes of 100 ps to 1 ns for singlet excitons in organic semiconductors) to successfully generate free charge carriers.[2,16,26,30]

Exciton dissociation results in the formation of a geminate pair, also known as a polaron, with the electron residing in the lowest unoccupied molecular orbital (LUMO) of the acceptor and the hole residing in the highest occupied molecular orbital (HOMO) of the donor. In systems where the donor is the primary light absorber, the LUMO energy offset (ΔE_{LUMO}) between the donor and the acceptor represents the driving force for exciton dissociation, and this offset needs to be at least equivalent to the exciton binding energy (0.2-0.3 eV).[3,16,32,33] However, systems with larger ΔE_{LUMO} values (> 1.0 eV) often display geminate pair dissociation quantum efficiencies approaching 100%.[3,33–35] A similar analysis can be made for the HOMO energy offset (ΔE_{HOMO}) in systems where the acceptor is the primary light absorber.[3,36] Once separated, the free charge carries must be transported to their respective electrodes before recombination occurs in order to generate photocurrent.

Charge transport in organic semiconductors is mainly based on a polaron hopping mechanism between neighboring molecules or polymer chain segments.[37] Consequently, the charge carrier mobilities can be strongly dependent on morphology, varying several orders of magnitude from a highly disordered, amorphous film (10^{-6} to 10^{-3} $cm^2V^{-1}S^{-1}$) to a highly ordered, crystalline films (> 1 $cm^2V^{-1}s^{-1}$).[32,37] Based on this mechanism of photocurrent generation, the optimal active layer morphology depends on the balance of several constraints: the exciton diffusion length, film thickness for optimal light absorption (>100 nm), and the existence of continuous pathways for free charge carriers to reach the respective electrodes.[29,30] These requirements suggest optimization through a bicontinuous morphology with a nanometer-scale domain size.

There are several parameters used to describe the device performance of OPVs. Perhaps the most important parameter used to describe and compare photovoltaic performance is the PCE (η) of the device, which is defined as the ratio of the maximum power produced (the product of the maximum short-circuit current density, J_{max}, and open-circuit voltage, V_{max}) to the power of the incident radiation (P_{in}), as shown in **Equation 1.1**.[31]

$$\eta = \frac{J_{max}V_{max}}{P_{in}} = \frac{J_{sc}V_{oc}FF}{P_{in}} \qquad (\mathbf{1.1})$$

PCE can be calculated from a simple current density versus voltage (*J-V*) curve generated under standard illumination conditions (denoted AM1.5), as depicted in **Figure 1.2**, and is directly related to three measured device parameters: short-circuit current density (J_{sc}), open-circuit voltage (V_{oc}), and fill factor (*FF*).[3,4]

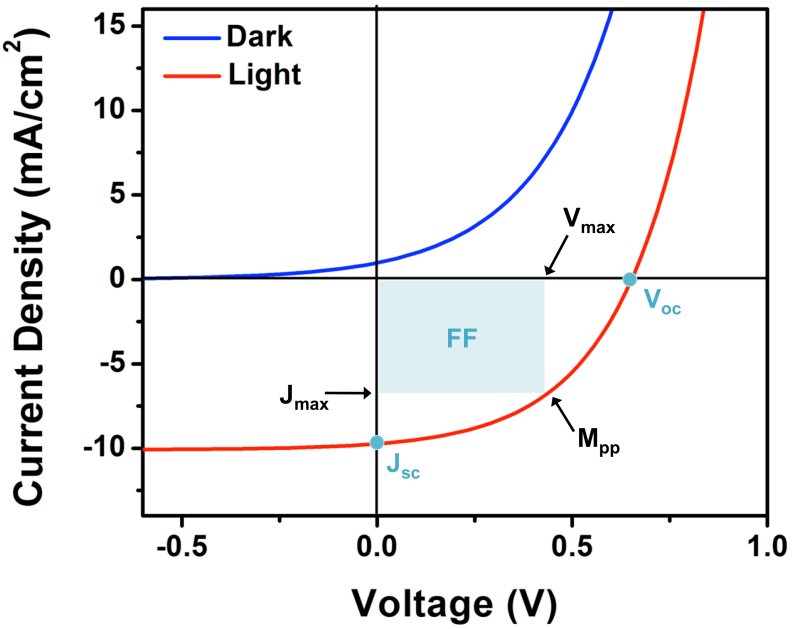

Figure 1.2. Typical current density *vs*. voltage (*J-V*) curve for an OPV device showing the critical parameters that determine device efficiency. These include short-circuit current density (J_{sc}), open-circuit voltage (V_{oc}), fill factor (*FF*), maximum short-circuit current (J_{max}), maximum open-circuit voltage (V_{oc}), and the maximum power produced (M_{pp}). Illustration adapted from ref [31].

The J_{sc} of the device is defined as the current at zero bias (i.e. when there is no potential difference across the device) and is related to the number of excitons created upon light absorption. Hence, a smaller optical band gap of the absorbing material leads to a higher the maximum J_{sc}, due to an increased overlap with the solar spectrum leading to increased exciton formation.[4,23,32,38]

The V_{oc} is the voltage produced when the current in the cell is equal to zero.[4] It has been shown that the V_{oc} is directly related to the energy difference between the HOMO (ionization potential) of the donor and the LUMO (electron affinity) of the acceptor, and a larger offset will give rise to a larger theoretical maximum V_{oc} for the device. However,

the larger the band gap of the absorbing material, the poorer the overlap between device's absorption and the solar spectrum, which will limit the overall device efficiency.[4,16,39]

The *FF* is the ratio of maximum power produced (M_{pp}) to the product of J_{sc} and V_{oc}. This parameter describes the shape of the *J-V* curve of the device, essentially characterizing how efficiently the photogenerated charges are extracted from the device. Therefore, the *FF* illustrates both the connectivity of pathways to the electrodes for a particular device and the prevalence of charge recombination events.[40] While many new devices have achieved high J_{sc} and/or V_{oc} values by tuning the material properties of the donor and/or acceptor, the *FF* often remains relatively modest (0.5-0.7) compared inorganic devices (0.85).[10,40,41]

Two other important parameters used to describe OPV performance are the external quantum efficiency (EQE) and the internal quantum efficiency (IQE) of a device. The EQE is the ratio of the collected electrons to the incident photons at a specific wavelength. This parameter describes the fraction of photoexcitations that result in useable charge carriers at the electrodes.[4] The IQE is related to the EQE and measures the ratio of collected charge carriers to absorbed photons of a specific energy. This value is always higher than the EQE for a particular device, often approaching 100% for optimized materials.[4,28,35] The IQE of a device is determined by three main steps in the photocurrent generation mechanism: exciton diffusion to the donor-acceptor interface, exciton dissocation and charge separation at the interface, and collection of the charges at the respective electrodes. Consequently, the IQE of a device is highly dependent on both the morphology of the active layer and the energy offsets of the donor and acceptor materials.[35,42]

ACTIVE LAYER MORPHOLOGY

The three typical active layer morphologies for OPVs are shown in **Figure 1.3**. The first efficient OPV, described by Tang in 1986[18], was based on a bilayer device morphology. This type of morphology is generally achieved through thermal evaporation techniques using small molecule semiconductors. While this morphology offers the most direct pathways for free charge carriers to the electrodes, thus reducing recombination events, exciton dissociation is limited to a very small interfacial area.[29,31] This can severely limit device performance for this type of device.

The advent of the bulk heterojunction (BHJ) morphology[43,44] has served as the starting point for steady increases in PCE over the past decade, with many of the best OPV devices based on this active layer morphology.[4,34,45] This type of morphology is typically achieved by solution-casting a mixture of donor and acceptor materials together to give a thin film composite with donor-acceptor interfaces throughout the active layer. This process is extremely sensitive to the processing conditions used, including choice of solvent, composition of the donor and acceptor materials, annealing time and temperature, thermodynamic interactions between the organic semiconductors, and purity of starting materials. Consequently, optimization and reproducibility of the BHJ morphology can be difficult to achieve.[4,29,46–58] Furthermore, the resulting structures can be significantly disordered due to the random phase separation of the constituent materials, leading to domains that are too large, too small, or discontinuous.[28] Perhaps the most significant drawback of the BHJ is that the interface morphologies that result are kinetically-trapped, non-equilibrium structures that are fundamentally unstable. As a result of this, morphology degradation, aggregation, or macrophase separation can occur over time.[22]

Block copolymers (BCPs) containing donor and acceptor segments offer a possible solution compared to their respective blends due to the covalent tether between the donor and acceptor segments, which leads to increased morphological stability. More importantly, block copolymers demonstrate inherent and well-understood microphase self-assembly behavior on the length scale of exciton diffusion.[4,25,28,30,31,59,60]

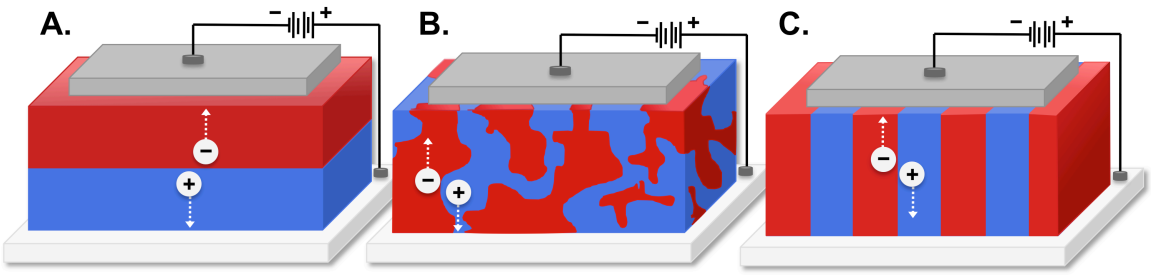

Figure 1.3. Schematic representation of active layer morphologies in OPVs: (A) bilayer morphology; (B) bulk heterojunction morphology; (C) vertically-aligned block copolymer morphology. Illustration adapted from red [4].

BLOCK COPOLYMER SELF-ASSEMBLY

Block copolymers are macromolecules that are comprised of two or more covalently linked homopolymers, known as blocks. When discussing block copolymers for OPV applications, there are two major types of polymer chains to consider: coils and rods. A coil describes a flexible, amorphous polymer chain, while a rod describes a conjugated, rigid polymer chain that usually adopts a crystalline, unidirectional conformation due to overlapping p-orbitals.[4] The microphase separation behavior in conventional coil-coil A-B diblock copolymers is a thermodynamic process that is well understood as a compromise between the immiscibility of the two covalently-linked blocks and the entropic penalty associated with chain stretching.[61–65] This phase behavior is controlled by three factors: the overall degree of polymerization (N), which is the total number of monomers incorporated into the macromolecule; the composition of the block

copolymer, described as the volume fraction (f_A) of block A; and the A-B segment-segment Flory-Huggins interaction parameter, χ, as shown in **Figure 1.4**.[62,65]

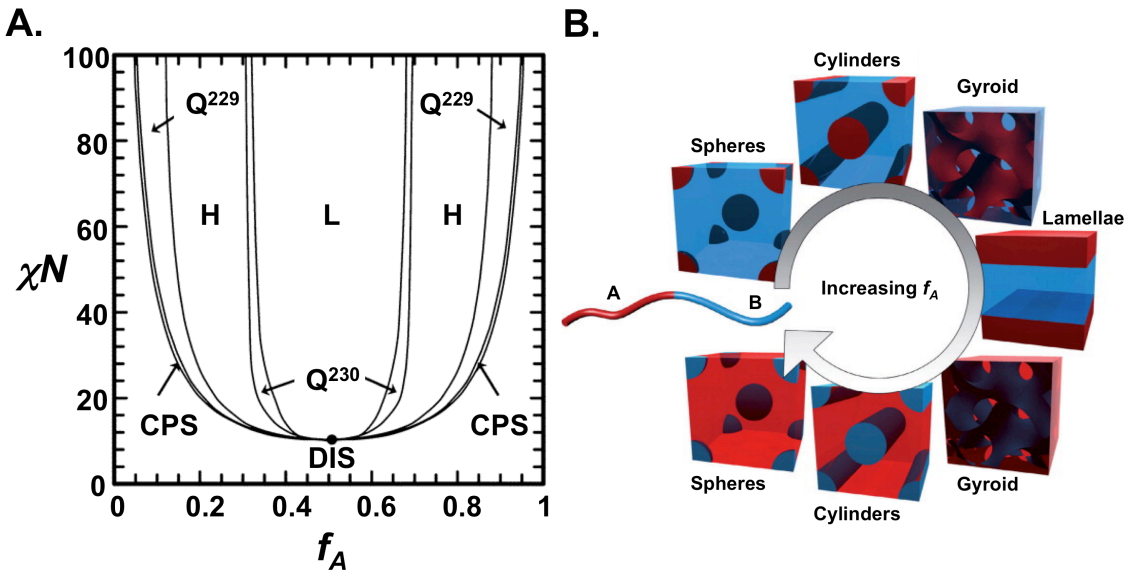

Figure 1.4. (A) Traditional coil-coil diblock copolymer phase diagram, where L = lamellae, H = hexagonally-packed cylinders, Q^{230} = gyroid, Q^{229} = body-centered cubic spheres, CPS = close-packed cubic spheres, DIS = disordered. Figure reprinted with permission from ref [69]; (B) Schematic representation of the possible morphologies formed by self-assembly of coil-coil diblock copolymers as a function of the volume fraction of block A (f_A). Figure reprinted with permission from ref [60].

The Flory-Huggins interaction parameter is temperature-dependent and describes the miscibility of the two blocks; a negative value of χ indicates favorable mixing, while a positive value indicates net replusions between the different polymer segments.[4,61] The product, χN, represents the segregation strength of the two chemically dissimilar blocks and controls the state of microphase separation. Weakly segregating copolymers, $\chi N <$ 10, will generally adopt isotropic, disordered morphologies because the thermodynamic driving force for self-assembly is not strong enough to overcome the associated entropic

penalty. As χN increases, the diblock copolymer segments overcome the order-disorder transition (ODT) and segregate into one of five thermodynamically stable microstructures, depending on the volume fractions of the constituent blocks (predicted to occur at $\chi N = 10.5$ for symmetric diblock copolymers).[61,65–67] Finally, when $\chi N > 100$, the block copolymer is categorized by the strong segregation regime.[68]

As first predicted by Leibler[65] and expanded on by Matsen, Bates, and Schick[62,69], nearly symmetric diblocks, with the volume fraction of block A ranging between approximately 0.4 and 0.6, demonstrate a lamellar morphology. As the compositional asymmetry increases, a narrow region of stability exists for a complex gyroid phase, which is followed by a large region of stability for a hexagonally-packed cylinder morphology. As the asymmetry of the diblock copolymer increases to volume fractions above 0.8 or below 0.2, the hexagonal phase gives way to a body-centered cubic sphere morphology, which is separated from the disordered phase by a very narrow region of close-packed spheres (see **Figure 1.4**).[61,70] It is important to note that as f_A deviates from 0.5, higher χN values are required for microphase separation.[4] Continuous morphologies such as lamellae, hexagonally-packed cylinders, and gyroid are well-suited for OPV applications. These morphologies offer large interfacial areas with nanometer domains sizes ideally-suited for exciton diffusion lengths, as well as continuous pathways for direct transport of generated free charge carriers to the respective electrodes. Furthermore, techniques for preparing ordered microstructures that are macroscopically aligned perpendicular to the electrodes are well established and have been successfully demonstrated for both conventional and functionalized diblock copolymers.[30,71–76]

Rod-containing block copolymers have a more complex phase diagram due to the anisotropic (orientational) interactions, and liquid crystalline behavior, of the rod blocks.[77–81] Due to the high immiscibility of the rod block and the coil block, which

results in a large value for χ, microphase separation can be achieved even at very low molecular weights.[68,81] Besides the traditional parameters used to describe coil-coil block copolymer phase behavior (i.e. the Flory-Huggins interaction, χN, and the composition of the block copolymer, described in this case by the coil volume fraction, f_{coil}), two additional parameters are used to characterize rod-coil systems.[78] First, the orientational behavior of the rod blocks (i.e. their propensity to crystallize) can be described by the Maier-Saupe interaction parameter, μN. This parameter is related to rod-rod alignment where steric repulsion favors liquid crystal formation.[38,78,82] Additionally, there is the geometrical asymmetry parameter (ν), which is defined as the ratio between the coil radius of gyration and the rod length. This parameter relates to the relative block size of the constituent blocks and describes the packing frustrations of the rod and coil blocks caused by size mismatch.[31,79] Due to the high propensity of the rod blocks to form planar domains as a result of their crystallization behavior, more of the phase diagram is covered by lamellae or liquid-crystalline structures. This can make it difficult to target non-lamellae morphologies such as hexagonally-packed cylinders without large degrees of geometrical and compositional asymmetry.[78,79]

Due to a wide range of interesting applications, there has been a lot research focusing on the phase behavior of rod-coil diblock copolymers. For example, Segalman and coworkers demonstrated that careful design of the rod block, in this case poly(3-(2'-ethyl)-hexylthiophene) (P3EHT), to enhance chemical dissimilarity allowed for balance between crystallization and microphase separation. This led to the formation of hexagonally-packed cylinders of an amorphous polylactide (PLA) block embedded within a semicrystalline P3EHT domain.[83] Similarly, Dai and coworkers were able to demonstrate the formation of a wide range of thermodynamically stable microstructures for block copolymers composed of poly(3-hexylthiophene) (P3HT) and poly(2-vinyl

pyridine) (P2VP), from nanofibril structures at low P2VP content ($f_{P2VP} \leq 0.2$), to ordered lamellae ($f_{P2VP} = 0.3 – 0.6$), to hexagonal packed cylinders at high P2VP content ($f_{P2VP} = 0.6 – 0.8$).[84] Here, the ratio of μ/χ plays an important role in determining the microstructures adopted by the block copolymer. This ratio describes whether microphase separation or liquid crystalline behavior will dominate for a particular rod-coil block copolymer. When μ/χ is greater than unity, liquid crystalline behavior (i.e. alignment of the rod blocks) dominates the phase behavior and the observed morphologies will resemble liquid crystal phases. Conversely, when μ/χ is less than unity, the adopted nanostructures will resemble typical coil-coil block copolymer morphologies.[4,31] This competition between microphase separation and orientational ordering leads to diverse phase behavior and distinct morphological structures, including arrowhead, zigzag, wavy lamellar, and smectic bilayers.[85] Furthermore, upon annealing, rod-based blocks often demonstrate long-range order in the form of nanowires or nanofibrils, which is particularly valuable for charge mobility.[86,87] **Figure 1.5** shows several possible morphologies adopted by rod-coil block copolymers.

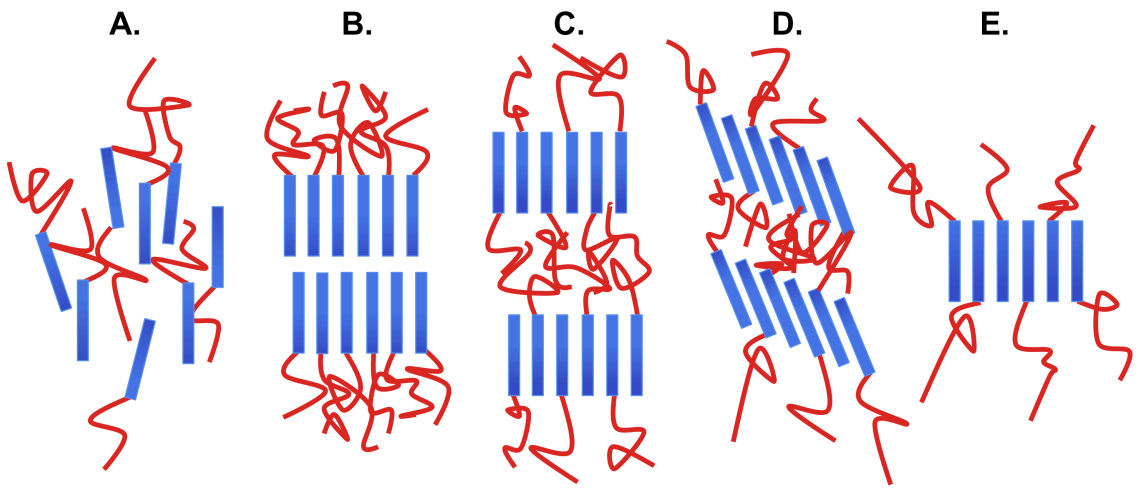

Figure 1.5. Self-assembly of rod-coil block copolymers into (A) nematic phase, (B) bilayer smectic A phase, (C) monolayer smectic A phase, (D) monolayer smectic C phase, and (E) "hockey pucks". Illustration adapted from ref [68].

A special class of rod-coil polymers is side-chain liquid crystalline (rod) block copolymers consisting of mesogenic units attached to an amorphous backbone, typically through a flexible alkyl spacer.[85] In contrast to the morphologies exhibited by typical rod-coil block copolymers, side-chain liquid crystalline polymers exhibit richer self-assembly characteristics that result from an interplay between ordering of the amorphous backbone block (following typical coil-coil self-assembly) and ordering of the side-chain rods (following liquid crystalline self-assembly behavior). Many of the traditional coil-coil block copolymer phases are predicted to occur for side-chain liquid crystalline block copolymers, with smectic ordering occurring within the microphases. This results in the formation of diverse hierarchical structures with microphase separation on length scales of 10-100 nm and liquid crystalline ordering on length scales of 3-10 nm.[88,89] Like with rod-coil block copolymers, accessible equilibrium morphologies are dependent on the molecular weight of the copolymer, the length of the rod units, the relative volume of

each block, and the energetic and anisotropic interactions between the different components.[85] For many side-chain liquid crystalline block copolymers, lamellar structures are observed for a larger volume fraction range than typical coil-coil systems. Furthermore, it has been observed that cylindrical domains preferentially form at very large volume fractions of the rod-containing block, although this is not true for all side-chain rod-coil block copolymer.[89–93] Importantly, microphase separation and liquid crystalline ordering can directly influence each other, and this has important consequences for the structures that can be obtained.[94]

DONOR-ACCEPTOR BLOCK COPOLYMERS FOR OPVS

Semiconducting properties in donor-acceptor block copolymers can be achieved in several ways: through conjugation of the polymeric backbone (rod-rod block copolymers); through the attachment of semiconducting molecules as pendant groups on a flexible backbone (termed coil-coil block copolymers for simplicity, although these polymers often resemble side-chain liquid crystalline polymers); or through the combination of a conjugated rod polymer with a coil block containing pendant semiconductors (rod-coil block copolymers).[4,30,38,68,95–97] Each of these types of block copolymers has been studied as semiconducting materials for OPVs. Furthermore, while the development of new semiconducting donor and acceptor materials is an important and prolific area of research, many donor-acceptor block copolymers utilize derivatives of common organic donors and acceptors materials, as shown in **Figure 1.6**.

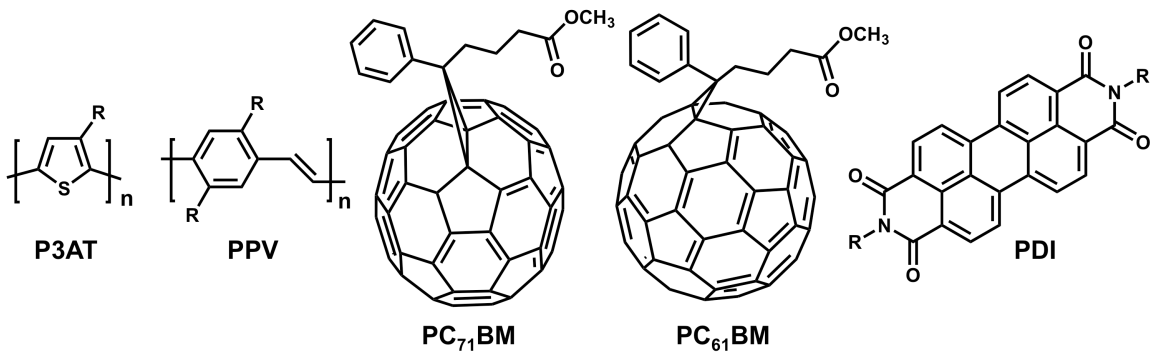

Figure 1.6. Chemical structures of some commonly used organic donor and acceptor semiconductors in the OPV literature.

Since the discovery by Shirakawa, MacDiarmid, and Heeger in 1977 that simple organic conjugated polymers such as polyacetylene, polypyrrole, and polythiophene could be made highly conducting (~10^3 Scm^{-1}) through redox doping, there has been much effort devoted to studying and expanding the classes of known conjugated polymers.[98–100] Charge carriers in conjugated polymers may be generated through photoexcitation or through chemical/electrochemical doping, and these types of materials have been widely studied as semiconducting materials for optoelectronic applications. The majority of conjugated polymers are much more stable in the p-doped state, and thus have found extensive use as donor materials. For example, poly(*p*-phenylene vinylene) (PPV) and polythiophene derivatives, such as P3HT, have been widely used. In particular, polythiophenes offer highly conjugated systems in which the π-electrons can be relatively easily removed without significant disruption to the polymer system. Quinoid character in polythiophenes is enhanced in the oxidized state and increases the conductivity of holes, making these effective hole-transporting materials. Furthermore, polythiophene derivatives are considerably more stable than PPV. As a result, P3HT has become the most widely utilized donor material due to its ease of preparation with

controlled and predetermined molecular weights, high solubility in organic solvents, well understood electronic behavior, and semicrystallinity.[16,68,101]

Recently, conjugated copolymers combining alternating electron-rich and electron-deficient moieties have been used to synthesize low band gap push-pull polymers for use as the donor materials in BHJ devices.[22,39,45,102–107] These low band gap polymers address one of the shortcomings of P3HT, which is that its relatively large band gap (E_g = 1.85 eV) limits the overlap of P3HT absorption with the solar spectrum. P3HT can only harvest photons with wavelengths less than 650 nm, 22.4% of available photons, severely limiting J_{sc}.[38] The incorporation of strong electron-donating and electron-accepting units in direct conjugation in the polymer backbone in these new donor materials raises the energy of the HOMO and lowers the energy of the LUMO of the conjugated polymers through hybridization.[108] The development of low band gap donor-acceptor polymers allows better harvesting of the solar spectrum (especially in the 1.4-1.9 eV region), and the use of these alternating copolymer materials as the donor component in BHJ devices has contributed significantly to the remarkable improvements in BHJ OPV PCEs.[2,109]

In terms of n-type semiconductors for OPV applications, fullerenes derivatives such as [6,6]-phenyl-C_{61}-butyric acid methyl ester ($PC_{61}BM$) or [6,6]-phenyl-C_{71}-butyric acid methyl ester ($PC_{71}BM$) are the most widely-utilized materials.[23,103,107,110–112] These modified fullerene (C_{60}) derivatives are ubiquitous in the literature as the acceptor component in OPV systems due to their deep-lying LUMO, which allows for photoinduced electron transfer from a wide range of organic donor materials. Furthermore, the presence of a triply degenerate LUMO allows for the stabilization of up to six electrons, and that, coupled with high electron mobility of up to 1 $V^2cm^{-1}s^{-1}$, ultrafast photoinduced charge transfer rates, and good solution processibility, makes these

fullerene derivatives some of the best acceptor materials to date.[16,96,113] Perylene diimide (PDI) derivatives have been developed as promising alternatives to PCBM acceptors due to their excellent chemical, thermal, and photochemical stability; large propensity towards crystalline or liquid crystalline ordering, resulting in high electron mobilities; large optical absorption with high molar absorptivity and fluorescence quantum yields of near unity; and chemical tunability at both the imide and core positions.[114,115] While these two classes of organic n-type semiconductors are highly prevalent in the literature, the development of new fullerene derivatives, as well as non-fullerene n-type materials, has been an important area of research recently, potentially allowing for better tuning of device properties and performance through careful selection of the donor and acceptor materials used.[116]

ROD-ROD BLOCK COPOLYMERS

Theory work by Meyers and coworkers[117] was among the first to suggest the use of fully-conjugated block copolymers of varying lengths to manipulate band gap for optoelectronic applications. Synthesis of these rod-rod block copolymers materials was then pioneered by Jenekhe and coworkers, demonstrating intra- and interchain energy transfer between donor and acceptor blocks in a triblock copolymer composed of poly(2,5-benzoxazole)-*b*-poly(benzobisthiazole-2,6-dily-1,4-phenylene)-*b*-poly(2,5-benzoxazole) (2,5-PBO-*b*-PBZT-*b*-2,5-PBO) (see **Figure 1.7**).[28,59] Owing to the high levels of anisotropic ordering as a result of their crystallinity, rod-rod block copolymers can demonstrate organization of the copolymer chains into large-area lamellae on the length scale of exciton dissociation.[113] For example, in 2013, Verduzo, Gomez and coworkers demonstrated the use of P3HT-*b*-poly(9,9-dioctylfluorene)-2,7-diyl-alt-[4,7-bis(thiophen-5-yl)-2,1,3-benzothiadiazole]-2',2"-diyl) (P3HT-*b*-PFTBT) as a fully

conjugated donor-acceptor block copolymer for OPV devices (see **Figure 1.7**).[118] The block copolymer was composed of 56 wt% P3HT, with an overall weight-average molecular weight (M_w) of 29 kg/mol. Upon annealing, the block copolymer self-assembled into a perpendicular lamellar morphology with domain spacing of approximately 18 nm, as determined from X-ray scattering measurements. Optimized OPV devices made with P3HT-*b*-PFTBT and annealed at 165 °C for 10 minutes demonstrated an average efficiency of 2.7 ± 0.4%, with J_{sc} = 5.0 mA/cm^2, V_{oc} = 1.14 V, and FF = 0.45, and a best device efficiency of 3.1%. This was compared to optimized blend devices of 2:1 wt% P3HT:PFTBT annealed at 100 °C for 20 min, which showed η = 1.0 ± 0.1%. When the block copolymer devices were treated to the same annealing conditions as the optimized blend devices, they demonstrated a decreased average efficiency of 1.5 ± 0.1%, attributed to the lack of microphase order achieved at lower annealing temperatures. Conversely, when the blend devices were exposed to the same annealing conditions used for the optimized block copolymer, their average efficiency dropped to 0.5 ± 0.1%, attributed to the formation of macrophase-separated domains.

Typically, phase separation of fully conjugated donor-acceptor block copolymers is more challenging than with traditional coil-coil block copolymers due to the intrinsic similarity of the two blocks having rigid backbones and alkyl side chains, as well as the low degrees of polymerization that can generally be achieved. An efficient approach to increase incompatibility of one block is through fluorination of the alkyl side chains.[119,120] In 2015, Friend, Sommer, and coworkers developed a rod-rod block copolymer composed of a P3HT donor segment and a semi-fluorinated poly(carbazole-*alt*-dithienylbenzothiadiazole) acceptor moiety (SF-PCDTBT) (**Figure 1.7**).[121] While PCDTBT is commonly used as a low band gap p-type material in combination with fullerenes, when combined with P3HT, it acts as the acceptor due to the alignment of

HOMO and LUMO energy levels. In this study, in order to maintain the electronic structure of the PCDTBT unit upon fluorination, an alkyl segment was introduced between the backbone and the perfluorinated segment, resulting in semi-fluorinated side chains. This SF-PCDTBT-*b*-P3HT copolymer demonstrated strongly increased dissimilarity between the donor and acceptor blocks, leading to microphase-separated structures for moderate molecular weight polymers, as determined by differential scanning calorimetry (DSC) and grazing incidence small-angle X-ray scattering (GISAXS). When the fluorinated side chains were replaced by hydrogen (H-PCDTBT) or hexyl chains (hex-PCDTBT), no microphase separation was observed. Furthermore, devices made usig SF-PCDTBT-*b*-P3HT exhibited the best solar cell performance of the three materials, reaching a PCE of 0.95%, compared to 0.0028% for hex-PCDTBT-*b*-P3HT and 0.55% for H-PCDTBT-*b*-P3HT.

Despite these and other recent developments, the self-assembly behavior of rod-rod block copolymers is not well understood. Moreover, the synthesis can be arduous, with the final polymers often exhibiting poor solubility in common organic solvents. Due to these challenges, only a limited number of fully conjugated donor-acceptor block copolymers have been reported,[122–127] and their use as active layer materials for OPV applications has been limited.[113]

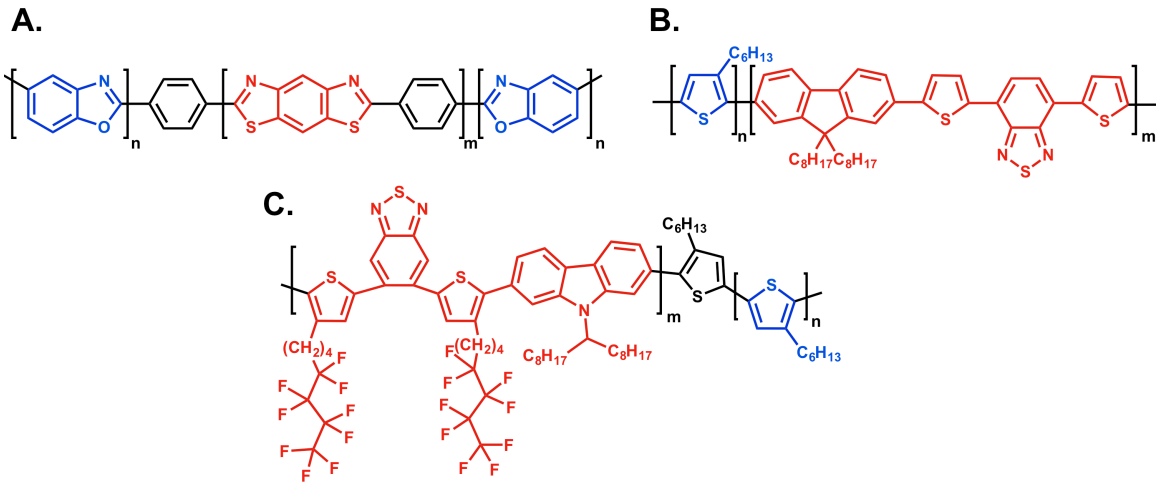

Figure 1.7. (A) Structure of rod-rod triblock copolymer 2,5-PBO-*b*-PBZT-*b*-2,5- PBO.[59] (B) Structure of rod-rod diblock copolymer P3HT-*b*-PFTBT.[118] (C) Structure of rod-rod diblock copolymer SF-PCDTBT-*b*-P3HT.[121] Blue and red represent the donor and acceptor portions of the molecule, respectively.

ROD-COIL BLOCK COPOLYMERS

Rod-coil block copolymers are the most studied type of block copolymers for OPV applications. Two main approaches have been adopted to synthesize rod-coil block copolymers. The first involves the synthesis of an end-functionalized rod polymer, which is subsequently attached to an end-modified coil polymer through a coupling reaction (sometimes referred to as the grafting-to method).[4,113] The advantage to this approach is that it allows for the optimization and complete characterization of each macromolecular block prior to coupling. However, while click chemistry, especially copper(I)-catalyzed alkyne-azide cycloadditions (CuAAC), has been successfully applied to synthesize rod-coil block copolymers in this manner, the low concentration of end groups can lead to lowered yields and the presence of homopolymer impurities.[128–130] In the second approach, an end-functionalized rod polymer is used to initiate the living polymerization of a coil block, usually through atom transfer radical polymerization (ATRP)[29,131–137],

reversible addition-fragmentation chain transfer (RAFT) polymerization[138,139], nitroxide-mediated radical polymerization (NMRP)[25,139–143], anionic polymerization[144,145], ring-opening polymerization (ROP), or ring-opening metathesis polymerization (ROMP) techniques.[146–148.4,38,113] This method, often referred to as the grafting-from method, has been the most widely utilized for synthesizing rod-coil block copolymers. Once synthesized, rod-coil donor-acceptor block copolymers can be utilized as either compatibilizers in BHJ OPVs or as the active layer material themselves.

ROD-COIL BLOCK COPOLYMERS AS COMPATIBILIZERS

When used as compatiblizers, rod-coil donor-acceptor block copolymers can reduce the interfacial energy between the immiscible donor and acceptor components in BHJ blends, leading to improvements in both phase stability and domain size control. In 2006, Fréchet and coworkers reported the first example of this, utilizing a diblock copolymer composed of a P3HT donor block and a C_{60}-containing acceptor block, as shown in **Figure 1.8**.[149] Norbornene end-functionalized P3HT was used as a macroinitiator for the ROMP of a C_{60}-functionalized monomer, resulting in a diblock copolymer with high fullerene content (50 wt%). BHJ blends of P3HT:PCBM are known to be thermally unstable due to the kinetically-trapped, non-equilibrium morphologies that result from spin-casting procedures.[4] While thermal annealing is necessary to promote the crystalline ordering of P3HT, it can also lead to aggregation and phase segregation of PCBM, lowering the interfacial area between the donor and acceptor. Addition of 17 wt% of the synthesized block copolymer to P3HT:PCBM blends resulted in complete disappearance of thermally-induced macrophase separation, as determined by transmission electron microscopy (TEM). Furthermore, stabilized device performance was achieved over longer annealing times.

In 2009, Fréchet and coworkers extended the technology to other blend systems, specifically studying blends of P3HT and PDI derivatives, illustrated in **Figure 1.8**.[150] Fréchet and coworkers synthesized a P3HT-*b*-poly(perylene diimide acrylate) (PPerAcr) block copolymer using RAFT polymerization of a PDI-containing acrylate monomer with a P3HT macroinitiator. The researchers demonstrated that addition of 25 wt% of the block copolymer as a compatibilizer to blend films of P3HT:PDI resulted in improvement of device performances from $\eta = 0.37\%$ to $\eta = 0.55\%$. This improvement was attributed to the formation of smaller, more favorable domain sizes upon addition of the compatibilizing block copolymer.

In the same year, Wudl and coworkers reported the use of a P3HT-*b*-poly(styrene-*co*-acrylate(C_{60})) block copolymer, shown in **Figure 1.8**, for use as a compatibilizer for P3HT:PCBM blend devices, demonstrating an efficiency increase of 35% with addition of only 5 wt% of the donor-acceptor block copolymer.[151] This notable increase in PCE was mainly attributed to an increase in J_{sc} upon addition of the block copolymer compatibilizer, caused by more favorable donor and acceptor domain sizes. There are many more examples of the design and use of donor-acceptor block copolymers as compatibilizers for BHJ blends, demonstrating one useful application of such materials in OPV devices.[152–155]

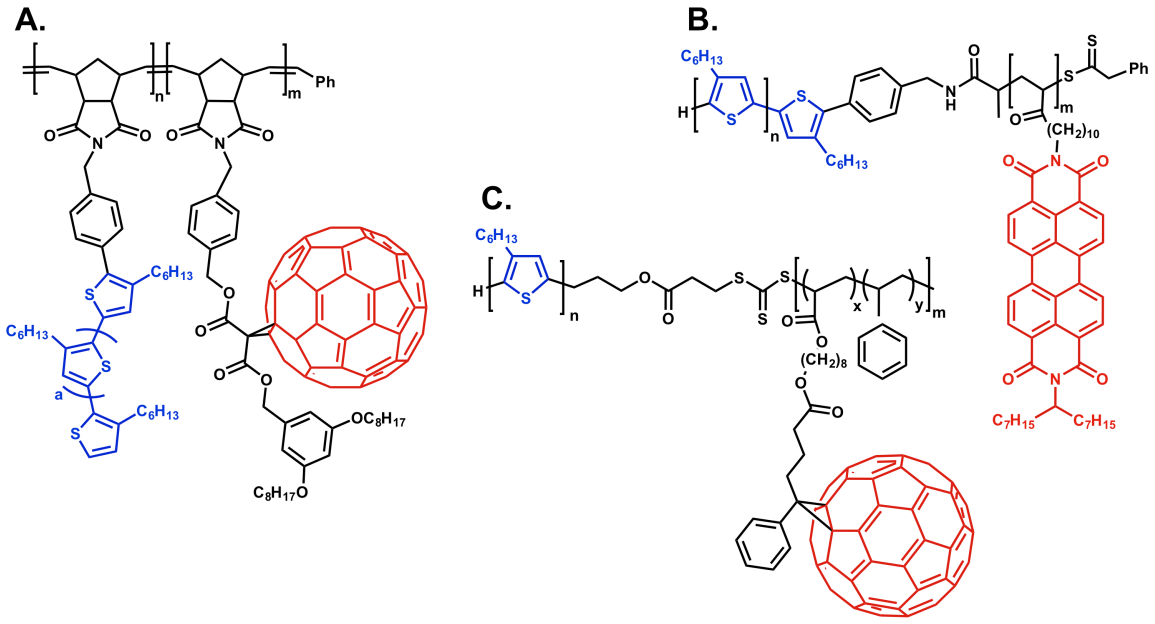

Figure 1.8. Examples of rod-coil block copolymer strucutres used as compatibilizer in BHJ OPVs: (A) Norbornene-based donor-acceptor block copolymer containing P3HT and $PC_{61}BM$ semiconducting moieties;[149] (B) P3HT-*b*-PPerAcr;[150] (C) P3HT-*b*-poly(styrene-*co*-acrylate(C_{60})).[151]

ROD-COIL BLOCK COPOLYMERS AS ACTIVE LAYER MATERIALS

More interesting is the use of rod-coil donor-acceptor block copolymers as the active layer in OPVs. It is an incredible coincidence that the size of the domains formed by microphase separation of block copolymers is on the same length scale as exciton diffusion. If exploited, this could drastically improve OPV efficiencies by facilitating both exciton dissociation and charge percolation in the active layer materials. In 2001, Hadziioannu and coworkers reported one of the first examples of a rod-coil donor-acceptor block copolymer. This system was based on a PPV donor derivative with solubilizing alkoxy groups that was modified with a (2,2,6,6-tetramethyl-piperidin-1-yl)oxyl (TEMPO)-based macroinitiator for the copolymerization of styrene and 4-chloromethylstyrene by NMRP.[25,142] Subsequent functionalization of the 4-

chloromethylstyrene groups with fullerene (C_{60}) through atom-transfer radical addition yielded the desired the rod-coil block copolymer PPV-*b*-PS/PMS(C_{60}), as shown in **Figure 1.9**. Thin films of this donor-acceptor block copolymer demonstrated strong photoluminescence quenching of the PPV donor emission, indicating efficient electron transfer to C_{60}. Moreover, the block copolymer formed ordered microporous honeycomb structures upon casting from carbon disulfide (CS_2). When employed as the active layer in an OPV device, the material demonstrated superior performance to an equivalent blend of the donor and acceptor homopolymers, largely due to a significant increase in J_{sc} for block copolymer device.[25]

As an extension of this donor-acceptor system, Hadziioannou and coworkers developed a new PPV-based nitroxide macroinitiator for the living polymerization of acrylates by NMRP as a possible means to increase the incompatibility of the two blocks (described by χ) and improve the ease of functionalization of the coil block.[156] Morphology comparison studies of rod-coil block copolymers containing alkoxy-substituted PPV (as the rod block) and copolymers of either polystyrene (PS) or polybutylacrylate (PBA) with 4-chloromethylstyrene (used for post-polymerization functionalization with fullerene acceptor moieties) demonstrated that the incorporation of the more flexible butylacrylate polymer allowed for the formation of highly ordered lamellae in thin films.[140] However, the effects of attaching C_{60} moieties onto the coil block on self-assembly behavior were not investigated in this study.

In later studies, the chloromethyl groups were replaced with azido functionality in order to reduce crosslinking and improve the grafting efficiency of C_{60} onto the modified PS.[157,158] This allowed for the use of a cycloaddition reaction to attach the desired fullerenes to the PS copolymer. Subsequent studies demonstrated that grafting density played an important role in the electronic properties of the fullerene acceptor, with

increasing C_{60} content leading to increased electron mobilities (60 wt% fullerene demonstrated charge mobilities of ~2 x 10^{-7} $cm^2V^{-1}s^{-1}$). Still, the electron mobility reported for this block copolymer was much lower than that of pristine $PC_{61}BM$ (~2 x 10^{-1} $cm^2V^{-1}s^{-1}$).[158] In 2008, an extensive study on effects of grafted-C_{60} on the morphology of the PPV-containing rod-coil block copolymer demonstrated that in the absence of the fullerene moieties, lamellar-like fibril structures were formed in bulk and thin films.[159] However, fullerene-containing copolymer films showed no lamellar structure and instead demonstrated the formation of aggregated nanocrystals of C_{60}. This fullerene aggregation dominated molecular self-assembly, introducing a kinetic barrier that impeded rod and coil nanodomain formation in these materials.

In order to overcome some of the challenges associated with PPV donor materials, including poor absorption overlap with the solar spectrum and weakened rod-rod interactions in the crystalline phase,[68,159] polythiophene derivatives, especially P3HT, have been extensively investigated as the donor rod component in rod-coil block copolymers. In 2009, Jo and coworkers reported a rod-coil donor-acceptor block copolymer based on a high molecular weight P3HT rod block used as a macroinitiator for the copolymerization of methyl methacrylate (MMA) and 2-hydroxyethyl methacrylate (HEMA) by ATRP.[132] A fullerene derivative functionalized with a carboxylic acid ([6,6]-phenyl-C_{61}-butyric acid) ($PC_{61}BA$) was chemically grafted to the HEMA units *via* a Steglich esterification process, resulting in ~9 fullerene moieties per copolymer. Annealing thin films of the copolymer resulted in the formation of a bicontinuous nanoscale structure with crystalline P3HT domains and no significant crystallization of the fullerene units. These thin films exhibited almost complete quenching of the P3HT photoluminescence (PL) in comparison to only partial PL quenching in a 1:1

P3HT:$PC_{61}BM$ blend film, indicating that the higher interfacial area in the block copolymer leads to more efficient charge transfer.

In 2010, Hadziioannou and coworkers reported a new rod-coil donor-acceptor block copolymer using regioregular P3HT as the donor rod component and poly(4-vinylpyridine) (P4VP) as the coil component, shown in **Figure 1.9**.[160] In this case, the P4VP block formed weak supramolecular interactions with the electron-deficient $PC_{61}BM$, resulting in $PC_{61}BM$ acceptors that were embedded in the coil domain of the block copolymer. This supramolecular approach allowed for the incorporation of high volume ratios of $PC_{61}BM$ to be used (~36%) without disrupting P3HT ordering or block copolymer nanostructure. Upon annealing, thin films of the P3HT-*b*-P4VP:$PC_{61}BM$ copolymer demonstrated increased structural ordering, while a 1:1 P3HT:P4VP blend exhibited macrophase separation, indicating that the block copolymer provides significantly improved structural and thermal stability. Devices made from P3HT-*b*-P4VP:$PC_{61}BM$ demonstrated very poor performance (η < 0.03%) due to preferential wetting of the P4VP block at the poly(3,4-ethylenedioxythiophene):poly(styrene sulfonate) (PEDOT:PSS) surface, which resulted in accumulation of $PC_{61}BM$ at the anode and introduction of a hole collection barrier. Upon switching to an inverted device configuration with the block copolymer deposited directly on top of the cathode, the efficiency of the device improved to 1.2%. This study demonstrated the importance that fabrication considerations can have on device performance.

In 2015, Thelakkat and coworkers developed a rod-coil donor-acceptor block copolymer containing P3HT as the conjugated donor block and a coil block containing hydroxyl-functionalized styrene moieties to which they grafted $PC_{71}BM$ *via* a Steglich esterification, illustrated in **Figure 1.9**.[161] In this case, each block was synthesized and characterized individually before coupling the copolymer together through a CuAAC

reaction. Subsequent reaction of $PC_{71}BA$ moieties with the hydroxystryene groups in the coil block yielded the donor-acceptor copolymer with near-quantitative grafting efficiency (86%) and an approximately 1:1 P3HT:$PC_{71}BM$ ratio in the final block copolymer. Structural analysis of the resulting material in both bulk and thin films demonstrated an ordered morphology with no indication of fullerene aggregation. This was the first demonstration of microphase ordering of rod-coil block copolymers containing C_{70} fullerene derivatives, which offer the advantage over C_{60} derivatives of an efficient absorption in the visible range.

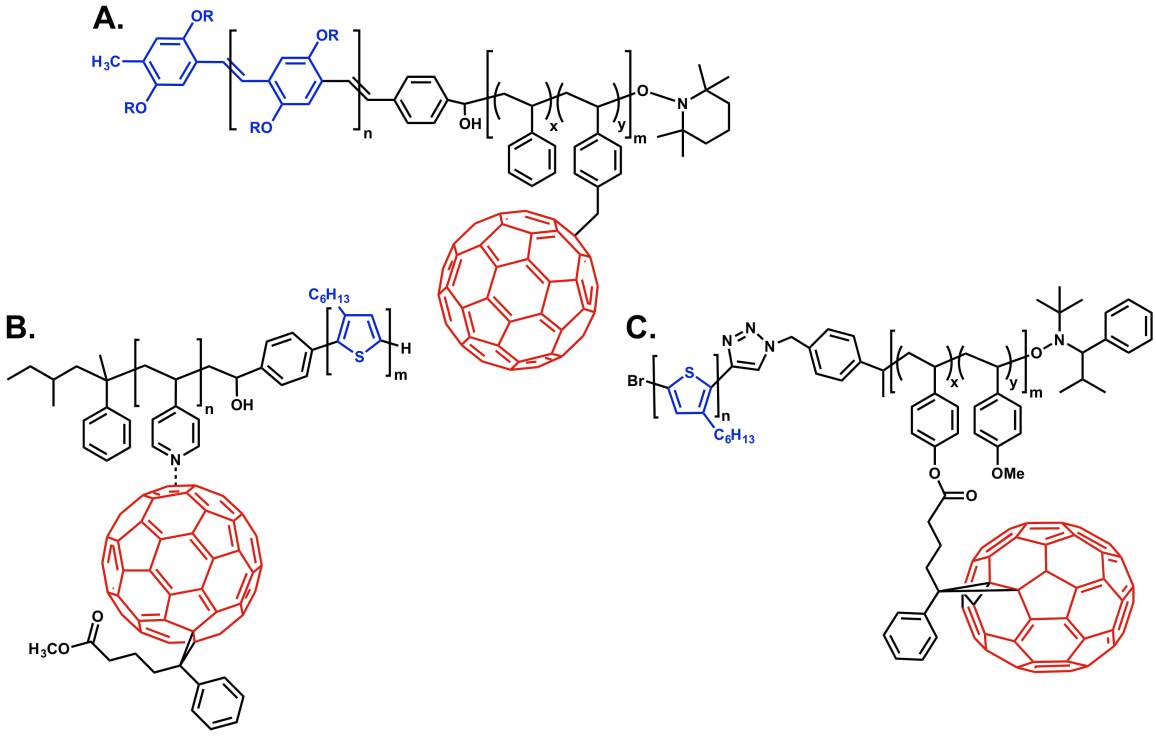

Figure 1.9. Examples of rod-coil block copolymer structures containing conjugated P3HT or PPV as the donor rod polymer and fullerene derivatives attached to a flexible coil polymer as the acceptor component: (A) PPV-*b*-P(S-*co*-MS(C_{60}));[142] (B) P3HT-*b*-P4VP:$PC_{61}BM$;[160] (C) P3HT-*b*-$PC_{71}BM$.[161]

Besides fullerene derivatives, perylene diimide (PDI) semiconductors have been extensively studied as the acceptor component in donor-acceptor block copolymers for use as the active layer of OPV devices. PDI derivatives offer several advantages over fullerene acceptors, including a strong absorbance in the visible region with high molar absorptivity, ease of synthetic modification at both the imide and bay position, high electron mobilities (on the order of 10^{1}-10^{-3} $cm^2V^{-1}s^{-1}$, and good electron-accepting properties due to a well-placed LUMO energy level (~4.0 eV).[115,162–167] In 2008, Thelakkat and coworkers reported a rod-coil block copolymer containing a P3HT donor block and a PPerAcr acceptor block, shown in **Figure 1.10**.[168] This fundamental study demonstrated microphase ordering into a cylindrical structure with randomly oriented cylinders of PPerAcr within a P3HT matrix. While this study did not expand on observed PL quenching of the block copolymer in thin films or demonstrate use of the material in a device, the authors demonstrated the first example of a rod-coil donor-acceptor block copolymer in which both blocks contained crystalline moieties.

Following this initial study, Emrick and coworkers reported the synthesis of a similar P3HT-*b*-PPerAcr copolymer (see **Figure 1.10**), this time incorporating the rod-coil block copolymer in an OPV device.[169] Solvent annealing yielded thin films with fibrillar morphology typical observed for high molecular weight P3HT-containing block copolymers. Complete PL quenching was observed, indicating efficient charge transfer between the two electronically active blocks. Incorporation into an OPV device, followed by a short thermal annealing process, led to an observed device efficiency of 0.49%, which was higher than that achieved by a similar blend device of P3HT and a PDI derivative (PCE = 0.4%).

In 2009, Segalman and coworkers synthesized a donor-acceptor rod-coil block copolymer based on a P3HT rod and a random coil copolymer of poly(butyl acrylate-*co*-

perylene diimide acrylate) (P3HT-*b*-P(BA-*co*-PerAcr)) to study the effects of nanoscale organization on device performance, illustrated in **Figure 1.10**.[29] Here, the butyl acrylate (BA) polymer was used as a plasticizer in the coil block to offset the bulky, crystalline PDI moieties and improve chain mobility and self-assembly behavior. They found that the amount of BA was very important. When in a large excess, the BA in the coil block acted as an insulating layer and had a detrimental impact device performance by limiting charge separation and transport. However, in a ratio of 2:1 BA:PDI, nanoscale organization of the active layer was improved without harming the overall device efficiencies. Furthermore, by controlling the annealing process used for device fabrication, Segalman and coworkers were able to control the degree of order in the self-assembled block copolymers, ranging from disordered polymer films, to short-range poorly-organized structures, to long-range cylindrical nanostructures. The active layers with well-defined but poorly-organized nanodomains had the highest PCE, while the active layer with long-range order performed very poorly. This was attributed to alignment of the ordered cylinders parallel to the electrodes, resulting in poor charge transport in the device. In the case of the short-range, poorly-organized nanostructures, the lack of organization actually resulted in more charge transport pathways, which led to higher device performance. This study illustrated again the importance of percolating, perpendicular pathways to the electrodes in order to have efficient photocurrent generation.

Typically, classical self-assembly behavior isn't observed in rod-coil block copolymers because crystallization dominates over microphase separation. In 2013, Thelakkat and coworkers reported the first example of classical coil-coil phase separation behavior in a rod-coil donor-acceptor block copolymer composed of a crystalline P3HT donor block and a liquid-crystalline PPerAcr acceptor block (see **Figure 1.10**).[170] They

achieved this by synthesizing high molecular weight block copolymers, which provided large enough χN values to allow microphase separation to occur in the melt. Two different block copolymers of P3HT-*b*-PPerAcr with high molecular weight P3HT (containing approximately seventy-five 3-hexylthiophene repeat units) and 47 and 64 wt% PPerAcr, respectively, were synthesized using a combination of CuACC chemisty to synthesize the alkoxyamine-functionalized P3HT, and NMRP, to polymerize the PPerAcr block. X-ray scattering measurements demonstrated that both block copolymers underwent microphase separation at high temperatures with no apparent crystallization. Upon cooling, crystallization of the donor and acceptor moieties occurred within the individual blocks without disrupting the microphase-separated structures. Following the typical coil-coil block copolymer phase diagram, the P3HT-*b*-PPerAcr nanostructures were consistent with those predicted for their respective volume fractions. Structure features of the materials were characterized using small-angle X-ray scattering (SAXS) and TEM measurements for bulk samples. These studies demonstrated that lamellar nanostructures were achieved in the block copolymer containing 47 wt% (44 vol%) PPerAcr with periodicity of ~40 nm, and cylindrical nanostructures were formed in the block copolymer containing 64 wt% (61 vol%) PPerAcr with periodicity of ~49 nm.

Recently, the same group demonstrated that the well-defined lamellar or cylindrical microstructures observed in bulk samples of donor-acceptor block copolymer P3HT-*b*-PPerAcr could be preserved in thin films.[171] The researchers studied both the cylindrical-forming (64 wt% PPerAcr) block copolymer and the lamellar-forming (47 wt% PPerAcr) block copolymers in three different sets of thin films. The first set of thin films was obtained directly from spin-casting without further thermal treatment. This fabrication process led to non-equilibrium, non-crystalline disordered structures. The second set of films was annealed above the melting point of the PPerAcr block (205-215

°C) to induce crystallization of both components without formation of well-developed microstructures. The final set of films was annealed above the melting point of P3HT (250 °C), leading to the formation of well-developed microphase-separated structures that were oriented parallel to the substrate, with crystalline order confined within the respective domains. Importantly, the microstructure periodicity was very similar to that found for the ordered bulk samples. The ordered P3HT-*b*-PPerAcr block copolymer thin films demonstrated ambipolar charge transport, but the measured charge carrier mobilities were lower than those of crystalline homopolymer films, especially for the lamellar microdomain films. The researchers proposed that this was likely due to the parallel orientation of the nanostructures with respect to the electrodes. While this study highlighted the advantage of using donor-acceptor block copolymers for the preparation of well-defined active layer morphologies, it is another example of one of the major challenges facing donor-acceptor block copolymers—achieving vertical alignment of the microstructure for efficient charge transport.

Another approach to rod-coil block copolymers is through the use of low band gap polymer donors in place of P3HT. This approach was recently demonstrated by Russell and coworkers using the low band gap polymer diketopyrrolopyrrole (DPP) as a highly crystalline donor polymer and macroinitiator for the controlled polymerization of a PDI acrylate monomer, yielding the donor-acceptor block copolymer DPP-*b*-PPerAcr, shown in **Figure 1.10**.[172] This polymer demonstrated all the prerequisites of a good OPV material—broad absorption in the visible region of the solar spectrum; good HOMO/LUMO energy level matching between the donor and acceptor, leading to efficient photoluminescence quenching in thin films; and extended π-π conjugation and high crystallinity for high charge carrier mobility. Thin film devices were prepared using this diblock copolymer as the single-material active layer and solvent annealing in

dichloromethane (DCM) yielded a device efficiency of 0.89%, improved from 0.25% in the pristine films.

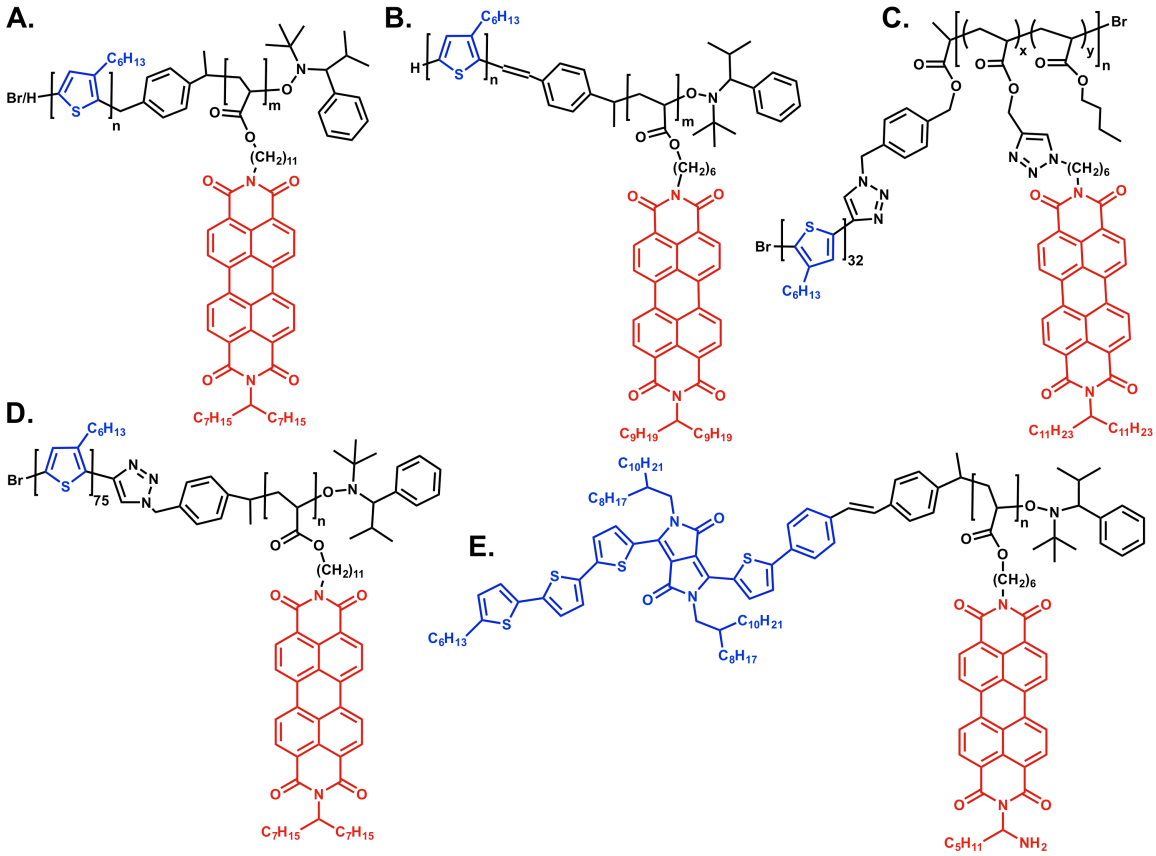

Figure 1.10. Examples of rod-coil donor-acceptor block copolymer structures utilizing a conjugated polymer donor rod block and a coil block containing pendant PDI acceptor moieties: (A) P3HT-*b*-PPerAcr, reported by Thelakkat and coworkers;[168] (B) P3HT-*b*-PPerAcr, reported by Emrick and coworkers;[169] (C) P3HT-*b*-P(BA-*co*-PerAcr), reported by Segalman and coworkers;[29] (D) P3HT-*b*-PPerAcr, reported by Thelakkat and coworkers;[170,171] (E) DPP-*b*-PPerAcr, reported by Russell and coworkers.[172]

COIL-COIL BLOCK COPOLYMERS

While rod-coil polymers are very promising materials for single-layer block copolymer active layers in OPVs, with a lot of progress being made in their development over the last decade, there are still limitations involving the understanding of their self-

assembly behavior. Consequently, there are very few examples of well-defined, nanoscale self-assembly in rod-coil block copolymer systems. Thus, the use of coil-coil block copolymers with pendant donor and acceptor moieties is an attractive option for achieving controllable and predictable nanoscale self-assembly behavior, as they are expected to behave more like traditional amorphous block copolymers. Despite this, there are very few examples of coil-coil donor-acceptor block copolymers in the literature.

One of the first classes of flexible coil-coil block copolymers containing pendant donor and acceptor functionalities was reported by Thelakkat and coworkers and based on pendant triphenylamine donor and perylene bisimide acceptor moieties.[95,173,174] By using NMRP, low polydispersity (*Đ*) block copolymers containing a poly(vinyltriphenylamine) (PvTPA) donor segment and a PPerAcr acceptor segment were synthesized, as shown in **Figure 1.11**. TEM cross-sections of thermally tempered bulk films indicated the formation of PDI nanowires embedded in the amorphous donor matrix for block copolymers with high weight fractions (79%) of PPerAcr.[174] This PvTPA-*b*-PPerAcr polymer was used to fabricate thin film OPV devices. Upon comparison to blend devices composed of the corresponding homopolymers in the same weight ratio (0.21 PvTPA, 0.79 PPerAcr), the block copolymer devices demonstrated a ten-fold increase in efficiency (η_{blend} = 0.007% to $\eta_{copolymer}$ = 0.07% for the block copolymer) and almost a seven-fold increase in J_{sc} ($J_{sc,\ blend}$ = 0.028 mAcm^{-2} to $J_{sc,\ copolymer}$ = 0.19 mAcm^{-2}).[95] This large increase was attributed to the favorable morphology of the block copolymer film, which showed nanoscale structure compared to the micrometer-sized domains found in the blend thin film. However, the nanoscale domains exhibited by the block copolymer were aligned preferentially parallel to the electrodes, resulting in the poor device performance.

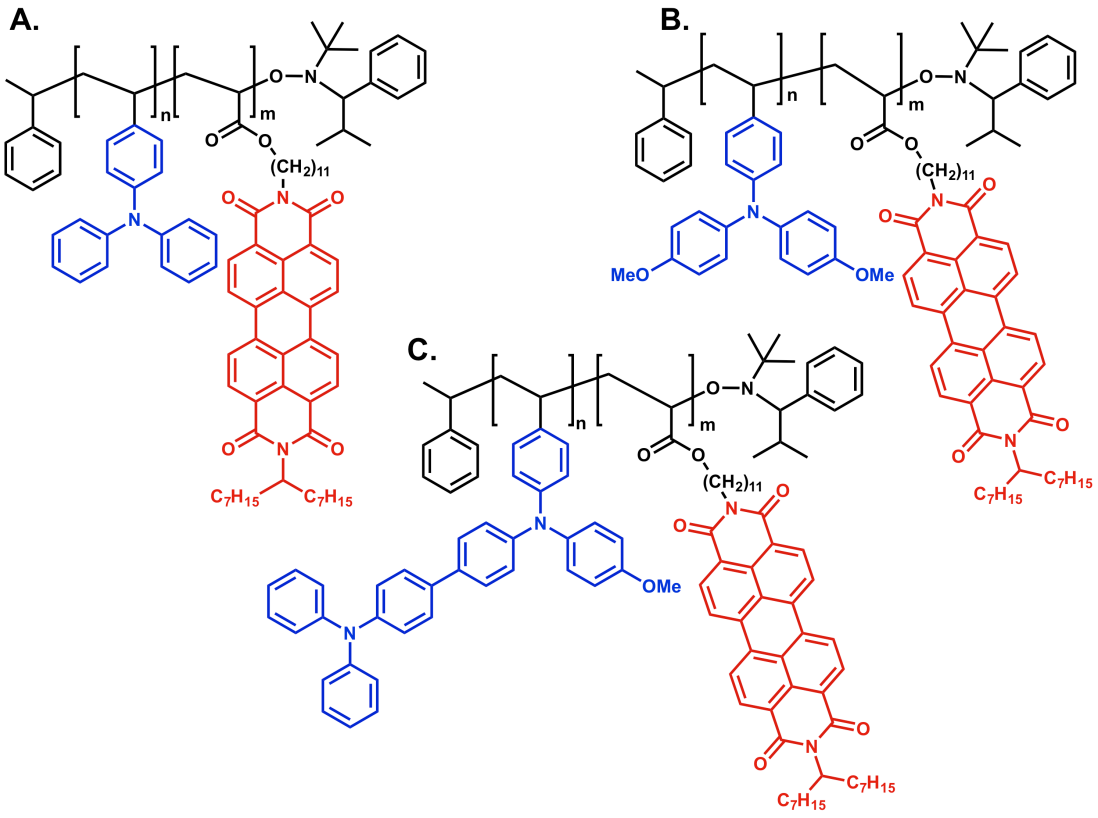

Figure 1.11. Examples of coil-coil block copolymer structures described in the literature: (A) PvTPA-*b*-PPerAcr; [95,173–175] (B) PvDMTPA-*b*-PPerAcr;[173] (C) PvDMTPD-*b*-PPerAcr.[173]

In a subsequent study, Thelakkat and coworkers synthesized a series of modified tripheylamine donors to incorporate into the donor-acceptor block copolymer as a way to study the effects of the HOMO energy level and morphology differences on OPV performance.[173] In this case, the donor segment of the block copolymer was composed of either poly(bis(4-methoxyphenyl)-4'-vinylphenylamine) (PvDMTPA) or poly(*N*,*N*'-bis(4-methoxyphenyl)-*N*-phenyl-*N*'-4-vinylphenyl-1,1'-biphenyl)-4,4'-diamine) (PvDMTPD) (see **Figure 1.11**). By using high PPerAcr weight fractions (72-86%), all of the diblock copolymers exhibited microphase-separated domains in the form of either long wire-like or short worm-like structures made of crystalline PDI embedded in the

donor matrix, based on the donor block length. The new donor polymers exhibited equivalent HOMO energy levels of 4.96 eV, compared to 5.24 eV for PvTPA. Upon incorporation into single-layer OPV devices, the PvDMTPD-*b*-PPerAcr device exhibited a four-fold improvement in PCE (η = 0.26%, J_{sc} = 1.21 mAcm^{-2}) and the PvDMTPA-*b*-PPerAcr exhibited a five-fold increase in PCE (η = 0.32%, J_{sc} = 1.14 mAcm^{-2}) compared to the previously studied PvTPA-*b*-PPerAcr (η = 0.07%, J_{sc} = 0.23 mAcm^{-2}). Furthermore, it was found that the long wire-like nanostructures were much more favorable for charge percolation.

In another study using the same PvTPA-*b*-PPerAcr block copolymer, the influences of molecular weight and phase segregation on charge separation, recombination, and device performance were investigated.[175] A series of block copolymers with weight ratios ranging between 73-90% PPerAcr and number-average molecular weights (M_n) between 9 kg/mol to 38 kg/mol were compared to a blend of the two homopolymers composed of 85 wt % PPerAcr and 15 wt % PvTPA. In thin film, the lowest molecular weight polymer exhibited the highest degree of PL quenching (99% quenched compared to pristine PPerAcr), with all three block copolymer films exhibiting higher PL quenching than the corresponding blend film (62% quenched). These results suggest that the proximity of generated excitons to interfacial boundaries in the block copolymer films leads to more efficient charge transfer. TEM images showed that as the molecular weight of the block copolymers decreased, the domain size of the associated wire-like structure also decreased (from approximately 25 nm to 12 nm). No ordered structures were observed in the smallest block copolymer film, likely due to a low order-disorder transition (ODT) temperature below room temperature as a result of the low degree of polymerization. Devices made with the intermediate molecular weight block copolymer, which demonstrated the smallest domain size, exhibited an average η =

0.075% and J_{sc} = 0.301 mAcm^{-2}, with a maximum PCE of η = 0.11%. Excitingly, this device outperformed the blend device by a factor of four.

CONCLUSION

While there has been a lot of progress in OPV research over the past two decades, the continued development of organic semiconducting materials, as well as an improved understanding of morphology and stability control of the active layer, is still needed. By addressing the major bottlenecks in OPV photocurrent generation, specifically charge separation and charge transport, OPVs can begin to complement, and even compete with, current inorganic solar technologies. Block copolymers containing donor and acceptor moieties, either as conjugated rod blocks or as semiconducting pendant groups, are promising materials for the continued development of OPVs. Many studies have demonstrated their potential as both compatibilizers for BHJ morphologies, as well as the stand-alone component in OPV active layers. One of the most significant challenges remaining for donor-acceptor block copolymers is achieving a microphase-separated structure with percolating pathways aligned perpendicular to the electrodes.

Chapter 2: Synthesis and Characterization of Norbornene-Type Donor and Acceptor Polymers using Ring-Opening Metathesis Polymerization

INTRODUCTION

Ring-opening metathesis polymerization (ROMP) is a living polymerization method in which an olefin, as part of a strained ring, undergoes cycloaddition with a metal alkylidene to create a metallocyclobutane (see **Figure 2.1**). One of the driving forces for ROMP is the relief of ring strain upon creation of the metallocycle, and each subsequent ring opening adds a monomer to the growing polymer chain through a catalyzed metathesis reaction. The slow turnover mechanism and the creation of a bulky polymer leads to consistently slow termination. As a result, the polymerization follows so-termed "living" conditions—characterized by rapid and complete initiation, irreversible propagation steps, and the absence of undesired termination or chain transfer reactions—yielding reproducible, precise polymers with low polydispersity indices.[176–180] In 2005, Schrock, Grubbs, and Chauvin received the Nobel Prize for their work on the study and development of ROMP using tungsten (W), molybdenum (Mo), and ruthenium (Ru) alkylidene catalysts. Their work has pioneered an entire field. The living nature of ROMP, coupled with mild reaction conditions and high functional group tolerance, allows for the synthesis of novel and interesting polymer architectures. These architectures include functional block copolymers, dendrimer or star-type branched polymers, and scaffold polymers for supramolecular assemblies.[176,181] By utilizing functionalized monomers (typically norbornene-type strained ring systems), or introducing functionality through modifications to the catalyst carbenoid ligands or termination reagents, polymers with precise and controllable functional groups can be synthesized with relative ease (see **Figure 2.1**). Furthermore, post-polymerization functionalization can also be utilized, and as an additional reactive handle, the double

bonds in the polymer backbone are also available for post-polymerization derivatization.[178,179] By tuning the polymer structure by ROMP, it is not only possible to define the quantity and the site(s) of the functional group(s), but also to build up regular, self-assembled structure through the construction of diblock- or mulitblock-copolymers. For these reasons, ROMP has been used to develop functional polymers for a myriad of applications including chemosensing, optoelectronics, bioimaging, self-healing materials, photoreactive materials, and lithography.

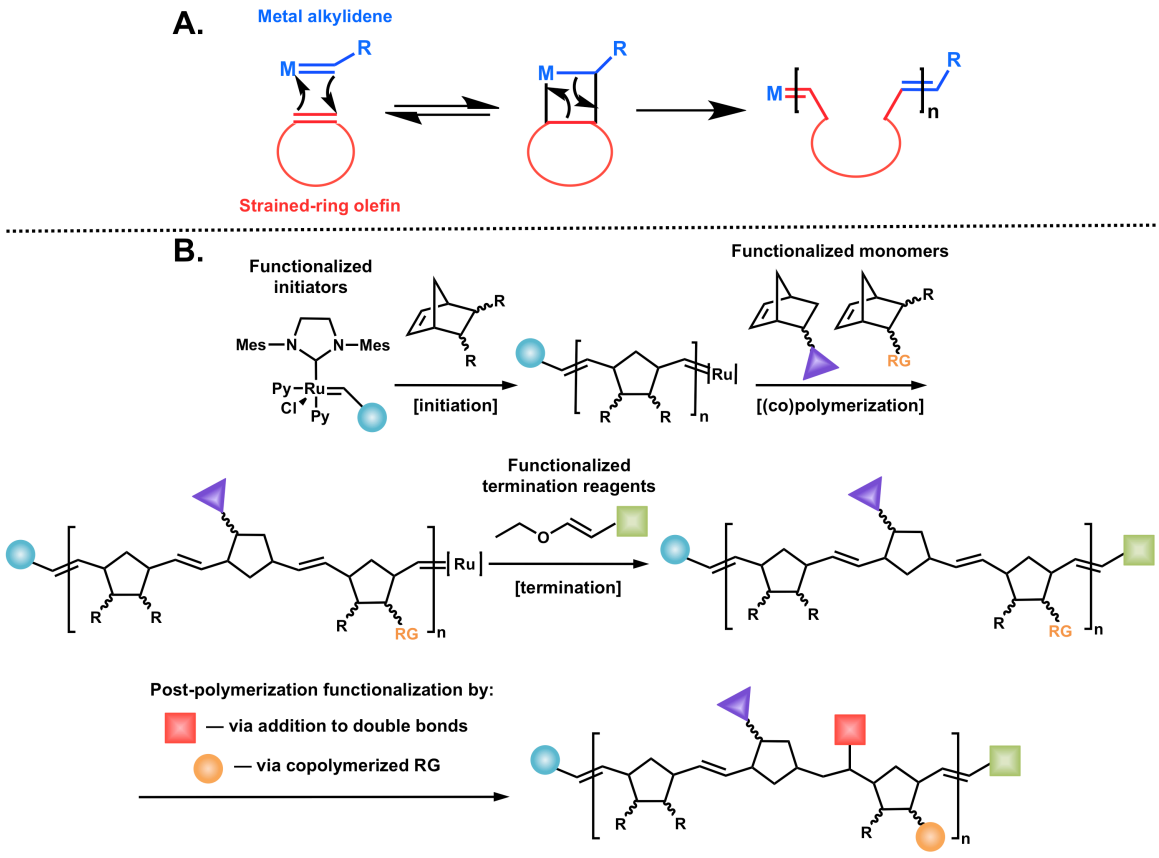

Figure 2.1. (A) Mechanism of ring-opening metathesis polymerization; (B) Possible functionalization pathways of ROMP polymers. Illustration adapted from ref [178].

Particularly interesting to organic photovoltaic applications (OPV) applications are ROMP polymers functionalized with organic semiconductors or conjugated ROMP polymers.[182] Conceptually, the most direct way of imparting optoelectronic functionality into ROMP polymers is through the functionalization of norbornene-type monomers with semiconducting pendant group. For example, in 2009 Kilbinger and coworkers reported the synthesis of polymerizable oligo(thiophene amide) monomers and the resultant ROMP block copolymerization with a linear solubilizing block (see **Figure 2.2**).[183] They found that neither the polymerization nor the presence of the solubilizing polymer significantly affected the electronic properties of the oligo(thiophene amide). Furthermore, drop-cast films onto a TEM grid demonstrated partial phase-separation into lamellar-type structures.

In 2012, Marder and coworkers designed norbornene-type monomers using perylene-3,4,9,10-tetracarboxylic diimides (PDI) as n-type materials. The PDI units were tethered to the norbornene moiety by either one of the imide nitrogen atoms or via linkage to the bay-position on the perylene core (see **Figure 2.2**).[184] After polymerization, the imide-linked PDI moieties demonstrated aggregation behavior by UV-Vis spectroscopy and powder X-ray diffraction (p-XRD). This pi-stacking behavior led to n-channel field-effect transistor behavior. Interestingly, the polymer with the bay-linked PDI moieties showed a monomer-like UV-Vis spectrum and no evidence for pi-stacking, leading to no measurable transistor behavior.[179,184] The large differences observed between the two PDI-containing polymers resulted from poor alignment of the conjugated PDI molecules along the polymer chain in the bay-tethered polymer as a result of unfavorable steric interactions of the solubilizing alkyl chains. This study demonstrates the importance of orientation and alignment of the pendant semiconductors on charge transport properties.

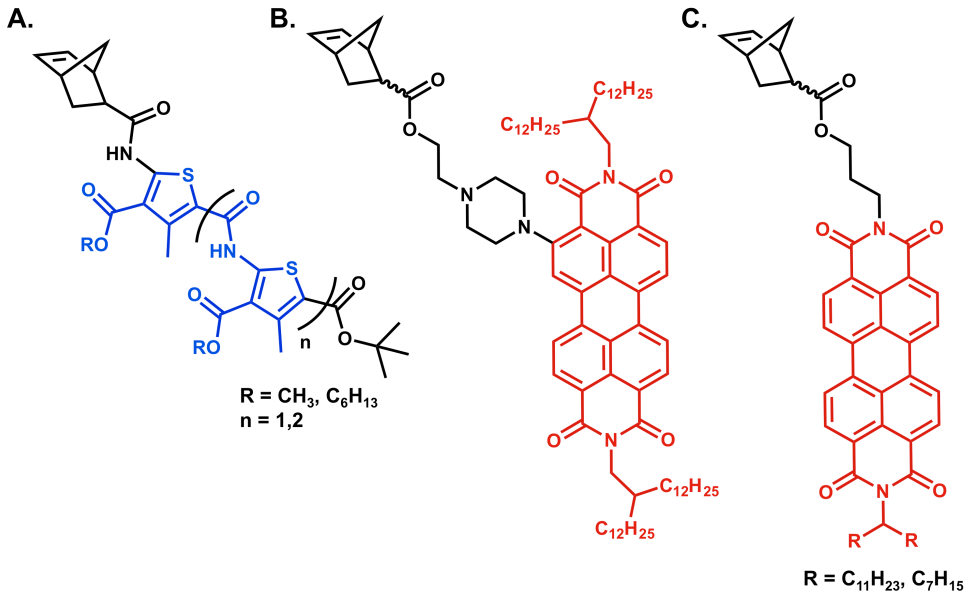

Figure 2.2. Examples of norbornene-type monomers with semiconducting pendant groups: (A) Oligo(thiophene amide)[183]; (B,C) Norbornene-type perylene diimides.[184]

Oligomers can serve as interesting materials to examine the electronic behavior of conjugated polymer systems such as polythiophene. The conductivity of polythiophene is a result of the conjugation of the aromatic thiophene rings through direct aromatic-aromatic (C_{sp2}—C_{sp2}) linkage. Polythiophenes can be drawn as either an aromatic structure with single bonds connecting the thiophene rings or as a quinoid structure in which the heterocycles are connected via double bonds (see **Figure 2.3**).[98,183,185] Polythiophenes offer highly conjugated systems in which π-electrons can be relatively easily removed without significant disruption to the polymer system. The quinoid character in polythiophenes is enhanced in the oxidized state and increases the conductivity of holes, making these effective hole-transporting materials.[185] Regioregular poly(3-hexylthiophene) (P3HT) is commonly used as the light absorber in efficient OPVs, with a band gap of 1.85 eV.[31] However, the high melting temperatures of P3HT

can lead to competition between crystallization and self-assembly, and block copolymers containing P3HT often demonstrate a fibrillar structure that may result from this competing crystallization.[31] Furthermore, it can be difficult to achieve the precise head-to-tail (HT) regioregularity required for good electrical conductivity in P3HT. Irregular couplings, such as head-to-head (HH) and tail-to-tail (TT) couplings, force the thiophenes to twist due to the steric demands associated with orientation of the alkyl chains. This can increase the band gap of the material, as well as lower of the conductivity.[186,187] While there are several methods to synthesize regioregular P3HT, such as the GRIM polymerization method,[186,188,189] oligothiophenes can serve as good models for the polymeric system. Oligothiophenes are promising as p-type materials due to strong absorption over a broad range of the solar spectrum, good charge mobility, and suitable frontier molecular orbital energy levels.[190] In addition, regiochemistry can be controlled, and chain and conjugation lengths are well defined.

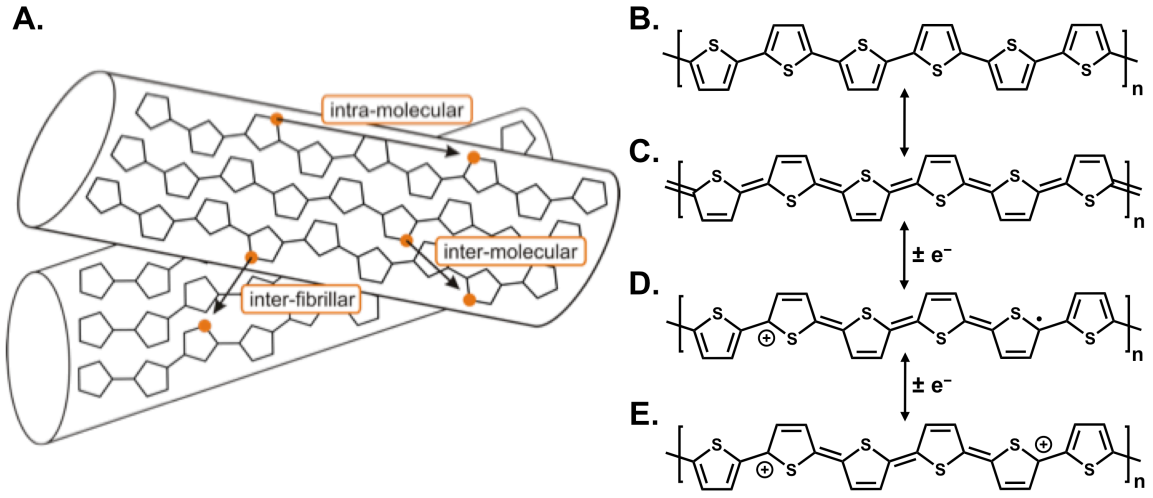

Figure 2.3. (A) Schematic representation of the potential conduction pathways of polythiophene in the solid state; (B–E) Structures of polythiophene and proposed charged species in oxidized polythiophene: (B) Aromatic structure of polythiophene, (C) Quinoid structure of polythiophene, (D) Polaron formation, (E) Bipolaron formation. Illustration adapted from ref [185].

Herein, the synthesis of norbornene-type monomers functionalized with a terthiophene (Ter) or sexithiophene (Sexi) donor pendant groups, which serve as oligomeric substitutes for P3HT, or a perylene diimide (PDI) acceptor pendant groups will be discussed. These norbornene-type monomers can be polymerized utilizing ROMP to achieve well-defined polymeric semiconducting materials. These homopolymers are characterized by photophysical and electrochemical methods to determine viability as donor and acceptor materials for OPV applications.

EXPERIMENTAL

Instrumentation

Nuclear magnetic resonance (NMR) spectroscopy was carried out on a Varian DirectDrive 400 MHz or 500 MHz spectrometer at ambient temperature, and specta were referenced internally to the residual solvent peaks. All chemical shifts are reported in ppm and coupling constants are given in Hertz (Hz). Absorption spectra were obtained on a Varian Cary 6000i UV-Vis-NIR spectrophotometer in Starna quartz fluorimeter cells with a 1.0 cm path length. Mass spectroscopy was performed with a Micromass Autospec Ultima HRMS (for CI^+) or an Agilent 6530 Q-TOF system (for ESI^+). Elemental analysis was performed by QTI, Whitehouse, NJ (www.qtionline.com). Gel permeation chromatography (GPC) was done on an Agilent 1100 Series Instrument with Viscoteck Triple Array Detector 302 Series in THF. Thermal gravimetric analysis (TGA) was performed on TA Instruments TGA Q50 under inert N_2 atmosphere with 3.5 °C/min ramp to 500 °C and then 8.0 °C/min ramp to 800 °C. Differential scanning calorimetry (DSC) was performed on a Mettler Toledo DSC-1 instrument model. All DSC samples ranged from 5-8 mg and followed the same run procedure with a N_2 flow rate of 50 mL/min: (1) Isothermal at 30 °C for 2 min; (2) Heating from 30 °C to 100 °C at 10 °C/min to remove

water and any residual solvent; (3) Isothermal at 100 °C for 2 min; (4) Cooling from 100 °C to 30 °C at 10 °C/min; (5) Isothermal at 30 °C for 2 min; (6) Heating from 30 °C to 350 °C at 10 °C/min; (7) Isothermal at 350 °C for 2 min; (8) Cooling from 350 °C to 30 °C at 10 °C/min. Fluorimetry experiments were carried out on a Photon Technology International QuantaMaster 4 spectrophotometer equipped with a 6-inch diameter K Sphere-B integrating sphere and using PTI software. All solution measurements were recorded in Starna quartz fluorimeter cells with a path length of 1.0 cm in dicholoromethane (DCM), unless otherwise noted. For quantum yield measurements, an integrating sphere was used. Quantum yields were calculated by dividing the area under the emission peak by the difference between the area under the excitation peak of the sample and the blank solution ($A_{em,\ sample}$ / ($A_{ex,\ blank}$ – $A_{ex,\ sample}$)). The reported quantum yields are the average of three trials.

Electrochemistry

Electrochemical experiments were carried out in a dry box under a N_2 atmosphere using a GPES system from Eco. Chemie B. V. All electrochemical experiments were performed using a three-electrode cell with a $Ag/AgNO_3$ reference electrode (silver wire in a 0.01 M silver nitrate solution with 0.1 M $[(n\text{-}Bu)_4N]^+[PF_6]^-$ ($TBAPF_6$) in acetonitrile), a 1.6 mm Pt button working electrode, and a Pt wire coil counter electrode. All measured potentials were referenced to the ferrocene/ferrocenium redox couple (Fc/Fc^+) as determined by the average of the $E_{1/2}$ values obtained before and after the experiment. The supporting electrolyte used was 0.1 M tetrabutylammonium hexafluorophosphate ($TBAPF_6$), purified by three successive recrystallizations from hot ethanol and dried for three days at 100-150 °C under high vacuum before use. All measurements were carried

out in DCM with scan rate of 100 mVs^{-1}. The HOMO and LUMO energy levels were found from the onset of oxidation and reduction, respectively, using **Equations 2.1**, **2.2**:

$$E_{HOMO} = [(E_{ox} - E_{1/2\ Fc}) + 4.8\ eV] \quad (\mathbf{2.1})$$

$$E_{LUMO} = [(E_{red} - E_{1/2\ Fc}) + 4.8\ eV] \quad (\mathbf{2.2})$$

Synthesis

General Considerations

Air- and/or moisture-sensitive reactions were carried out in heat-gun-dried glassware using standard Schlenk techniques under a dry N_2 atmosphere. Dry solvents were collected in solvent bulbs from an Innovative Technology PureSolv 400 solvent purification system and stored over 3Å molecular sieves. *N*-bromosuccinimide (NBS) was recrystallized from deionized (DI) H_2O before use. All other chemicals were used as received from commercial suppliers unless otherwise specified. Thin layer chromatography (TLC) was performed using Silicycle silica gel 60 F_{254} pre-coated aluminum sheets. Column chromatography was performed using Silicycle Silica Flash® F60.

Synthesis of Terthiophene and Sexithiophene Donor Monomers [2.1—2.21]

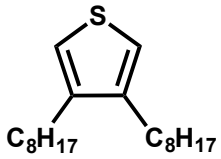

3,4-dioctylthiophene [2.1]: 3,4-dibromothiophene (40.32 g, 18.43 mL, 166.7 mmol) and Ni(dppp)Cl_2 (0.65 g, 1.2 mmol) were dissolved in dry diethyl ether (400 mL) in a dry three-neck round-bottomed flask equipped with a reflux condenser and addition funnel under N_2. The reaction vessel was cooled to 0 °C in an ice bath. Octylmagnesium

bromide (2M in Et_2O, 200 mL, 400 mmol) was transferred to the addition funnel *via* cannula and added dropwise to the stirring reaction solution over approximately 2 hrs. Upon complete addition of the Grignard reagent, the reaction was warmed to room temperature and then heated at reflux overnight under a N_2 atmosphere. Upon completion, the reaction was dark brown in color. The reaction was cooled to 0 °C in an ice bath and concentrated HCl (50 drops) in DI H_2O (200 mL) was added dropwise to quench the reaction. Upon addition of the acidic solution, the reaction violently bubbled and went from a dark brown, homogeneous solution to an opaque light brown, heterogenous solution. The precipitated solid was removed *via* vacuum filtration through celite. The remaining solution was transferred to a separatory funnel, diluted with DI H_2O (500 mL), and extracted with DCM (3 x 200 mL). The combined organic phase was dried over $MgSO_4$, vacuum filtered, and concentrated *in vacuo* to afford a light brown oily solution. The crude material was further purified by vacuum distillation (bath temperature: 180 °C – 210 °C, bp: ~ 140 °C – 180 °C) to yield a clear, light brown oil (40.16 g, 78%). ^{1}H NMR (400 MHz, $CDCl_3$) δ: 6.89 (s, 2H), 2.51 (t, 4H, J = 8.0), 1.62 (m, 4H), 1.34 (m, 20H), 0.89 (t, 6H, J = 6.2).

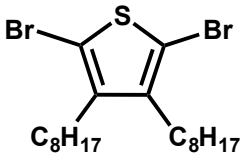

2,5-dibromo-3,4-dioctylthiophene [2.2]: 2.1 (43.36 g, 140.7 mmol) was dissolved in dimethylformamide (DMF, 900 mL) in a foil-wrapped round-bottomed flask and cooled to 0 °C in an ice bath. NBS (49.42 g, 277.8 mmol) was dissolved in DMF (500 mL) and added dropwise to the stirring solution over 2 hrs *via* a foil-wrapped addition funnel. The reaction was warmed to room temperature overnight. Upon

completion, the reaction was quenched with aqueous sodium thiosulfate ($Na_2S_2O_3$, 1000 mL), transferred to a separatory funnel, and extracted with hexanes (6 x 500 mL). The combined organic phases were washed with DI H_2O (4 x 200 mL) and brine (2 x 500 mL), and dried over $MgSO_4$. The filtered solution was concentrated *in vacuo* to afford a clear yellow oil (65.60 g, 98%). ^{1}H NMR (400 MHz, $CDCl_3$) δ: 2.51 (t, 4H, J = 8.0), 1.46 (m, 4H), 1.31 (m, 20H), 0.88 (t, 6H, J = 6.8).

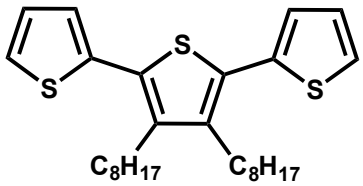

3',4'-dioctyl-2,2':5',2''-terthiophene [2.3]: 2.2 (26.22 g, 56.2 mmol), 2-(tributylstannyl)thiophene (58.75 g, 50.0 mL, 157.4 mmol), LiCl (11.91 g, 281.0 mmol), and $PdCl_2(PPh_3)_2$ (2.13 g, 3.0 mmol) were dissolved in DMF (300 mL) in a round-bottomed flask equipped with a reflux condenser. The reaction solution was heated at reflux in a hot oil bath overnight, during which the reaction became dark brown in color. Upon completion, the reaction was cooled to room temperature, transferred to a separatory funnel, and extracted with hexanes (3 x 300 mL). The combined organic phases were washed with 1M NaOH (aq) (2 x 150 mL) and DI H_2O (1 x 200 mL), dried over $MgSO_4$, vacuum filtered, and concentrated *in vacuo*. The crude product was purified by silica gel column chromatography (hexanes) to afford the desired product as a light green oil (26.55 g, 97%). ^{1}H NMR (400 MHz, $CDCl_3$) δ: 7.31 (dd, 2H, J = 5.0, 1.2), 7.14 (2H, dd, J = 3.6, 1.2), 7.07 (dd, 2H, J = 5.2, 3.6), 2.69 (m, 4H), 1.57 (m, 4H), 1.41 (m, 4H), 1.30 (m, 16H), 0.89 (m, 6H). ^{13}C {^{1}H} NMR (100 MHz, $CDCl_3$) δ: 140.08, 136.21, 129.79, 127.30, 125.82, 125.25, 31.88, 31.39, 30.76, 29.90, 29.26, 28.13, 22.69, 14.12.

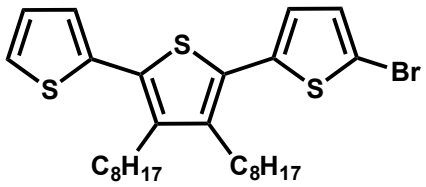

5-bromo-3',4'-dioctyl-2,2':5',2''-terthiophene [2.4]: 2.3 (4.65 g, 9.8 mmol) was dissolved in DMF (100 mL) in a round-bottomed flask equipped with an addition funnel. The reaction vessel was wrapped in aluminum foil and cooled to 0 °C in an ice bath with stirring. NBS (1.73 g, 9.8 mmol) was dissolved in DMF (50 mL) in a foil-wrapped erlenmeyer and transferred to the addition funnel, which was then sealed with a rubber septum and kept under N_2. The NBS solution was added dropwise to the stirring solution of terthiophene over 1 hr. After the NBS addition was completed, the reaction was warmed to room temperature overnight. Upon completion, the reaction was quenched with aqueous $Na_2S_2O_3$ (200 mL) and extracted with DCM (3 x 150 mL). The organic phases were combined and washed with DI H_2O (3 x 150 mL), brine (1 x 100 mL), and dried over $MgSO_4$. The filtered solution was concentrated *in vacuo* to remove DCM and the crude material was purified by silica gel column chromatography (hexanes). The collected pure material was isolated by rotary evaporation to afford a light green oil (3.90 g, 73% yield). ^{1}H NMR (400 MHz, $CDCl_3$) δ: 7.30 (dd, 1H, J = 5.2, 1.2), 7.11 (dd, 1H, J = 3.6, 1.2), 7.05 (dd, 1H, J = 5.2, 3.6), 6.99 (d, 1H, J = 4.0), 6.86 (d, 1H, J = 4.0), 2.65 (m, 4H), 1.52 (m, 4H), 1.38 (m, 4H), 1.28 (m, 16H), 0.88 (t, 6H, J = 7.2). ^{13}C {^{1}H} NMR (100 MHz, $CDCl_3$) δ: 140.60, 140.10, 137.74, 135.91, 130.36, 130.15, 128.78, 127.35, 126.05, 125.99, 125.46, 111.72, 31.87, 30.78, 30.78, 30.72, 29.83, 29.23, 28.08, 22.69, 14.12. HRMS (CI^+): calcd for $C_{28}H_{39}BrS_3$ m/z 552.1377, found 552.1364.

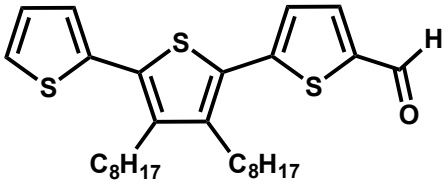

3',4'-dioctyl-[2,2':5',2''-terthiophene]-5-carbaldehyde [2.5]: Finely-ground magnesium turnings (0.48 g, 19.7 mmol) were suspended in dry THF (30 mL) in a three-neck round-bottomed flask fitted with a reflux condenser under N_2. Dibromoethane (77 μL, 0.90 mmol) was added in one portion. **2.4** (9.88 g, 17.9 mmol) was dissolved in dry THF (10 mL) in a second round-bottomed flask under N_2 and transferred *via* cannula to the stirring reaction mixture. The reaction was heated at reflux overnight. Upon completion, the reaction solution was transferred *via* cannula to a clean three-necked flask fitted with a reflux condenser under N_2. Dry DMF (3.44 mL, 44.8 mmol) was added dropwise, and the reaction was heated at reflux overnight. Upon completion, the reaction was removed from heat, cooled to room temperature, and then cooled to 0 °C in an ice bath. 1.0 M HCl (35 mL) was added dropwise, and the reaction mixture was transferred to a separatory funnel, and extracted with DCM (4 x 50 mL). The combined organic phase was titrated with 10% aqueous KOH until the solution was neutral and then separated, washed with brine (1 x 100 mL), and dried over $MgSO_4$. The filtered solution concentrated *in vacuo* and the crude material was purified by silica gel column chromatography (1:1 v/v hexanes:DCM). The pure material was concentrated *via* rotary evaporation to afford a viscous dark maroon oil (4.94 g, 55%). ^{1}H NMR (400 mHz, $CDCl_3$) δ: 9.88 (s, 1H), 7.70 (d, 1H *J* = 4), 7.35 (dd, 1H *J* = 4.8, 1.2), 7.23 (d, 1H *J* = 4.4), 7.17 (dd, 1H *J* = 3.6, 1.2), 7.08 (dd, 1H *J* = 5.2, 3.6), 2.76 (t, 2H *J* = 8), 2.69 (t, 2H *J* = 8.4), 1.55 (m, 4H), 1.41 (m, 4H), 1.29 (m, 16H), 0.89 (t, 6H *J* = 6.8). ^{13}C {^{1}H} NMR (400 mHz, $CDCl_3$) δ: 182.63, 146.52, 142.08, 140.75, 136.87, 135.49, 132.23, 128.70,

127.51, 126.41, 126.02, 31.88, 30.71, 30.44, 29.92, 29.86, 29.24, 28.42, 28.05, 22.67, 14.14.

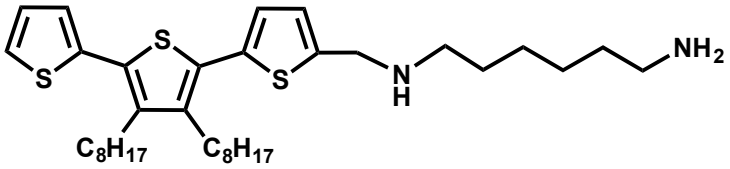

N1-((3',4'-dioctyl-[2,2':5',2''-terthiophen]-5-yl)methyl)hexane-1,6-diamine

[2.6]: 1,6-diaminohexane (2.49 g, 21.2 mmol) was dissolved in MeOH (65 mL) in a three-necked round-bottomed flask fitted with a reflux condenser and an addition funnel under N_2. **2.5** (3.54 g, 7.1 mmol) dissolved in 1:1 v/v MeOH:$CHCl_3$ (350 mL) was added dropwise *via* the addition funnel to the stirring amine solution over 6 hrs. Upon complete addition, the reaction was heated at reflux overnight. After cooling to room temperature, $NaBH_4$ (1.07 g, 28.2 mmol) was added in small portions and the reaction was stirred overnight at room temperature. Once completed, the reaction was concentrated *in vacuo*, redissolved in DCM (250 mL), and washed with DI H_2O (4 x 250 mL) and brine (1 x 200 mL). The organic phase was concentrated *in vacuo*, and the crude material was redissolved in hexanes (250 mL), washed with DI H_2O (4 x 250 mL) and brine (1 x 250 mL), and dried over $MgSO_4$. The filtered solution was concentrated *in vacuo* to afford a viscous orange oil (3.78 g, 89%). ^{1}H NMR (400 mHz, $CDCl_3$) δ: 7.27 (dd, 1H *J* = 5.2, 1.2), 7.09 (dd, 1H *J* = 3.6, 1.2), 7.03 (dd, 1H *J* = 5.2, 3.6), 6.93 (d, 1H *J* = 3.6), 6.83 (d, 1H *J* = 3.2), 3.95 (s, 2H), 2.65 (m, 6H), 1.53-1.24 (m, 40H), 0.85 (t, 6H *J* = 4). HRMS (CI^+): calcd for $C_{35}H_{56}N_2S_3$ *m/z* 600.3606, found 600.3603.

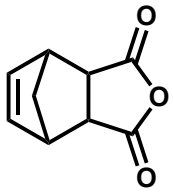

3a,4,7,7a-tetrahydro-4,7-methanoisobenzofuran-1,3-dione [2.7]:

Dicyclopentadiene (DCPD) (150 mL) was freshly cracked *via* a short path distillation (bath temperature: 180 °C, bp: ~ 60 °C) and collected into a massed round-bottomed flask to afford a clear liquid (86.46 g, 110 mL, 1189.0 mmol). Maleic anhydride (116.60 g, 1189.0 mmol) was freshly ground with a mortar and pestle, then transferred to a 2 L erlenmyer flask with benzene (1 L) and heated gently to (mostly) dissolve. The reaction vessel was cooled to 0 °C in an ice bath and cyclopentadiene was added *via* pipette. The ice bath was removed and the reaction was warmed to room temperature. After 15 minutes of stirring, a large amount of white, fluffy solid crashed out of solution. The reaction was stirred overnight. Upon completion, a series of precipitations were performed by adding hexanes to the mother liquor solution (benzene), cooling to 0 °C over an hour, and collecting the white solid via vacuum filtration until no further precipitate was collected. The solid fractions were combined and dried under high vacuum to afford a white solid that ranged from fluffy to crystalline needles (159.41 g, 82%). ^{1}H NMR (400 MHz, $CDCl_3$) δ: 6.32 (t, 2H, J = 1.8), 3.58 (m, 2H), 3.51 (m, 2H), 1.78 (dt, 1H, J = 9.2, 1.8), 1.57 (d, 1H, J = 9.3). ^{13}C {^{1}H} NMR (100 MHz, $CDCl_3$) δ: 171.25, 135.52, 52.74, 47.05, 46.10.

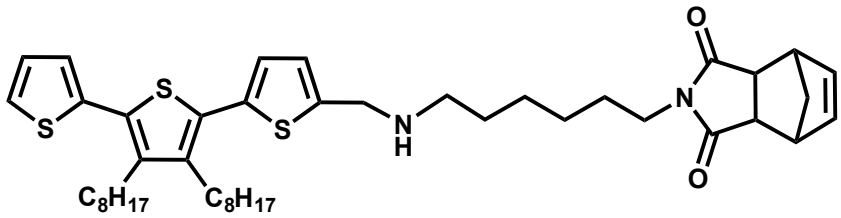

2-(6-(((3',4'-dioctyl-[2,2':5',2''-terthiophen]-5-yl)methyl)amino)hexyl)-3a,4,7,7a-tetrahydro-1H-4,7-methanoisoindole-1,3(2H)-dione [2.8]: 2.7 (0.18 g, 1.1 mmol) and **2.6** (0.65 g, 1.1 mmol) were combined in a small glass vial with teflon-wrapped threads. The vial was loosely capped with a Teflon-lined lid, heated with a heat-gun for 2 mins until all solids had melted, and then heated to 125 °C in a hot oil bath for 2 hrs with stirring. Upon completion, the crude material was purified by silica gel column chromatography (2:1 v/v DCM:MeOH to 1:3 v/v DCM:MeOH) to afford the pure material as a viscous, burgundy oil (0.59 g, 72%). ^{1}H NMR (400 mHz, $CDCl_3$) δ: 7.28 (m, 1H), 7.09 (m, 1H), 7.04 (m, 1H), 6.95 (m, 1H), 6.90 (m, 1H), 6.06 (s, 2H), 3.99 (s, 2H), 3.35 (s, 2H), 3.29 (m, 2H), 3.21 (s, 2H), 2.65 (m, 6H), 1.70 (d, 1H), 1.50 (m, 7H), 1.38 (m, 8H), 1.26 (m, 18H), 0.86 (t, 6H J = 4.8). ^{13}C {^{1}H} NMR (400 mHz, $CDCl_3$) δ: 177.73, 140.08, 139.88, 134.38, 127.30, 125.76, 125.46, 125.21, 53.41, 53.19, 45.69, 44.86, 38.23, 31.86, 30.73, 29.89, 29.24, 28.10, 27.67, 26.64, 22.67, 14.12. HRMS (ESI^+): calcd for $C_{44}H_{62}N_2O_2S_3$ m/z 747.40462 ($[M+H]^+$), found 747.40605.

Alternative Route to 2-(6-(((3',4'-dioctyl-[2,2':5',2''-terthiophen]-5-yl)methyl)amino)hexyl)-3a,4,7,7a-tetrahydro-1H-4,7-methanoisoindole-1,3(2H)-dione [2.8]: 2.7 (0.27 g, 1.7 mmol) was dissolved in 1,2-dichloroethane (5 mL) in a small glass vial with Teflon-wrapped threads. **2.6** (1.00 g, 1.7 mmol) was dissolved in 1,2-dichloroethane (4 mL) and added in one portion to the reaction vessel with vigorous stirring. The reaction was sealed with a Teflon-lined plastic lid and heated to 70 °C for 7 days. Upon completion, the reaction mixture was concentrated *in vacuo* and the crude

mixture was purified by silica gel column chromatography (DCM with 10% MeOH to 1:2 v/v DCM:MeOH). The collected pure material was concentrated *in vacuo* to afford a viscous, burgundy oil (0.82 g, 66%).

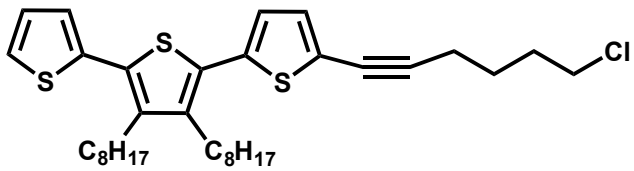

5-(6-chlorohex-1-yn-1-yl)-3',4'-dioctyl-2,2':5',2''-terthiophene [2.9]: 2.4 (1.64 g, 2.9 mmol) was dissolved in dry DCM (20 mL) and diisopropylamine (60 mL) in a 100-mL Schlenk flask under N_2. The resulting solution was sparged for 45 mins with N_2, then $Pd(PPh_3)_4$ (0.34 g, 0.3 mmol) and CuI (0.06 g, 0.3 mmol) were added to the reaction vessel under strong N_2 backpressure, followed by 6-chlorohexyne (0.64 g, 0.67 mL, 5.5 mmol) *via* syringe and needle. The reaction vessel was equipped with a reflux condenser and heated to 50 °C overnight under N_2 . After 15 hrs, the reaction mixture had gone from orange to dark brown. The reaction was cooled to room temperature, poured into EtOAc (100 mL), and quenched with saturated aqueous $(NH_4)_2SO_4$ (100 mL). The resultant solution was transferred to a separatory funnel and the layers were separated. The organic phase was washed with saturated ammonium sulfate ($(NH_4)_2SO_4$, 1 x 50 mL), DI H_2O (2 x 100 mL), and brine (1 x 100 mL), and dried over $MgSO_4$. The filtered solution was concentrated *in vacuo* and purified by silica gel column chromatography (3:1 v/v hexanes:DCM) to yield the desired light green oil (1.48 g, 85%). ^{1}H NMR (400 MHz, $CDCl_3$) δ: 7.29 (dd, 1H, *J* = 5.2, 1.2), 7.11 (dd, 1H, *J* = 3.6, 1.2), 7.04 (m, 2H), 6.94 (d, 1H, *J* = 4.0), 3.59 (t, 2H, *J* = 6.4), 2.65 (m, 4H), 2.49 (t, 2H, *J* = 7.0), 1.93 (m, 2H), 1.77 (m, 2H), 1.52 (m, 4H), 1.32 (m, 20H), 0.87 (m, 6H). ^{13}C {^{1}H} NMR (100 MHz, $CDCl_3$) δ: 140.44, 140.23, 136.69, 136.02, 131.53, 130.12, 129.37, 127.36, 125.94, 125.41,

125.28, 123.37, 94.51, 74.31, 44.52, 31.88, 31.61, 30.73, 30.68, 29.88, 29.25, 28.20, 28.089, 25.72, 22.69, 19.12, 14.13. HRMS (CI^+): calcd for $C_{34}H_{47}ClS_3$ *m/z* 586.2528, found 586.2526.

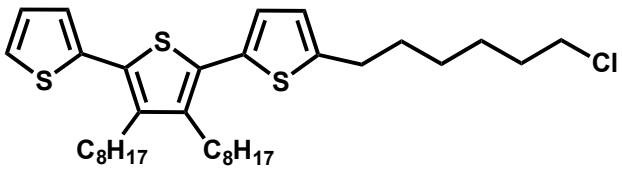

5-(6-chlorohexyl)-3',4'-dioctyl-2,2':5',2''-terthiophene [2.10]: 2.9 (1.472 g, 2.5 mmol) was added to a round-bottomed flask and dissolved in EtOAc (15 mL). Pd/C (10% Pd on activated C, 0.29 g) was added and the flask was sealed with a rubber septum and copper wire. The reaction mixture was sparged with H_2 for 20 minutes, after which the vent needle was removed and the H_2 pressure was allowed to build slightly before removing the sparging needle. The reaction was stirred at room temperature overnight under H_2 atmosphere. Upon completion, the reaction was filtered through celite to remove the catalyst and concentrated *in vacuo* to afford the desired oil (1.47 g, 99%). ^1H NMR (400 MHz, $CDCl_3$) δ: 7.27 (dd, 1H, *J* = 5.2, 1.2), 7.10 (dd, 1H, *J* = 3.6, 1.2), 7.03 (dd, 1H, *J* = 5.2, 3.6), 6.91 (d, 1H, *J* = 3.6), 6.70 (d, 1H, *J* = 3.6), 3.52 (t, 2H, *J* = 6.4), 2.80 (t, 2H, *J* = 7.6), 2.65 (m, 4H), 1.74 (m, 4H), 1.40 (m, 28H), 0.87 (t, 6H, *J* = 6.4). $^{13}C\{^1H\}$ NMR (100 MHz, $CDCl_3$) δ: 145.62, 140.04, 139.53, 133.67, 130.35, 127.29, 125.69, 125.46, 125.12, 124.41, 45.06, 32.49, 31.89, 31.36, 30.74, 29.97, 29.90, 29.26, 28.30, 28.18, 26.59, 22.69, 14.13. HRMS (CI^+): calcd for $C_{34}H_{51}ClS_3$ *m/z* 590.2841, found 590.2839.

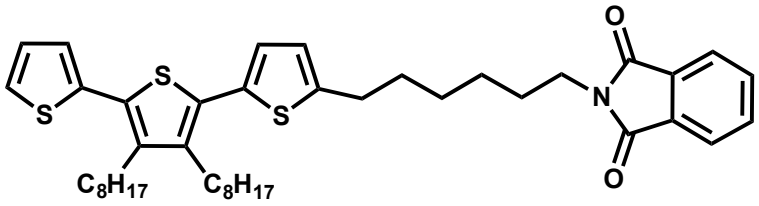

2-(6-(3',4'-dioctyl-[2,2':5',2''-terthiophen]-5-yl)hexyl)isoindoline-1,3-dione [2.11]: 2.10 (3.13 g, 5.3 mmol) was dissolved in DMF (35 mL) in a round-bottomed flask. Potassium phthalimide (1.48 g, 8.0 mmol) was added and the resulting suspension was stirred vigorously overnight at 75 °C. Upon cooling, the reaction mixture was diluted with DCM and DI H_2O, and transferred to a separatory funnel. Upon separation, the aqueous phase was extracted with DCM (3 x 50 mL). The combined organic phases were washed with DI H_2O (1 x 50 mL), brine (2 x 50 mL), and dried over $MgSO_4$. The filtered solution was concentrated *in vacuo* and purified by silica gel column chromatography (1:1 v/v DCM:hexanes) to yield the desired product (3.72 g, quantitative). ^{1}H NMR (400 MHz, $CDCl_3$) δ: 7.82 (m, 2H), 7.68 (m, 2H), 7.27 (dd, 1H, J = 5.2, 1.2), 7.09 (dd, 1H, J = 3.6, 1.2), 7.03 (dd, 1H, J = 5.2, 3.6), 6.89 (d, 1H, J = 3.6), 6.66 (d, 1H, J = 3.6), 3.67 (t, 2H, J = 7.2), 2.78 (t, 2H, J = 7.6), 2.64 (m, 4H), 1.68 (quintet, 4H, J = 7.2), 1.52 (m, 4H), 1.39 (m, 8H), 1.26 (m, 20H), 0.86 (m, 6H). ^{13}C {^{1}H} NMR (100 MHz, $CDCl_3$) δ: 168.45, 145.72, 140.01, 139.48, 136.37, 133.84, 133.58, 132.14, 130.40, 129.22, 127.27, 125.65, 125.44, 125.08, 124.35, 123.15, 37.95, 31.88, 31.58, 31.38, 30.74, 29.99, 29.90, 29.87, 29.24, 28.66, 28.52, 28.11, 26.59, 22.68, 14.12.

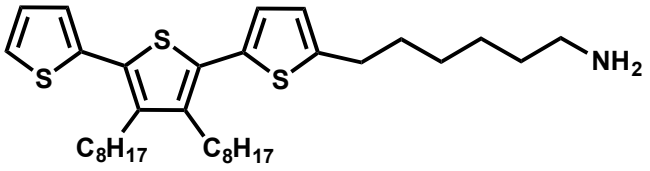

6-(3',4'-dioctyl-[2,2':5',2''-terthiophen]-5-yl)hexan-1-amine [2.12]: 2.11 (3.56 g, 5.1 mmol) was dissolved in 1:3 v/v DCM:EtOH (40 mL) in a round-bottomed flask.

Hydrazine hydrate (80 wt% solution, 1.6 mL, 25.6 mmol) was added *via* syringe and needle, the reaction flask was equipped with a reflux condenser, and the reaction was heated to 55 °C for 2 hrs, during which a fluffy, white solid precipitated out of solution. The reaction mixture was transferred to a separatory funnel and diluted with DCM and DI H_2O. The layers were separated and the aqueous phase was extracted with DCM (2 x 50 mL). The organic phases were combined and washed with DI H_2O (1 x 100 mL) and brine (1 x 100 mL) and dried over $MgSO_4$. The filtered solution was concentrated *in vacuo* to yield the crude product, which was used without further purification (2.80 g, 97%). ^{1}H NMR (400 MHz, $CDCl_3$) δ: 7.24 (dd, 1H, *J* = 5.2, 1.2), 7.05 (dd, 1H, *J* = 3.6, 1.2), 6.99 (dd, 1H, *J* = 5.2, 3.6), 6.85 (d, 1H, *J* = 3.6), 6.66 (d, 1H, *J* = 3.6), 2.74 (t, 2H, *J* = 7.6), 2.58 (m, 6H), 1.62 (quintet, 2H, *J* = 7), 1.47 (m, 4H), 1.28 (m, 28H), 0.81 (t, 6H, *J* = 8.0). ^{13}C {^{1}H} NMR (100 MHz, $CDCl_3$) δ: 145.45, 139.48, 138.90, 135.50, 132.67, 129.57, 128.34, 126.61, 124.91, 124.68, 124.43, 123.65, 42.39, 32.94, 31.13, 30.88, 29.95, 29.24, 29.07, 28.50, 28.22, 27.30, 25.85, 21.93, 13.14. HRMS (CI$^+$): calcd for $C_{34}H_{53}NS_3$ *m/z* 571.3340, found 571.3340.

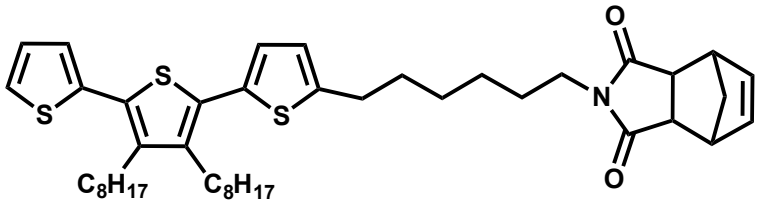

2-(6-(3',4'-dioctyl-[2,2':5',2''-terthiophen]-5-yl)hexyl)-3a,4,7,7a-tetrahydro-1*H*-4,7-methanoisoindole-1,3(2*H*)-dione [2.13]: 2.12 (2.80 g, 4.9 mmol) and **2.7** (0.80 g, 4.9 mmol) were dissolved in toluene (60 mL) in a round-bottomed flask equipped with a reflux condenser, and the reaction was heated to 120 °C overnight. Upon cooling, the reaction was dried over MgSO, vacuum filtrated, and concentrated *in vacuo*. The crude

product was purified by silica gel column chromatography (DCM) to yield a green oil (3.52 g, quantitative). ^{1}H NMR (400 MHz, $CDCl_3$) δ: 7.27 (dd, 1H, *J* = 5.6, 1.2), 7.09 (dd, 1H, *J* = 3.6, 1.2), 7.03 (dd, 1H, *J* = 5.2, 3.6), 6.90 (d, 1H, *J* = 3.2), 6.69 (d, 1H, *J* = 4.0), 6.07 (t, 2H, *J* = 1.8), 3.36 (m, 2H), 3.30 (t, 2H, *J* = 7.4), 3.21 (m, 2H), 2.77 (t, 2H, *J* = 7.6), 2.64 (m, 4H), 1.70 (dt, 1H, *J* = 2.0, 8.8), 1.65 (m, 2H), 1.52 (m, 5H), 1.35 (m, 26H), 0.86 (t, 6H, *J* = 6.8). ^{13}C {^{1}H} NMR (100 MHz, $CDCl_3$) δ: 177.74, 145.69, 140.01, 139.48, 136.36, 134.39, 133.60, 129.24, 127.28, 125.65, 125.43, 125.09, 124.36, 52.21, 45.70, 44.88, 38.34, 31.88, 31.37, 30.74, 29.98, 29.88, 29.87, 29.24, 28.61, 28.11, 27.70, 26.61, 22.68, 14.12. HRMS (CI^+): calcd for $C_{43}H_{59}NO_2S_3$ *m/z* 717.3708, found 717.3712. Elemental Analysis: Theoretical: C, 71.92; H, 8.28; N, 1.95; found: C, 71.81; H, 8.19; N, 1.95.

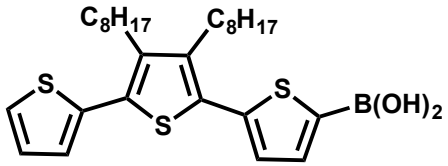

(3',4'-dioctyl-[2,2':5',2''-terthiophen]-5-yl)boronic acid [2.14]: Finely-ground magnesium turnings (0.047 g, 1.93 mmol) were suspended in dry THF (5 mL) in a schlenk flask fitted with a reflux condenser under N_2. **2.4** (0.72 g, 1.3 mmol) was dissolved in dry THF (5 mL) in a round-bottomed flask under N_2 and then transferred via cannula to the schlenk flask. The reaction was heated to reflux and vigorously stirred for 3 hrs, during which the reaction went from a clear, light green solution to a dark yellow-brown solution. The reaction was cooled to room temperature, and then to -78 °C in a dry ice/acetone bath. Trimethylborate (0.3 mL, 2.6 mmol) was dissolved in dry THF (5 mL) in a small round-bottomed flask under N_2 and then transferred in one portion *via* cannula to the reaction vessel. The reaction was stirred at -78 °C for 1 hr, then removed from the

dry ice/acetone bath and warmed to room temperature overnight with stirring under N_2. Upon completion, the reaction mixture was cooled to 0 °C in an ice bath and 10% HCl (10 mL), DI H_2O (20 mL), and Et_2O (20 mL) were added sequentially. After stirring for 5 minutes the reaction was warmed room temperature and transferred to a separatory funnel. The aqueous phase was extracted with Et_2O (1 x 75 mL). The combined organic phases were washed with DI H_2O (1 x 75 mL), brine (1 x 75 mL), and dried over $MgSO_4$. The reaction mixture was collected *via* vacuum filtration, concentrated *in vacuo*, and recrystallized twice from hexanes to yield a light green solid that was used without further characterization (0.406 g, 60%).

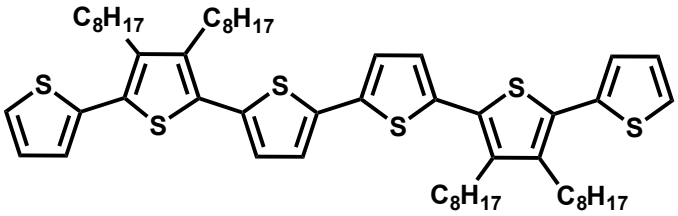

3',3'''',4',4''''-tetraoctyl-2,2':5',2'':5'',2''':5''',2'''':5'''',2''''':sexithiophene

[2.15]: 2.4 (0.14 g, 0.25 mmol) was dissolved in THF (20 mL) in a Schlenk flask, sealed with a rubber septum, and sparged with N_2 for 30 minutes. Meanwhile, Na_2CO_3 (0.14 g, 1.3 mmol) was dissolved in DI H_2O (5 mL) in a round-bottomed flask, sealed with a rubber septum, and sparged with N_2 for 30 minutes. The reaction vessels were cooled to 0 °C in an ice bath, and **2.14** (0.17 g, 0.33 mmol) and $Pd(PPh_3)_4$ (0.03 g, 0.02 mmol) were added to the Schlenk flask under a strong nitrogen backpressure. The basic aqueous solution was transferred to the Schlenk flask *via* cannula and the reaction was sparged with N_2 for 10 minutes before warming to room temperature. The reaction vessel was equipped with a reflux condenser under N_2 and heated to reflux for 6 hrs. Upon completion, the reaction was cooled to room temperature, diluted with DI H_2O and

hexanes, and transferred to a separatory funnel. The aqueous layer was extracted with hexanes (2 x 50 mL). The combined organic phases were washed with DI H_2O (2 x 50 mL), brine (1 x 50 mL), and dried over $MgSO_4$. The crude product was collected *via* vacuum filtration, concentrated *in vacuo*, and purified by silica gel column chromatography (5:1 v/v hexanes:DCM) to yield a orange-yellow oil that crystallized upon sitting (0.23 g, 98%). ^{1}H NMR (400 mHz, $CDCl_3$) δ: 7.33 (dd, 2H, J = 4.8, 1.2), 7.16 (m, 4H), 7.07 (m, 4H), 2.74 (m, 8H), 1.60 (m, 8H), 1.46 (m, 8H), 1.33 (m, 32H), 0.92 (m, 12H). ^{13}C {^{1}H} NMR (400 mHz, $CDCl_3$) δ: 140.21, 136.68, 136.11, 135.23, 129.99, 127.33, 126.29, 125.84, 125.31, 123.77, 31.91, 31.89, 30.74, 30.67, 29.91, 29.26, 28.24, 28.16, 22.71, 14.14. HRMS (CI^+): calcd for $C_{56}H_{78}S_6$ *m/z* 942.4428, found 942.2219.

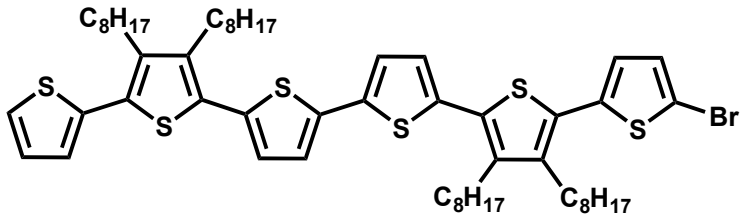

5-bromo-3',3'''',4',4''''-tetraoctyl-2,2':5',2'':5'',2''':5''',2'''':5'''',2'''''-sexithiophene [2.16]: 2.15 (2.36 g, 2.50 mmol) was dissolved in 1:1 v/v $CHCl_3$:acetic acid (AcOH) (600 mL) in a foil-wrapped 1-L round-bottomed flask. The reaction was cooled to 0 °C in an ice bath. NBS (0.40 g, 2.25 mmol) dissolved in 1:1 v/v $CHCl_3$:AcOH (100 mL) was added slowly to the reaction solution. Then, the reaction vessel was sealed with a rubber septum and stirred at 0 °C under a N_2 atmosphere for 3 hrs. Upon completion, the reaction was poured into saturated aqueous $Na_2S_2O_3$ (300 mL) and transferred to a separatory funnel. The aqueous phase was extracted with DCM (3 x 250 mL). The combined organic phases were washed with DI H_2O (3 x 400 mL) and brine (1

x 400 mL), dried over $MgSO_4$, collected *via* vacuum filtration, and concentrated *in vacuo*. The crude product was purified by silica gel column chromatography (hexanes) to afford an orange oil (0.55 g, 60%). ^{1}H NMR (500 MHz, $CDCl_3$) δ: 7.32 (dd, 1H, *J* = 5.2, 1.5), 7.14 (m, 3H), 7.07 (dd, 1H, *J* = 5.0, 3.5), 7.05 (t, 2H, *J* = 3.8), 7.02 (d, 1H, *J* = 3.8), 6.88 (d, 1H, *J* = 3.8), 2.69 (m, 8H), 1.58 (m, 8H), 1.42 (m, 8H), 1.30 (m, 32H), 0.89 (m, 12H). HRMS (CI^+): calcd for $C_{56}H_{77}BrS_6$ *m/z* 1022.3512, found 1022.3522 [M^+].

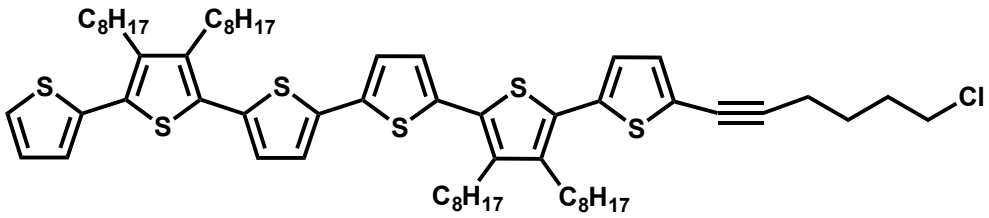

5-(6-chlorohex-1-yn-1-yl)-3',3'''',4',4''''-tetraoctyl-2,2':5',2'':5'',2''':5''',2'''':5'''',2''''':5''''',2'''''-sexithiophene [2.17]: 2.16 (0.89 g, 0.87 mmol) was dissolved in dry DCM (8 mL) and diisopropylamine (24 mL) in a 100-mL Schlenk flask under N_2. The resulting solution was sparged for 30 minutes with N_2. Then, $Pd(PPh_3)_4$ (0.10 g, 0.09 mmol) and CuI (0.02 g, 0.09 mmol) were added to the reaction vessel under strong N_2 backpressure, followed by 6-chlorohexyne (0.20 mL, 0.19 g, 1.63 mmol) *via* syringe and needle. The reaction vessel was equipped with a reflux condenser and heated to 50 °C overnight under N_2. Upon completion, the reaction was cooled to room temperature, poured into EtOAc (75 mL), and quenched with ammonium sulfate (100 mL). The solution was transferred to a separatory funnel and the layers were separated. The organic phase was washed with saturated aqueous $(NH_4)_2SO_4$ (1 x 100 mL), DI H_2O (2 x 100 mL), and brine (1 x 100 mL), and dried over $MgSO_4$. The filtered solution was concentrated *in vacuo* and purified by silica gel column chromatography (5:1 v/v hexanes:DCM) to yield the desired bright orange oil, which upon sitting crystallized to

afford an orange solid (0.90 g, 97%). ^{1}H NMR (400 MHz, $CDCl_3$) δ: 7.28 (dd, 1H, *J* = 5.2, 1.2), 7.11 (m, 3H), 7.04 (m, 4H), 6.95 (d, 1H, *J* = 4), 3.60 (t, 2H, *J* = 6.4), 2.69 (m, 8H), 2.50 (t, 2H, *J* = 7), 1.94 (m, 2H), 1.76 (m, 2H), 1.55 (m, 8H), 1.33 (m, 40H), 0.87 (m, 12H). ^{13}C {^{1}H} NMR (100 MHz, $CDCl_3$) δ: 140.30, 139.96, 136.55, 136.31, 135.00, 131.24, 129.23, 127.05, 126.15, 126.024, 125.57, 125.06, 123.55, 44.20, 31.57, 31.29, 30.34, 29.58, 28.94, 27.88, 25.39, 22.37, 18.81, 13.81. LRMS (MALDI, Cl^{+}): calcd for $C_{62}H_{85}ClS_6$ *m/z* 1056.0, found 1056.0.

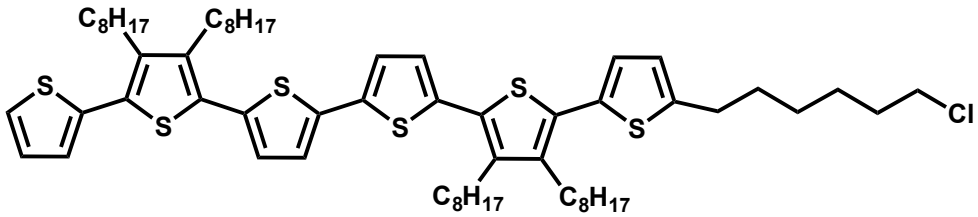

5-(6-chlorohexyl)-3',3'''',4',4''''-tetraoctyl-2,2':5',2'':5'',2''':5''',2'''':5'''',2'''''-sexithiophene [2.18]: 2.17 (0.13 g, 0.12 mmol) was added to a round-bottomed flask and dissolved in EtOAc (10 mL). Pd/C (10% Pd on activated C, 0.03 g) was added and the flask was sealed with a rubber septum and copper wire. The reaction mixture was sparged with H_2 for 30 minutes, after which the vent needle was removed and the H_2 pressure was allowed to build slightly before removing the sparging needle. The reaction was stirred at room temperature overnight under H_2 atmosphere. Upon reaction completion, the solution was filtered through celite to remove the catalyst and concentrated *in vacuo* to afford the desired product as an orange oil (0.12 g, quantitative). ^{1}H NMR (400 MHz, $CDCl_3$) δ: 7.30 (dd, 1H, *J* = 5.2, 1.2), 7.12 (dd, 1H, *J* = 3.2 1.2), 7.11 (d, 2H, *J* = 4), 7.05 (dd, 1H, *J* = 5.2, 3.6), 7.02 (t, 2H, *J* = 4), 6.92 (d, 1H, *J* = 3.2), 6.71 (d, 1H, *J* = 3.6), 3.53 (t, 2H, *J* = 6.6), 2.81 (t, 2H, *J* = 7.4), 2.68 (m, 8H), 1.74 (m, 4H), 1.55 (m, 4H), 1.36 (m, 48H), 0.86 (m, 12H). ^{13}C {^{1}H} NMR (100 MHz, $CDCl_3$) δ: 145.74, 140.24, 139.68,

136.75, 136.54, 136.11, 135.41, 135.18, 133.58, 130.56, 129.60, 129.08, 127.36, 126.33, 126.19, 125.87, 125.53, 125.35, 124.46, 123.79, 123.76, 45.05, 32.49, 31.90, 31.36, 30.74, 30.68, 29.98, 29.90, 29.26, 28.31, 28.24, 28.18, 26.59, 22.70, 14.13. LRMS (MALDI, Cl^+): calcd for $C_{62}H_{89}ClS_6$ *m/z* 1060.6, found 1060.6.

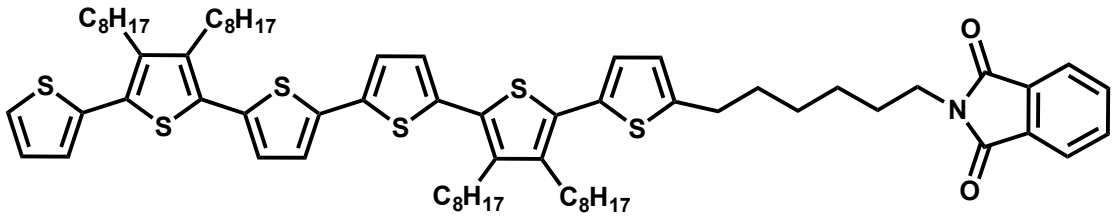

2(6-(3',3'''',4',4''''-tetraoctyl-[2,2':5',2'':5'',2''':5''',2'''':5'''',2''''':5''''',2'''''-sexithiophen]-5-yl)hexyl)isoindoline-1,3-dione [2.19]: 2.18 (1.01 g, 0.95 mmol) was dissolved in DMF (28 mL) and THF (10 mL) in a round-bottomed flask. Potassium phthalimide (0.26 g, 1.43 mmol) was added and the resulting suspension was stirred overnight at 80 °C. Upon cooling, the reaction mixture was diluted with DCM (50 mL) and DI H_2O (50 mL), and transferred to a separatory funnel. Upon separation, the aqueous phase was extracted with DCM (2 x 75 mL). The combined organic phases were washed with DI H_2O (1 x 100 mL) and brine (1 x 100 mL), and dried over $MgSO_4$. The filtered solution was concentrated *in vacuo* and purified by silica gel column chromatography (1:1 v/v DCM:hexanes) to yield the desired product as an orange oil (1.07 g, 96%). ^{1}H NMR (400 MHz, $CDCl_3$) δ: 7.82 (m, 2H), 7.69 (m, 2H), 7.30 (dd, 1H, *J* = 5.2, 1.2), 7.12 (dd, 1H, *J* = 3.6, 1.2), 7.10 (d, 2H, *J* = 3.6), 7.05 (dd, 1H, *J* = 5.2, 3.6), 7.02 (dd, 2H, *J* = 3.6, 5.4), 6.90 (d, 1H, *J* = 3.6), 6.69 (d, 1H, *J* = 3.6), 3.67 (t, 2H, *J* = 7.2), 2.79 (t, 2H, *J* = 7.6), 2.69 (m, 8H), 1.68 (m, 4H), 1.54 (m, 4H), 1.33 (m, 48H), 0.86 (m, 12H).^{13}C {^{1}H} NMR (100 MHz, $CDCl_3$) δ: 168.15, 145.54, 139.92, 139.34, 136.46, 136.19, 135.81, 135.14, 133.53, 133.18, 131.83, 129.64, 129.30, 128.71, 127.04, 126.02,

125.85, 125.56, 125.20, 125.03, 124.09, 123.43, 122.85, 37.64, 31.58, 31.06, 30.42, 29.70, 20.59, 28.94, 28.35, 28.21, 27.92, 27.80, 26.27, 22.38, 13.82. LRMS (MALDI, Cl^+): calcd for $C_{70}H_{93}NO_2S_6$ *m/z* 1171.6, found 1171.6

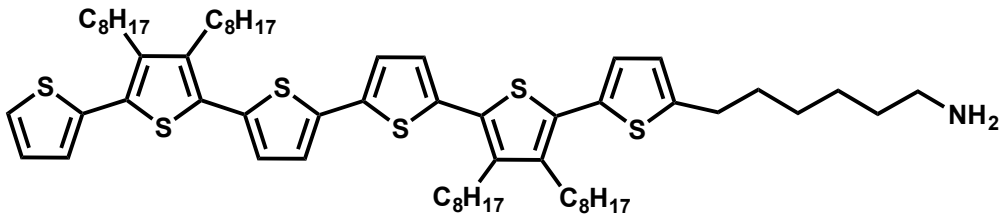

6-(3',3'''',4',4''''-tetraoctyl-[2,2':5',2'':5'',2''':5''',2'''':5'''',2'''''-sexithiophen]-5-yl)hexan-1-amine [2.20]: 2.19 (0.47 g, 0.40 mmol) was dissolved in 1:2 v/v DCM:EtOH (15 mL) in 25-mL round-bottomed flask. Hydrazine hydrate (80 wt%, 0.2 mL, 4.0 mmol) was added via syringe, the reaction flask was equipped with a reflux condenser, and the reaction was heated to 50 °C overnight open to air, during which a large amount of white solid crashed out of solution. Upon completion, the reaction mixture was transferred to a separatory funnel and diluted with DCM (25 mL) and DI H_2O (25 mL). The layers were separated and the aqueous phase was extracted with DCM (2 x 50 mL). The organic phases were combined and washed with DI H_2O (1 x 50 mL) and brine (1 x 50 mL), and dried over $MgSO_4$. The filtered solution was concentrated *in vacuo* to yield the crude product, which was used without further purification (0.40 g, 96%). ^1H NMR (400 MHz, $CDCl_3$) δ: 7.24 (dd, 1H, *J* = 5.2, 1.2), 7.12 (m, 3H), 7.25 (m, 3H), 6.92 (d, 1H, *J* = 3.2), 6.70 (d, 1H, *J* = 3.6), 2.80 (t, 2H, *J* = 7.6), 2.68 (m, 10H), 1.69 (m, 2H), 1.56 (m, 2H), 1.33 (m, 52H), 0.86 (m, 12H). LRMS (MALDI, Cl^+): calcd for $C_{62}H_{91}NS_6$ *m/z* 1041.6, found 1041.6.

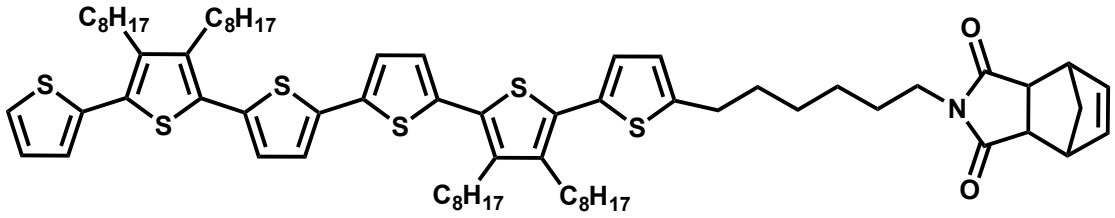

2-(6-(3',3'''',4',4''''-tetraoctyl-[2,2':5',2'':5'',2''':5''',2'''':5'''',2''''':5''''',2'''''-sexithiophen]-5-yl)hexyl)-3a,4,7,7a-tetrahydro-1*H*-4,7-methanoisoindole-1,3(2*H*)-dione [2.21]: 2.20 (0.88 g, 0.84 mmol) and **2.7** (0.14 g, 0.84 mmol) were dissolved in toluene (25 mL) in a 50-mL round-bottomed flask equipped with a reflux condenser. The reaction was heated to 115 °C overnight, open to air. Upon cooling, the reaction was dried over $MgSO_4$, vacuum filtered, and concentrated *in vacuo*. The crude product was purified by silica gel column chromatography (DCM) to yield an orange oil (0.70 g, 67%). ^{1}H NMR (500 MHz, $CDCl_3$) δ: 7.29 (dd, 1H, *J* = 5.0, 1), 7.12 (dd, 1H, *J* = 3.5, 1.0), 7.10 (d, 2H, *J* = 3.5), 7.05 (dd, 1H, *J* = 5.3, 3.5), 7.02 (dd, 2H, *J* = 5.8, 3.5), 6.91 (d, 1H, *J* = 3.5), 6.70 (d, 1H, *J* = 3.5), 6.08 (t, 2H, *J* = 1.8), 3.37 (m, 2H), 3.31 (t, 2H, *J* = 7.3), 3.19 (m, 2H), 2.78 (t, 2H, *J* = 7.5), 2.68 (m, 8H), 1.69 (m, 2H), 1.54 (m, 4H), 1.36 (m, 52H), 0.87 (m, 12H). ^{13}C {^{1}H} NMR (125 MHz, $CDCl_3$) δ: 177.72, 145.83, 140.22, 139.67, 136.80, 136.54, 136.14, 135.47, 135.19, 134.41, 133.54, 130.63, 129.98, 129.63, 129.07, 127.34, 126.49, 126.19, 125.89, 125.53, 125.34, 124.41, 123.80, 123.75, 52.21, 45.72, 44.90, 38.35, 31.89, 31.37, 30.73, 30.67, 30.00, 29.89, 29.69, 29.26, 28.61, 28.24, 28.12, 27.71, 26.63, 22.68, 14.11. LRMS (MALDI, Cl^+): calcd for $C_{71}H_{97}NO_2S_6$ *m/z* 1187.7, found 1187.7. Elemental Analysis: Theoretical: C, 71.73; H, 8.22; N, 1.18; found: C, 70.39; H, 8.11; N, 1.16.

Synthesis of Perylene Diimide Acceptor Monomer [2.22–2.28]

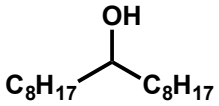

heptadecan-9-ol [2.22]: Ethyl formate (3.66 g, 4.0 mL, 49.4 mmol) was dissolved in dry THF (80 mL) in a three-neck round-bottomed flask equipped with an addition funnel under a N_2 atmosphere. The reaction vessel was cooled to -78 °C in a dry ice/acetone bath and octylmagnesium bromide (2.0 M in Et_2O, 75.0 mL, 148.2 mmol) was cannula-transferred to the addition funnel and added dropwise over 1 hr. The dry ice/acetone bath was removed and the reaction was warmed to room temperature overnight with stirring. Upon completion, the reaction was cooled to 0 °C in an ice bath and MeOH was added dropwise to quench the reaction (25 mL). Upon MeOH addition, the reaction first became murky, then clear and homogeneous, and finally a white solid precipitated out of solution. The reaction solution was transferred to a separatory funnel, diluted with MeOH (100 mL) and saturated aqueous NH_4Cl (100 mL), and extracted with Et_2O (3 x 200 mL) and EtOAc (1 x 200 mL). The organic phases were combined, washed with brine (1 x 300 mL), and dried over $MgSO_4$. The solution was collected *via* vacuum filtration and concentrated *in vacuo* to afford a pale, yellowish oil. Recrystallization in ACN afforded a coarse white solid (11.24 g, 89%). ^{1}H NMR (400 MHz, $CDCl_3$) δ: 3.58 (m, 1H), 1.44 (m, 4H), 1.29 (m, 24H), 0.88 (t, 6H, J = 7.0).

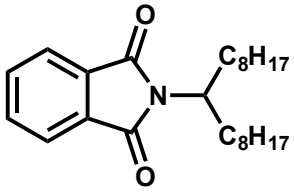

2-(heptadecan-9-yl)isoindoline-1,3-dione [2.23]: 2.22 (6.16 g, 24.0 mmol), phthalimide (3.53 g, 24.0 mmol), and triphenylphosphine (6.35 g, 24.2 mmol) were

added to a Schlenk flask equipped with a 50-mL addition funnel, cycled 3x on high vacuum, and suspended in dry Et_2O (100 mL) (solid did not dissolve). Meanwhile, diisopropylazodicarboxylate (DIAD) (5.24 g, 5.1 mL, 25.9 mmol) was dissolved in dry Et_2O (35 mL) in a 100-mL Schlenk flask. After stirring briefly under N_2, the DIAD solution was cannula-transferred to the addition funnel and added dropwise to the stirring reaction mixture at room temperature. Upon addition of the DIAD solution, the reaction mixture became clear and homogeneous. The reaction was stirred overnight at room temperature (after 4 hrs, a white solid precipitated out of solution). Upon completion, the reaction was vacuum filtered to remove the solid precipitate and concentrated *in vacuo* to afford a yellow oil. The crude product was further purified by silica column chromatography (3:1 v/v hexanes:DCM to 1:1 v/v hexanes:DCM) to collect the product as a clear, colorless oil (8.58 g, 93%). ^{1}H NMR (400 MHz, $CDCl_3$) δ: 7.82 (m, 2H), 7.70 (m, 2H), 4.18 (m, 1H), 2.06 (m, 2H), 1.68 (m, 2H), 1.26 (m, 24H), 0.84 (m, 6H).

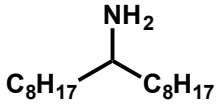

heptadecan-9-amine [2.24]: **Route A:** **2.23** (3.79 g, 9.8 mmol) was dissolved in EtOH (60 mL) in a 250-mL round-bottomed flask. Hydrazine hydrate (80 wt% solution, 3.08 g, 3.08 mL, 49.2 mmol) was added to the solution *via* syringe and needle. The reaction vessel was equipped with a reflux condenser open to air and heated to 75 °C in a hot oil bath. After 30 mins of stirring, a white solid had precipitated out of solution. The reaction continued to stir at 75 °C for an additional 2 hrs, after which the reaction was cooled to room temperature, diluted with DCM (50 mL) and DI H_2O (50 mL), and transferred to a separatory funnel. The aqueous layer was extracted with DCM (2 x 100 mL), and the combined organic phases were washed with DI H_2O (2 x 100 mL), brine (1

x 100 mL), and dried over $MgSO_4$. Vacuum filtration, followed by concentration *in vacuo*, yielded the crude product as a clear, taupe oil, which was used without further purification (2.50 g, quantitative). ^{1}H NMR (400 MHz, $CDCl_3$) δ: 2.66 (m, 1H), 1.36 (m, 28H), 0.87 (t, 6H, J = 7.0). ^{13}C {^{1}H} NMR (100 MHz, $CDCl_3$) δ: 51.21, 38.18, 31.883, 29.83, 29.62, 29.29, 26.18, 22.66, 14.10. HRMS (ESI$^+$): calcd for $C_{17}H_{37}N$ *m/z* 256.2999, found 256.3001.

Route B: 9-heptadecanone (1.52 g, 6.0 mmol), ammonium acetate (4.74 g, 61.4 mmol), and sodium cyanoborohydride (0.27 g, 4.3 mmol) were added to a round-bottomed flask, suspended in MeOH (25 mL), and stirred at room temperature open to air for 3 days. The progress of the reaction was monitored by TLC in $CHCl_3$. During the course of the reaction, the solution went from a heterogenous suspension to clear and homogeneous. Upon completion, the reaction was quenched with the dropwise addition of concentrated HCl (5 mL), and concentrated *in vacuo* to afford a white solid. The solid was resuspended in DI H_2O (100 mL) and 10% KOH (aq) solution was added to pH ~ 10. The solution was transferred to a separatory funnel and extracted with $CHCl_3$ (3 x 100 mL), dried over Na_2SO_4, and concentrated *in vacuo* to afford a yellowish oil that was used without further purification (1.22 g, 80%). ^{1}H NMR (400 MHz, $CDCl_3$) δ: 2.64 (m, 1H), 1.32 (m, 28H), 0.84 (t, 6H, J = 6.8).

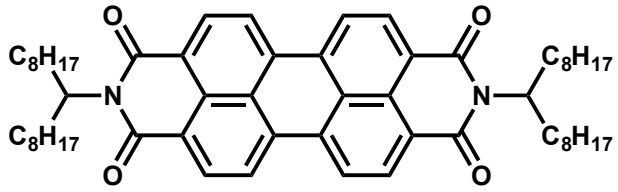

2,9-di(heptadecan-9-yl)anthra[2,1,9-*def*:6,5,10-*d'e'f'*]diisoquinoline-1,3,8,10(2*H*,9*H*)-tetraone [2.25]: 2.24 (5.83 g, 22.8 mmol), 3,4,9,10-perylenetetracarboxylate dianhydride (4.26 g, 10.9 mmol), and imidazole (25.3 g, 372.2

mmol) were added to a round-bottomed flask and sealed with a rubber septum and copper wire. The reaction vessel was heated to 160 °C in hot oil bath for 5 hrs, after which the reaction was cooled to room temperature. The reaction mixture was diluted with hexanes (300 mL) and sonicated to dissolve the solid (3x). The combined hexanes rinses were concentrated *in vacuo* to afford a dark red solid. The remaining solid in the reaction vessel was dissolved in THF (75 mL), precipitated into 2M HCl (1 L), and vacuum filtered to collect. This solid was combined with the solid afforded from the hexanes washes and both were dissolved in 2:1 v/v DCM:hexanes, dried over Na_2SO_4, and concentrated *in vacuo*. The resulting crude material was purified by silica column chromatography (3:1 v/v DCM:hexanes) to afford a bright red solid (9.12 g, 97%). ^{1}H NMR (400 MHz, $CDCl_3$) δ: 8.64 (m, 8H), 5.18 (m, 1H), 2.24 (m, 2H), 1.86 (m, 2H), 1.28 (m, 48H), 0.822 (t, 12H, J = 6.8). ^{13}C {^{1}H} NMR (100 MHz, $CDCl_3$) δ: 163.57, 134.53, 131.88, 129.61, 126.47, 123.04, 54.75, 32.35, 31.81, 29.53, 29.49, 29.23, 26.94, 25.81, 22.61, 14.07. HRMS (CI$^+$): calcd for $C_{58}H_{78}N_2O_4$ *m/z* 866.5962, found 866.5950.

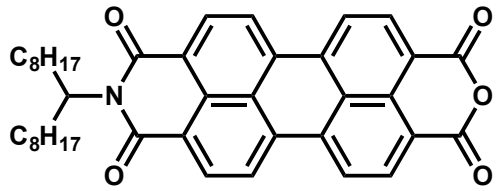

9-(heptadecan-9-yl)-1*H*-isochromeno[6',5',4':10,5,6]anthra[2,1,9-*def*]isoquinoline-1,3,8,10(9*H*)-tetraone [2.26]: 2.25 (1.03 g, 1.2 mmol) was dissolved in DCM (50 mL), transferred to a round-bottomed flask, and concentrated *in vacuo*. **2.25** was redissolved in *t*-BuOH (40 mL) in a round-bottomed flask and freshly ground KOH pellets (0.281 g, 4.7 mmol) were added. The round-bottomed flask was equipped with a reflux condenser open to air and heated to 90 °C in a hot oil bath. After 4.5 hrs, TLC in DCM with 10% AcOH showed no remaining starting material. The reaction vessel was

cooled to room temperature overnight. Upon complete cooling, the reaction mixture was poured into glacial AcOH (50 mL) and 2M HCl (25 mL) and stirred at room temperature for 1 hr. The mixture was then transferred to a separatory funnel and extracted with $CHCl_3$ (3 x 100 mL). The combined organic layers were washed with DI H_2O until pH ~ 7 (2 x 200 mL) and brine (1 x 100 mL), and dried over Na_2SO_4. The crude product mixture was vacuum filtered, rinsing with copious amounts of $CHCl_3$ (a small amount of insoluble brick red solid remained on the filter paper), and purified further by silica column chromatography (DCM) to afford a red solid (0.296 g, 40%). ^{1}H NMR (400 MHz, $CDCl_3$) δ: 8.69 (m, 8H), 5.18 (m, 1H), 2.23 (m, 2H), 1.86 (m, 2H), 1.27 (m, 24H), 0.825 (t, 6H, J = 7.4). ^{13}C {^{1}H} NMR (100 MHz, $CDCl_3$) δ: 160.04, 133.65, 123.99, 123.22, 119.09, 32.38, 31.86, 29.54, 29.28, 27.00, 22.67, 14.13. HRMS (CI^+): calcd for $C_{41}H_{43}NO_5$ m/z 630.3219, found 630.3201.

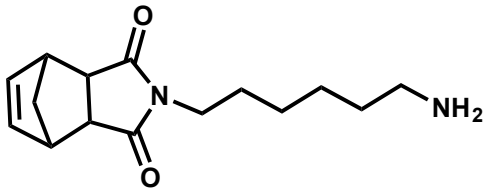

2-(6-aminohexyl)-3a,4,7,7a-tetrahydro-1*H*-4,7-methanoisoindole-1,3(2*H*)-dione [2.27]: 2.7 (1.00 g, 6.0 mmol) and 1,6-diaminohexane (2.12 g, 18.3 mmol) were added to a round-bottomed flask and dissolved in glacial AcOH (30 mL). The round-bottomed flask was equipped with a reflux condenser open to air and heated to 105 °C in a hot oil bath for 3.5 hrs before cooling to room temperature. The reaction mixture was transferred to a separatory funnel, diluted with DI H_2O (20 mL), and extracted with DCM (3 x 50 mL). The organic phases were combined and concentrated *in vacuo* to afford a clear, yellowish oil (first fraction, 1.27 g, 81%). Saturated $NaHCO_3$ was added to the

aqueous layer in the separatory funnel (25 mL) to neutral pH, and this was extracted with DCM (3 x 100 mL). The combined organic phases were concentrated *in vacuo* to afford a clear oil (second fraction, 0.27 g, 17%). Upon sitting both samples solidified to give an off-white solid. By ^{1}H NMR both fractions were consistent with product formation, although the second DCM extraction was slightly more pure. ^{1}H NMR (400 MHz, $CDCl_3$) δ: 6.08 (t, 2H, *J* = 2.0), 3.37 (m, 2H), 3.24 (m, 2H), 3.03 (t, 2H, *J* = 7.4), 2.84 (t, 2H, *J* = 7.6), 1.73 (d, 1H, *J* = 8.8), 1.61 (m, 2H), 1.53 (d, 1H, *J* = 8.4), 1.42 (m, 2H), 1.33 (m, 2H), 1.25 (m, 2H).

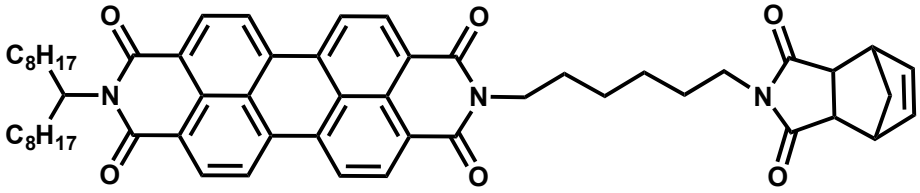

2-(6-(1,3-dioxo-1,3,3a,4,7,7a-hexahydro-2*H*-4,7-methanoisoindol-2-yl)hexyl)-9-(heptadecan-9-yl)anthra[2,1,9-*def*:6,5,10-*d'e'f'*]diisoquinoline-1,3,8,10(2*H*,9*H*)-tetraone [2.28]: 2.26 (0.53 g, 0.84 mmol) was dissolved in DCM (50 mL), transferred to a round-bottomed flask, and concentrated *in vacuo*, before redissolving in 1:4 v/v DMF:toluene (20 mL). **2.27** (0.36 g, 1.38 mmol) was transferred to the round-bottomed flask. The reaction vessel was equipped with a reflux condenser open to air and heated to 130 °C in a hot oil bath overnight. Upon completion, the reaction was concentrated *in vacuo* to yield the crude product as a red solid. This was purified by two sequential silica column chromatography (the first was run in 2% MeOH/DCM, the second was run in 6% MeOH/DCM) to afford the pure material as a dark red solid (0.60 g, 82%). ^{1}H NMR (400 MHz, $CDCl_3$) δ: 8.52 (broad m, 2H), 8.40 (d, 2H, *J* = 8.0), 8.35 (d, 2H, *J* = 8.4), 8.28 (d, 2H, *J* = 8.4), 6.10 (s, 2H), 5.17 (m, 1H), 4.11 (t, 2H, *J* = 7.6), 3.37 (broad s, 2H), 3.32 (t,

2H, *J* = 7.4), 3.23 (broad s, 2H), 2.26 (m, 2H), 1.88 (m, 2H), 1.72 (m, 3H), 1.52 (d, 1H, *J* = 8.8), 1.46-1.20 (broad m, 30H), 0.81 (t, 6H, *J* = 6.8). ^{13}C {^{1}H} NMR (100 MHz, $CDCl_3$) δ: 177.70, 162.97, 134.40, 134.14. 133.87, 130.94, 129.28, 128.94, 125.91, 122.88, 122.76, 122.67, 54.81, 52.18, 45.68, 44.85, 40.37, 38.31, 32.33, 31.81, 29.56, 29.50, 29.24, 27.88, 27.66, 26.99, 26.62, 22.61, 14.06. HRMS (CI^+): calcd for $C_{56}H_{63}N_3O_6$ *m/z* 873.4717, found 873.4700. Elemental analysis: theoretical: C, 76.95; H, 7.26; N, 4.81; found: C, 76.63; H, 7.13; N, 4.83.

Polymerizations of Donor and Acceptor homopolymers [P2.1 – P2.3]

All polymerizations were carried out in small glass vials with Teflon-lined lids in a glovebox under N_2 atmosphere in dry DCM using Grubbs' 2nd Generation (G2) catalyst. The amount of G2 used was determined by the desired molecular weight of the resultant homopolymer using **Equation 2.3**, where *[M]* is the initial molar concentration of monomer added, *[I]* is the initial molar concentration of G2 added, and $MW_{monomer}$ is the molecular weight of the monomer used.

$$M_n = \left({}^{[\mathrm{M}]}\!/_{[I]}\right) \times MW_{monomer} \quad (\mathbf{2.3})$$

Polymerizations were terminated with 2-3 mL ethyl vinyl ether upon removal from glovebox. The reaction solution was then concentrated *in vacuo* and all polymers were purified by precipitation into MeOH (3x). Ter homopolymers were precipitated from small amounts of 1:4 DCM:hexanes (~3 mL); Sexi homopolymers were precipitated from small amounts of 1:2 DCM:hexanes (~2 mL); PDI homopolymers were precipitated from small amounts of DCM (~2 mL). Polymers were characterized by ^{1}H NMR ($CDCl_3$), GPC (THF), DSC, and TGA. Polydispersity (*Đ*) was determined using GPC.

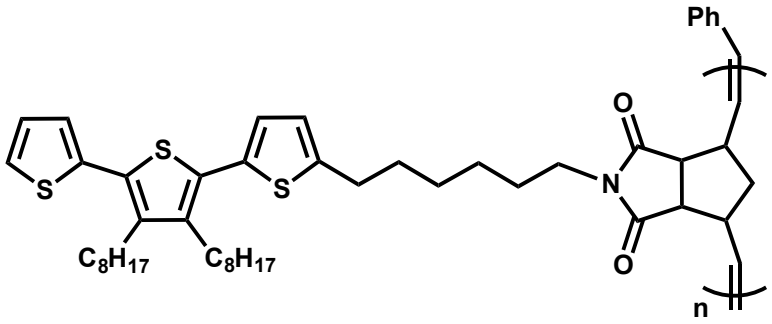

Poly(2-(6-(3',4'-dioctyl-[2,2':5',2''-terthiophen]-5-yl)hexyl)isoindoline-1,3-dione) [P2.1]: ^{1}H NMR (representative homopolymer, 400 MHz, $CDCl_3$) all signals broad singlets unless otherwise stated, δ: 7.24 (1H), 7.08 (1H), 7.00 (1H), 6.88 (1H), 6.67 (1H), 5.67-5.56 (broad d, 2H), 3.46 (2H), 3.14 (2H), 2.86 (2H), 2.74 (2H), 2.63 (4H), 1.88 (1H), 1.63 (2H), 1.52 (5H), 1.37-1.24 (broad m, 26H), 0.86 (6H).

Table 2.1. Molecular weight characterization of Ter homopolymers (**P2.1** series).

Polymer	*[M]/[I]*[a]	M_n (GPC)[b] (kg/mol)	M_n (theoretical)[c] (kg/mol)	$Đ$[b]
P2.1a	25	36.2	18.0	1.26
P2.1a-2	25	32.5	18.0	1.21
P2.1b	75	54.7	53.8	1.32
P2.1c	100	81.5	71.8	1.36
P2.1c-2	100	71.8	71.8	1.26
P2.1d	150	102.9	107.7	1.26
P2.1d-2	150	106.6	107.7	1.18
P2.1e	200	112.8	143.6	1.16
P2.1f	300	115.0	215.4	1.25

[a]*[M]/[I]* indicates the initial molar ratio of **2.13** (*[M]*) to G2 catalyst (*[I]*). Assuming complete conversion, *[M]/[I]* = N_n; [b]Determined from GPC in THF, calibrated with polystyrene standards; [c]Theoretical molecular weights calculated from M_n= N_n x 718.13 g/mol (**2.13** molecular weight), assuming 100% conversion. In several cases, two batches of Ter homopolymer with the same *[M]/[I]* ratio were synthesized and both are included in the table to demonstrate the reproducibility of the polymerization.

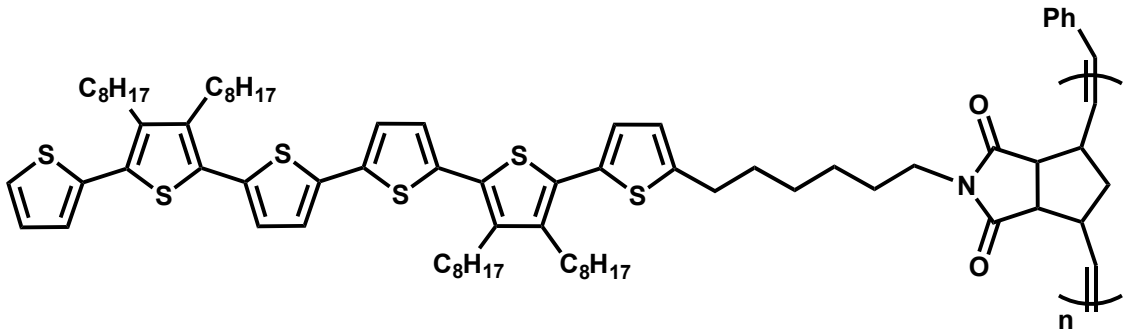

Poly(2-(6-(3',3'''',4',4''''-tetraoctyl-[2,2':5',2'':5'',2''':5''',2'''':5'''',2''''':5''''',2'''''-sexithiophen]-5-yl)hexyl)-3a,4,7,7a-tetrahydro-1*H*-4,7-methanoisoindole-1,3(2*H*)-dione) [P2.2]: ^{1}H NMR (representative homopolymer, 400 MHz, CD_2Cl_2) all signals broad singlets unless otherwise stated δ: 7.30 (1H), 7.10-6.90 (6H), 6.88 (1H), 6.67 (1H), 5.66-5.54 (broad d, 2H), 3.44 (2H), 3.15 (2H), 2.88 (2H), 2.67 (8H), 1.83 (1H), 1.64-1.26 (broad m, 59H), 0.86 (12H).

Table 2.2. Molecular weight characterization of Sexi homopolymer (**P2.2** series).

Polymer	*[M]/[I]*[a]	M_n(GPC)[b] (kg/mol)	M_n (theoretical)[c] (kg/mol)	$Đ$[b]
P2.2a	25	40.0	29.7	1.19
P2.2b	100	133.0	118.9	1.28
P2.2c	150	174.0	178.3	1.79
P2.2d	300	303.2	356.7	1.81

[a]*[M]/[I]* indicates the initial molar ratio of **2.21** (*[M]*) to G2 catalyst (*[I]*). Assuming complete conversion, *[M]/[I]* = N_n; [b]Determined from GPC in THF, calibrated with polystyrene standards; [c]Theoretical molecular weights calculated from M_n= N_n x 1188.92 g/mol (**2.21** molecular weight), assuming 100% conversion.

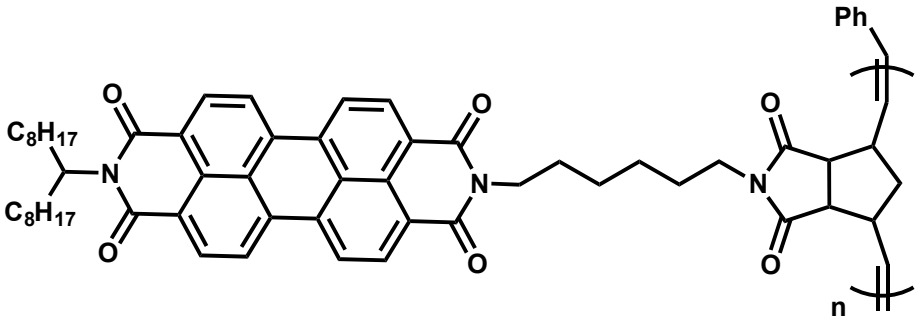

Poly(2-(6-(1,3-dioxo-1,3,3a,4,7,7a-hexahydro-2*H*-4,7-methanoisoindol-2-yl)hexyl)-9-(heptadecan-9-yl)anthra[2,1,9-*def*:6,5,10-*d*'*e*'*f*']diisoquinoline-1,3,8,10(2*H*,9*H*)-tetraone) [P2.3]: ^{1}H NMR (representative homopolymer, 400 MHz, $CDCl_3$) all signals broad singlets unless otherwise stated, δ: 8.12-7.76 (broad m, 8H), 5.77 (2H), 5.07 (1H), 3.99 (2H), 3.52 (2H), 3.24 (2H), 2.98 (2H), 2.18 (2H), 1.92 (3H), 1.69 (1H), 1.36-1.22 (broad m, 32H), 0.83 (6H).

Table 2.3. Molecular weight characterization of PDI homopolymers (**P2.3** series).

Polymer	*[M]/[I]*[a]	M_n(GPC)[b] (kg/mol)	M_n (theoretical)[c] (kg/mol)	$Đ$[b]
P2.3a	25	283.0	21.9	1.01
P2.3b	75	324.2	65.6	1.01
P2.3c	100	353.1	87.4	1.01
P2.3d	150	390.3	131.1	1.02
P2.3d-2	150	205.8	131.1	1.79
P2.3e	200	427.4	174.8	1.05

[a]*[M]/[I]* indicates the initial molar ratio of **2.28** (*[M]*) to G2 catalyst (*[I]*). Assuming complete conversion, *[M]/[I]* = N_n; [b]Determined from GPC in THF, calibrated with polystyrene standards; [c]Theoretical molecular weights calculated from M_n= N_n x 874.14 g/mol (**2.28** molecular weight), assuming 100% conversion.

RESULTS AND DISCUSSION

Synthesis

The conjugated Ter molecule (**2.3**) and the polymerizable norbornene dione (**2.7**) were synthesized following modified literature procedures.[185,191,192] Monomer **2.8**, featuring a secondary amine linkage between the conjugated Ter core and polymerizable backbone, was prepared as outlined in **Scheme 2.1**. Octyl chains were introduced through a Kumada coupling between 3,4-dibromothiophene and octylmagnesium bromide to yield compound **2.1**. These octyl chains were added in order to improve the solubility of the final material. Compound **2.1** was subsequently brominated at the 2- and 5-positions with NBS to yield compound **2.2**. Compound **2.2** was reacted in a Stille coupling with (2-tributylstannyl)thiophene to yield Ter (**2.3)**, which was subsequently reacted with NBS to yield the asymmetrically brominated Ter moiety (**2.4**). Following a Bouveault aldehyde synthesis procedure, compound **2.4** was treated with magnesium turnings to form a Grignard reagent, which was then reacted *in-situ* with DMF to produce a hemiaminal magnesium salt. The hemiaminal was hydrolyzed using HCl to give the desired aldehyde (**2.5)**. Subsequent reaction of compound **2.5** with 1,6-diaminohexane yielded compound **2.6**. Originally, condensation of compound **2.6** with 3a*R*,4*R*,7*S*,7a*S*)-3a,4,7,7a-tetrahydro-4,7-epoxyisobenzofuran-1,3-dione (oxygen-bridged norbornene dione) was envisaged as a route to Ter monomer **2.8**. However, although the first nucleophilic attack and subsequent formation of the amide-acid is facile, the second nucleophilic attack (and ring-closing step) to make the imide can require forcing (basic or high temperature) conditions. Despite several attempts, imide formation in this reaction was never observed. It is hypothesized that under forcing conditions, a retro Diels-Alder reaction may occur, which is made favorable due to the regeneration of aromaticity by furan and maleic anhydride, thus hindering imide formation. Switching to 3a,4,7,7a-tetrahydro-4,7-

methanoisobenzofuran-1,3-dione (methylene-bridged norbornene dione, compound **2.7**) yielded the desired Ter monomer (**2.8**) in 14-16% overall yield. Polymerization attempts using compound **2.8** were unsuccessful, possibly due to the presence of the secondary amine, which could bind to the Ru metal center of Grubbs' catalysts, deactivating it. For this reason, a new synthetic route to Ter monomer **2.13** was designed, in which the secondary amine linkage was replaced with an alkyl group.

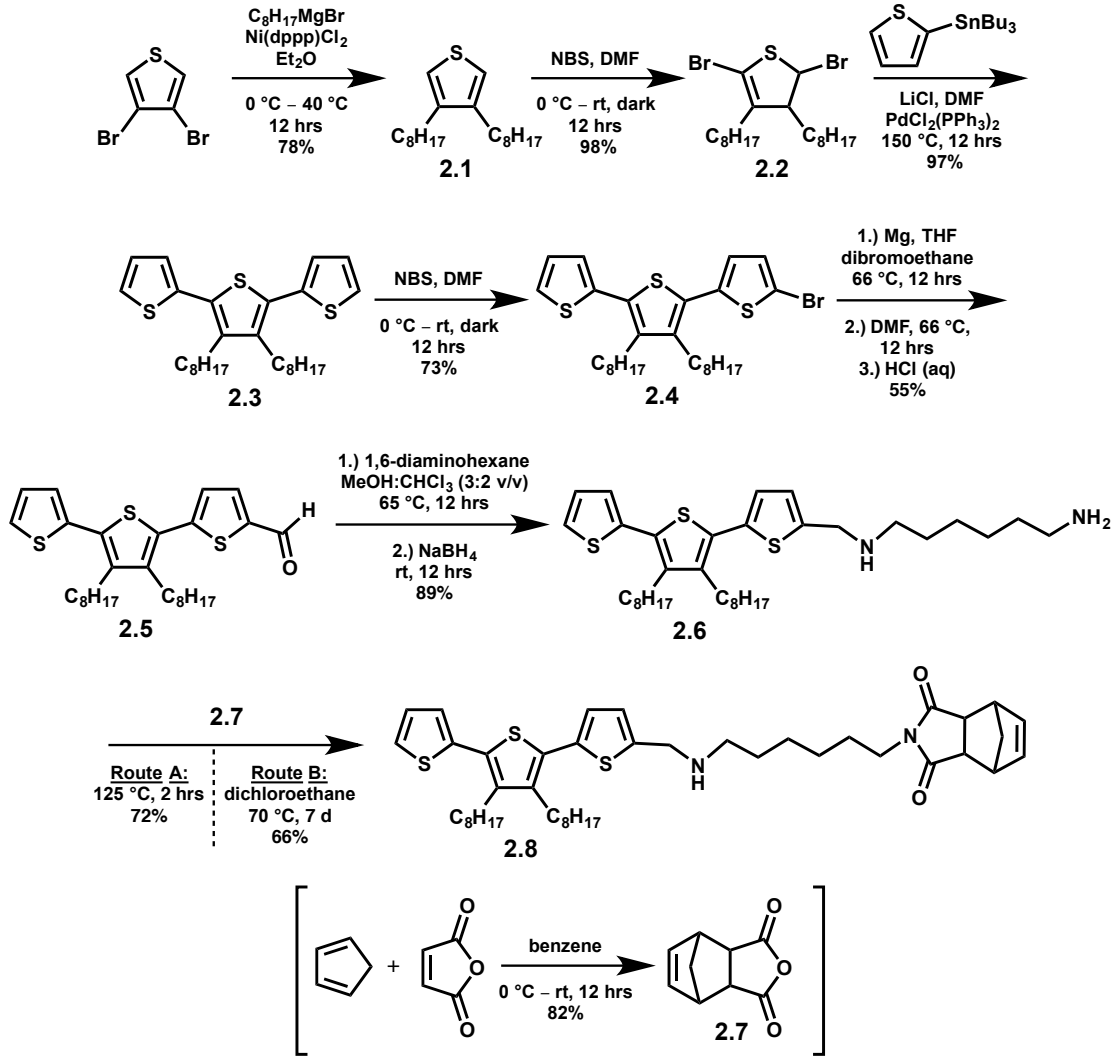

Scheme 2.1. Synthetic route for Ter monomer **2.8**.

Monomer **2.13** was prepared following the synthetic pathway outlined in **Scheme 2.2**. Asymmetrically brominated Ter (**2.4**) was reacted in a Sonogashira coupling reaction with 6-chlorohexyne to yield compound **2.9**. This alkyne was reduced to the alkane in a hydrogenation reaction using Pd/C to yield compound **2.10**. Subsequent reaction of compound **2.10** in a two-step Gabriel amine synthesis—first reacting with potassium phthalimide in a nucleophilic substitution reaction to yield the protected amine (**2.11**), and then deprotecting with hydrazine hydrate—gave the terminal free amine (**2.12**). This amine was then condensed with the norbornene dione, compound **2.7**, to give the desired Ter monomer (**2.13**) in good (36%) overall yield over 10 steps.

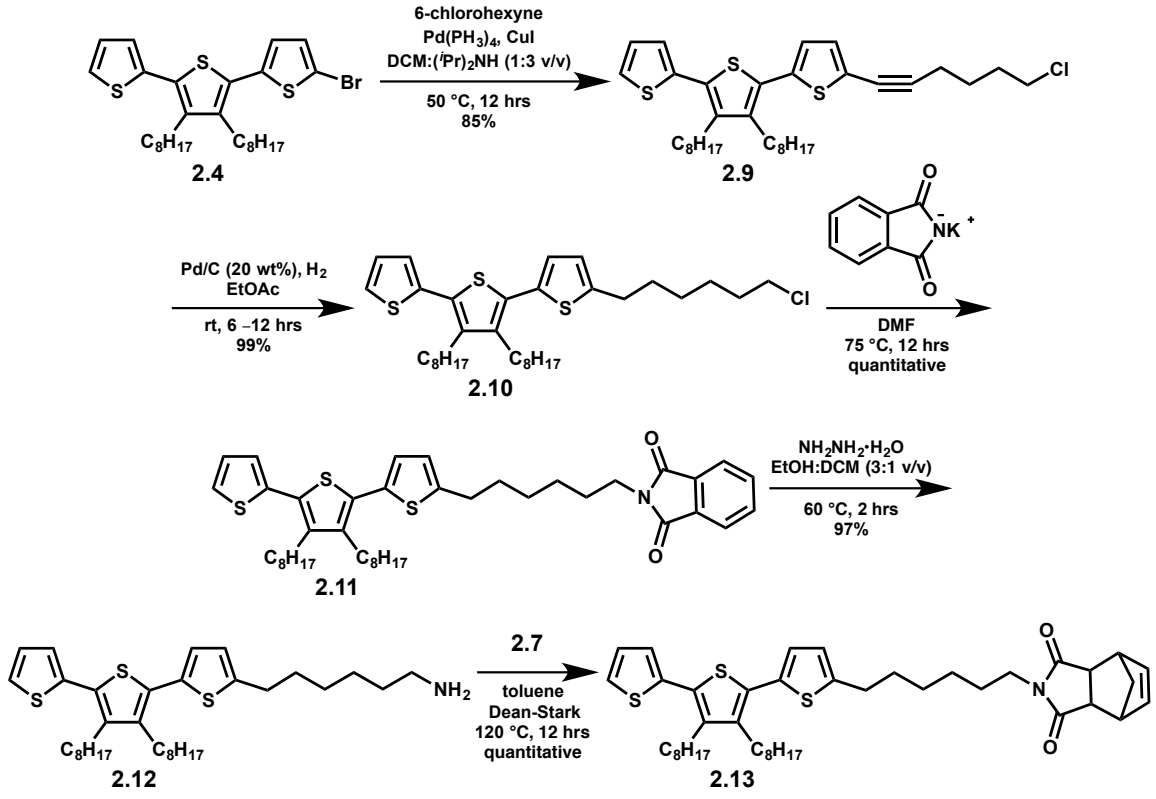

Scheme 2.2. Synthetic route for Ter monomer **2.13**.

The synthesis of the norbornene-type monomer with Sexi pendant group (**2.21**) follows a similar synthetic route as that for Ter monomer **2.13** and is outlined in **Scheme 2.3**. Again, long alkyl chains were appended to the Sexi core in order to improve the solubility of the final material. The synthesis begins with reaction of asymmetrically brominated Ter (**2.4**) with elemental magnesium to form a Grignard reagent, followed by *in situ* addition of trimethylborate to yield the desired boronic acid (**2.14**) upon acidic workup. A subsequent Suzuki cross-coupling reaction of compound **2.14** with a second equivalent of compound **2.4** gave the desired Sexi product (**2.15**) in good yield. This synthetic route to compound **2.15** is advantageous to a previously reported synthesis involving a two-step, one-pot redox-type coupling reaction of Ter (**2.3**) using *n*-BuLi and $Fe(acac)_3$, which gave low and inconsistent yields, possibly due to the formation of higher oligomeric products.[193] Asymmetric bromination of compound **2.15** using NBS yielded compound **2.16**, which was then reacted with 6-chlorohexyne in a Sonogashira cross-coupling reaction to yield compound **2.17**. This was followed by reduction of the alkyne (**2.17**) to an alkane (**2.18**) using Pd/C. Compound **2.18** was reacted with potassium phthalimide in a two-step Gabriel amine synthesis, deprotecting the phthalimide (**2.19**) with hydrazine hydrate to give a free amine endgroup (**2.20**). This free amine (**2.20**) was condensed with the norbornene dione, compound **2.7**, to yield the desired monomer with Sexi pendant group (**2.21**) in 9% overall yield over 13 steps.

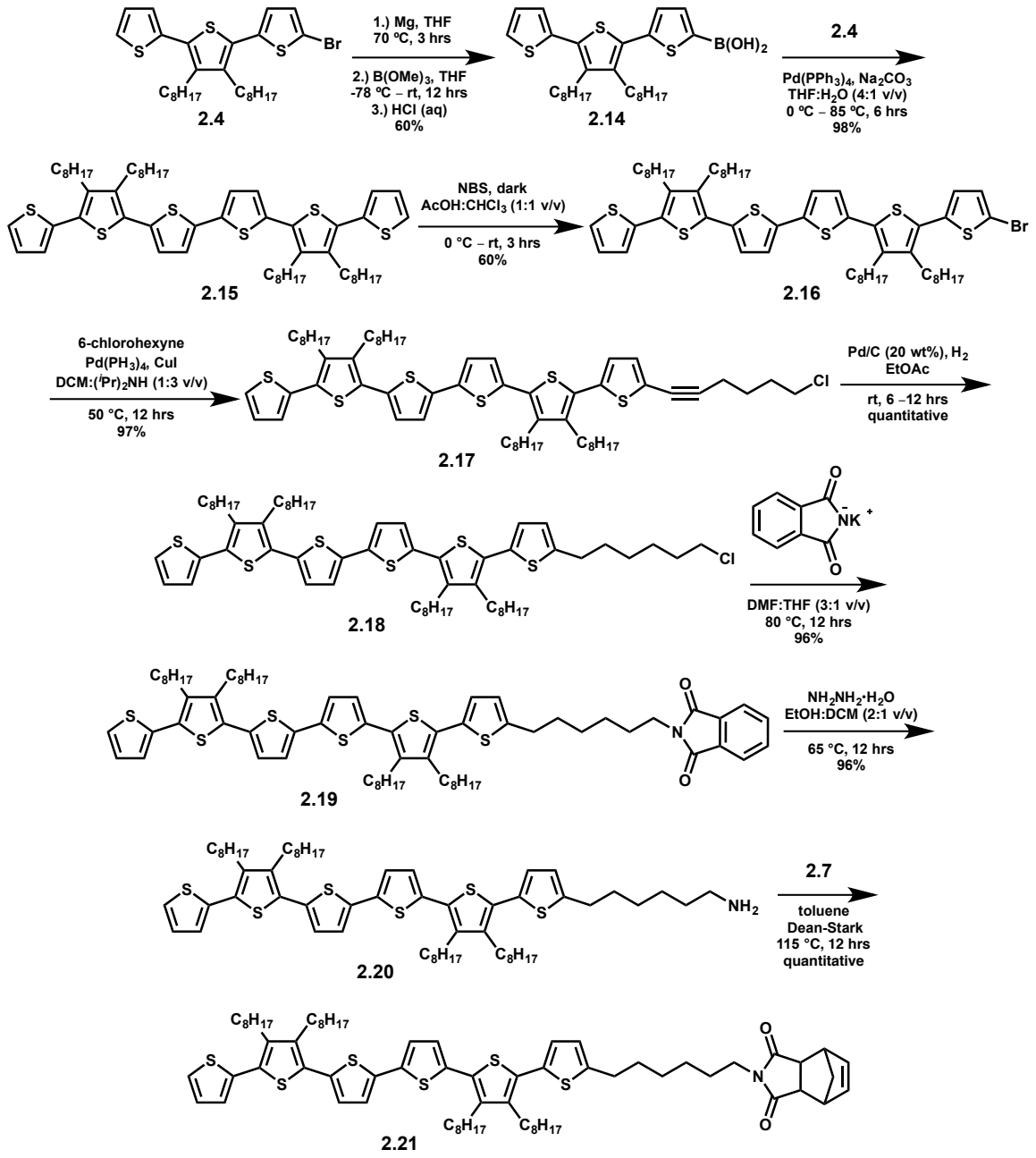

Scheme 2.3. Synthetic route to Sexi monomer **2.21**.

The synthesis of the PDI monomer (**2.28**) follows modified literature procedures and is outlined in **Scheme 2.4**.[194–197] The PDI core was modified with branched octyl chains in order to improve the solubility of the final material. While both the imide and bay positions on the PDI core are synthetically accessible for this modification, the imide position was chosen for the ease of synthesis. Modification at the imide position also maintains the electronic properties of the parent PDI material, as modification at the bay positions can affect the electronic properties of the resultant product. The branched octyl amine, compound **2.24**, could be synthesized by two different routes. The first synthetic route (**Route A**) begins with the Grignard reaction of ethyl formate with octyl magnesium bromide to yield the branched alcohol derivative (**2.22**). Compound **2.22** was then reacted in a Mitsunobu reaction with phthalimide, using triphenylphosphine and diisopropyl azodicarboxylate (DIAD), to yield the phthalimide-protected amine (**2.23**). Deprotection with hydrazine hydrate gave the desired free amine, compound **2.24**, in 83% yield over the 3 steps. In the second synthetic route (**Route B**), direct reductive amination of 9-heptadecanone, using ammonium acetate (NH_4OAc) to form the intermediate imine and sodium borohydride ($NaBH_4$) as the reducing agent, gave compound **2.24** in 80% yield. Since both synthetic routes could be carried out in the same amount of time and gave similar yields, the choice of route depended on the availability of starting materials. Once synthesized, compound **2.24** was reacted with 3,4,9,10-perylenetetracarboxylic dianhydride to yield the symmetric diimide (**2.25**), which was then asymmetrically saponified to yield the imide-anhydride, compound **2.26**. The norbornene dione, compound **2.7**, was modified with a terminal free amine via reaction with 1,6-diaminohexane to yield compound **2.27**. This route was chosen to prevent difficult purification procedures, since compound **2.7** could be easily synthesized in one step, and 1,6-diaminohexane is commercially available. The hexane linkage between the

norbornene backbone and the PDI pendant group was chosen because synthesis of the ethyl derivative resulted in a monomer that did not undergo polymerization, possibly due to the steric hindrance at the catalytic center. Furthermore, it was hypothesized that the longer hexyl-linkage in both the p-type and n-type monomers could aid in nanoscale self-assembly in the block copolymer materials by allowing for more chain mobility in the block segments.[29] Condensation of compound **2.27** with the asymmetric perylene intermediate (**2.26**) yielded the desired monomer **2.28** in 40-42% yield over 5-7 steps.

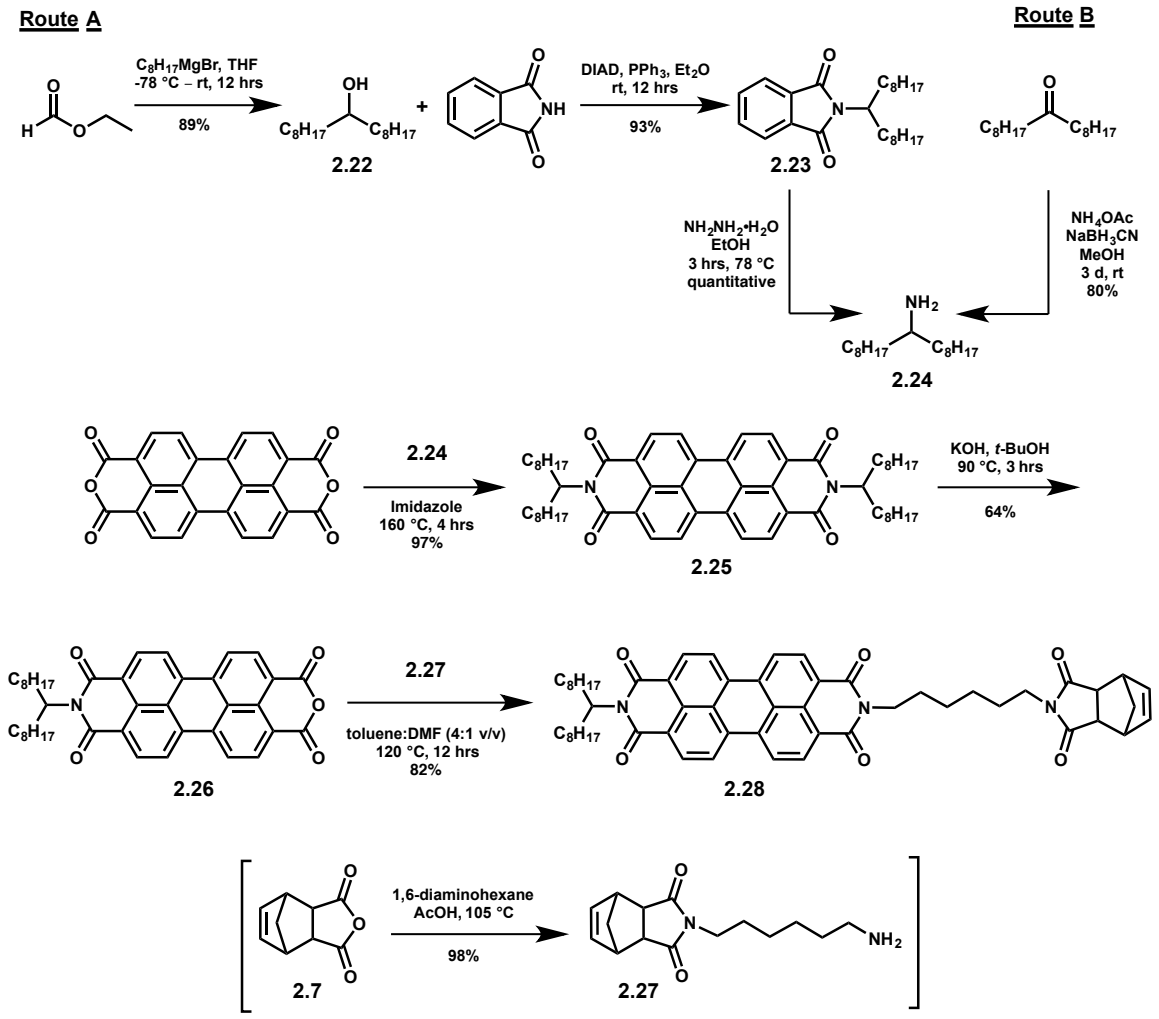

Scheme 2.4. Synthetic route to PDI monomer **2.28**.

Polymerization

Both p-type/donor (Ter **2.13**, Sexi **2.21**) and n-type/acceptor (PDI **2.28**) monomers were polymerized by ROMP using G2 in DCM under a N_2 atmosphere to yield the corresponding homopolymers. The good solubility of the monomers and resulting homopolymers in common organic solvents allowed for characterization by ^1H NMR and GPC. The polymerization of all of three monomers were shown to be living, with the number-average molecular weight (M_n) of the homopolymer tracking linearly with ratio of monomer to catalyst added, as shown in **Figures 2.4 – 2.6**. GPC molecular weight values for the PDI homopolymers (**P2.3** series) are higher than expected, likely due to aggregation of the PDI moieties in THF, leading to an artificially large hydrodynamic radius.[167] **Figures 2.4 – 2.6** also show the TGA analysis of representative samples of the Ter (**P2.1**), Sexi (**P2.2**), and PDI (**P2.3**) homopolymers. All the materials show high thermal stability under nitrogen, with degradation onset temperatures above 375 °C. The high thermal stability of the donor and acceptor homopolymers is very desirable, not only for thermal annealing purposes, but also for potential applications in organic photovoltaic devices.

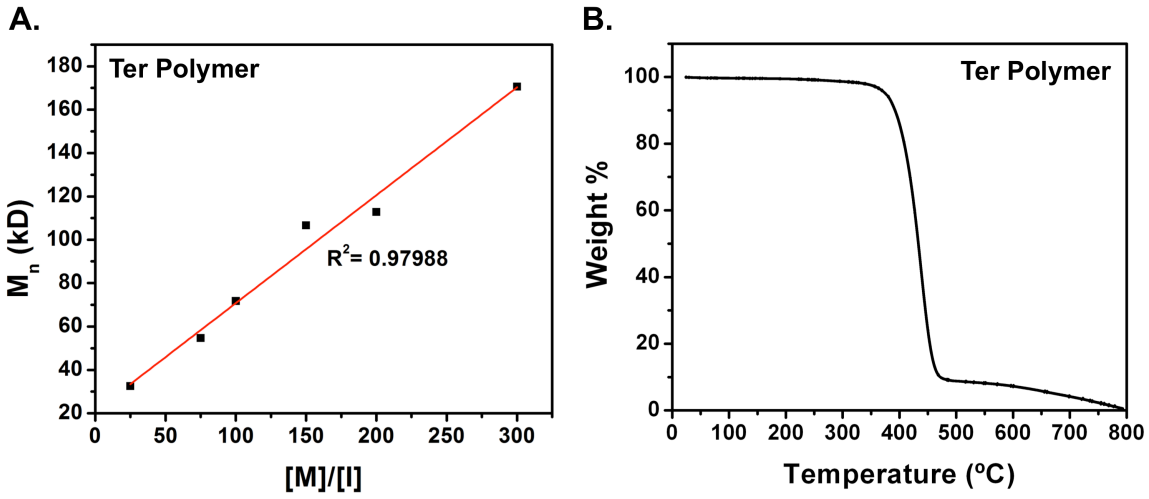

Figure 2.4. (A) Living polymerization plot (M_n vs. *[M]/[I]*) for homopolymerization of Ter monomer **2.13**, where M_n represents the number-average molecular weight as determined by GPC in THF and *[M]/[I]* represents the molar ratio of monomer to G2 catalyst added; (B) TGA plot showing thermal degradation profile of Ter polymer **P2.1**, T_{onset} = 408 °C.

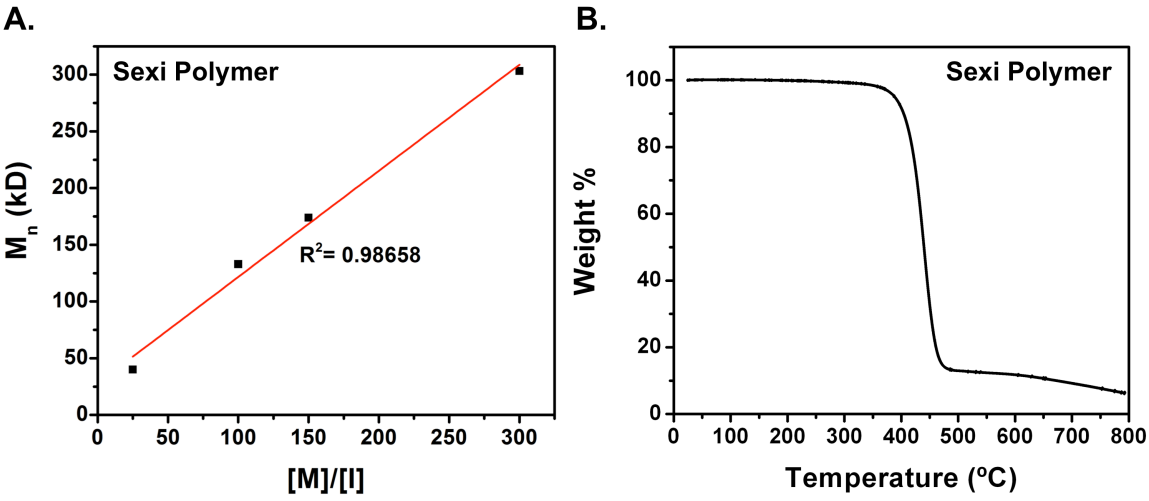

Figure 2.5. (A) Living polymerization plot (M_n vs. *[M]/[I]*) for homopolymerization of Sexi monomer **2.21**, where M_n represents the number-average molecular weight as determined by GPC in THF and *[M]/[I]* represents the molar ratio of monomer to G2 catalyst added; (B) TGA plot showing thermal degradation profile of Sexi polymer **P2.2**, T_{onset} = 417 °C.

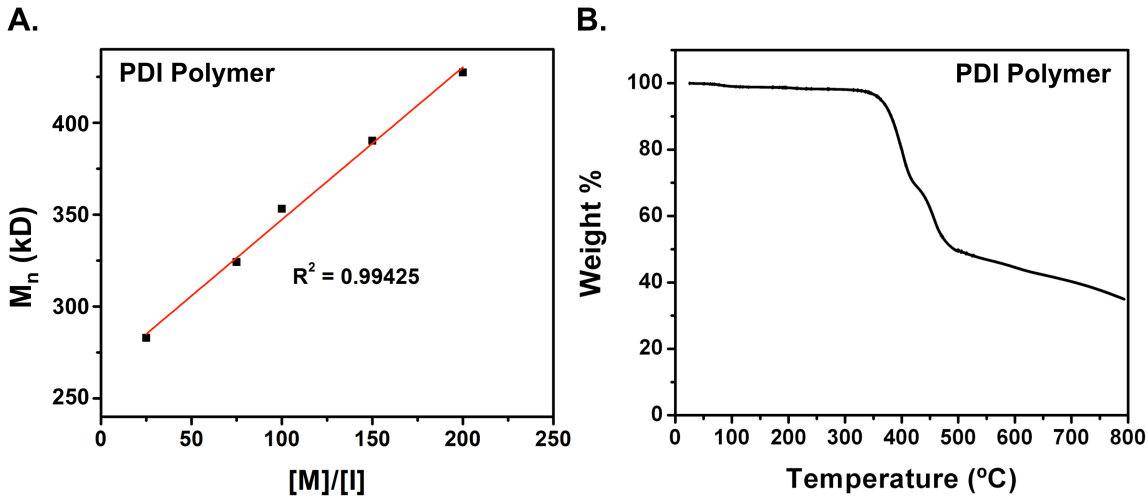

Figure 2.6. (A) Living polymerization plot (M_n vs. *[M]/[I]*) for homopolymerization of PDI monomer **2.28**, where M_n represents the number-average molecular weight as determined by GPC in THF and *[M]/[I]* represents the molar ratio of monomer to G2 catalyst added; (B) TGA plot showing thermal degradation profile of PDI polymer **P2.3**, T_{onset} = 378 °C.

DSC was used to investigate thermal phase transitions in the polymeric materials, specifically the glass transition temperature (T_g). The T_g is the temperature at which an amorphous (or semicrystalline) material goes from a hard, brittle "glassy" solid to a rubber-like "flowing" state, and represents the temperature above which the envisaged donor-acceptor block copolymers would need to be heated to achieve self-assembly by thermal annealing. DSC of the Ter (**P2.1**) and Sexi (**P2.2**) donor homopolymers show T_g's around 100 °C (117 °C for **P2.1**, 102 °C for **P2.2**), well below their respective thermal degradation temperatures (**Figure 2.7**). The Sexi homopolymer (**P2.2**) also shows an endothermic melting transition at T_m = 246 °C, consistent with the crystalline nature of the Sexi moiety. The PDI homopolymer (**P2.3**) exhibits a T_g at 205 °C, similar to values previously reported for PPerAcr polymers with a long alkyl spacers (**Figure 2.8**).[167,198] There is also an endothermic melting transition at T_m = 276 °C. These phase

transitions are similar to those idenitified by Thelakkat and coworkers for their PPerAcr polymer, with a hexyl linkage to the polymer backbone and a branched heptyl solubilizing group at the imide position, which exhibits a liquid crystal Smectic C (SmC) phase between 298 °C and room temperature.[167,197,198]

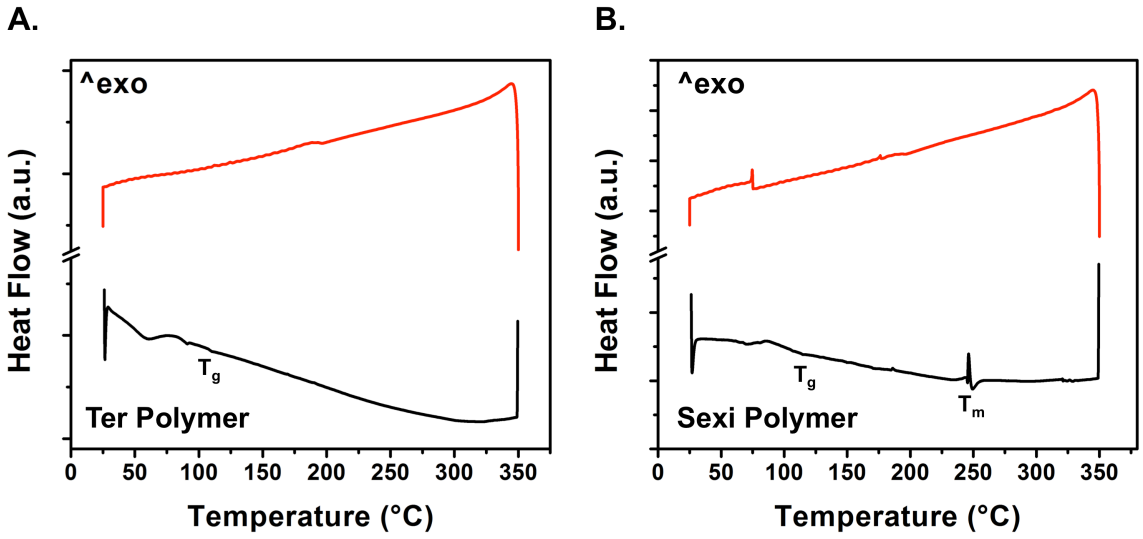

Figure 2.7. DSC traces (black line shows heating cycle, red line shows cooling cycle) for (A) Ter polymer **P2.1**; (B) Sexi polymer **P2.2**.

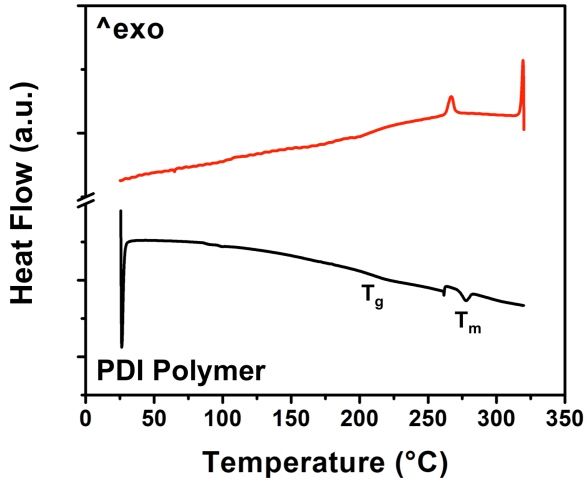

Figure 2.8. DSC trace (black line shows heating cycle, red line shows cooling cycle) for PDI polymer **P2.3**.

Photophysical and Electrochemical Characterization

The Ter (**2.13**), Sexi (**2.21**), and PDI (**2.28**) monomers, as well as the Ter (**P2.1**), Sexi (**P2.2**), and PDI (**P2.3**) homopolymers, were characterized by UV-Vis absorption spectroscopy, fluorescence spectroscopy, and cyclic voltammetry (CV). Compiled photophysical is summarized in **Table 2.4** and electrochemical data is summarized in **Table 2.5**. The data shown in **Table 2.4** and **Table 2.5** corresponds to the Sexi polymer **P2.2c** (N_n = 150), Ter polymers **P2.1d** and **P2.1d-2** (N_n = 150 for both), and PDI polymer **P2.3d-2** (N_n = 150).

Table 2.4. Photophysical characterization of donor and acceptor monomers (**2.13**, **2.21**, **2.28**) and homopolymers (**P2.1**, **P2.2, P2.3**).

Compound	λ_{abs}[a] **(nm)**	ε[b] **($M^{-1}cm^{-1}$)**	λ_{ex}[c] **(nm)**	λ_{em}[c] **(nm)**	**% (Φ)[c]**	$E_g(opt)$[d] **(eV)**
Ter Monomer 2.13	343	17,700	348	440	16 ± 3	2.93
Ter Polymer P2.1	344	14,899	354	443	22 ± 6	2.90
Sexi Monomer 2.21	417	47,300	417	534	70 ± 10	2.51
Sexi Polymer P2.2	418	43,400	418	555	48 ± 3	2.47
PDI Monomer 2.28	457 488 525*	86,499	525	575	100 ± 4	2.27
PDI Polymer P2.3	492* 526	39,245	492 525	532 575 644	87 ± 9	2.10

[a]Determined from UV-Vis spectroscopy in DCM, * indicates λ_{max}; [b]Molar absorptivity, reported per repeat unit for polymers using: $\varepsilon_{repeat\ unit} = \varepsilon_{polymer}/(M_n^{GPC}/MW_{monomer})$; [c]Determined from fluorescence spectroscopy in DCM, quantum yields (Φ) taken in solution as an average of three trials; [d]Optical band gap calculated from the red edge of the UV-Vis absorption profile taken in DCM.

Table 2.5. Electrochemical characterization of donor and acceptor monomers (**2.13**, **2.21**, **2.28**) and homopolymers (**P2.1**, **P2.2, P2.3**).

Compound	HOMO[a] (eV)	LUMO (eV)	E_g(EC)[d] (eV)
Ter Monomer 2.13	-5.23	-2.00[b]	–
Ter Polymer P2.1	-5.15	-2.25[b]	–
Sexi Monomer 2.21	-5.05	-2.54[b]	–
Sexi Polymer P2.2	-4.99	-2.52[b]	–
PDI Monomer 2.28	-5.95	-3.83[c]	2.12
PDI Polymer P2.3	-5.92	-3.79[c]	2.13

[a]Determined from onset of oxidation in CV under N_2 atmosphere in DCM using $E_{HOMO} = [(E_{ox} - E_{1/2\ of\ Fc}) + 4.8\ eV]$, where -4.8 eV represents the energy level of ferrocene vs. vacuum; [b]E_{LUMO} calculated by adding the optical band gap to the E_{HOMO}; [c]E_{LUMO} determined from onset of reduction in CV under N_2 atmosphere in DCM using $E_{LUMO} = [(E_{red} - E_{1/2\ of\ Fc}) + 4.8\ eV]$; [d]Electrochemical band gap determined from the onsets of oxidation and reduction in the CVs.

For the Ter donor monomer (**2.13**) and homopolymer (**P2.1**), there is no significant change in the absorption maximum going from monomer to polymer. High molar absorption coefficients and broad absorption over a large range of the solar spectrum are desirable attributes for materials used in organic photovoltaic applications. The molar absorption coefficient of **2.13** was found to be ε = 17,000 $M^{-1}cm^{-1}$, which decreased to ε = 14,899 $M^{-1}cm^{-1}$ for **P2.1**, possibly due to aggregation caused by slightly lowered solubility. Optical band gaps of 2.93 eV for **2.13** and 2.90 eV for **P2.1** were determined from the red edge of the absorption profile (**Figure 2.9A**). There is a slight bathochromic shift in the excitation maximum going from monomer to polymer (**Figure 2.10A**). There is also a broad red-edge shoulder in the emission of the Ter polymer compared to the monomer, but the emission maxima are centered at 440 nm for both

materials. This broadening may be again attributed to some aggregation behavior in the polymeric material. Quantum yields were comparable for the Ter monomer and Ter polymer, and were determined to be 16 ± 3% for **2.13** and 22 ± 6% for **P2.1**. Photophysical studies for the Ter homopolymer series (see **Table 2.1**, **P2.1a** – **P2.1f**) show that the absorption, excitation, emission, and optical band gap ($E_{g,opt}$) of the pendant Ter semiconductor are independent of the molecular weight of the homopolymer (**Figure 2.11**). This is a very important attribute, since self-assembly behavior is dependent on molecular weight; in order to be useful as an organic semiconductor for the desired application, the electronic properties of the material need to be consistent across a range of molecular weights.

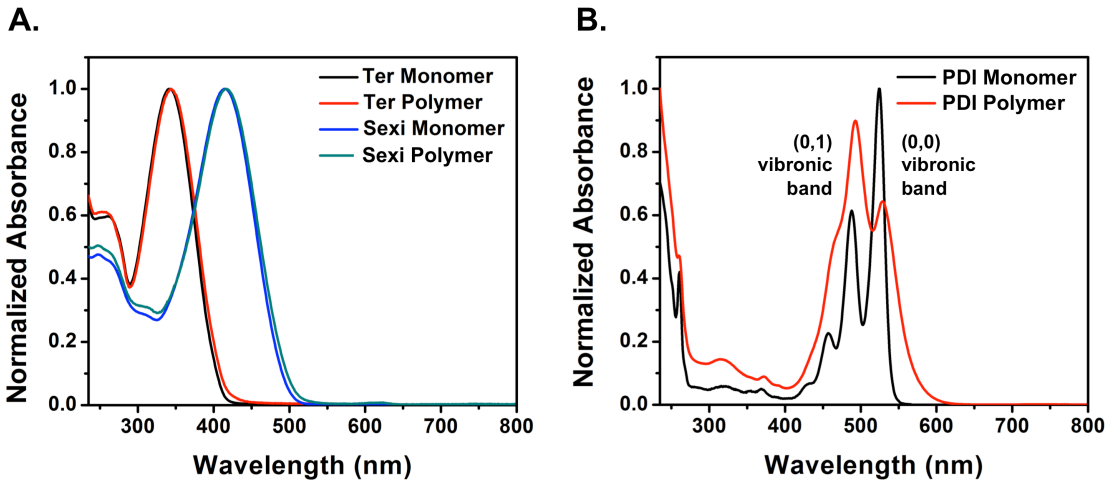

Figure 2.9. (A) Absorption spectra for donor materials: Ter monomer **2.13** (black, λ_{abs} = 343 nm), Ter polymer **P2.1** (red, λ_{abs} = 344 nm), Sexi monomer **2.21** (blue, λ_{abs} = 417 nm), and Sexi polymer **P2.2** (green, λ_{abs} = 418 nm); (B) Absorption spectra for acceptor materials: PDI monomer **2.28** (black, λ_{abs} = 525 nm) and PDI polymer **P2.3** (red, λ_{abs} = 492 nm).

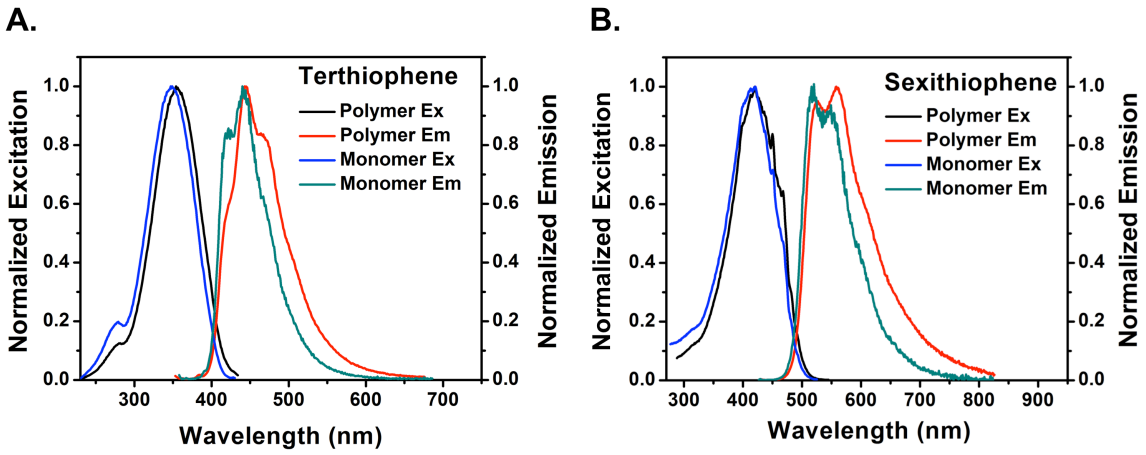

Figure 2.10. Excitation and emission spectra corresponding to: (A) Ter monomer **2.13** (λ_{ex} = 348 nm, λ_{em} = 440 nm) and Ter polymer **P2.1** (λ_{ex} = 343 nm, λ_{em} = 443 nm); (B) Sexi monomer **2.21** (λ_{ex} = 417 nm, λ_{em} = 534 nm) and Sexi homopolymer **P2.2** (λ_{ex} = 418 nm, λ_{em} = 555 nm).

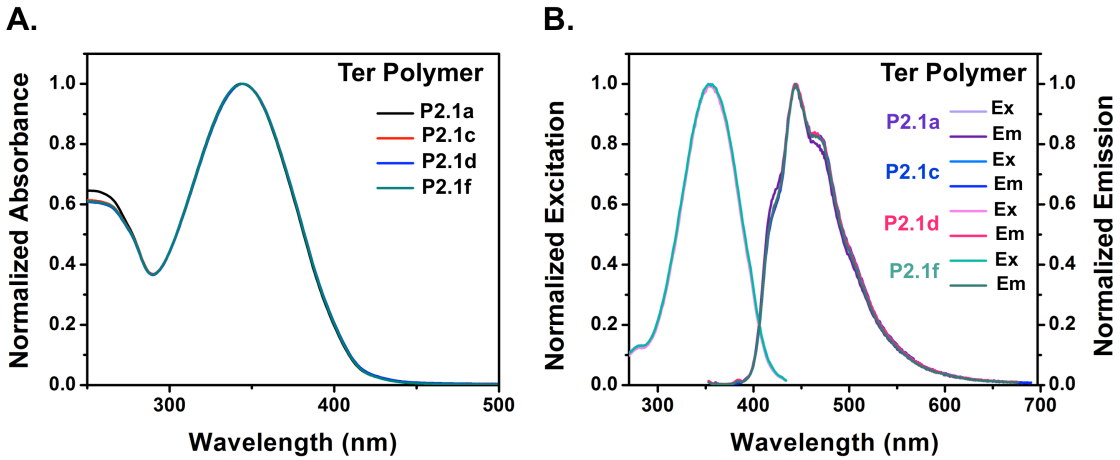

Figure 2.11. (A) UV-Vis absorption profiles of the selected Ter homopolymer from series (**P2.1a** – **P2.1f**, see **Table 2.1**) demonstrating that the λ_{max} is not affected by the molecular weight of the polymer material (λ_{max} = 344 nm); (B) Emission and excitation spectra of selected Ter homopolymers demonstrating that λ_{ex} and λ_{em} are independent of the molecular weight of the homopolymer (λ_{ex} = 343–350 nm, λ_{em} = 444 nm).

The electrochemical behavior of the Ter donor monomer (**2.13**) and homopolymer (**P2.1**) was studied by CV (**Figure 2.12A**), and the HOMO energy level of the materials

was determined from the onset of oxidation (see **Table 2.5**). For both the Ter monomer and polymer, no onset of reduction was observed, so the LUMO energy levels were calculated using the HOMO and the optical band gap. The HOMO and LUMO levels of the Ter monomer **2.13** were found to be -5.23 eV and -2.00 eV, respectively. Similar values were found for the Ter polymer **P2.1**, with HOMO and LUMO levels of -5.15 eV and -2.25 eV, respectively.

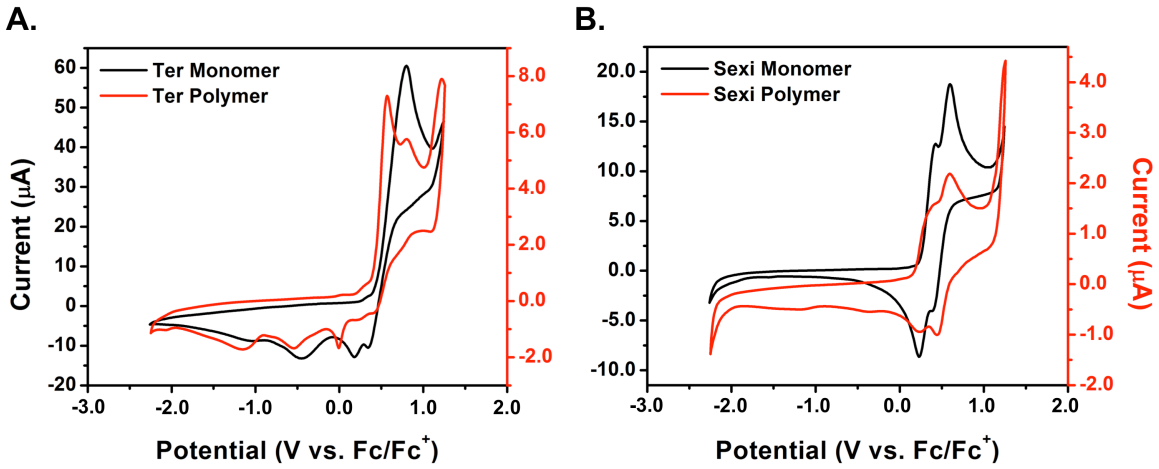

Figure 2.12. CV scans in DCM under inert atmosphere of (A) Ter monomer **2.13** (black) and Ter polymer **P2.1** (red); (B) Sexi monomer **2.21** (black) and the Sexi homopolymer **P2.2** (red). The black x-axes correspond to the monomer CV scans and the red x-axes correspond to the polymer CV scans.

Polymerization of the Ter monomer leads to a slight stabilization of the oxidized species, as evidence in the CV scan (shown in **Figure 2.12A**) by the decrease in peak oxidation potential from 0.80 V vs. Fc/Fc^+ for **2.13** to 0.56 V vs. Fc/Fc^+ for **P2.1**. This lowered oxidation potential is likely the result of π-π interactions between adjacent Ter moieties along the polymer, backbone, which help stabilize the positive charge that is created upon oxidation. Electrochemical studies for the Ter homopolymer series show that the onset of oxidation, and thus the HOMO energy level, of the pendant Ter

semiconductor does not change significantly as the molecular weight of the homopolymer increases (**Figure 2.13**).

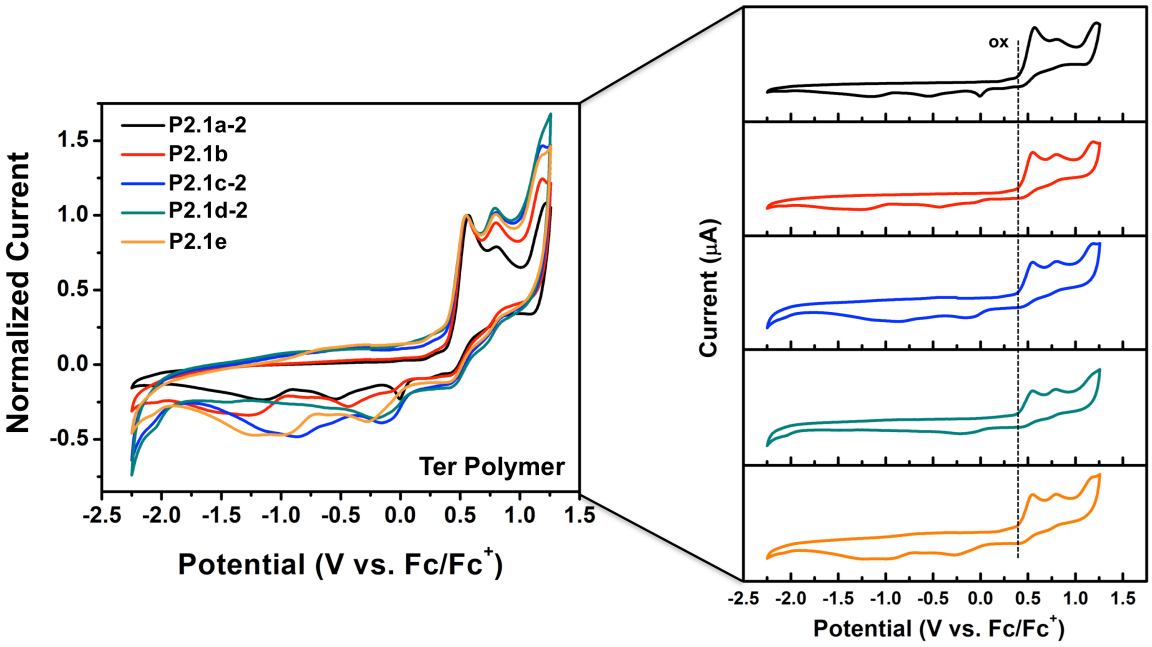

Figure 2.13. Overlay of CV scans showing electrochemical behavior of selected Ter homopolymers from polymer series **P2.1a** – **P2.1f** (see **Table 2.1**), onsets of oxidation (shown in parentheses) are reported vs. Fc/Fc^+: **P2.1a-2** (0.36 V); **P2.1b** (0.34 V); **P2.1c-2** (0.34 V); **P2.1d-2** (0.35 V); **P2.1e** (0.34 V). The dotted line on the stacked plot represents the average onset of oxidation for the homopolymer series.

In the case of the Sexi monomer (**2.21**) and homopolymer (**P2.2**), optical band gaps ($E_{g,opt}$) were determined to be 2.51 eV for **2.21** and and 2.47 eV for **P2.2** (**Figure 2.9A**). These optical band gaps are smaller than the Ter materials due to the increased conjugation of the Sexi semiconductor. The molar absorption coefficients of the Sexi materials were also increased compared to those of the Ter semiconductors, with the Sexi monomer **2.21** exhibiting a molar absorptivity of ε = 47,300 $M^{-1}cm^{-1}$, which decreased slightly to ε = 43,400 $M^{-1}cm^{-1}$ for the Sexi polymer **P2.2**. It is not surprising that the molar absorption coefficients of the Sexi semiconductor materials are higher than that of

Ter, as it has been shown that molar absorptivity increases with higher degrees of oligomerization in conjugated materials. This increase is attributed to the higher cross section of the more rigid, extended oligomers, which enhances photon absorption.[183]

The excitation maximum is centered around 418 nm for both the Sexi monomer and polymer, however the emission maximum shifts from 534 nm (**2.21**) to 555 nm (**P2.2**) (see **Figure 2.10B**), likely due to π-π interactions between adjacent Sexi moieties along the polymer chain. Solution quantum yields in DCM were determined to be 70 ± 10 for the Sexi monomer **2.21** and 48 ± 3 for the Sexi polymer **P2.2**. This large decrease in the quantum yield of the Sexi polymer is likely related to intrachain aggregation in the polymer. Photophysical studies of the series Sexi homopolymers (see **Table 2.2**, **P2.2a** – **P2.2d**) show that the absorption, excitation, emission, and optical band gap ($E_{g,opt}$) of the pendant Sexi semiconductor are independent of the molecular weight of the homopolymer (see **Figure 2.14**).

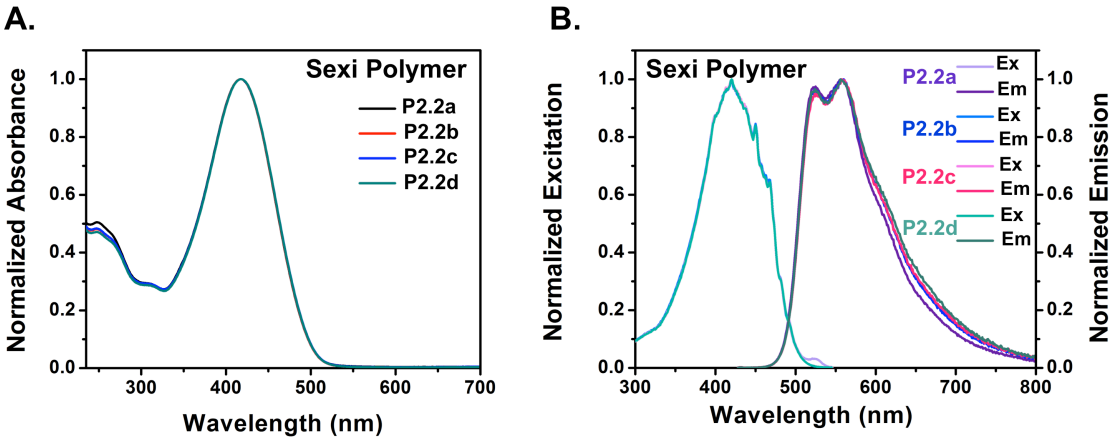

Figure 2.14. (A) UV-Vis absorption profiles of the Sexi homopolymer series (**P2.2a** – **P2.2d**, see **Table 2.2**) demonstrating that the λ_{max} is not affected by the molecular weight of the polymer material (λ_{max} = 418 nm); (B) Emission and excitation spectra of the Sexi homopolymer series demonstrating that the λ_{ex} and λ_{em} are independent of the molecular weight of the homopolymer (λ_{ex} = 418 nm, λ_{em} = 555 nm), although there is a very slight broadening of the red edge of emission with increasing molecular weight.

The electrochemical behavior of the Sexi donor monomer (**2.21**) and homopolymer (**P2.2**) were also studied by CV (**Figure 2.9B**). The HOMO energy level was calculated from the onset of oxidation to be -5.05 eV for **2.21** and -4.99 eV for **P2.2**. Similar to the Ter materials, no reductive event was observed for the Sexi materials within the DCM solvent window. The LUMO energy level was determined from the HOMO energy level and the optical band gap ($E_{g,opt}$), giving values of -2.54 eV for **2.21** and -2.52 eV for **P2.2**. Overall, the HOMO, LUMO, and band gap energy levels of the Sexi monomer are retained in the homopolymer, as shown for the Ter donor materials. Additionally, electrochemical studies show that the onset of oxidation, and thus the highest occupied molecular orbital (HOMO) energy level, of the Sexi moiety does not change significantly as the molecular weight of the homopolymer increases (**Figure 2.15**).

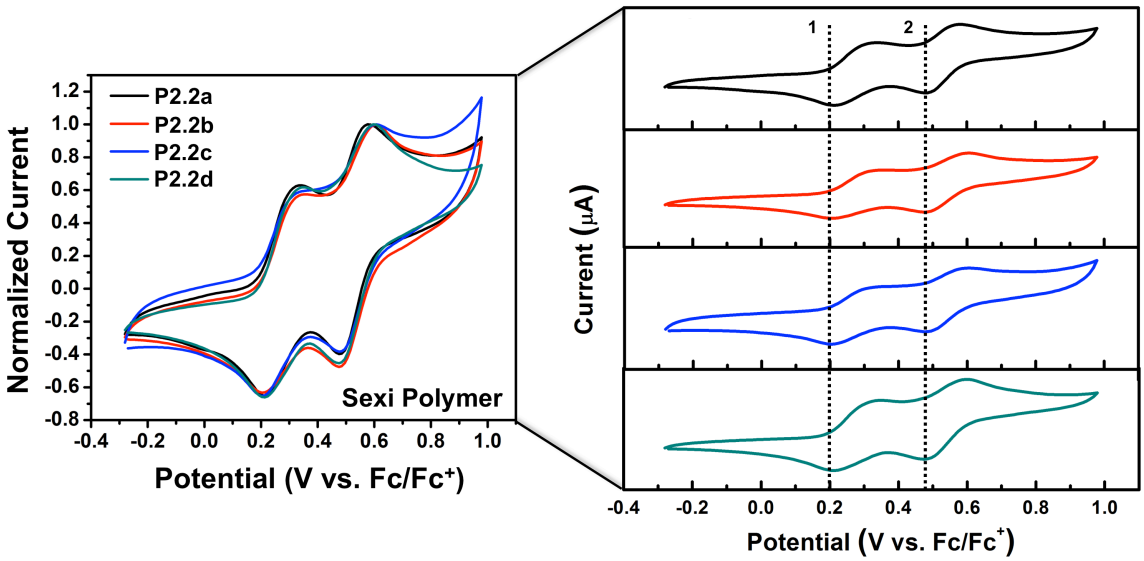

Figure 2.15. Overlay of oxidative CV scans showing electrochemical behavior of the Sexi homopolymer series (**P2.2a** – **P2.2d**, see **Table 2.2**), onsets of oxidation (shown in parentheses) are reported vs. Fc/Fc^+: **P2.2a** (0.19 V); **P2.2b** (0.19 V); **P2.2c** (0.19 V); **P2.2d** (0.18 V). The dotted lines on the stacked plot represent the average onset of oxidation for the first and second one-electron oxidation events for the homopolymers.

The molar absorption coefficient for the PDI monomer (**2.28**) was determined to be ε = 86,499 $M^{-1}cm^{-1}$. The molar absorptivity per repeat unit of the PDI polymer was found to be ε = 39,245 $M^{-1}cm^{-1}$ (**P2.3**). This large decrease is molar absorptivity in the polymer is likely due to aggregation along the polymer chain. In the PDI absorption profile (see **Figure 2.9B**), the (0,1) vibronic transition band is centered at 490 nm and the (0,0) vibronic transition band is centered at 525 nm (**Figure 2.6B**). It has been shown that for free PDI units, the intensity of the (0,1) band is lower than that of the (0,0) band, and the monomer **2.28** follows this trend.[199,200] In the polymer system, the (0,1) band shows an increase in intensity relative to the (0,0) band, which is indicative of the formation of cofacially-aligned PDI units known as H-aggregates. The strong vibronic coupling of the H-aggregates leads to this enhancement in the (0,1) vibronic band compared to nonaggregated PDI molecules.[201–204] Furthermore, this aggregation behavior can enhance electron-transport characteristics in PDI materials.[114,184]

Interestingly, when the PDI semiconductors are attached as pendant groups to the polymeric backbone, it is the solubility of the backbone that determines the degree of aggregation between PDI units.[199] When the polymer backbone is well-solvated, the polymer chains are completely extended, allowing for strong vibronic coupling between the evenly-spaced PDI pendant groups. However, when the amorphous polymer backbone is poorly solvated, aggregation is decreased due to poor alignment of the PDI units. This solvent-dependent aggregation can be tracked by comparing the (0,0) and (0,1) vibronic transition bands in the UV-Vis absorption profile of the material, and this behavior can affect choice of solvent during device fabrication or for thin film studies, when aggregation may not be desirable before thermal annealing. **Figure 2.16** shows the UV-Vis profiles of the PDI monomer **2.28** and PDI homopolymers **P2.3a** (N_n = 25) and **P2.3d** (N_n = 150) in different solvents. **P2.3a** and **P2.3d** were chosen because of their

different numbers of PDI repeat units on the polymer chain (25 and 150, respectively). As the polymer backbone solubility increases from *o*-dichlorobenzene, to DCM, to toluene, the amount of aggregation between the PDI units in the homopolymer also increases, as evidenced by the large increase in the (0,1) vibronic band at 490 nm compared to the (0,0) vibronic band at 525 nm. The monomer shows no change in the UV-Vis profile in the different solvents, demonstrating that this phenomenon is confined to the polymeric material when the adjacent PDI units are spaced at equidistance in a core-to-core arrangement along the backbone. Furthermore, the smaller PDI polymer (**P2.3a**) shows slightly increased (0,0) vibronic band intensity compared to the larger polymer (**P2.3d**) in all of the solvents, suggesting that there is less aggregation with less repeat units.

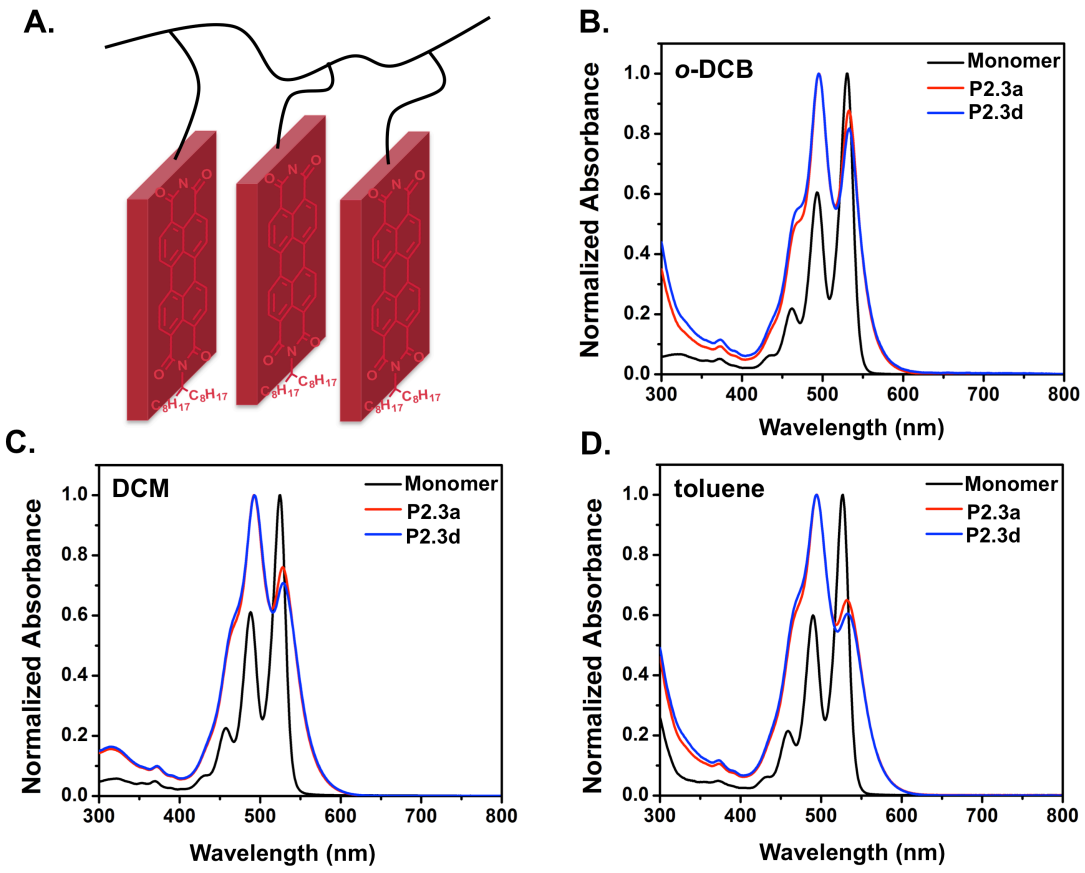

Figure 2.16. PDI aggregation behavior in different solvents: (A) schematic of favorable core-to-core alignment (H-aggregation) of PDI units in the polymer material; UV-Vis profile of PDI monomer **2.28** (black) and PDI homopolymers **P2.3a** (red) and **P2.3d** (blue) in (B) *o*-dichlorobenzene, (C) DCM, and (D) toluene demonstrating solvent-dependent aggregation in the polymer materials.

Optical band gaps of 2.27 eV for the PDI monomer **2.28** and 2.10 eV for the PDI homopolymer **P2.3** were determined from the red edge of the absorption profile. The decrease in optical band gap going from monomer to polymer is attributed to the red-edge spectral broadening observed in the PDI absorption profile due aggregation. In the emission spectra, the PDI monomer (**2.28**) shows strong vibronic structure (distinct Frank-Condon states) consistent with its rigid structure (see **Figure 2.17**). Excitation at

525 nm gives an emission maximum at 575 nm with a very small Stokes shift, again consistent with the rigid structure. The polymer (**P2.3**) excitation spectrum looks very similar to the monomer, but the emission spectrum shows a broad emission band centered around 650 nm, which has been correlated to the presence of H-aggregation in the polymer chain.[199] When the polymer is excited at 490 nm, the absorption maxima of the H-aggregates, the intensity of the emission at 650 nm increases, consistent with H-aggregate emission. Quantum yields were determined to be 100 ± 4% for the PDI monomer and 87± 9% for the PDI polymer.

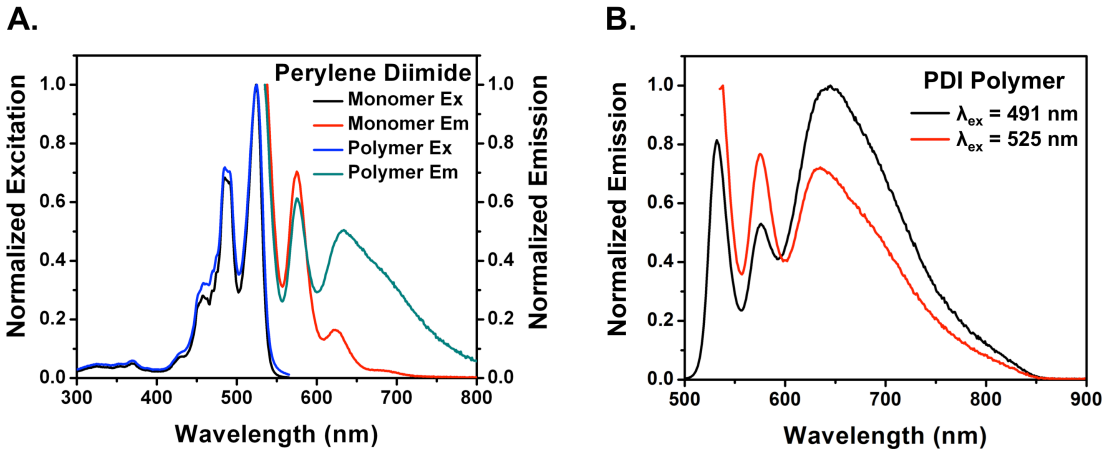

Figure 2.17. Excitation and emission spectra corresponding to: (A) PDI monomer **2.28** (λ_{ex} = 525 nm, λ_{em} = 575 nm) and PDI polymer **P2.3** (λ_{ex} = 525 nm, λ_{em} = 575 nm); (B) PDI polymer **P2.3** showing increased excimer emission (centered at 640 nm) upon excitation at 491 nm.

Photophysical studies show that the absorption, excitation, and emission characteristics of the PDI material are also independent of molecular weight (see **Figure 2.18**). Interestingly, the PDI homopolymer series (see **Table 2.3**, **P2.3a** – **P2.3e**) used to study the effect of molecular weight on the photophysical and electrochemical properties shows increased H-aggregation compared to the original PDI homopolymer (**P2.3d-2**),

possibly due to a more stringent column purification of the precursor monomer used. This may explain the much higher GPC molecular weight values for the PDI homopolymer series **P2.3a** – **P2.3e**, as increased aggregation could drastically increase the hydrodynamic radius of the PDI homopolymer. It is likely that there was a very slight amount of impurity present in the original monomer used to synthesize **P2.3d-2**, as the concentration of the suspected impurity was low enough that it was not detected by ^{1}H NMR. However, incorporation of even a small amount of unfunctionalized norbornene dione (**2.7**) into the polymer chain could disrupt the vibronic coupling between neighboring PDI pendants, lowering the overall aggregation in the homopolymer material. Although this doesn't significantly affect the absorption, excitation, or optical band gap, it does increase the intensity of the aggregate emission peak centered at 640 nm.

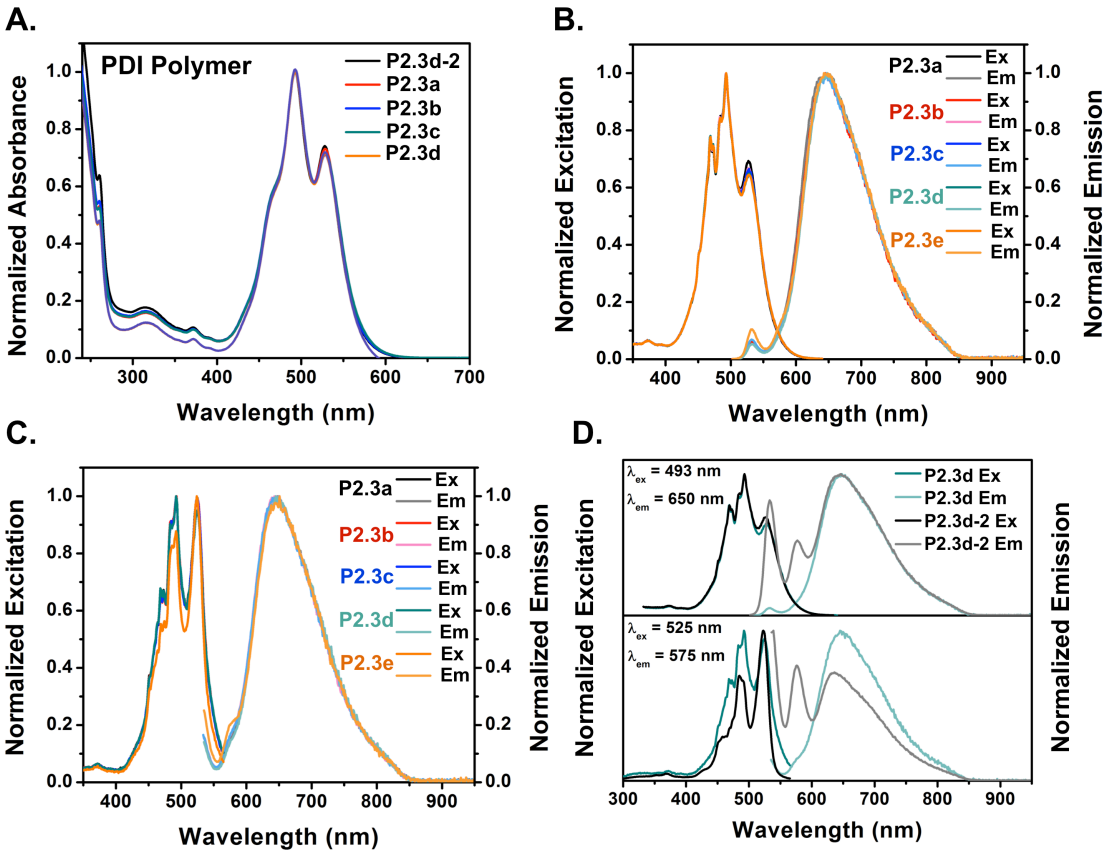

Figure 2.18. UV-Vis and fluorescence spectroscopy of the PDI polymer series (**P2.3a** – **P2.3e**, see **Table 2.3**): (A) Normalized UV-Vis of PDI homopolymers demonstrating that λ_{abs} is not affected by the molecular weight of the polymer material (λ_{abs} = 493, 528 nm); (B,C) Emission and excitation spectra of the PDI homopolymer series demonstrating that λ_{ex} and λ_{em} are independent of the molecular weight of the homopolymer using either excitation, (B) λ_{ex} = 493 nm, λ_{em} = 650 nm, (C) λ_{ex} = 525 nm, λ_{em} = 575 nm. The change in the excitation profile at 493 nm from that of the absorbance profile is likely caused by change in the geometry of the excited molecule from that of the ground state (ie. excimer formation); (D) Stacked fluorescence spectroscopy comparison of **P2.3d** and **P2.3d-2** (N_n = 150 for both), showing the increased H-aggregate emission at 640 nm, and the concurrent disappearance of the non-aggregated PDI emission at 575 nm, in **P2.3d**.

During CV, the PDI monomer (**2.28**) shows two distinct one-electron reversible reduction waves at negative potentials, as well as an oxidation event at positive potential

(see **Figure 2.19**). From these, the HOMO energy level was calculated to be -5.95 eV and the LUMO energy level was calculated to be -3.83 eV. Again, the HOMO and LUMO levels change very little going from monomer to polymer, with calculated HOMO and LUMO levels for the PDI polymer (**P2.3**) of -5.92 eV and -3.79 eV, respectively. Electrochemical band gaps for the acceptor material were determined to be 2.12 eV for the PDI monomer **2.28** and 2.13 eV for the PDI homopolymer **P2.3**. These values match the optical band gaps determined for the PDI materials well. Electrochemical studies of the series of PDI homopolymers (**P2.3a** – **P2.3e**, see **Table 2.3**) show that the onsets of oxidation and reduction, and thus the HOMO and LUMO energy levels, are independent of molecular weight (**Figure 2.20**).

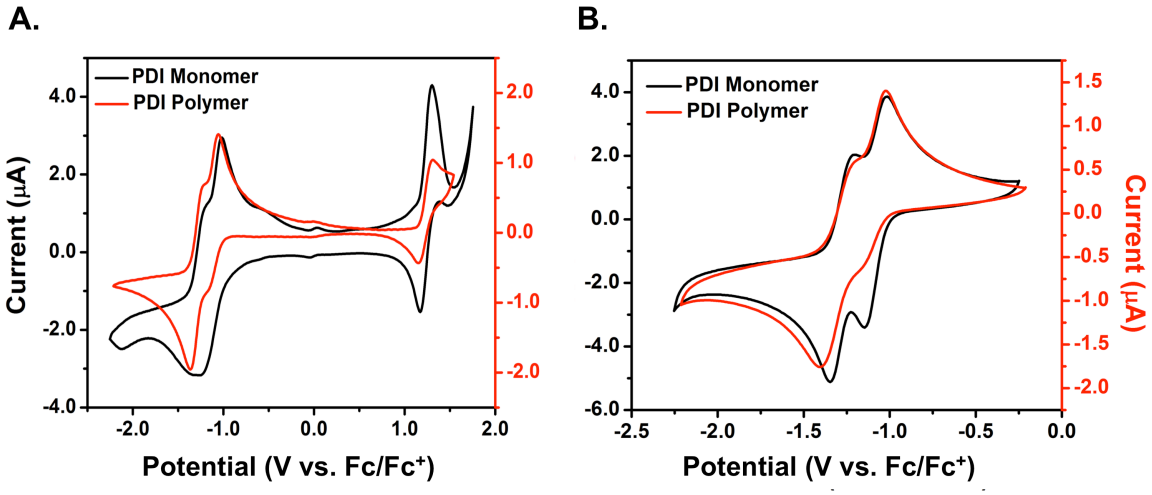

Figure 2.19. CV scans in DCM under inert atmosphere of PDI monomer **2.28** (black) and PDI polymer **P2.3** (red): (A) full scan; (B) reductive scan. The black x-axes correspond to the monomer CV scans and the red x-axes correspond to the polymer CV scans.

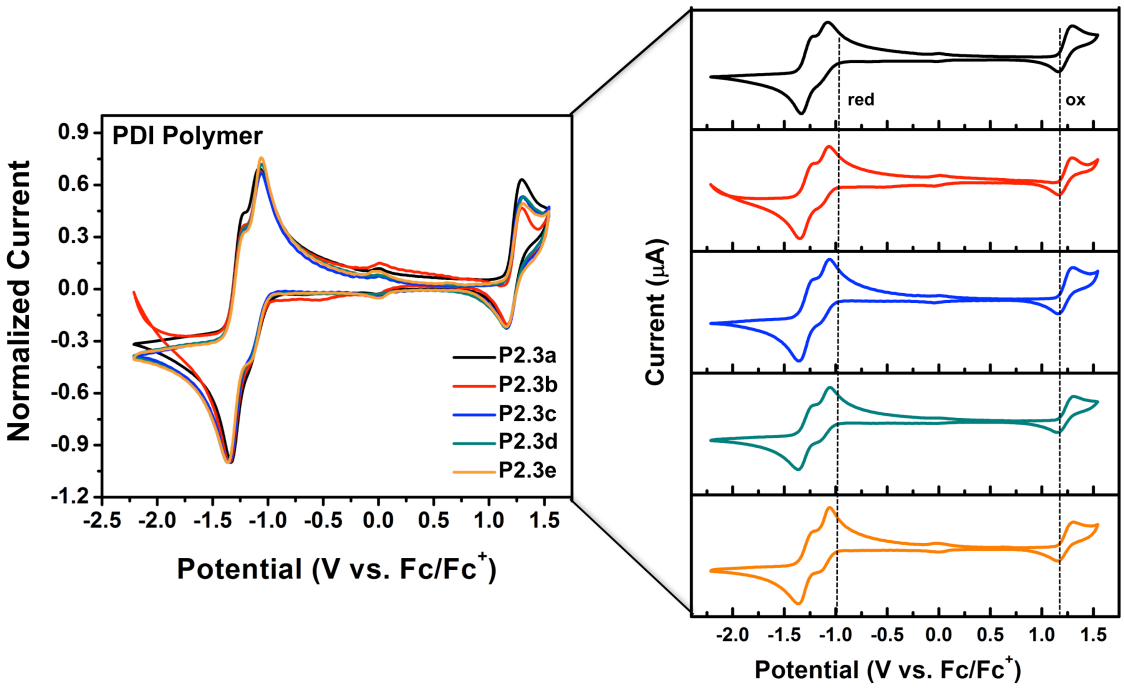

Figure 2.20. Overlay of CV scans showing electrochemical behavior of PDI homopolymer series (**P2.3a – P2.3e**, see **Table 2.3**), onsets of oxidation and reduction (shown in parentheses) are reported vs. Fc/Fc^+: **P2.3a** (1.15V, -0.98 V); **P2.3b** (1.17 V, -1.02 V); **P2.3c** (1.16 V, -1.01 V); **P2.3d** (1.15 V, -1.00 V), **P2.3e** (1.16 V, -1.01 V). The dotted line labeled "ox" on stacked plot represents the average onset of oxidation and the dotted line labeled "red" represents the average onset of reduction.

The well-matched energy levels of both the Ter and Sexi donor materials with the PDI acceptor are promising for application in OPVs. In order to have efficient exciton dissociation and charge transfer, there needs to be a downhill energetic driving force that exceeds the exciton binding energy (with exciton binding energies ranging between 0.3 – 1.0 eV). In systems where both the donor and acceptor are strong light absorbers (as is the case here for the donor-acceptor pairs), both the LUMO offset (ΔE_{LUMO}) and the HOMO offset (ΔE_{HOMO}) between the donor and acceptor materials become important. ΔE_{LUMO} represents the downhill driving force for electron transfer from donor to acceptor and ΔE_{HOMO} represents the driving force for hole "back-transfer" from acceptor to

donor.[3,36] In the case of ΔE_{LUMO}, a small offset is usually desirable for reduced voltage losses in the photovoltaic cell. However, in several cases, the highest internal quantum efficiencies have been reported for systems showing large LUMO offsets (0.5 – 1.0 eV) due to the increased generation of free charges.[16,205] In fact, it has been shown that systems with large offset values (> 1.0 eV) often display geminate pair dissociation quantum efficiencies approaching 100%, while systems with more modest offset values (0.2 – 0.3 eV) can exhibit suppressed charge dissociation.[12,33]

Recently, Durrant and coworkers reported a large study of donor and acceptor materials, where they demonstrated that the energy offset of the materials is a key determinant of charge separation efficiency.[33] The energy offset driving charge separation (ΔE_{CS}) is described by the energy difference between the singlet exciton and the polaron energies, and is related to the LUMO offset by $\Delta E_{CS} = \Delta E_{LUMO} - E_{exc}^{b}$, where E_{exc}^{b} represents the exciton binding energy. In addition, they also demonstrated that the magnitude of ΔE_{CS} required to achieve efficient charge photogeneration is material dependent. For example, in bulk heterojunction (BHJ) blends of polythiophene polymers with PCBM, the energy offset required to drive charge separation is ~ 0.9 eV (corresponding to ΔE_{LUMO} = 1.2 eV, and E_{exc}^{b} = 0.3 eV). In the designed donor-acceptor systems, ΔE_{LUMO} is calculated as 1.27 eV for the Sexi-PDI system and 1.54 eV for the Ter-PDI system, based on the homopolymer LUMO energy levels. This leads to ΔE_{CS} = 0.97 eV for Sexi-PDI system and 1.24 eV for Ter-PDI system, suggesting that both systems may demonstrate high charge separation efficiencies.

Furthermore, the difference between the HOMO of the donor and the LUMO of the acceptor determines the maximum theoretical open circuit voltage (V_{oc}) that can be attained by the device. Based on the electrochemical band gap determined from the homopolymer CVs, this is equal to 1.4 eV for the Ter-PDI donor-acceptor pair and 1.2

eV for the Sexi-PDI donor-acceptor pair. For the commonly utilized donor-acceptor pair P3HT-PCBM, this value is equal to 1.0 eV, and for PPV-PCBM this is equal to 1.2 eV.[16] These values match well with those determined for the HOMO-LUMO gap (V_{oc}) for the Ter-PDI and Sexi-PDI donor-acceptor pairs described here.

Stern-Volmer Quenching Characterization

The efficiency of charge- and energy-transfer processes that may occur in the donor-acceptor system can be roughly approximated by the spectral overlap between the emission of the donor and the excitation of the acceptor, with a larger spectral overlap suggesting better electronic communication.[206,207] Overlay of these spectra for the Ter and PDI monomers (**2.13** and **2.28**, respectively) and polymers (**P.21** and **P2.3**, respectively) are shown in **Figure 2.21**. Going from monomer to polymer, there is an increase in the spectral overlap, due to the red-edge shoulder of the Ter polymer emission.

The efficiency of charge transfer between the Sexi and PDI semiconductors was also estimated by the spectral overlap. Overlay of the photophysical spectra of the Sexi donor emission with the PDI acceptor excitation shows that both monomeric (**2.21** and **2.28**, respectively) and polymeric (**P2.2** and **P2.3**, respectively) systems have large spectral overlap (see **Figure 2.22**). In fact, in the monomer system, the emission maximum of Sexi, centered at 534 nm, aligns almost perfectly with the excitation maximum of PDI, centered at 525 nm, leading to a large spectral overlap area. In the polymeric system, the bathochromic shift in the Sexi emission spectra leads to a slight decrease in spectral overlap.

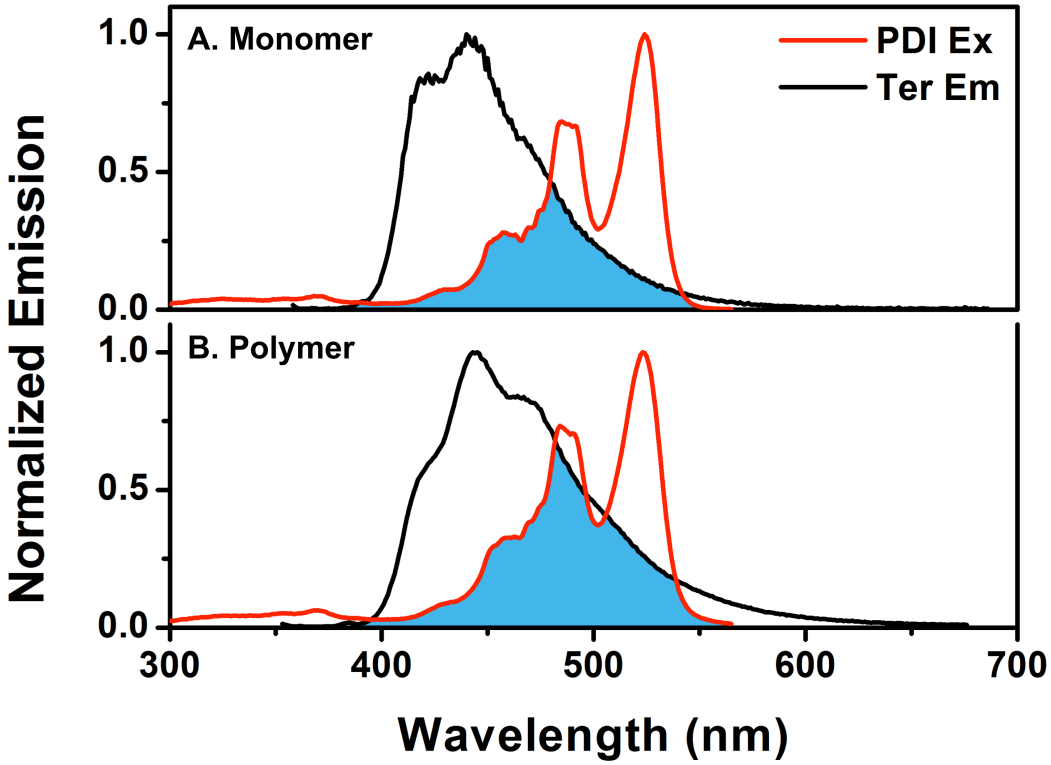

Figure 2.21. Orbital overlap spectra of (A) Ter monomer (**2.13**) emission and PDI monomer (**2.28**) excitation; (B) Ter polymer (**P2.1d**) emission and PDI polymer (**P2.3d-2**) excitation. The orbital overlap is indicated in blue.

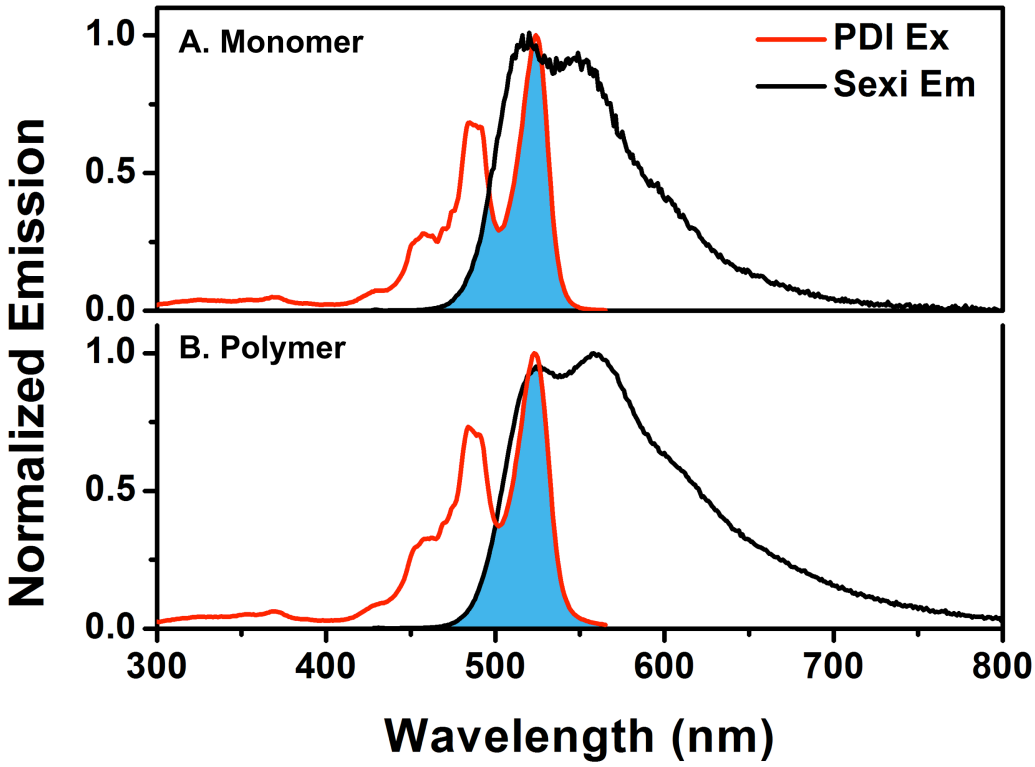

Figure 2.12. Orbital overlap spectra of (A) Sexi monomer (**2.21**) emission and PDI monomer (**2.28**) excitation; (B) Sexi polymer (**P2.2c**) emission and PDI polymer (**P2.3d-2**) excitation. The orbital overlap is indicated in blue.

The efficiency of electronic communication can be quantified using a Stern-Volmer (SV) analysis, which relates donor emission quenching to the concentration of added acceptor. SV quenching experiments were performed by monitoring the photoluminescence (PL) intensity of the Ter or Sexi fluorophore as a function of added PDI fluorophore using fluorescence spectroscopy. Stock solutions of the Ter monomer (**2.13**), Ter polymer (**P2.1d**), Sexi monomer (**2.21**), Sexi polymer (**P2.2c**), PDI monomer (**2.28**), and PDI polymer (**P2.3d-2**) were made in DCM. Following a typical procedure, the emission and excitation spectra of the Ter monomer were recorded, and then small aliquots of a PDI monomer stock solution were added to the Ter monomer solution and

mixed well using the syringe and needle. The Ter monomer emission intensity at λ_{em} = 442 nm (with λ_{ex} = 345 nm) was recorded after each addition of PDI monomer solution. This same procedure was repeated for the Ter polymer, first taking the emission and excitation spectra of the pure Ter polymer solution, then adding small aliquots of PDI polymer stock solution to the Ter polymer solution and monitoring the Ter polymer emission at λ_{em} = 442 nm (with λ_{ex} = 345 nm). The same procedure was followed for the Sexi-PDI donor-acceptor monomer and polymer systems. In these studies, the emission quenching of the Sexi donor was monitored at λ_{em} = 514 nm (with λ_{ex} = 417 nm) for the monomeric system and λ_{em}= 520 nm (with λ_{ex} = 418 nm) for the polymeric system.

The Ter emission intensity was plotted as a function of PDI concentration (in mg/mL) yielded the SV plot, with the slope of this plot is related to the efficiency of donor PL quenching. While quenching of the Ter emission occurs in both systems, the monomer system has a steeper SV slope, indicating more efficient emission quenching processes (see **Figure 2.23** and **Figure 2.24**). This can be attributed to the likelihood of collisional quenching of monomers in solution compared to that of polymers in solution.

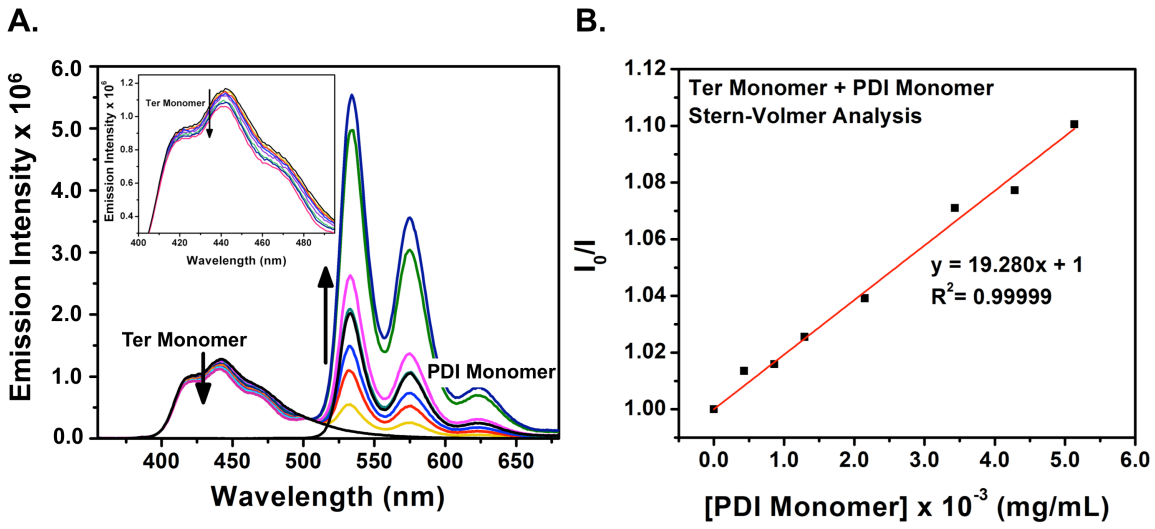

Figure 2.23. SV analysis for Ter monomer and PDI monomer: (A) PL quenching of Ter monomer with added PDI monomer. Emission spectra for the Ter and PDI materials before mixing are shown in black; (B) SV plot of Ter monomer PL quenching as a function of PDI monomer concentration, monitored at λ_{em} = 442 nm.

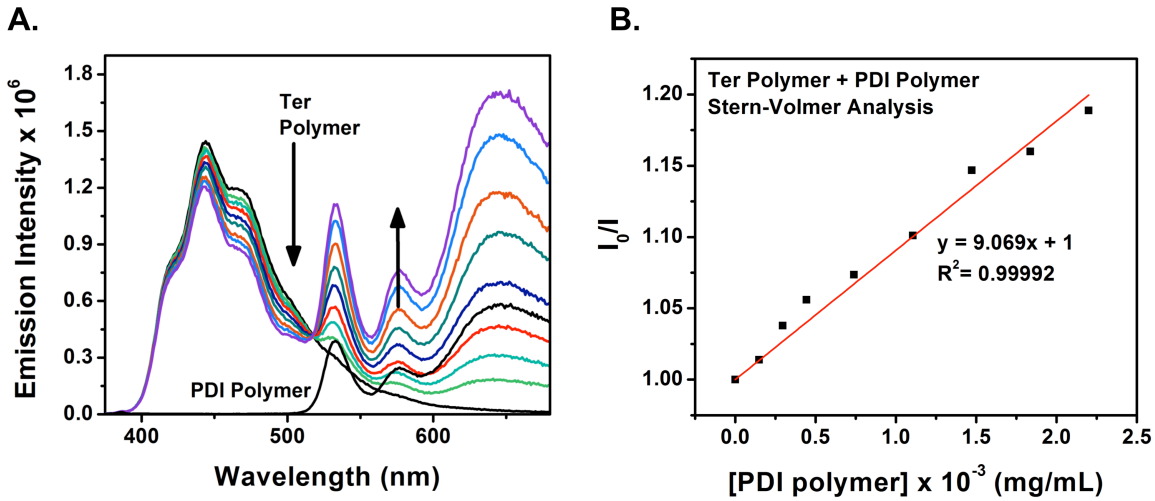

Figure 2.24. SV analysis for Ter polymer and PDI polymer: (A) PL quenching of Ter polymer with added PDI polymer. Emission spectra for the Ter and PDI materials before mixing are shown in black; (B) SV plot of Ter polymer PL quenching as a function of PDI polymer concentration, monitored at λ_{em} = 442 nm.

In the case of the Sexi-PDI donor-acceptor system, it is important to note that due to the increased overlap in the photophysical profiles of the Sexi and PDI fluorophores, it is more difficult to quantitatively monitor the PL quenching of Sexi upon addition of PDI. In both the monomer and polymer systems, there is a red shift in the emission spectrum with increasing concentrations of PDI (see **Figure 2.25** and **Figure 2.26**). The SV slope is steeper for the monomer, and the cause may be two-fold: first, the spectral overlap decreases slightly in the polymer system as a result of the red shift in the Sexi emission maximum; and second, the likelihood of collisional quenching decreases in the polymer system due to decreased solubility. Still, the SV plots for the Sexi-PDI system show more efficient quenching than the Ter-PDI system, which correlates with the better spectral overlap of the Sexi-PDI donor-acceptor couple.

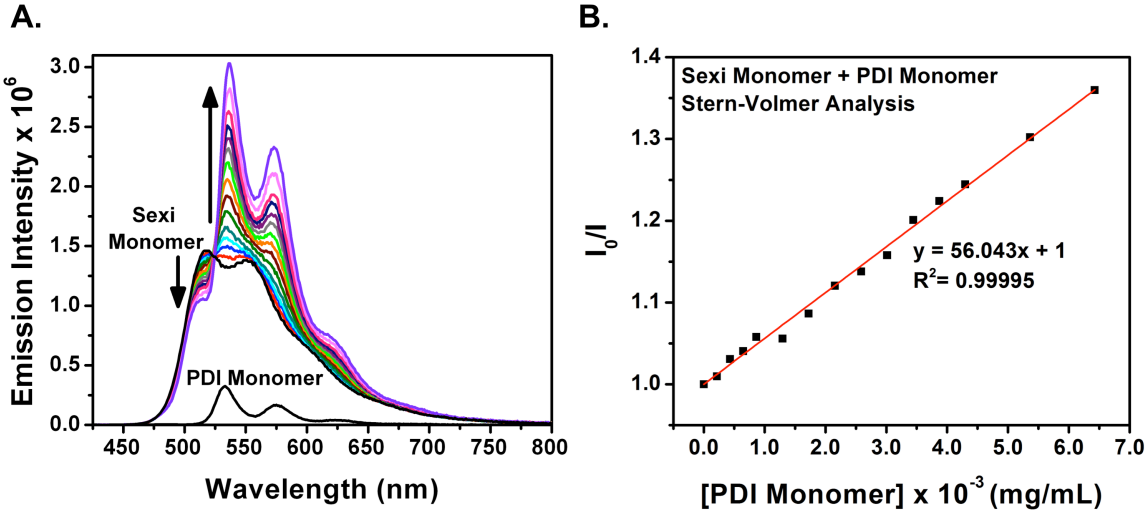

Figure 2.25. SV analysis for Sexi monomer and PDI monomer: (A) PL quenching of Sexi monomer with added PDI monomer. Emission spectra for the Sexi and PDI materials before mixing are shown in black; (B) SV plot of Sexi monomer PL quenching as a function of PDI monomer concentration, monitored at λ_{em} = 514 nm.

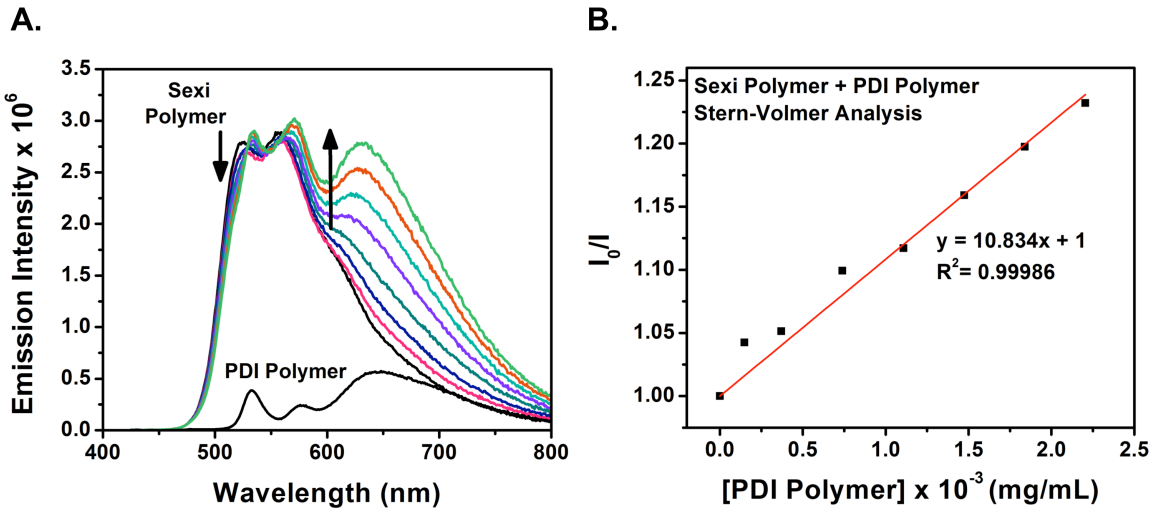

Figure 2.26. SV analysis for Sexi polymer and PDI polymer: (A) PL quenching of Sexi polymer with added PDI polymer. Emission spectra for the Sexi and PDI materials before mixing are shown in black; (B) SV plot of Sexi polymer PLquenching as a function of PDI polymer concentration, monitored at λ_{em} = 520 nm.

CONCLUSION

Norbornene-type monomers containing donor (p-type) oligothiophene (Ter, Sexi) or acceptor (n-type) PDI semiconducting pendant groups were synthesized. These monomers were used to synthesize a series of donor and acceptor homopolymers containing semiconducting pendant groups tethered to a flexible coil-type backbone using ROMP. Electrochemical and photophysical studies show well-matched frontier molecular orbital energy levels between the donor and acceptor units, strong absorption profiles in the visible spectrum, and good spectral overlap for potential use in OPVs. Furthermore the molecular weight of the polymeric materials has little effect on the electrochemical and photophysical properties of the attached semiconducting moieties. Additionally, Stern-Volmer quenching studies suggest promising charge and/or energy transfer characteristics in solution. With all of these promising results, these materials seem

promising for incorporation into donor-acceptor coil-type block copolymers for potential use as OPV active layer materials.

Chapter 3: Synthesis and Characterization of Donor-Acceptor Block Copolymers Containing Oligothiophene and Perylene Diimide Semiconducting Pendant Groups

INTRODUCTION

Block copolymers (BCPs) containing pendant donor and acceptor moieties are well suited for organic photovoltaic (OPV) applications due to their inherent nanoscale self-assembly behavior. However, few traditional coil-coil BCP systems with donor and acceptor functionalities have been reported. The use of pendant donor and acceptor molecules on an amorphous backbone leads to polymers that bear resemblance to classical coil-coil BCPs. The self-assembly behavior of these copolymers is well-understood as a compromise between the immiscibility of the blocks and the entropic penalty associated with chain stretching.[61–63] The resultant morphology in these BCPs can be tuned by varying the overall molecular weight and the volume fraction of the individual blocks, and accessible continuous morphologies include cylindrical, lamellar, or gyroidal phases. Additionally, methods for preparing macroscopically aligned domains that are perpendicular to the electrodes are well established for BCPs without electronic functionality.[71,74]

The organization and alignment of nanoscale domains are crucial aspects for emerging technologies such as nanomembranes, lithography, microelectronics, or OPVs. Numerous strategies have been devised to generate periodic nanoscale patterns, including using various etching processes or removable templates. BCP self-assembly offers a promising route towards controlled microdomains, with the size and structure of the resultant morphologies dictated by molecular weight and volume fraction, respectively.[208,209] However, while self-assembly behavior in classical block copolymers is well understood, most applications require precise control over the orientation of the

microdomains. Though the differing interactions of each individual block with the air- and surface- interfaces usually favor parallel alignment, vertical alignment is often desirable. Vertical alignment can be achieved by several different methods, and the use of electric fields, magnetic fields, mechanical shear forces, temperature gradients, patterned substrates, or controlled solvent vapor annealing have shown promise in controlling the spatial orientation of the microdomains.[71,73,208,210–213]

In 2013, Thelakkat and coworkers reported one of the first successful attempts at vertical alignment of a coil-coil amphiphilic semiconducting block copolymer in thin film.[208] In this study, the researchers designed a diblock copolymer composed of a pendant group triphenyldiamine (poly(*N*,*N'*-bis(4-methoxyphenyl)- *N*-phenyl-*N'*-4-triazolylphenyl-(1,1'-biphenyl)-4,4'-diamine (PDMTPD)) hole-conducting block and a hydrophilic poly(styrene sulfonate) block (PEt_3NH^+SS) utilizing a combination of RAFT polymerization and copper-catalyzed azide-alkyne cycloaddition (CuAAC) chemistry (see **Figure 3.1A**). By varying the weight ratio of the hole conductor block from 52 wt% to 79 wt%, and treating the thin films with saturated dimethylformamide (DMF) vapor to solvent anneal, a lamellar morphology was achieved for the PDMTPD-*b*-PEt_3NH^+SS copolymer with the lowest PDMTPD content. Increasing the semiconductor content altered the structure toward cylindrical microdomains that were oriented perpendicular to the substrate, as determined by atomic force microscopy (AFM) and grazing incidence small-angle X-ray scattering (GISAXS) measurements. This study represents the first example of controlled vertical alignment of a semiconductor-containing block copolymer. While the described block copolymer isn't an organic donor-acceptor block copolymer, the authors mention that the hydrophilic poly(styrene sulfonate) block could allow for the incorporation of semiconducting inorganic materials such as TiO_2, which could serve as the acceptor component in a hybrid organic-inorganic donor-acceptor system.

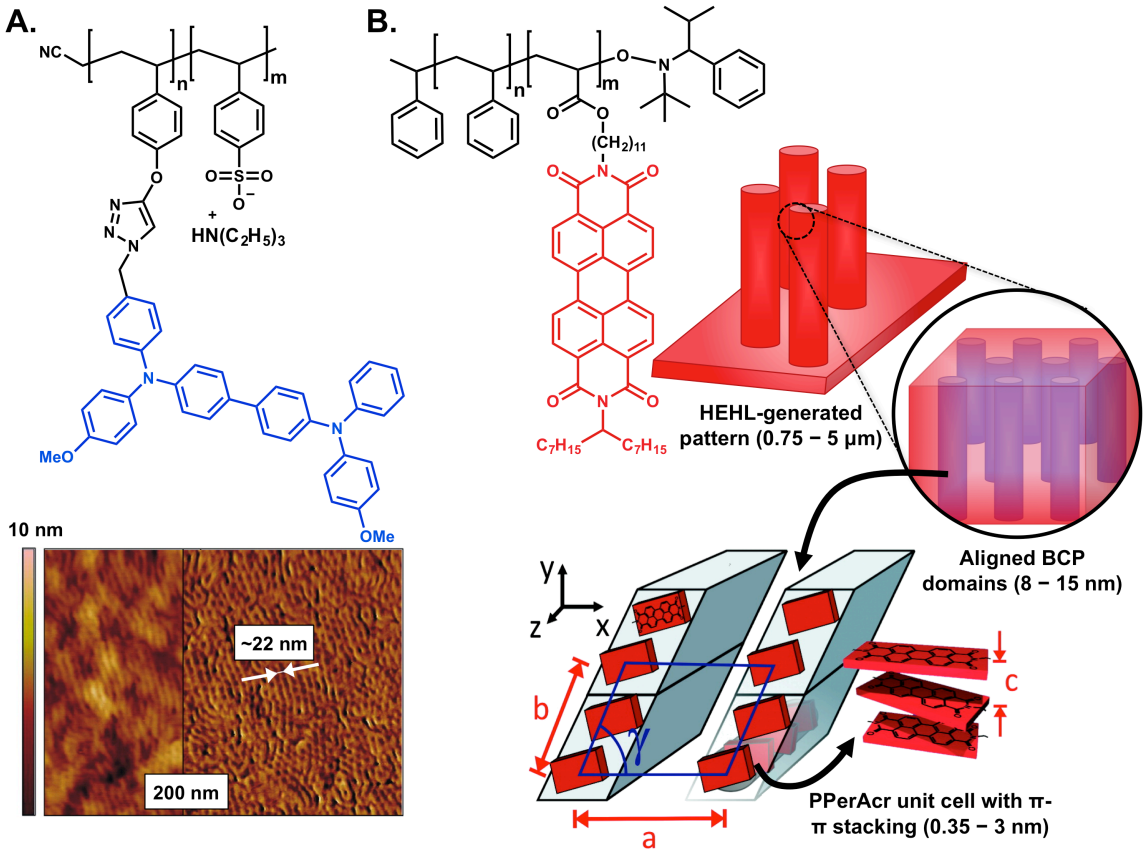

Figure 3.1. (A) Structure of PDMTPD-*b*-PEt$_3$NH$^+$SS[208] and AFM height (left) and phase (right) images of solvent annealed thin film with 52 wt% of the hole-conducting block PDMTPD. AFM images reprinted with permission from ref [208]; (B) Structure of PS-*b*-PPerAcr[214] and schematic of the HEHL-generated structural hierarchy consisting of micrometer-sized columns composed of an aligned cylindrical morphology with molecular order created by the crystalline stacking of the PBI moieties. HEHL schematic adapted from ref [214].

In the same year, Steiner, Thelakkat, and coworkers reported another study, this time looking at vertical alignment of a diblock copolymer containing a poly(perylene diimide acrylate) (PPerAcr) electron-conducting block and a poly(styrene) (PS) block using a patterning method known as hierarchical electohydrodynamic lithography (HEHL) (see **Figure 3.1B**).[214] To carry out HEHL alignment, thin films of the BCP were

confined by assembling a capacitor consisting of a BCP-film covered electrode opposed by a second electrode, with an air gap between the film and the upper electrode. This assembly was then heated above the glass transition temperature (T_g) of the BCP to thermally anneal or, alternatively, solvent vapor annealed in chloroform ($CHCl_3$). Subsequently, a voltage was applied between the two electrodes. The HEHL alignment protocol resulted in a hierarchical structure with three distinct length scales: (1) micrometer-sized polymer pillars containing (2) a 10 nm cylindrical BCP microphase morphology aligned perpendicular to the substrate surface with (3) 0.35–3.0 nm crystalline PDI π-π stacked structures on the molecular length scale. The crystalline order of the PDI moieties improved conductivity across the BCP film by 2 orders of magnitude compared to the as-cast film, and by an order of magnitude compared to a film annealed in the absence of any electric field. Again, while this study doesn't represent the alignment of a donor-acceptor block copolymer film, it is highly promising and could be potentially extended to BCPs with two functional blocks.

The ultimate goal of the research effort involving the synthesis of donor-acceptor block copolymers and the control of their self-assembly behavior is the creation of a fully functional device. While research in this area has been ongoing for over a decade, the realization of a BCP-based OPV device with ordered and vertically aligned domains remains an outstanding challenge.[4,28,30,161,170,171,214] With this in mind, donor-acceptor block copolymers containing oligothiophene donor and perylene diimide (PDI) acceptor pendant groups attached to a flexible norbornene-backbone were synthesized and characterized (**Figure 3.2**).

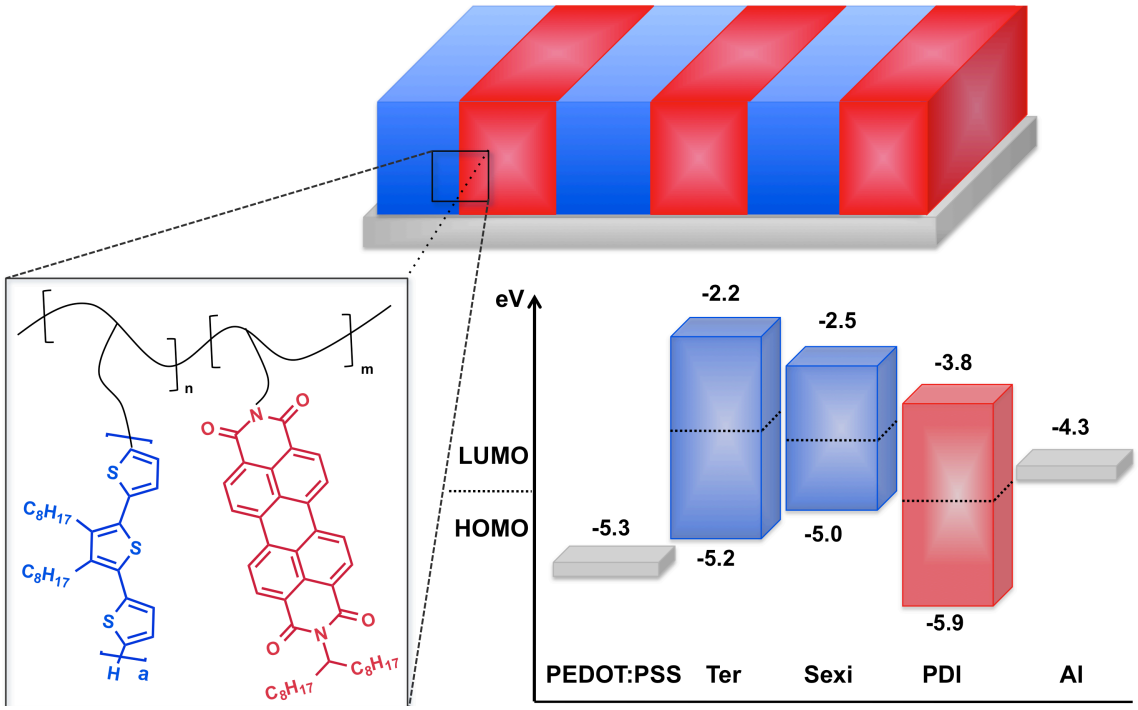

Figure 3.2. Schematic representation of desired perpendicularly-oriented active layer morphology for donor-acceptor BCPs consisting of a poly(norbornene) backbone with pendant terthiophene (Ter, a = 1) or sexithiophene (Sexi, a = 2) donor (represented in blue) and PDI acceptor (represent in red) semiconductors. The calculated HOMO and LUMO levels (eV) for the donor and acceptor homopolymers are also shown. For all block copolymers discussed *vide infra*, n = m.

Electrochemical studies were used to determine the frontier molecular orbital energy levels of the donor and acceptor moieties in the block copolymers. Photophysical studies of the donor-acceptor copolymers with varying block lengths were used to characterize charge/energy transfer in solution, demonstrating the effects of the donor-acceptor interface distance on intrachain charge transfer. Calculations using the Weller equation and the Förster equation indicate favorable charge and energy transfer processes between the donor and acceptor segments. Continuous wave electron paramagnetic resonance (cw-EPR) spectroscopy under ambient light was used to study the formation of

charge transfer states in the block copolymer materials. The cw-EPR spectroscopy demonstrates the formation of persistent, distinguishable radical cations and radical anions that are stabilized across the donor and acceptor domains, respectively. Finally, small-angle X-ray scattering (SAXS) measurements were used to investigate bulk self-assembly behavior in the semiconducting block copolymers, demonstrating the formation of ordered morphology in bulk samples and suggesting the ability to make self-assembled nanostructures from the described donor-acceptor BCPs.

EXPERIMENTAL

Instrumentation

Nuclear magnetic resonance (NMR) spectroscopy was run on a Varian DirectDrive 400 MHz or 500 MHz spectrometer at ambient temperature and the spectra were referenced internally to the residual solvent peaks. All chemical shifts are reported in ppm and coupling constants are given in Hertz (Hz). Absorption spectra were obtained on a Varian Cary 6000i UV-Vis-NIR spectrophotometer in Starna quartz fluorimeter cells with a 1.0 cm path length. Mass spectroscopy was performed with a Micromass Autospec Ultima HRMS (for CI^+) or an Agilent 6530 Q-TOF system (for ESI^+). Elemental analysis was performed by QTI, Whitehouse, NJ (www.qtionline.com). Gel permeation chromatography (GPC) was performed on an Agilent 1100 Series Instrument with Viscoteck Triple Array Detector 302 Series in THF. Thermal gravimetric analysis (TGA) was performed on TA Instruments TGA Q50 under inert N_2 atmosphere with 3.5 °C/min ramp to 500 °C and then 8.0 °C/min ramp to 800 °C. Differential scanning calorimetry (DSC) was performed on a Mettler Toledo DSC-1 instrument model. All DSC samples ranged from 5-8 mg and followed the same run procedure with a N_2 flow rate of 50 mL/min: (1) Isothermal at 30 °C for 2 min; (2) Heating from 30 °C to 100 °C at 10

°C/min to remove water and any residual solvent; (3) Isothermal at 100 °C for 2 min; (4) Cooling from 100 °C to 30 °C at 10 °C/min; (5) Isothermal at 30 °C for 2 min; (6) Heating from 30 °C to 280 °C at 10 °C/min; (7) Isothermal at 280 °C for 2 min; (8) Cooling from 280 °C to 30 °C at 10 °C/min. Fluorimetry experiments were carried out on a Photon Technology International QuantaMaster 4 spectrophotometer equipped with a 6-inch diameter K Sphere-B integrating sphere and using PTI software. All solution measurements were recorded in Starna quartz fluorimeter cells with a path length of 1.0 cm in dicholoromethane (DCM), unless otherwise noted. EPR experiments were recorded on a Bruker EMX-Plus X-band spectrometer at 293 K with 2 mW microwave power and 0.5-1 G modulation amplitude. Simulated spectra were obtained using SimFonia software. Small-angle X-ray scattering (SAXS) analysis was performed using Cu Kα radiation (λ = 1.5418 Å) from a Molecular Metrology instrument equipped with a high brilliance rotating copper anode source and a two-dimensional 120 mm gas-filled multiwire detector. Vertical focus was attained with a single-crystal Ge mirror, and horizontal focus and wavelength selection were acquired with an asymmetrically cut Si(111) monochromator. The beam center was calibrated using the primary reflection peak of silver behenate set at 1.076 nm^{-1}. The SAXS holder-to-holder distance (between the front and back chambers) was 624 nm. Prior to SAXS analysis, samples were annealed at 280 °C under vacuum for 15 hours, unless otherwise noted.

Electrochemistry

Electrochemical experiments were carried out in a dry box under a N_2 atmosphere using a GPES system from Eco. Chemie B. V. All the electrochemical experiments were performed using a three-electrode cell with a $Ag/AgNO_3$ reference electrode (silver wire in a 0.01 M silver nitrate solution with 0.1 M $[(n\text{-}Bu)_4N]^+[PF_6]^-$ ($TBAPF_6$) in acetonitrile),

a 1.6 mm Pt button working electrode, and a Pt wire coil counter electrode. All measured potentials were referenced to the ferrocene/ferrocenium redox couple (Fc/Fc^+) as determined by the average $E_{1/2}$ value obtained before and after the experiment. The supporting electrolyte used was 0.1 M tetrabutylammonium hexafluorophosphate ($TBAPF_6$) that was purified by three successive recrystallizations from hot ethanol and dried for three days at 100-150 °C under high vacuum. All measurements were carried out in DCM with scan rate of 100 mVs^{-1}. The HOMO and LUMO energy levels were found from the onset of oxidation and reduction using the **Equations 2.1**, **2.2** (see **Chapter 2**).

Synthesis

Polymerizations of Donor-Acceptor Copolymers [P3.1 – P3.4]

All polymerizations were carried out in small glass vials with Teflon-lined lids in a glovebox under N_2 atmosphere in dry DCM using Grubbs' 2nd Generation (G2) catalyst. All donor-acceptor BCPs contain equimolar ratios of donor (the norbornene polymer with either Ter or Sexi pendant groups) and acceptor (the norbornene polymer with PDI pendant groups). Donor-acceptor BCPs were synthesized starting with the donor block and monitoring by TLC until complete consumption of the donor monomer (Ter **2.13** or Sexi **2.21**). Then, the PDI monomer (**2.28**) was added to the stirring polymerization solution. Upon complete consumption of the PDI monomer, as determined by TLC, the copolymers were removed from the glovebox and terminated with excess ethyl vinyl ether (~2-3 mL). Random copolymers (RCP) were synthesized for comparison by adding both monomers at the same time and polymerizing with G2 until complete consumption of the monomeric materials, as determined by TLC. The reaction solutions were concentrated *in vacuo* and all polymers were purified *via* precipitation into MeOH (3x)

from either small amounts of DCM (~2 mL) or DCM:hexanes (1:1 v/v, ~2 mL). The amount of G2 used was determined by the desired molecular weight of the resultant copolymers using **Equation 2.3**. Polymers were characterized by ^{1}H NMR ($CDCl_3$), GPC (THF), DSC, and TGA. Polydispersity (*Đ*) was determined using GPC. ^{1}H NMR indicates inclusion of both monomers into the RCPs and BCPs in close to the theoretical 1:1 molar ratio of the donor and acceptor pendant groups.

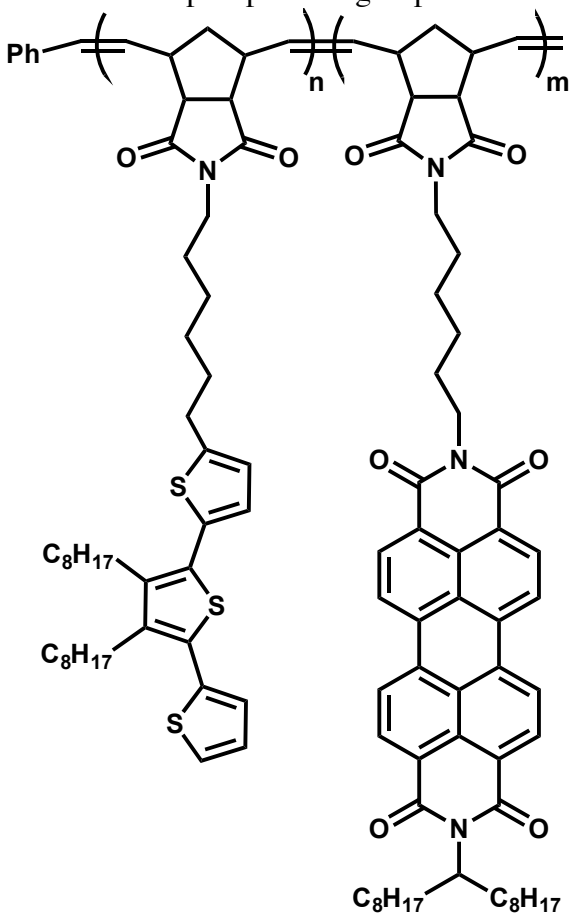

Poly(2-(6-(3',4'-dioctyl-[2,2':5',2''-terthiophen]-5-yl)hexyl)isoindoline-1,3-dione)-*block*-poly(2-(6-(1,3-dioxo-1,3,3a,4,7,7a-hexahydro-2*H*-4,7-methanoisoindol-2-yl)hexyl)-9-(heptadecan-9-yl)anthra[2,1,9-*def*:6,5,10-*d'e'f'*]diisoquinoline-1,3,8,10(2*H*,9*H*)-tetraone) (Ter-*b*-PDI) [P3.1]: ^{1}H NMR (representative block

copolymer, 400 MHz, $CDCl_3$) all signals broad singlets, δ: 8.50-7.60 (8H), 7.26 (1H), 7.09 (1H), 7.02 (1H), 7.00 (1H), 6.66 (1H), 5.78-5.58 (4H), 5.08 (1H), 4.01 (2H), 3.47 (4H), 3.35-2.82 (8H), 2.75 (2H), 2.64 (2H), 2.20 (2H), 1.93 (3H), 1.80-1.50 (9H), 1.37-1.25 (58H), 0.86-0.83 (12H).

Poly(2-(6-(3',4'-dioctyl-[2,2':5',2''-terthiophen]-5-yl)hexyl)isoindoline-1,3-dione)-*random*-poly(2-(6-(1,3-dioxo-1,3,3a,4,7,7a-hexahydro-2*H*-4,7-methanoisoindol-2-yl)hexyl)-9-(heptadecan-9-yl)anthra[2,1,9-*def*:6,5,10-*d'e'f'*]diisoquinoline-1,3,8,10(2*H*,9*H*)-tetraone) (Ter-*r*-PDI) [P3.2]: ^{1}H NMR (400 MHz, $CDCl_3$) all signals broad singlets, δ: 8.50-7.60 (8H), 7.23 (1H), 7.00 (2H), 6.80 (1H), 6.63 (1H), 5.80-5.50 (4H), 5.10 (1H), 4.05 (2H), 3.47 (4H), 3.19 (6H), 2.92 (2H), 2.73 (2H), 2.57 (2H), 2.21 (2H), 1.92 (4H), 1.71-1.23 (66H), 0.82 (12H).

Table 3.1. Molecular weight characterization of Ter-PDI copolymers.

Polymer	*[M]/[I]*[a]	N_n[b]	M_n(GPC)[b] (kg/mol)	M_n (theoretical)[c] (kg/mol)	$Đ$[b]
P3.1a	75	150	206.9	119.2	1.43
P3.1b	42	84	181.4	66.9	1.02
P3.1c	14	28	133.0	21.0	1.06
P3.2	150	150	261.6	119.2	1.09

[a]*[M]/[I]* indicates the initial molar ratio of **2.13** (*[M]*) to G2 catalyst (*[I]*). Assuming complete conversion, $[M]/[I] = N_n$ (per block); [b]N_n describes the overall degree of polymerization; [c]Determined from GPC in THF, calibrated with polystyrene standards; [d]Theoretical number-average molecular weight calculated using $M_n = N_{n,\ Ter}\ (MW_{Ter}) + N_{n,\ Sexi}\ (MW_{PDI})$ for BCPs, assuming 100% conversion and living polymerization conditions. For RCP, $M_n = N_n(MW_{Ter} + MW_{PDI})/2$; MW_{Ter} = 713.18 g/mol and MW_{PDI} = 874.14 g/mol.

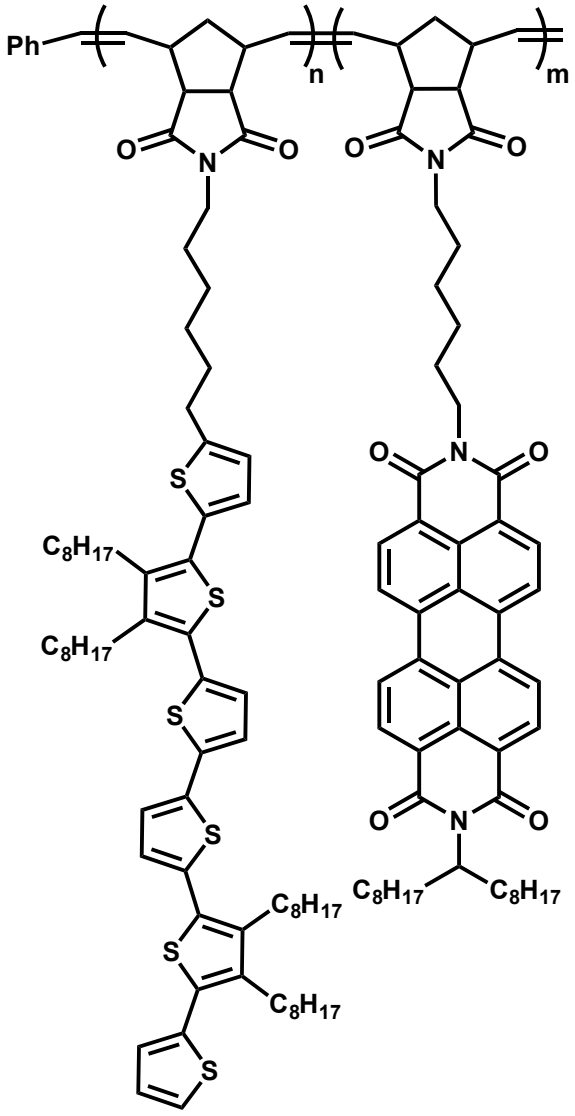

Poly(2-(6-(3',3'''',4',4''''-tetraoctyl-[2,2':5',2'':5'',2''':5''',2'''':5'''',2''''':5''''',2'''''-sexithiophen]-5-yl)hexyl)-3a,4,7,7a-tetrahydro-1*H*-4,7-methanoisoindole-1,3(2*H*)-dione)-*block*-poly(2-(6-(1,3-dioxo-1,3,3a,4,7,7a-hexahydro-2*H*-4,7-methanoisoindol-2-yl)hexyl)-9-(heptadecan-9-yl)anthra[2,1,9-*def*:6,5,10-*d'e'f'*]diisoquinoline-1,3,8,10(2*H*,9*H*)-tetraone) (Sexi-*b*-PDI) [P3.3]: ^{1}H NMR (representative block copolymer, 400 MHz, $CDCl_3$) all signals broad singlets, δ: 8.45-7.50 (8H), 7.28 (1H),

7.15-6.92 (6H), 6.85 (1H), 6.65 (1H), 5.85-5.50 (4H), 5.10 (1H), 4.00 (2H), 3.65-2.80 (12H), 2.78-2.60 (8H), 2.20 (2H), 1.95 (3H), 1.80-1.20 (93H), 0.84 (18H).

Poly(2-(6-(3',3'''',4',4''''-tetraoctyl-[2,2':5',2'':5'',2''':5''',2'''':5'''',2''''':5''''',2'''''-sexithiophen]-5-yl)hexyl)-3a,4,7,7a-tetrahydro-1*H*-4,7-methanoisoindole-1,3(2*H*)-dione)-*random*-poly(2-(6-(1,3-dioxo-1,3,3a,4,7,7a-hexahydro-2*H*-4,7-methanoisoindol-2-yl)hexyl)-9-(heptadecan-9-yl)anthra[2,1,9-*def*:6,5,10-*d'e'f'*]diisoquinoline-1,3,8,10(2*H*,9*H*)-tetraone) (Sexi-*r*-PDI) [P3.4]: ^{1}H NMR (400 MHz, CD_2Cl_2) all signals broad singlets, δ: 8.50-7.50 (8H), 7.35 (1H), 7.10-6.80 (7H), 6.70 (1H), 5.80-5.50 (4H), 5.10 (1H), 4.00 (2H), 3.45 (4H), 3.30-2.85 (8H), 2.80-2.50 (8H), 2.20 (2H), 1.95 (3H), 1.80-1.20 (93H), 0.85 (18H).

Table 3.2. Molecular weight characterization of Sexi-PDI copolymers.

Polymer	*[M]/[I]*[a]	N_n[b]	M_n(GPC)[b] (kg/mol)	M_n (theoretical)[c] (kg/mol)	$Đ$[b]
P3.3a	75	150	162.2	154.7	1.11
P3.3b	50	100	274.6	103.2	1.02
P3.3c	25	50	211.3	51.6	1.01
P3.3d	15	30	179.6	30.9	1.80
P3.4	150	150	263.8	154.7	1.16

[a]*[M]/[I]* indicates the initial molar ratio of **2.13** (*[M]*) to G2 catalyst (*[I]*). Assuming complete conversion, $[M]/[I] = N_n$ (per block); [b]N_n describes the overall degree of polymerization; [c]Determined from GPC in THF, calibrated with polystyrene standards; [d]Theoretical number-average molecular weight calculated using $M_n = N_{n,\ Sexi}\ (MW_{Sexi}) + N_{n,\ PDI}\ (MW_{PDI})$ for BCPs, assuming 100% conversion and living polymerization conditions. For RCP, $M_n = N_n(MW_{Sexi} + MW_{PDI})/2$; MW_{Sexi} = 1188.92 g/mol and MW_{PDI} = 874.14 g/mol.

RESULTS AND DISCUSSION

Copolymerizations were carried out using ROMP with G2 in DCM under inert atmosphere to synthesize BCPs comprised of either a Ter or Sexi donor block with a PDI

acceptor block. RCPs were synthesized for comparison. **Table 3.1** and **Table 3.2** summarize the molecular weight characterization of the Ter-PDI and Sexi-PDI copolymer series, respectively. All copolymer materials contain the donor and acceptor blocks in an equimolar ratio, as verified by ^{1}H NMR, but have different block lengths as a consequence of the *[M]/[I]* ratio used, and thus different overall molecular weights. For several BCPs, the calculated theoretical molecular weight is lower than that determined by GPC using polystyrene standards. This is likely due, in part, to aggregation of the PDI segment of the block copolymers, which may result in a larger hydrodynamic radius and an artificially high molecular weight.[167] TGA of representative samples of the donor-acceptor Ter-PDI and Sexi-PDI random and block copolymers shows high thermal stability > 375 °C for all materials (see **Figure 3.2** and **Figure 3.3**).

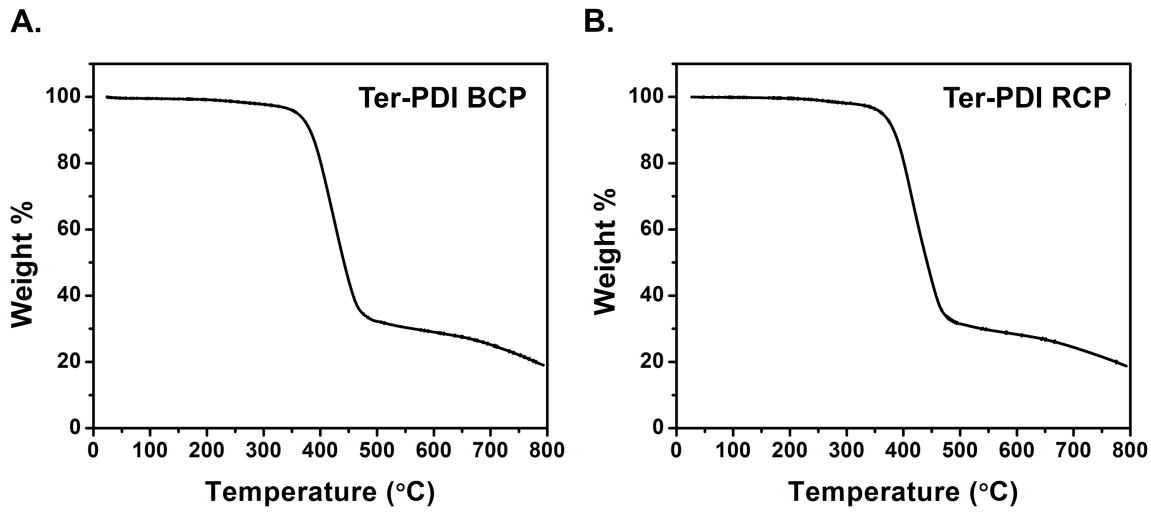

Figure 3.2. TGA plots showing thermal degradation profiles of (A) Ter-PDI BCP **P3.1a (75)**, T_{onset} = 388 °C; (B) Ter-PDI RCP **P3.2**, T_{onset} = 390 °C. The number in parentheses indicates the number of repeat units per block in the BCP.

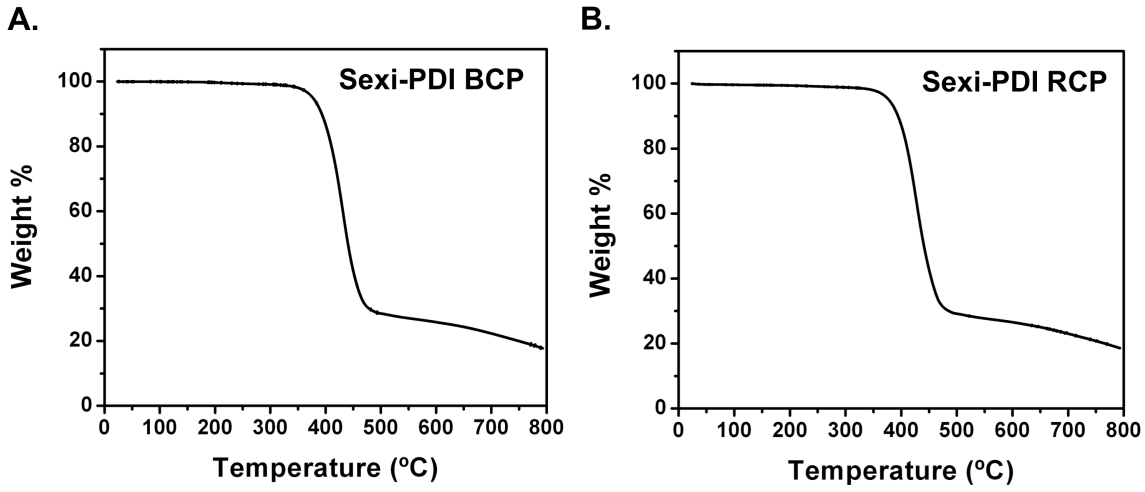

Figure 3.3. TGA plots showing thermal degradation profiles of (A) Sexi-PDI BCP **P3.3a (75)**, T_{onset} = 400 °C; (B) Sexi-PDI RCP **P3.4**, T_{onset} = 398 °C. The number in parentheses indicates the number of repeat units per block in the BCP.

DSC analysis of the Ter-PDI RCP (**P3.2**) shows a T_g = 119 °C. For the Ter-PDI BCPs, the DSC trace of **P3.1a (75)** shows a T_g = 97 °C. The smaller BCP, **P3.1b** (42 repeat units/block), shows two T_g's with onsets at 101 °C and 220 °C (see **Figure 3.4**). Similarly, the Sexi-PDI RCP (**P3.4**) shows a T_g with onset of 110 °C (see **Figure 3.5**). For the Sexi-PDI BCPs, the DSC trace of **P3.3a (75)** doesn't show a clear T_g, but there is an apparent melting transition at T_m = 276 °C. It is unclear if this melting transition corresponds to the Sexi or PDI semiconducting moieties, as both are crystalline materials. The transition itself resembles that observed for the Sexi homopolymer (**P2.2**), but the temperature of the transition is more closely related to the T_m observed for the PDI homopolymer (**P2.3**). For the smaller Sexi-PDI BCP, **P3.3b (50)**, there are two distinct T_g's around 105 °C and 240 °C. The presence of two distinct T_g's for the smaller donor-acceptor block copolymers suggests the presence of two distinct domains. This is promising, as it suggests that the Flory-Huggins parameter is high enough to induce self-

segregation in the block copolymer materials, suggesting potential for self-assembly upon annealing.

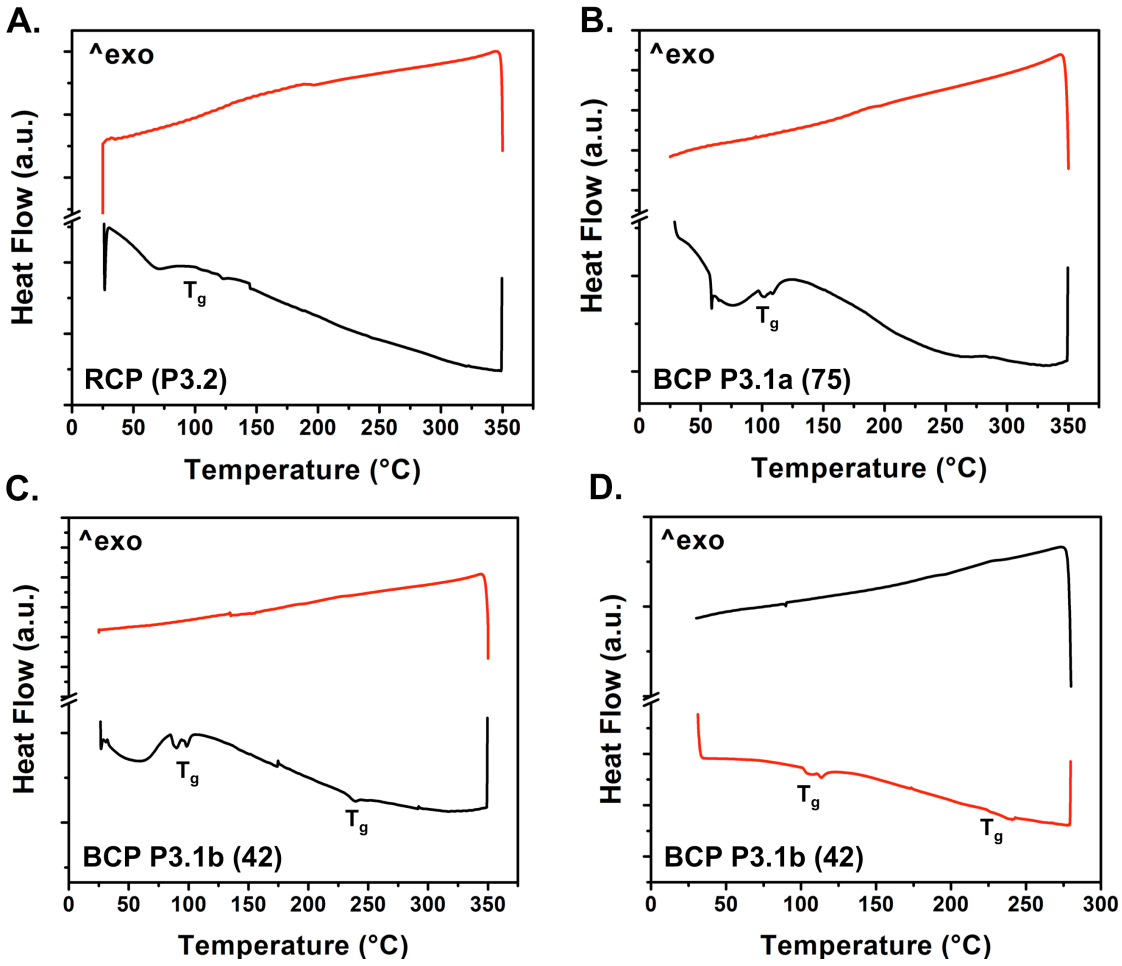

Figure 3.4. DSC traces for Ter-PDI copolymer materials (black line shows heating cycle, red line shows cooling cycle): (A) RCP **P3.2**; (B) BCP **P3.1a (75)**; (C,D) **P3.1b (42)**, (C) shows the initial DSC run and (D) shows a second DSC run to lower temperatures using a new sample of the copolymer material.

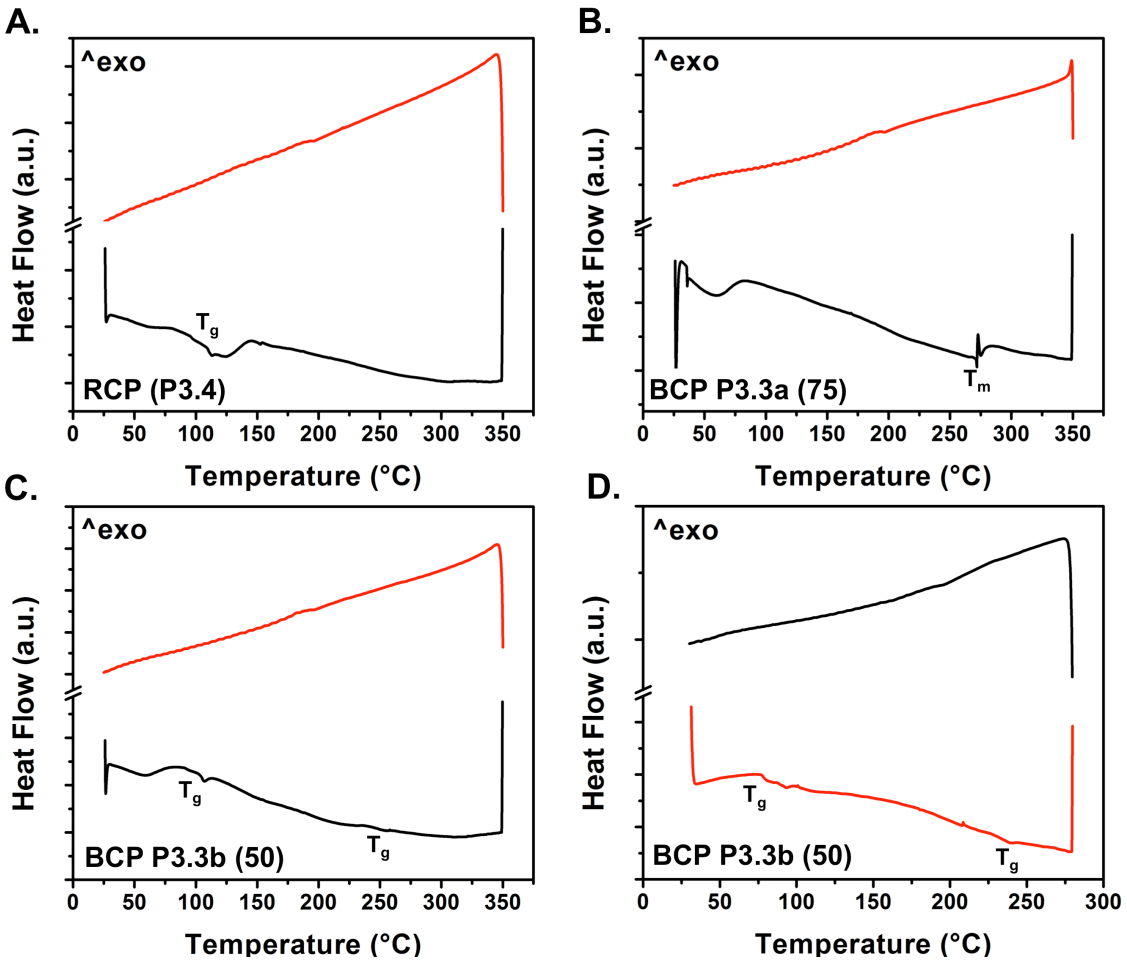

Figure 3.5. DSC traces for Sexi-PDI copolymer materials (black line shows heating cycle, red line shows cooling cycle): (A) RCP **P3.4**; (B) BCP **P3.3a (75)**; (C,D) BCP **P3.3b (50)**, (C) shows the initial DSC run and (D) shows a second DSC run to lower temperatures using a new sample of the copolymer material.

Photophysical and Electrochemical Characterization

The UV-Vis absorption spectra of the Ter-PDI RCP and BCP materials are shown in **Figure 3.6A**. The UV-Vis absorption spectra of the Sexi-PDI RCP and BCP materials are shown in **Figure 3.6B**.

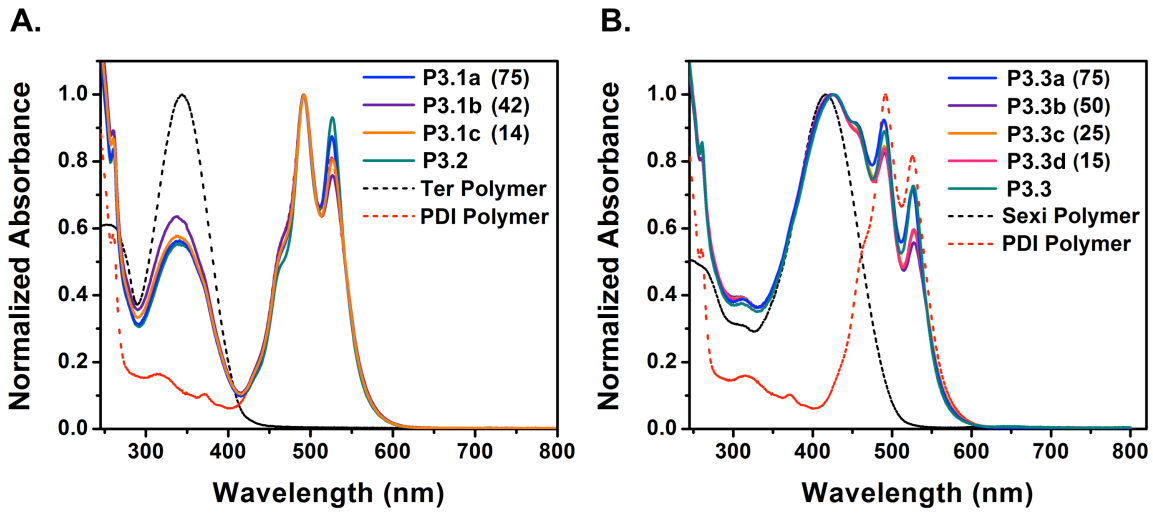

Figure 3.6. Normalized UV-Vis spectra of (A) Ter-PDI BCPs and RCP. Ter polymer (**P2.1**, black dotted line) and PDI polymer (**P2.3**, red dotted line) are shown for comparison; (B) Sexi-PDI BCPs and RCP. Sexi polymer (**P2.2**, black dotted line) and PDI polymer (**P2.3**, black dotted line) are shown for comparison. The numbers in parentheses indicate the number of repeat units per block in the BCP materials.

For all of the Ter-PDI copolymers, the UV-Vis absorption spectrum consists of an approximate superposition of the UV-Vis absorption of the two individual chromophores, with λ_{abs} = 340 nm, corresponding to the Ter chromophore absorption, and λ_{abs} = 490 nm and 525 nm, corresponding to the PDI chromophore absorption. Interestingly, the BCP series show an increase in the ratio of the (0,1) to (0,0) vibronic transition bands for the PDI chromophore absorption compared to the RCP. This suggests that more H-aggregation occurs in the PDI segemtn of the BCP. This is not surprising given the increased number of PDI units in close proximity in the BCP compared to the RCP, where the PDI chromophores are presumably more intermixed with the Ter chromophores. This is supported by the fact that the (0,0) vibronic band intensity decreases with increasing block length in the BCP series, suggesting that aggregation of the PDI chromophores is enhanced as the number of repeating PDI units increases. In

both the RCP and BCP systems, the distinct absorptions corresponding to each of the chromophores suggest that there is minimal interaction between the PDI and Ter units in the ground state.

The absorption spectra of the Sexi-PDI BCP series can also be approximated as a linear combination of the homopolymer spectra, with λ_{abs} = 425 nm, corresponding to the Sexi chromophore absorption, and λ_{abs} = 490 nm and 525 nm, corresponding to the PDI chromophore absorption. These peaks indicate inclusion of both monomers into the copolymer materials. For the Sexi-PDI copolymers, there is a large area of overlap in the absorption spectra of the Sexi and PDI chromophores. There is also not a clear trend in the aggregation behavior of the PDI units in these copolymer materials. It is interesting to note that the Sexi absorption shows a slight bathochromic shift in the copolymer series compared to the Sexi homopolymer. The reason for this is not clearly understood. If this phenomenon were solely related to aggregation between neighboring Sexi moieties along the polymer backbone, it would also be present in the homopolymer material. Therefore, it is hypothesized that the observed bathochromic shift results from π-π interactions between the conjugated Sexi and PDI units at chain interfaces in the ground state. For OPV applications, the Ter and Sexi donor semiconductors and the PDI acceptor semiconductor have strong optical absorption in the visible region, and thus exciton photogeneration can occur in both blocks.

The electrochemical behavior of representative Ter-PDI and Sexi-PDI copolymer samples was studied using cyclic voltammetry (CV). These CV scans show distinct reduction and oxidation events corresponding to the individual donor and acceptor components, with onsets of oxidation and reduction matching well with those seen for the homopolymers (see **Figure 3.7**).

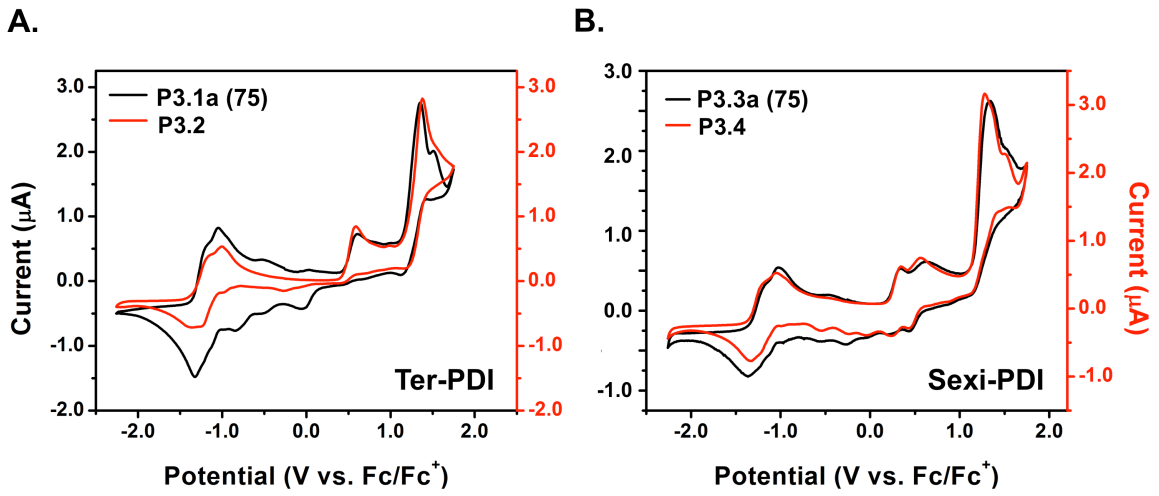

Figure 3.7. CV scans in DCM under inert atmosphere of (A) Ter-PDI BCP **P3.1a (75)** (black line) and Ter-PDI RCP **P3.2** (red line); (B) Sexi-PDI BCP **P3.3a (75)** (black line) and Sexi-PDI RCP **P3.4** (red line).

For the Ter-PDI BCP **P3.1a (75)** there are two oxidation events, with onsets at 0.41 V vs. Fc/Fc^+, corresponding to oxidation of the Ter moiety, and 1.11 V vs. Fc/Fc^+, corresponding to oxidation of the PDI (see **Figure 3.7A**). There is also a reductive event with onset at -1.03 V vs. Fc/Fc^+ that corresponds to PDI reduction. The Ter-PDI RCP **P3.2** shows a very similar electrochemical profile. From these CV onsets, the HOMO and LUMO energy levels for the BCP were calculated as -5.21 eV and -3.77 eV, respectively. These values match closely with those determined for the individual donor and acceptor homopolymers, demonstrating that copolymerization does not affect the electrochemical properties of the semiconducting units. From these values, a "realized" band gap (i.e. the $HOMO_{donor}$– $LUMO_{acceptor}$ difference) for the Ter-PDI donor-acceptor BCP can be estimated at 1.4 eV.

Similarly, for the Sexi-PDI BCP **P3.3a (75)** there are onsets of oxidation at 0.16 V vs. Fc/Fc^+, corresponding to oxidation of the Sexi moiety, and 1.12 V vs. Fc/Fc^+, corresponding to oxidation of the PDI (see **Figure 3.7B**). There is also a reductive event

with onset at -1.03 V vs. Fc/Fc^+ that corresponds to PDI reduction. Again, the Sexi-PDI RCP **P3.4** shows a very similar electrochemical profile. The HOMO and LUMO energy levels for the BCP were calculated as -4.96 eV and -3.77 eV, respectively. These values are very similar to those determined for the individual Sexi and PDI homopolymers. From these values, a "realized" band gap for the Sexi-PDI donor-acceptor BCP can be estimated at 1.2 eV.

The fluorescence spectra of the Ter-PDI copolymers are shown in **Figure 3.8** and the fluorescence spectra of the Sexi-PDI copolymer series are shown in **Figure 3.9**. Excitation of the Ter-PDI BCPs (**P3.1a – P3.1c**) at 340 nm, the maximum absorption of Ter, results in emission from both the Ter and PDI fluorophores. A similar result is observed for the Ter-PDI RCP (**P3.2**). For all of the copolymers, excitation at 525 nm results in an emission profile that mirrors the emission of the PDI homopolymer (**P2.3**), including the H-aggregation character.

It should be noted that **P3.1a (75)** (the longest chain Ter-PDI BCP) and **P3.2** (Ter-PDI RCP) were synthesized using the same batch of PDI monomer (**2.28**) that was used to polymerize the PDI homopolymer **P2.3d-2**. These copolymers have similar photophysical profiles to **P2.3d-2**—demonstrating decreased excimer emission (centered at λ = 630 nm). **P3.1b (42)** and **P3.1c (14)** were synthesized using the same batch of **2.28** used to polymerize the remaining PDI homopolymer series, **P2.3a – P2.3e**. Not surprisingly, **P3.1b (42)** and **P3.1c (14)** demonstrate increased H-aggregation behavior and excimer emission. This is also true for the Sexi-PDI copolymer series, where **P3.3a (75)** (the longest block BCP) and **P3.4** (Sexi-PDI RCP) were synthesized using the first batch of PDI monomer **2.28**. Meanwhile, **P3.3b – P3.3d** were synthesized using the second batch of **2.28** and show more aggregate-based emission, comparatively. For both the Ter-PDI and Sexi-PDI copolymer series, the shorter-block materials show increased

PDI emission compared to Ter/Sexi upon excitation at $\lambda_{max,donor}$ in the normalized spectra, with the RCPs demonstrating the most PDI character upon donor excitation. This suggests that closer interfaces between the donor and acceptor lead to increased electronic communication, resulting in more charge (and possibly energy) transfer events between the semiconductors.

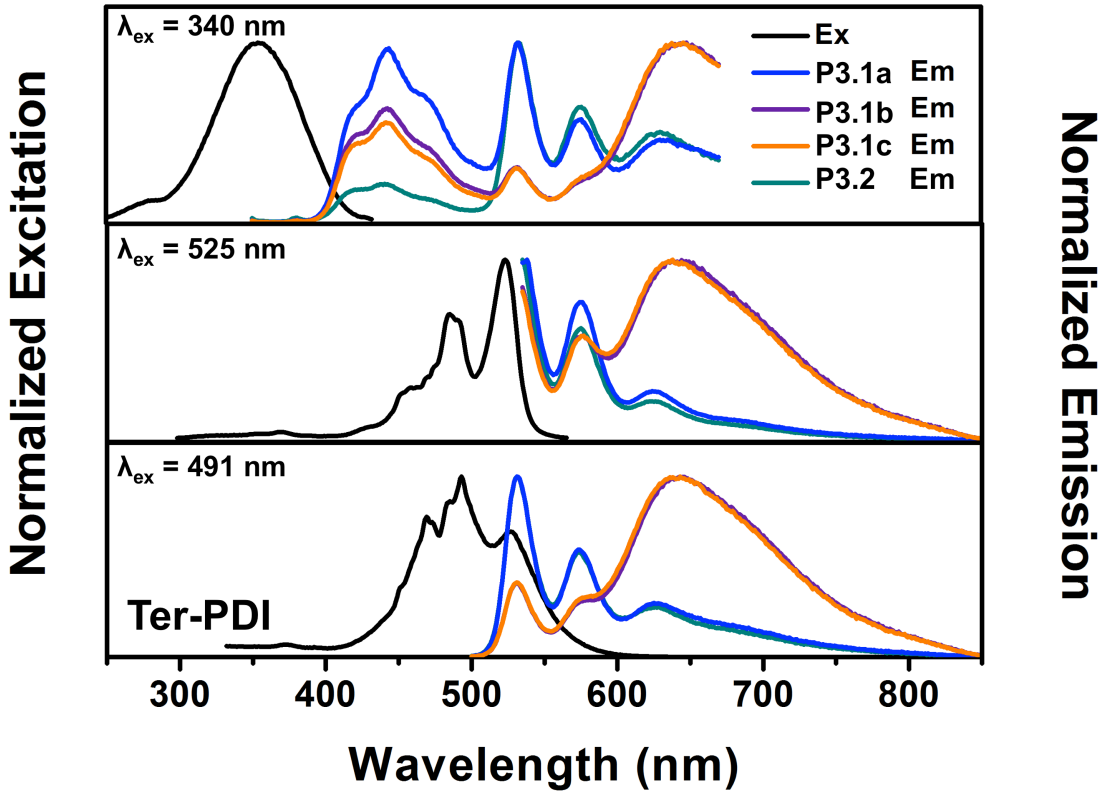

Figure 3.8. Normalized excitation and emission spectra of the Ter-PDI copolymer series: (top) Excitation at the Ter absorbance maximum (λ_{ex} = 340 nm) and resultant emission; (middle) Excitation at the non-aggregated PDI absorbance maximum (λ_{ex} = 525 nm) and resultant emission; (bottom) Excitation at the aggregated PDI absorbance maximum (λ_{ex} = 491 nm).

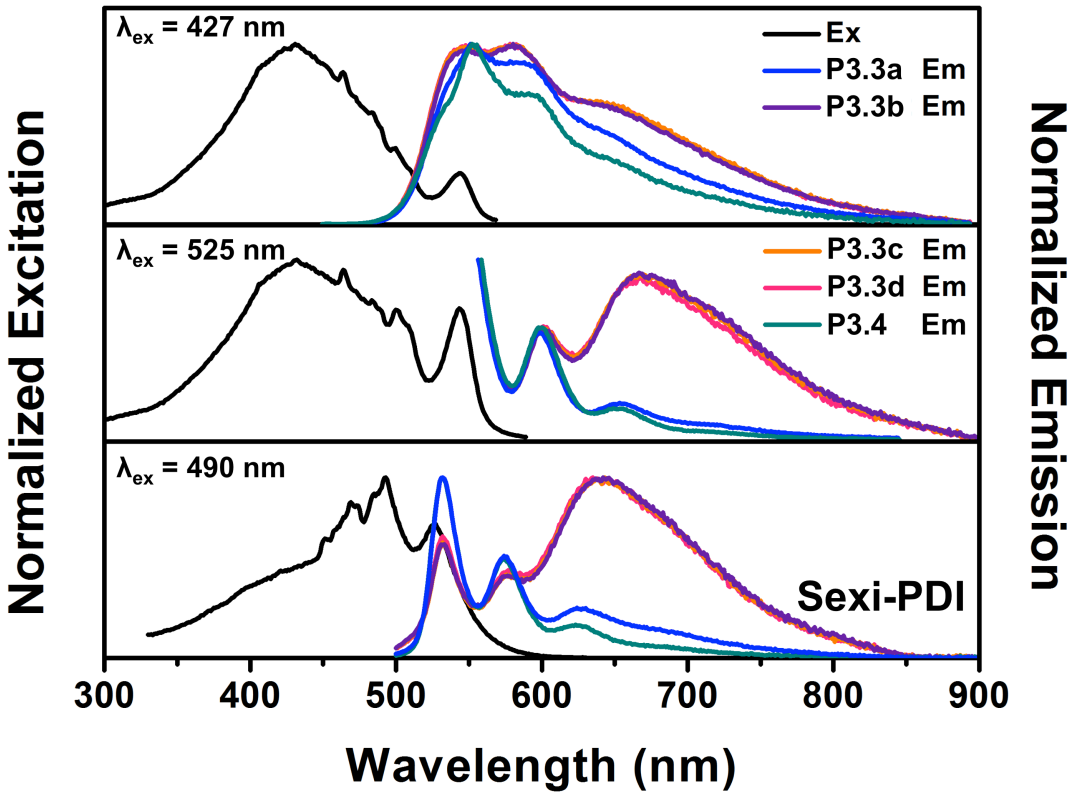

Figure 3.9. Normalized excitation and emission spectra of Sexi-PDI copolymer series: (top) Excitation at Sexi absorbance maximum (λ_{ex} = 427 nm) and resultant emission; (middle) Excitation at non-aggregated PDI absorbance maximum (λ_{ex} = 525 nm) and resultant emission; (bottom) Excitation at aggregated PDI absorbance maximum (λ_{ex} = 490 nm).

Copolymer Emission Quenching Studies

To quantify the amount of donor PL quenching in solution for the different copolymers, the optical density (OD), analogous to the absorbance, of the donor component in each BCP was adjusted to be approximately 0.1. It is important to note that the acceptor OD was not normalized. Consequently, it is difficult to make any conclusive statements about changes in the acceptor emission in relation to donor PL quenching because longer block lengths of acceptor would result in higher emission intensity due to a higher number of fluorophores. **Figure 3.10** shows the UV-Vis absorption spectra of

the Ter-PDI (**P3.1 – P3.2**) and Sexi-PDI (**P3.3 – P3.4**) copolymer series used for the PL quenching studies, demonstrating the normalized OD of the donor component.

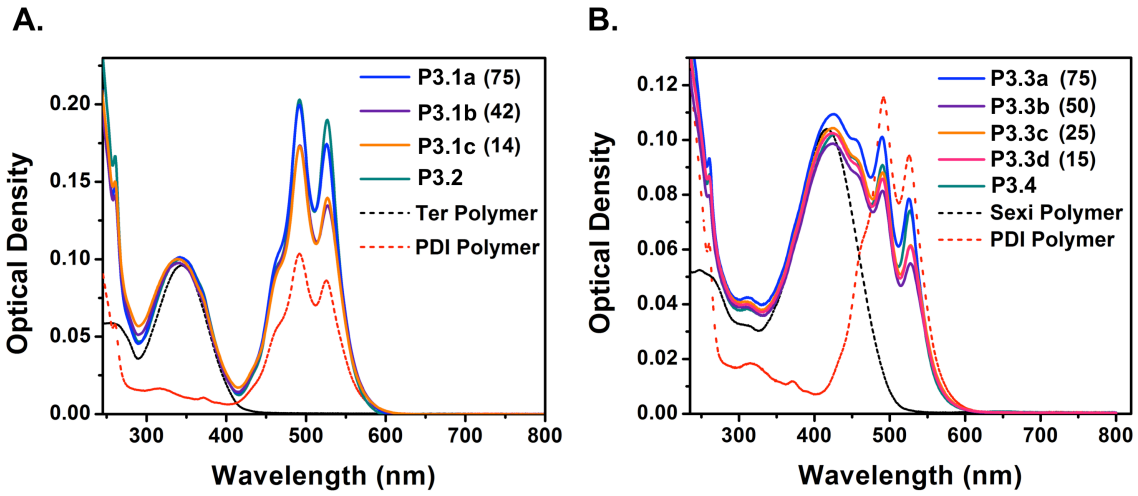

Figure 3.10. UV-Vis absorption spectra as a function of optical density (OD) of (A) the Ter-PDI BCPs (**P3.1a – P3.1c**) and RCP (**P3.2**); (B) the Sexi-PDI BCPs (**P3.3a – P3.3d**) and RCP (**P3.4**). Homopolymer spectra are shown as dotted lines. Numbers in parentheses represent the theoretical number of repeat units per block in the BCPs.

By systematically shortening the distance between the donor and acceptor blocks in the Ter-PDI BCPs (**P3.1a – P3.1c**) and Sexi-PDI BCPs (**P3.3a – P3.3d**), the effects of interfacial distance on charge (and possibly energy) transfer were explored. This systematic shortening is represented by the decrease in number of repeat units (and thus length) of the donor and acceptor blocks from 75 to 14. The donor PL quenching was monitored quantitatively by comparing the emission intensity of the copolymers to that of the donor homopolymer (see **Figure 3.11** and **Figure 3.12**).

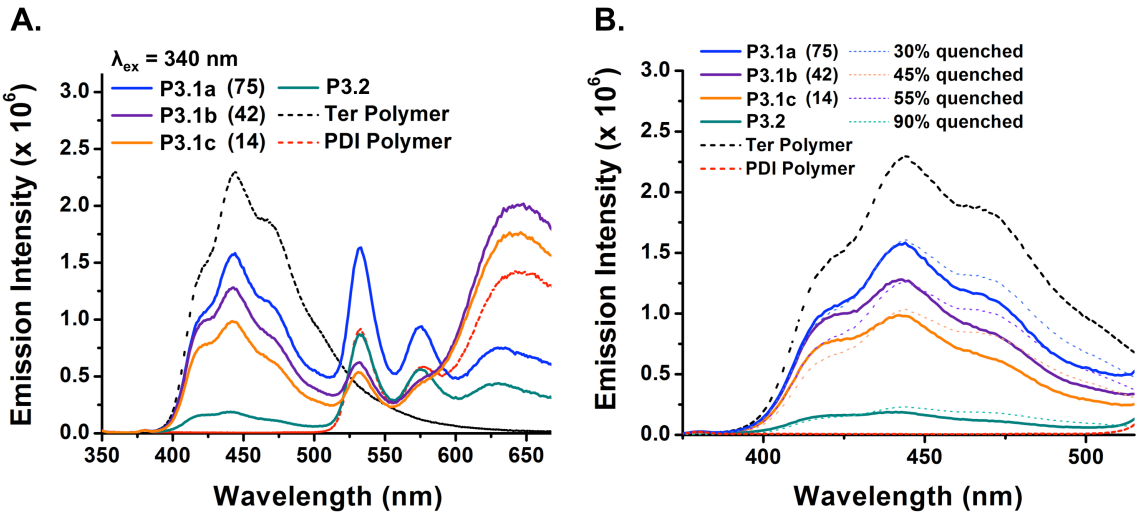

Figure 3.11. (A) PL donor quenching for Ter-PDI copolymers (λ_{ex} = 340 nm) as a function of block length. Emission of Ter polymer **P2.1** (dotted black line) and PDI polymer **P2.3** (red dotted line) shown for comparison. PDI emission is negligible at λ_{ex} = 340 nm. Numbers in parentheses represent theoretical number of repeat units per block; (B) Zoomed-in view of Ter donor emission in copolymer series (solid lines) with corresponding quenching estimates (dotted lines). Estimated donor PL quenching based on Ter homopolymer emission.

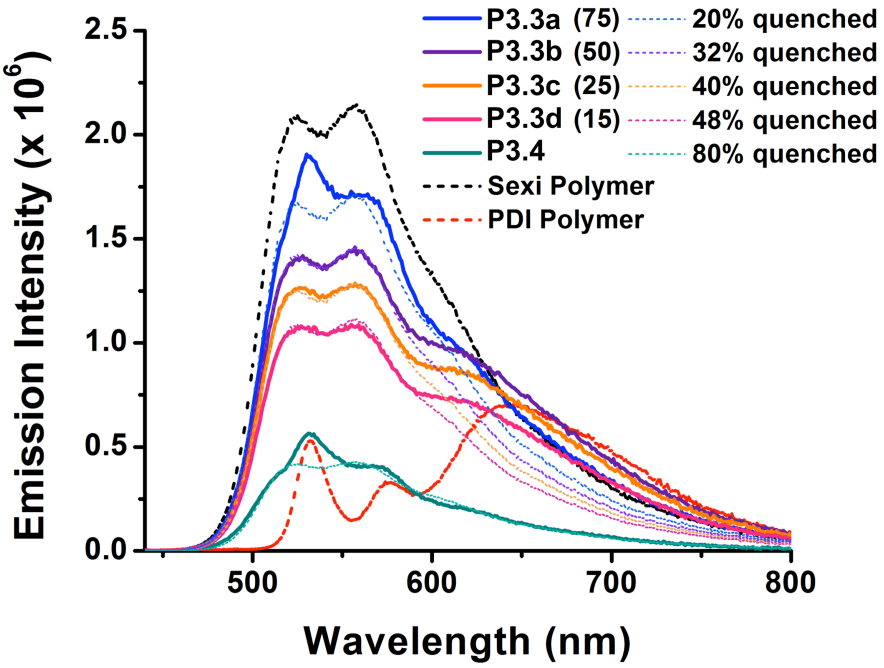

Figure 3.12. PL donor quenching for Sexi-PDI copolymers (λ_{ex} = 427 nm) as a function of block length. Solid lines represent measured PL intensity and dotted lines correspond to the estimated donor PL quenching based on Sexi homopolymer emission (black dotted line). PDI polymer **P2.3** (red dotted line) shown for comparison.

For the Ter-PDI copolymers, as the number of repeat units decreases from 75 to 14 units per block, the amount of donor PL quenching increases from 30% to 55%. This is likely due to intrachain charge transfer at donor-acceptor interfaces, which leads to strong quenching of the PL quantum efficiency, as demonstrated previously by Thelakkat and coworkers for a P3HT-PPerAcr donor-acceptor block copolymer.[215] For the Sexi-PDI copolymers, the relationship between block length and donor quenching is similar, with an increase in donor PL quenching from 20% to 48% as the repeat units per block decreased from 75 to 15. It should be noted that for the Sexi-PDI copolymers, PDI emission cannot be discounted at λ_{ex} = 427 nm. This may cause the estimation for Sexi

emission quenching to be artificially low, as some of the emission corresponds to the PDI fluorophore.

The Ter-PDI RCP demonstrates PL quenching of 90% in solution, presumably due to the increased number of interfaces between the donors and acceptors in the polymer chain as a result of an alternating or semi-alternating arrangement. In this way, the RCP represents an ideal case in solution, with very small intrachain interfacial distances between the donors and the acceptors. Similarly, the Sexi-PDI RCP demonstrates the most efficient PL quenching (80%) for the Sexi-PDI copolymer series due to the proximity of intrachain interfaces, leading to increased charge transfer events. It is also possible that energy transfer could account for a portion of the donor emission quenching, since it is also a favorable process as a result of the large spectral overlap of the Ter/Sexi donor emission with the PDI excitation. These results are very promising because they suggest that upon self-assembly into ordered, continuous domains with donor-acceptor interfaces throughout the active layer, charge transfer will be a very efficient process, as long as the donor and acceptor domain sizes closely match the exciton diffusion lengths. This is most accurately represented by the almost quantitative donor PL quenching in RCP materials, as well as by the increasing amount of donor PL quenching with increasing proximity of donor and acceptor moieties (i.e. shorter block lengths).

In order to better understand the energy and charge transfer processes that may be occurring in the donor-acceptor copolymer systems, equations describing Förster energy transfer (**Equations 3.1 – 3.3**) and electron transfer (**Equation 3.4**) were applied to the Ter-PDI and Sexi-PDI systems.[200,206,216] The results are summarized for the Ter-PDI copolymers in **Table 3.3** and for the Sexi-PDI copolymers in **Table 3.4**.

$$k_T = \frac{1}{\tau_D}\left(\frac{R_0}{R}\right)^6 \qquad (3.1)$$

$$R_0^6 = \Phi_D \kappa^2 \frac{9000\ln(10)}{128\pi^5 N_A n^4}\int_0^\infty F_D(\lambda)\,\varepsilon_A(\lambda)\lambda^4 d\lambda \qquad (3.2)$$

$$\eta = 1 - \frac{F_{DA}}{F_D} \qquad (3.3)$$

$$\Delta G^0 = e\left(E_{ox,D} - E_{red,A}\right) - \Delta G(S_1 \leftarrow S_0) + \frac{e^2}{4\pi\varepsilon_0}\left[\frac{1}{\varepsilon}\left(\frac{1}{r} - \frac{1}{d}\right) - \frac{1}{\varepsilon}\frac{1}{r}\right] \qquad (3.4)$$

Equation 3.1 represents the rate of energy transfer from donor to acceptor as a function of donor-acceptor separation (R) for Förster energy transfer. Here, τ_D represents the decay time of the excited state of the donor in absence of acceptor. R_0 combines normalization factors and spectral properties for the system, representing the donor-acceptor distance at which energy transfer efficiency is 50%. R_0 can be calculated from **Equation 3.2**. In this equation; Φ_D represents the donor fluorescence quantum yield, K^2 is the dipole orientation factor (which is equal to 2/3 for randomly-distributed, free donor and acceptor molecules); n is the refractive index of the solvent (n = 1.424 for DCM at 20 °C); $F_D(\lambda)$ is the fluorescence intensity of the donor at wavelength λ; and $\varepsilon_A(\lambda)$ is the molar absorptivity of the acceptor at wavelength λ.[200,216] For **Equation 3.2**, the wavelength-integrated donor fluorescence intensity is normalized to 1, and it is common to refer to this integral as the spectral overlap, J, between the emission spectrum of the donor and the excitation (or absorption) spectrum of the acceptor.

For the energy transfer efficiency (η) calculation, shown in **Equation 3.3**, F_{DA} corresponds to peak area of the donor emission in the copolymers and F_D corresponds to the peak area of the donor homopolymer emission. These were integrated from 385 to

510 nm upon excitation at 340 nm for the Ter materials, and integrated from 457 to 842 nm upon excitation at 417 nm for the Sexi materials. Slit widths were kept the same for all measurements. For both the Sexi homopolymer and Sexi-PDI copolymers, λ_{ex} = 417 nm was used due to the lower emission intensity of the PDI homopolymer at this wavelength comparted to λ_{ex} = 427 nm. There is no significant change in the emission profiles of the Sexi homopolymer or Sexi-PDI copolymers at these two wavelengths, and only a slight increase in the emission intensity of the copolymers at λ_{ex} = 427 nm. It is likely that the larger discrepancy between the calculated energy transfer efficiency (η) and estimated Sexi PL quenching in the copolymers is due to the overlap between the emission profiles of the Sexi and PDI fluorophores.

For the Weller equation (see **Equation 3.4**), E_{ox} and E_{red} represent the onsets of oxidation and reduction of the Ter/Sexi donor and PDI acceptor determined from the copolymer CVs. $\Delta G(S_1 \leftarrow S_0)$ represents the excitation energy of the donor, 3.05 eV for Ter and 2.54 eV for Sexi, calculated from the intersection of the absorption and emission spectra of the donor homopolymer. ε is the dielectric constant of DCM (8.93 eV at 25 °C), used for both the electrochemical and photophysical measurements; r is the electronic radius of the PDI, Ter, and Sexi ions, and has been roughly estimated at 0.5 nm for all ions.[200,216] d corresponds to the center-to-center distance between the two fluorophores and has been set at 20 Å, which is the maximum distance that can be reached. This calculation was also completed with d set to 5 Å for comparison, since electron transfer becomes more favorable as the donor and acceptor get closer together.

The Förster radius, R_0, which represents the donor-acceptor distance at which energy transfer efficiency is 50%, was determined using the donor homopolymer emission spectrum and the acceptor homopolymer excitation spectrum (integrated with PTI analysis software) to be 3.52 nm for the Ter-PDI donor-acceptor pair and 3.92 nm for

the Sexi-PDI donor-acceptor pair. This indicates that the Sexi-PDI donor-acceptor couple can undergo efficient energy transfer from further distances than the Ter-PDI couple. Energy-transfer efficiency (η) was determined using the ratio, F_{DA}/F_D, describing the donor emission intensity in the presence (F_{DA}) and absence (F_D) of the acceptor. The values calculated using this equation match well with the previous quenching estimation fittings in **Figures 3.11** and **3.12**.

The Weller equation was used to determine if excited-state electron-transfer was favorable for the Ter-PDI and Sexi-PDI systems.[200,216] Using a donor-acceptor distance of 20 Å, values of ΔG^0_{RCP} = -1.74 eV and ΔG^0_{BCP} = -1.68 eV were obtained for the Ter-PDI copolymers, and values of ΔG^0_{RCP} = -1.39 eV and ΔG^0_{BCP} = -1.43 eV were obtained for the Sexi-PDI copolymers. These values suggest that electron-transfer from both donors to the PDI acceptor is favorable. These results support that in the self-assembled bulk active layer, the proximity of the donor and acceptor domains will lead to highly efficient exciton dissociation.

Table 3.3. Analysis of energy and charge transfer for the Ter-PDI copolymers.

Ter-PDI Copolymers	R_0[a] (nm)	η[b]	Estimated Ter Quenching[c]	ΔG^0 (eV)[d] (d = 20 Å)	ΔG^0 (eV)[d] (d = 5 Å)
P3.1a (75)	3.52	0.34	0.30	-1.68	-4.83
P3.1b (42)	3.52	0.43	0.45	-1.68	-4.83
P3.1c (14)	3.52	0.56	0.55	-1.68	-4.83
P3.2	3.52	0.93	0.90	-1.74	-4.88

[a]Determined using the PTI analysis software on the fluorescence spectrophotometer; [b]Determined using emission spectra integrated from 385 to 510 nm with λ_{ex} = 340 nm; [c]Determined using the Ter homopolymer emission intensity spectra to estimate the extent of PL quenching; [d]Calculated using **Equation 3.4**, assumptions are stated above.

Table 3.4. Analysis of energy and charge transfer for the Sexi-PDI copolymers.

Sexi-PDI Copolymers	R_0 [a] (nm)	η [b]	Estimated Sexi Quenching[c]	ΔG^0 (eV)[d] (d = 20 Å)	ΔG^0 (eV)[d] (d = 5 Å)
P3.3a (75)	3.92	0.12	0.20	-1.43	-4.57
P3.3b (50)	3.92	0.18	0.32	-1.43	-4.57
P3.3c (25)	3.92	0.26	0.40	-1.43	-4.57
P3.3d (15)	3.92	0.38	0.48	-1.43	-4.57
P3.4	3.92	0.79	0.80	-1.39	-4.53

[a]Determined using the PTI analysis software on the fluorescence spectrophotometer; [b]Determined using emission spectra integrated from 457 to 842 nm with λ_{ex} = 417 nm; [c]Determined using the Sexi homopolymer emission intensity spectra to estimate the extent of PL quenching; [d]Calculated using **Equation 3.4**, assumptions are stated above.

Electron Paramagnetic Resonance Spectroscopy

In OPVs, diffusion of the photogenerated exciton to the donor-acceptor interface results in the formation of spin-paired donor radical cations (positive polarons) and acceptor radical anions (negative polarons), often referred to as charge transfer (CT) states. The separation of these Coulombically-bound CT states into free charges is required for high charge extraction efficiencies.[217,218] The present knowledge of charge separation in, for example, polymer:fullerene blends, is largely based on optical spectroscopy studies.[219] While PL experiments can be particularly useful for studying the impact of CT states on the luminescence spectrum of a donor-acceptor pair, these techniques require the CT states to recombine and thus are insensitive to long-lived CT states. In contrast, EPR can directly probe the presence of CT states in donor-acceptor systems.[219] Due to the low dielectric constants of organic semiconductors, larger separation distances between the donor and acceptor are required to achieve "stable" charge separation (~ 30 Å).[217] cw-EPR was used to investigate the formation of radical

cations and radical anions in the Sexi-PDI donor-acceptor copolymers (**P3.3a – P3.3d**, **P3.4**) generated upon illumination under ambient light. For comparison, the PDI homopolymer (**P2.3**) was electrochemically reduced and the Sexi homopolymer (**P2.2**) was chemically oxidized to characterize the acceptor radical anion and donor radical cation, respectively.

PDI homopolymer radical anions were generated by electrochemical reduction of a dropcast thin film of **P2.3d-2** on stainless steel in a blank solution of 0.1 M $TBAPF_6$ electrolyte in dry acetonitrile (ACN) under nitrogen. The reduction potential was held constant at approximately -1.0 V vs. Fc/Fc^+, which represents the onset of PDI reduction, until the film had changed from red to dark violet in color. The film was washed with dry ACN, carefully dried, and dissolved in dry DCM. This solution was transferred to a 1.4 mm o.d. quartz tube and sealed under N_2. Sexi homopolymer radical cations were generated by chemical oxidation of **P2.2c** with tris(4-bromophenyl)ammoniumyl hexachloroantimonate in dry DCM (1 equivalent of oxidant was used per 1 equivalent of homopolymer, based on M_n^{GPC}). This solution was transferred to a 1.4 mm o.d. quartz tube and sealed under N_2. For solution EPR samples, 7.9 ± 0.2 mg of **P3.3a (75)**, **P3.3b (50)**, **P3.3d (15)**, and **P3.4** were dissolved in dry DCM (0.5 mL) in 1.4 mm o.d. quartz tubes and sealed under N_2. For solid samples, 7.9 ± 0.2 mg of each copolymer was transferred to a 1.4 mm o.d. quartz tube and sealed under N_2.

Both homopolymer materials show strong and persistent radical signals, with a small amount of hyperfine coupling present in the PDI radical anion spectra (see **Figure 3.13**). Furthermore, the radical cation and radical anion signals have distinct g-factors, allowing them to be distinguished from one another.

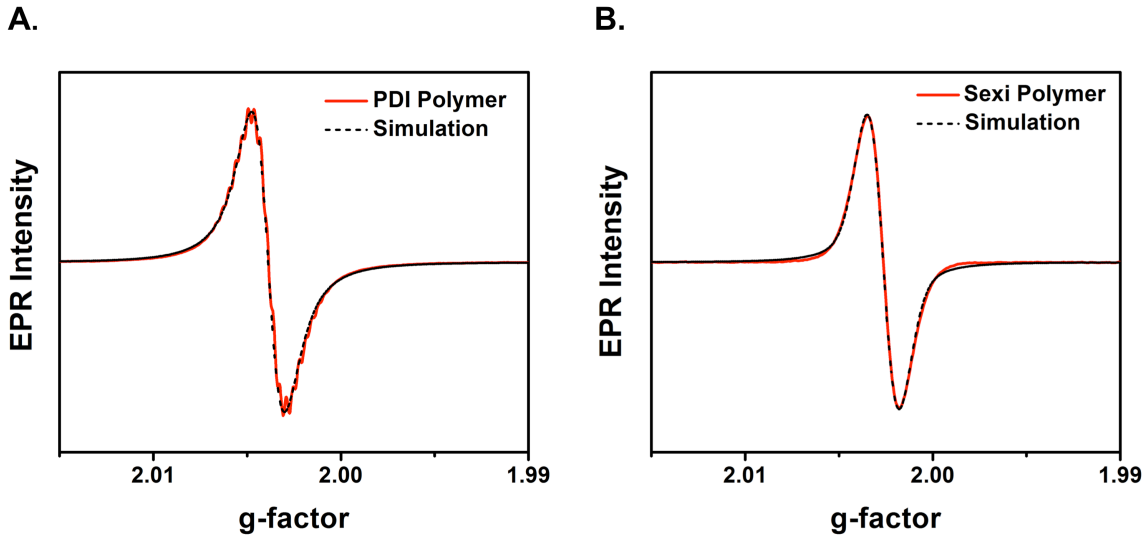

Figure 3.13. EPR signals (red line) and corresponding simulations (black dotted line) for (A) PDI homopolymer (**P2.3d-2**) acceptor radical anion, generated from electrochemical reduction; (B) Sexi homopolymer (**P2.2c**) donor radical cation, generated from chemical oxidation.

To study the effects of donor-acceptor intrachain interfacial distance on photoinduced charge separation and formation of CT states, Sexi-PDI RCP (**P3.4**), and Sexi-PDI BCPs **P3.3a (75)**, **P3.3b (50)**, and **P3.3d (15)** were studied by EPR, both in DCM solution and in the solid state. Persistent radical species were generated in all copolymers upon exposure to ambient light. Furthermore, in both solid and solution states, as the chain length of the donor and acceptor blocks increased from 15 to 75 repeat units each, the EPR intensity also increased (see **Figure 3.14** and **Figure 3.15**) This increase is related to the number of radicals that can be stabilized on donor and acceptor segments. As the chain lengths of the block copolymers increase, more unpaired spins can be accommodated, increasing the signal intensity. The Sexi-PDI RCP shows the weakest signal due to strong coupling of the generated spin-pairs. Assuming that the RCP has an alternating or semi-alternating arrangement of donor and acceptor repeat units, the

Coulombically-bound CT states would not be able to delocalize across neighboring donor or acceptor units. Thus, the generated radical anion and radical cation spin pair would remain strongly coupled, quenching the EPR signal.

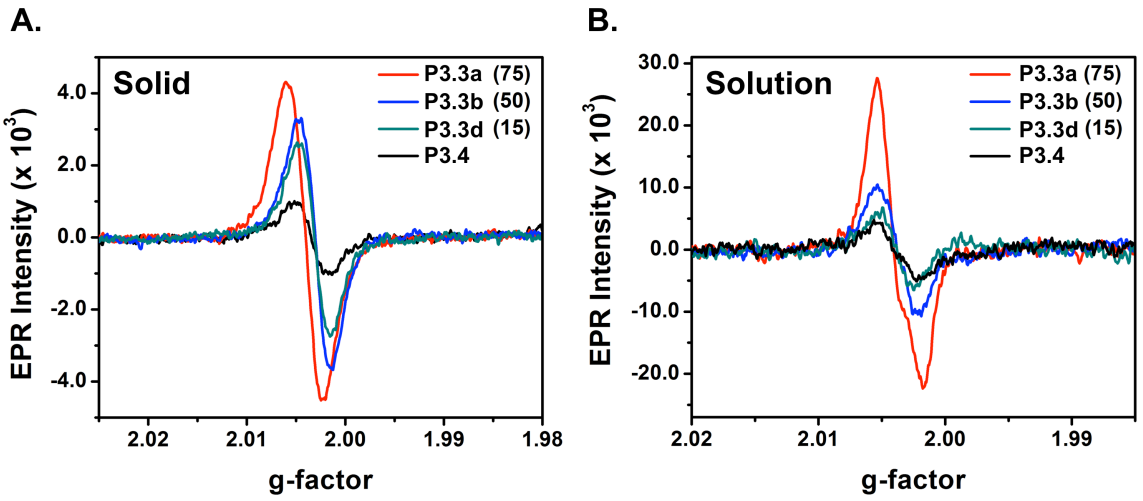

Figure 3.14 (A) Solid state cw-EPR signals from photogenerated charges using the same amount (7.9 mg) of Sexi-PDI copolymers; (B) Solution cw-EPR signals from photogenerated charges on the Sexi-PDI copolymers using the same solution concentration (7.9 mg in 0.5 mL DCM) for all samples. The different block lengths are denoted by the numbers in parentheses.

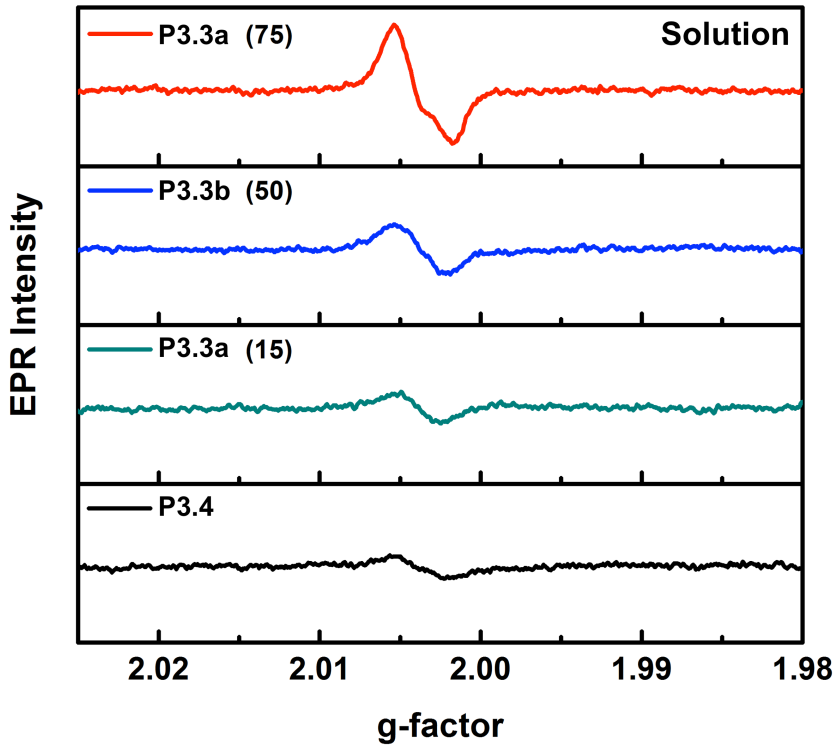

Figure 3.15. Solution cw-EPR signals from photogenerated charges on Sexi-PDI copolymer materials of different block lengths. The Sexi-PDI RCP (**P3.4**) is shown for comparison. As the block length decreases, the EPR signal intensity decreases. For **P3.3a (75)**, there are two overlapping signals, corresponding to the acceptor radical anion and donor radical cation. In **P3.3b (50)** and **P3.4**, the same overlap is also present, although the decreased signal makes it harder to see.

In solution, the Sexi-PDI BCP **P3.3a** EPR signal shows contributions from both the PDI radical anion and the Sexi radical cation. This overlap of signals can also be seen for Sexi-PDI BCP **P3.3b**, although the EPR signal is weaker for the shorter BCPs (see **Figure 3.15**). This overlap in signals suggests that upon charge separation, the block copolymer is able to stabilize both the radical cations and radical anions on the donor and acceptor domains, respectively. For **P3.3a**, this EPR signal can be modeled as a combination of the corresponding signals of the PDI radical anion and the Sexi radical

cation (see **Figure 3.16**). In terms of OPV applications, it is likely that these materials will show high charge extraction efficiencies as a result of efficient charge separation.

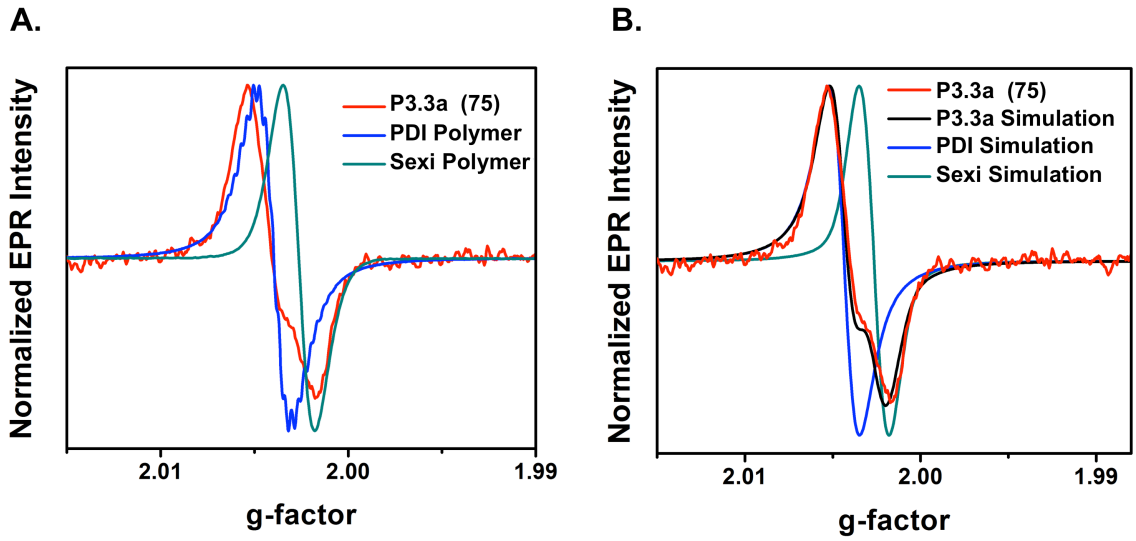

Figure 3.16. (A) Overlay of normalized EPR signals for Sexi homopolymer (**P2.2c**) radical cation (green), PDI homopolymer (**P2.3d-2**) radical anion (blue), and Sexi-PDI BCP (**P3.3a**) (red); (B) Overlay of normalized **P3.3a** EPR signal (red) and corresponding simulation (black), fitted using the PDI polymer radical anion (blue) and Sexi polymer radical cation (green) signals.

Structural Analysis by Small-Angle X-ray Scattering

Given the promising results discussed above, bulk self-assembly of the donor-acceptor BCPs was investigated using SAXS at room temperature. Bulk samples were prepared by annealing overnight at 280 °C, well above the T_g's of both blocks, to induce microphase self-assembly. As a consequence of the crystalline or liquid crystalline nature of the donor and acceptor semiconducting moieties, crystallization processes are in competition with classical microphase separation of the two blocks, and crystallization of the semiconducting pendant groups can disrupt the self-assembly of the BCP.[170] Amorphous polymers containing PDI pendant groups have been shown to form a lamella-

columnar liquid crystalline phase in bulk and, much like P3HT, oligothiophenes can exhibit a strong driving force for crystallization-induced structural ordering.[87,217,220–222] **Figure 3.17** shows the SAXS data obtained from bulk samples of the Ter-PDI BCPs and Sexi-PDI BCPs at room temperature. A low angle peak can be seen for both the Ter-PDI BCP **P3.1b (42)** ($q^* = 0.26$ nm^{-1}) and Sexi-PDI BCP **P3.3b (50)** ($q^* = 0.22$ nm^{-1}), indicating nanoscale separation into an ordered morphologies for the copolymers with $N_n \approx 100$. From this scattering peak, a nanoscale periodicity (d) of 24.2 nm for **P3.1b (42)** and 28.6 nm for **P3.3b (50)** can be calculated at room temperature ($d = 2\pi/q^*$).[223] This domain size is well-suited for exciton diffusion lengths, which are on the order of 5-10 nm. Furthermore, by applying a Lorentz correction to the data, a second ordering peak at 2q* can be resolved, indicating the formation of lamellar domains in the bulk materials. Additionally, two higher angle scattering peaks ($q = 1.30$ nm^{-1}, 2.34 nm^{-1}) suggest that one or both of the individual blocks form (liquid) crystalline structures within the self-assembled microdomains, with length scales on the order of 5 nm (see **Figure 3.18**).[170,220,224]

While, there are no apparent low angle scattering peaks associated with polymer self-assembly in the other bulk BCPs, it is possible that some short-range crystallization is occurring, as evidenced by the weaker/broadened signals at higher scattering angles, as shown in **Figure 3.18**. Since PDI and conjugated oligothiophenes both have high charge mobilities in the crystalline state (PDI: 10^{-3} cm^2 V^{-1} s^{-1}; P3HT: 10^{-3} to 10^{-1} cm^{2}V^{-1}s^{-1}),[74,200,225] crystallization of the donor and acceptor semiconducting moieties within a periodic self-assembled structure is ideal for photovoltaic applications. The results suggest that given perpendicular alignment with the electrodes, high power conversion efficiencies may be possible with these donor-acceptor BCP materials.

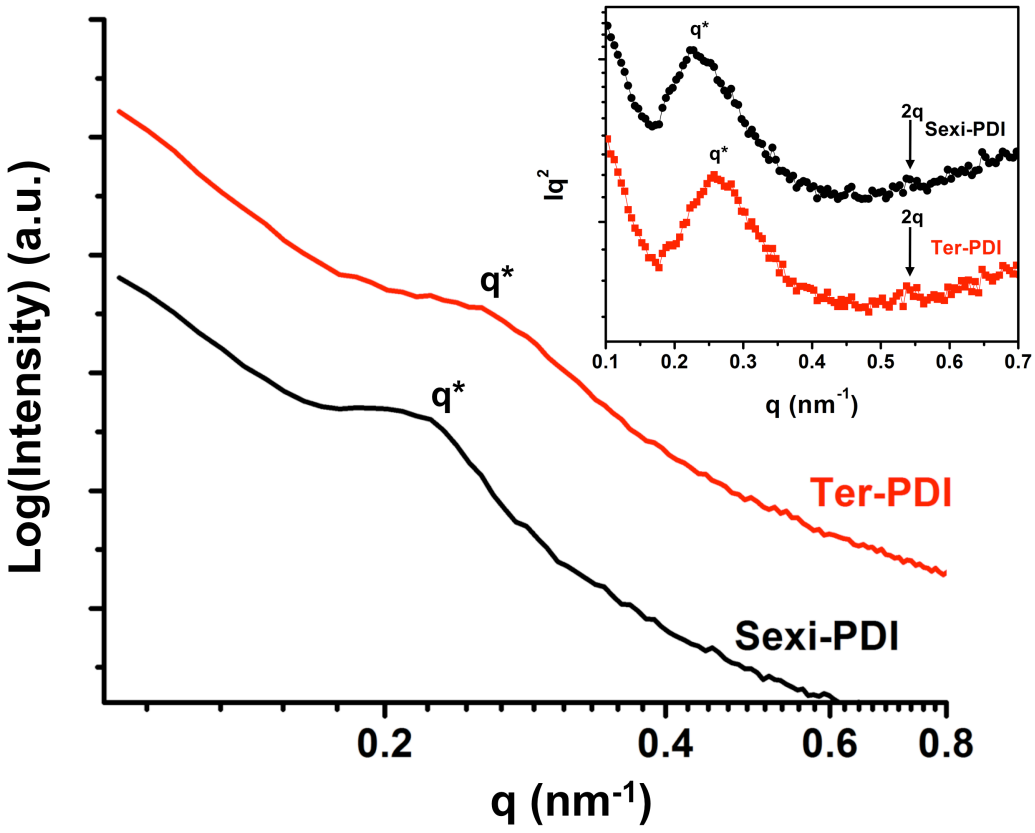

Figure 3.17. SAXS diffraction patterns for Ter-PDI BCP **P3.1b (42)** (red) and Sexi-PDI BCP **P3.3b (50)** (black) at room temperature. The inset shows the same data after a Lorentz correction to better resolve the weak secondary scattering peaks. From the Lorentz correction, a second ordering peak at 2q* can be resolved, indicating the formation of a lamellar morphology.

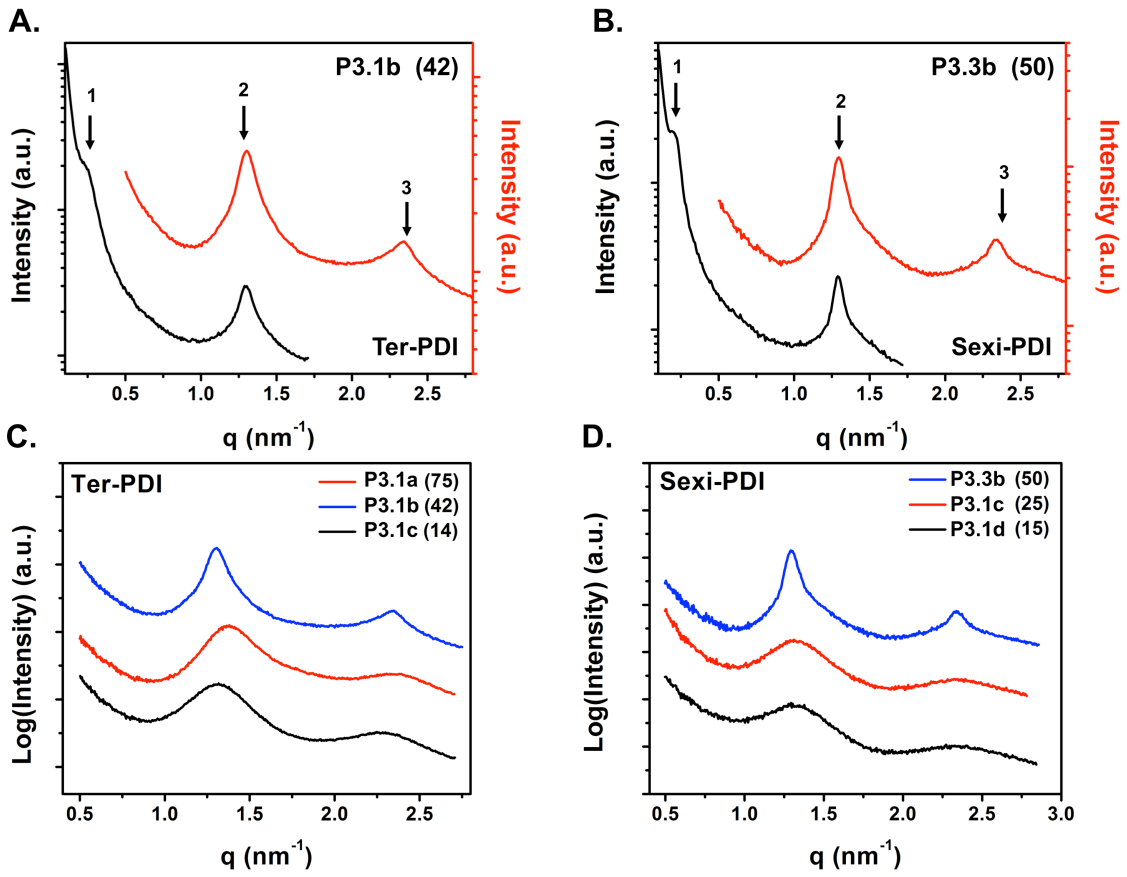

Figure 3.18. (A,B) SAXS scattering data from back chamber (black) and front chamber (red) for (A) Ter-PDI **P3.1b (42)** and (B) Sexi-PDI **P3.3b (50)**. The peak labeled 1 indicates q*. The intermediate scattering peaks, labeled 2 and 3, indicate (liquid) crystalline structure within the microdomains; (C,D) Intermediate angle scattering data for (C) Ter-PDI BCP series and (D) Sexi-PDI BCP series, showing (liquid) crystalline ordering within the microphase structure of one or both individual blocks.

CONCLUSION

By attaching oligothiohene donor and PDI acceptor pendant groups to a flexible norbornene-type backbone, coil-coil donor-acceptor BCPs were synthesized using ROMP. Both the Ter-PDI and Sexi-PDI donor-acceptor copolymers demonstrate well-matched frontier molecular orbital energy levels for efficient exciton dissociation and charge transfer. Photophysical and EPR measurements demonstrate that charge transfer

occurs between the donor and acceptor domains upon photoexcitation. Furthermore, solution PL quenching studies indicate that the location of the donor-acceptor interface plays an important role in the efficiency of intrachain charge transfer. SAXS measurements show that bulk microphase separation occurs upon thermal annealing for Ter-PDI and Sexi-PDI BCPs with $N_n \approx 100$. These bulk materials self-assemble into lamellar structures with domain sizes between 24–28 nm. All of these results demonstrate the ability to make well-ordered coil-coil donor-acceptor block copolymers with potential applications in OPV technologies. In addition, due to the flexibility and functional group tolerance of the designed synthetic route, a myriad of functional polymers that can be tailored to specific applications beyond light-harvesting materials can be imagined.

HYBRID ORGANIC-INORGANIC BLOCK COPOLYMERS

Chapter 4: Towards Hybrid Inorganic-Organic Block Copolymers—Synthesis and Characterization of Norbornene-type Copolymers Containing Semiconducting Terthiophene and Lewis-Basic Oligoethylene Glycol Pendant Groups

INTRODUCTION

Organic photovoltaics (OPVs) have attracted substantial research interest as cost-effective alternatives compared to their inorganic counterparts such as Si and GaAs for converting solar energy into electricity. OPVs benefit from solution processing and roll-to-roll manufacturing options. Furthermore, the high optical absorption coefficients of organic semiconductors allow for active layer thicknesses of a few hundred nanometers, leading to potential consumer applications where fabrication of lightweight, flexible devices is required. While OPVs offer a multitude of benefits, organic semiconductors often suffer from relatively low charge carrier mobilities due, in part, to weak intermolecular van der Waals interactions.[226] On the other hand, inorganic semiconductors have intrinsically high carrier mobilities, as well as high environmental and chemical stability. However, traditional inorganic solar cells can require elevated temperature and vacuum for the growth of high-quality single crystals or epitaxial thin films.[226,227] Polymer-inorganic hybrid solar cells represent a promising alternative to typical OPVs by combining the high charge mobility and good physical and chemical stability of inorganic nanomaterials with the solution-processability, flexibility, and strong optical absorption of organic semiconductors.[228–230] The introduction of inorganic nanocrystals into organic semiconducting materials provides an organic-inorganic interface for charge transfer, and the intrinsically high electron mobility of inorganic materials enables fast and efficient charge separation and charge transport, thus limiting

current losses *via* recombination.[227] To date, various inorganic nanocrystals have been used as electron acceptors in these types of hybrid devices, including CdS, CdSe, CdTe, ZnO, SnO_2, TiO_2, Si, PbS, and PbSe.[226–229,231–235]

There are two principal methods used to prepare hybrid inorganic-organic solar cells. One method is to form a blended bulk heterojunction (BHJ) by dispersing the inorganic nanocrystals directly within the conjugated polymer (see **Figure 4.1**). This can be done by either blending preformed nanocrystals in solution with the organic donor material or by generating the inorganic semiconductor *in situ* inside of the organic material.[230] The generation of inorganic semiconductor *in situ* is achieved by depositing an organometallic precursor from solution with the semiconducting polymer during spin-casting. The organometallic precursor is then converted into an inorganic network inside of the polymer *via* reaction with water in the surrounding atmosphere. This approach has been demonstrated with metal oxide semiconductors such as ZnO using diethyl zinc (DEZ) as the organometallic precursor.[236–238] The formation of BHJ structures from dispersion of the inorganic semiconductors within the polymer materials results in a large number of donor-acceptor interfaces for charge separation, although control of the BHJ morphology during fabrication can be challenging.

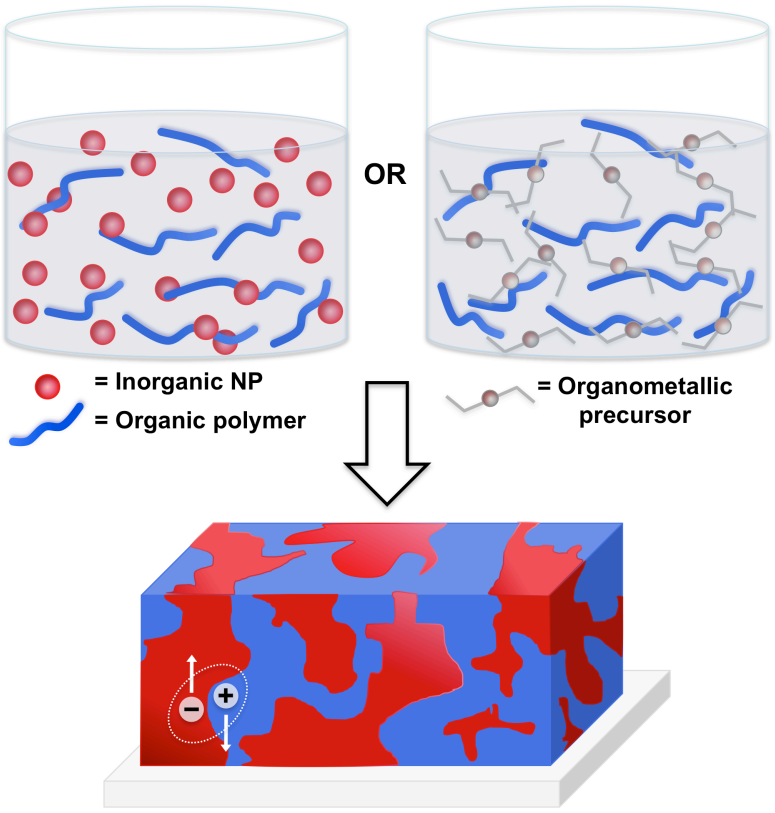

Figure 4.1. Schematic of blending method used for fabrication of hybrid inorganic-organic solar cells in which a conjugated polymer is spin-cast from solution with either pre-synthesized nanoparticles (NPs) or organometallic precursors in order to make a composite film.

As depicted in **Figure 4.2**, an alternative fabrication route for preparing inorganic-organic hybrid solar cells is to infiltrate the polymer into rigidly connected inorganic nanostructures that have been pre-grown onto the desired substrate.[230] While well-connected pathways can be formed in this way, it can be challenging to achieve complete infiltration of the polymer into the free spaces in the inorganic structures.

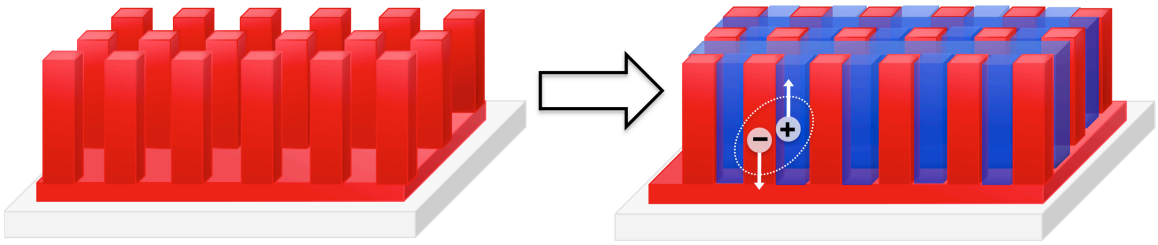

Figure 4.2. Schematic of the infiltration method used for the fabrication of hybrid inorganic-organic solar cells in which a pre-patterned inorganic semiconductor is back-filled with conjugated polymer to form an interpenetrating network.

The performance of polymer-inorganic BHJ hybrid solar cells depends on the optimized mixing and resulting morphology of the inorganic nanocrystals with the conjugated polymer. This becomes challenging in inorganic-organic hybrid systems because of the strong incompatibility between the inorganic acceptor and the organic donor materials due, in part, to the complex surface chemistry of inorganic semiconductors.[227,230] This incompatibility can be addressed in several ways. For example, the use of mixed solvent systems during deposition can aid in solubilizing and dispersing the inorganic semiconductors. In addition, utilizing solubilizing capping agents can not only stabilize the nanomaterials, but also help to improve the compatibility of the inorganic materials and organic polymers.[230] **Figure 4.3** shows a schematic of a typical BHJ hybrid solar cell with commonly used organic conjugated polymers. **Figure 4.4** shows average band gaps associated with typical donor and acceptor semiconductor materials.

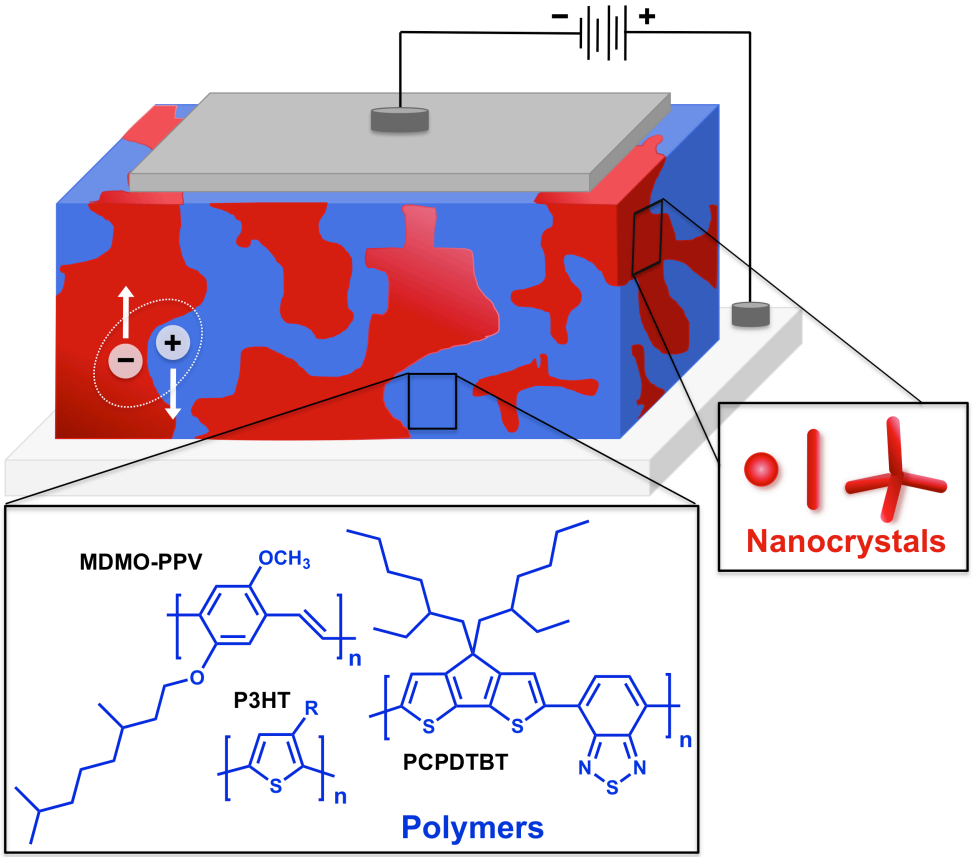

Figure 4.3. Schematic of hybrid BHJ solar cell with structures of typical conjugated donor polymers and nanocrystal morphologies.

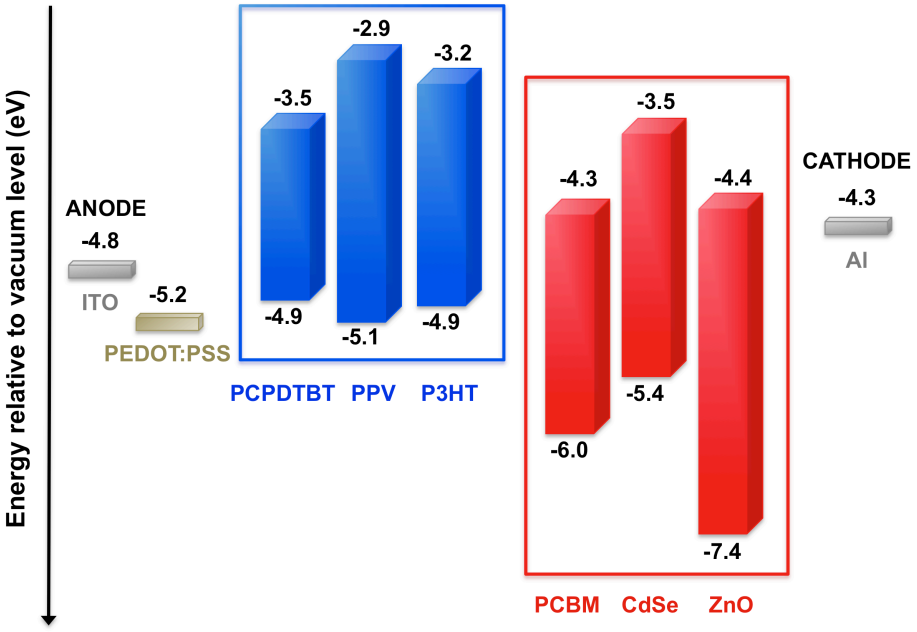

Figure 4.4. Schematic of determined HOMO and LUMO energy levels, and resulting band gaps, for common donor and acceptor semiconductors used in photovoltaic applications. Figure adapted from ref [235].

In 2002, Alivisatos and coworkers reported one of the first successful examples of a hybrid polymer-inorganic solar cell with a power conversion efficiency (PCE, η) of η = 1.7%.[227] The hybrid photovoltaic (PV) device was based on CdSe nanorods as a 90 wt% dispersion in the conjugated polymer poly(3-hexylthiophene) (P3HT). As inorganic nanocrystals increase in aspect ratio from spherical to rod-like, they transition from the molecular regime closer to a 1-D wire and become increasingly less soluble. In order to increase solubility of the nanocrystals in the conjugated polymer, the researchers developed a miscible solvent mixture consisting of pyridine, which is a good solvent and ligand for the CdSe, and chloroform ($CHCl_3$), which is a good solvent for the conjugated polymer. This mixed solvent system aided in the favorable dispersion of the CdSe nanorods within P3HT polymer thin films. The researchers went on to demonstrate that the absorption, and consequently the band gap, of the CdSe semiconductor could be

tuned by altering the diameter of the nanorods as a result of the quantum confinement effect. This allowed for the tailoring of a more complementary absorption of the CdSe nanorods and the P3HT polymer, leading to an optimized spectral overlap between 300 nm to 720 nm. Furthermore, it was found that quantum confinement also led to an enhancement in the absorption coefficient compared with the bulk material, which allowed for the fabrication of thinner devices. Finally, by controlling the nanorod length charge transport through the film could be tuned. In networks consisting of shorter nanoparticles, electron transport was dominated by a hopping mechanism, while in networks consisting of longer particles band conduction was prevalent, the latter leading to a notable increase by a factor of 3 in the external quantum efficiency (EQE) of the fabricated devices.

In 2010, Rumbles and coworkers reported that replacing the semiconducting nanoparticles or nanorods with 3-D nanocrystals improved the electron percolations in hybrid inorganic-organic devices. The researchers demonstrated a PCE of $\eta \approx 3.2\%$ for blends of CdSe tetrapods and low-band gap polymer poly[2,6-(4,4-bis-(2-ethylhexyl)-4H-cyclopenta[2,1-b;3,4-b'}dithiophene)-*alt*-4,7-(2,1,3-benzothiadiazole)] (PCPDTBT) (see **Figure 4.3** for structure).[239] The best performing devices were based on 90 wt% CdSe tetrapods in PCPDTBT. The CdSe tetrapods had an average arm diameter of ~5 nm, with average arm lengths between 30-50 nm. By utilizing the low-band gap polymer PCPDTBT, the absorption of the device could be extended from 350 nm to 800 nm. The notable feature of this work was the use of the low-band gap polymer, which allowed for more efficient light harvesting—in the composite film containing 90 wt% CdSe, only 34% of light absorption was due to the nanocrystals, while 66% was correlated to absorption by PCPDTBT.

While CdSe nanocrystals offer the advantage of a visible absorption, which can contribute to light harvesting in PV devices, and some of the best hybrid devices have been reported using this inorganic semiconductor, the precursors utilized in the synthesis are highly toxic. Metal oxides, such TiO_2 and ZnO, are promising alternative inorganic semiconductors for use in hybrid inorganic-organic solar cells. Metal oxides usually have large band gaps (> 3 eV) that prevent absorption in a useful spectral range for light harvesting. Therefore, these semiconductors can only be utilized as the electron acceptor in hybrid devices, which can lead to decreased photocurrents. However, they offer the advantage of being substantially less toxic than other II-VI semiconductors.[229,230] Furthermore, they are environmentally friendly and cheap to synthesize using low-cost, wet chemical methods. In addition, a large range of morphologies, from nanowires to nanorods and nanoparticles can be achieved *via* solution methods, enabling full compatibility with the solution fabrication of polymer-based solar cells. Interestingly, the optimal polymer-inorganic semiconductor ratios used in polymer-metal oxide hybrid solar cells are typically lower than those used in CdSe hybrid systems. For example an optimized P3HT-TiO_2 hybrid BHJ device with PCE of $\eta \approx 2.2\%$, as described in 2009 by Chen and coworkers[240], and a P3HT-ZnO BHJ device with PCE of $\eta \approx 2.0\%$, reported by Janssen and coworkers in 2009[236], both utilized substantially lower metal oxide volume fractions of approximately 20% as compared 60 vol% typically used in CdSe devices.[230,235]

APPLICATIONS OF ZNO IN HYBRID SOLAR CELLS

The first example of a BHJ hybrid solar cell based on ZnO nanocrystals was reported in 2004 by Janssen and coworkers, utilizing ~5 nm ZnO nanoparticles (NPs) blended with the conjugated donor polymer poly[2-methoxy-5-(3',7'-dimethyloctyloxy)-

1,4-phenylenevinylene] (MDMO-PPV, see **Figure 4.3** for structure).[241] The ZnO NPs were prepared by the hydrolysis and condensation of zinc acetate dehydrate ($Zn(OAc)_2 \bullet 2H_2O$) with potassium hydroxide (KOH) in MeOH. The synthesized NPs were insoluble in pure MeOH, but the addition of a less polar solvent such as $CHCl_3$, DCM, or chlorobenzene (CB) allowed for preparation of stable solutions. Furthermore, the high solubility of MDMO-PPV in the solvent mixture allowed for simultaneous spin-casting of both materials. Devices made from thin films (~100 nm thickness) of MDMO-PPV:ZnO, using 67 wt% ZnO, gave PCEs of η = 1.4% at 1.7 sun equivalent white-light illumination and η = 1.6% at 0.71 sun equivalents. Between 60 wt% and 75 wt% ZnO NPs, the PCEs of the fabricated devices were relatively insensitive to the MDMO-PPV:ZnO ratio. However, using less than 60 wt% ZnO led to a large decrease in the current density, and utilizing over 75 wt% ZnO gave films of very poor quality due to increased aggregation of ZnO NPs. Charge transfer efficiency was investigated by photoluminescence (PL) measurements. Up to 85% of MDMO-PPV emission was quenched by the addition of 75 wt% ZnO due to the ultrafast deactivation of the donor excited state by electron transfer to the n-type ZnO NPs. The residual PL was attributed to excitons that were formed too far from an interface to undergo dissociation before recombination or decay. In a later study, Janssen and coworkers investigated the effect of nanocrystal geometry and size on device performance, but optimized devices did not outperform the previously reported efficiency of η = 1.6%.[242] Adding *n*-propylamine as a stabilizing and solubilizing ligand for the ZnO NPs aided in preventing aggregation in the thin film but did not improve device performance. This was rationalized by a loss in electron transport across the surfactant interface layer.

In 2006, Janssen and coworkers reported hybrid inorganic-organic solar cells based on ZnO NPs, this time utilizing regioregular P3HT as the donor polymer.[243] While

MDMO-PPV is a widely studied conjugated p-type polymer for OPV applications, P3HT demonstrates higher hole mobilities and an improved spectral overlap, and thus has become ubiquitous in the literature as the polymeric donor material to which others are compared. Using similar fabrication methods as with the previously discussed MDMO-PPV:ZnO composite films,[241] the best P3HT:ZnO BHJ device, using 26 vol% ZnO and having a thickness of ~200 nm, demonstrated an estimated PCE of η = 0.9%. Thermal annealing at 80 °C was crucial to achieving high device performance due to improvements in chain ordering in the P3HT domains, which resulted in increased hole mobility. Atomic force microscopy (AFM) indicated that increasing the ZnO content in the films led to increased film roughness, from the formation of large ZnO aggregates. Upon addition of the ZnO NPs, UV-Vis spectroscopy demonstrated a blue shift of the P3HT π-π^* transition band, accompanied by a loss of weak vibronic structure in the absorption profile, indicating a decrease in polymer chain stacking and an increase in conformational disorder caused by mixing with ZnO. Photoluminescence spectroscopy demonstrated incomplete P3HT emission quenching and photoinduced absorption (PIA) spectroscopy indicated the presence of triplet-triplet absorption of P3HT, which served as evidence that charge-carrier generation was not quantitative in the composite thin films. From these studies, two important conclusions were reached. First, intimate mixing of the ZnO NPs and the conjugated polymer was not achieved. Second, large P3HT domains of length scales much greater than exciton diffusion lengths existed in the thin films. The researchers hypothesized that the poor nanoscale mixing of the ZnO NPs with the P3HT, caused by the hydrophilic surface of ZnO, resulted in the observed low PCEs.

While ZnO nanocrystals are usually first synthesized by hydrolysis and then dispersed in the conjugated polymer film to form a BHJ composite, it is also possible to construct the ZnO phase *in situ* from the highly reactive DEZ precursor. This

organometallic precursor is soluble in organic solvents and can be cast into thin films together with the conjugated polymer. Then, upon exposure to air, the precursor material reacts with ambient moisture resulting in well-dispersed ZnO NPs throughout the polymer film.[229,230] In 2005, Janssen and coworkers utilized this synthesis technique to fabricate MDMO-PPV:ZnO hybrid solar cells with a maximum efficiency estimated at η = 1.1% using 15 vol% ZnO.[237] The composite films were made by spin-casting the DEZ precursor with MDMO-PPV from a mixture of CB/THF/toluene under a relative humidity of 40%. In order to achieve smooth films, THF was used to stabilize the DEZ by coordination to the zinc atom and moderate the hydrolysis and condensation reactions of DEZ to form ZnO. The thin films were then annealed at 110 °C for 30 minutes in N_2 at 40% relative humidity. Upon heating, the UV-Vis absorption onset for the thin film shifted to 375 nm, indicating the formation of ZnO. Furthermore, powder X-ray diffraction (p-XRD) indicated the formation of crystalline ZnO, with an estimated size of 6 ± 1 nm. Even before annealing, the composite thin films demonstrated a 50% decrease in emission compared to pristine MDMO-PPV, almost irrespective of the amount of DEZ used. This PL quenching was attributed to electron transfer from the singlet-excited state of the conjugated polymer to the partially condensed ZnO precursor. Upon annealing, the PL quenching increased, with a residual donor emission of only ~20%. This residual PL was attributed to excitons that could not reach a polymer-ZnO junction, suggesting that up to 80% of the absorbed photons resulted in charge formation in the hybrid film.

One disadvantage of the *in situ* metal oxide approach for the fabrication of the ZnO phase in hybrid systems is the use of highly reactive DEZ, which can lead to degradation of PPV derivatives through breaking of the reactive *trans*-vinyl bonds in the conjugated polymer backbone.[238] The predominant degradation mechanism of conjugated polymers is *via* photo-oxidation and the chemical reaction deliberately induced to form

the ZnO can accelerate polymer degradation. This was observed by Blom and coworkers in 2007 for BHJ hybrid films of MDMO-PPV:ZnO made using the DEZ precursor.[238] Upon addition of DEZ, there is a blue shift in the absorption spectrum of MDMO-PPV, accompanied by deterioration of hole transport through the material. This is consistent with reduction of the polymer backbone conjugation length as a result of polymer degradation. In order to avoid this degradation, regioregular P3HT was utilized, which is more stable (i.e. more resistant to oxidation under identical circumstances) than PPV derivatives due to the absence of *trans*-vinyl bonds. The researchers found that the absorbance of P3HT in CB was unaffected by processing under humid conditions, with or without the DEZ precursor. Furthermore, no change in hole mobility in the P3HT films with DEZ was observed. Using the same procedure as for the *in situ* preparation of ZnO from DEZ in the MDMO-PPV:ZnO hybrid devices, P3HT:ZnO hybrid devices with 15 vol% of ZnO were fabricated and an estimated efficiency of η = 1.4% was achieved without optimization. This improvement in device performance was mainly due to a large increase in the J_{sc}. However, this was opposed by a decrease in V_{oc}, which is a bulk property governed by the energy difference between the HOMO level of the donor (P3HT: ~4.9 eV, MDMO-PPV: ~5.2 eV) and the LUMO level of the acceptor, in this case the conduction band edge (CBE) of the synthesized ZnO (~4.4 eV). The HOMO of P3HT is three tenths of an electronvolt closer to the CBE, leading to the observed V_{oc} decrease.

As all of these studies demonstrate, the efficiency of BHJ polymer-inorganic hybrid solar cells depends on the intimacy of mixing of the donor and acceptor semiconductors used in the device, as well as the presence of percolation pathways to transport charges to the electrodes. In 2009, Janssen and coworkers fabricated and analyzed a series of P3HT:ZnO hybrid solar cell with different film thicknesses based on

the *in situ* preparation of ZnO NPs, utilizing electron tomography to spatially resolve the morphology of the resultant BHJ.[236] The active layer was fabricated following similar techniques as previously described: spin-casting a blend of DEZ and P3HT from a solvent mixture of CB/toluene/THF in humid conditions to initiate the hydrolysis of DEZ and formation of $Zn(OH)_2$, and annealing at 100 °C to complete the condensation reaction to form interpenetrating networks of ZnO. A 50 wt% composition of ZnO NPs in P3HT gave the best performance (corresponding to 20 vol% ZnO). Furthermore, it was observed that the device performance improved with increasing active layer thickness, with the best device performance of $\eta = 2\%$ obtained for a 225-nm composite film. These findings differ from typical P3HT:fullerene OPVs, where optimal fullerene content usually exceeds 50 wt% and increasing active layers thicknesses above ~100 nm generally results in decreased device performance due to charge collection limitations.

Janssen and coworkers went on to analyze the effects of film thickness on active layer morphology and device performance.[236] Utilizing PIA spectroscopy, and studying P3HT:ZnO composite films with thicknesses of 44 nm, 55 nm, and 115 nm, the researchers observed characteristic absorption bands related to the P3HT polymer radical cation, demonstrating photoinduced charge generation. However, an absorption corresponding to the P3HT triplet state was also observed, indicating that quenching of the initially formed singlet exciton in the P3HT:ZnO blend was not quantitative, leaving time for intersystem crossing to the triplet state for a significant fraction of the formed excitons. Comparatively, the thicker films showed an increase in radical cation absorption intensity relative to the triplet absorption, suggesting higher carrier generation efficiency with increasing film thickness. This correlates with the calculated internal quantum efficiencies (IQE) for the films. IQE describes the ratio of J_{sc} to the number of absorbed photons per unit area and time (i.e. it describes the number of free charges

collected per photons absorbed). For the P3HT:ZnO composite films, IQE increased significantly from 20% for 50-nm-thick films to 50% for films with active layer thicknesses greater than 150 nm. This indicates that not only are more photons absorbed as the active layer thickness increases, but also that these photons are more efficiently transferred into collected current. This is counterintuitive, as it would be expected that charge collection would become more difficult for thicker layers owing to the larger distances over which the carriers need to be transported.

Detailed transmission electron microscopy (TEM) analyses were carried out on free-standing composite films of P3HT:ZnO with thicknesses of 57 nm, 100 nm, and 167 nm. As the active layer thickness increased, the films demonstrated finer phase-separated domains. The thinnest film (57 nm) showed domains of P3HT that were substantially larger than the exciton diffusion lengths, consistent with the large triplet signals observed in the PIA measurements, as well as the low IQE in the thin devices. Statistical morphology analysis of the 3D-TEM images using electron tomography yielded several important results. First, while the calculated ZnO volume fraction in the two thickest films was close to the expected value (19 vol%) based on the DEZ:P3HT ratio used to spin-cast the films, the ZnO content in the thinner film was much lower at 13%. This was attributed to evaporation of the DEZ precursor during spin-casting as a result of the higher spin rate used to achieve the thinner film. Next, the distance distribution from P3HT to ZnO in the films was estimated. For the 100- and 167-nm-thick films, most of the P3HT lies well within a shortest distance of 10 nm from ZnO (matching well with exciton diffusion lengths of ~10 nm in P3HT). However, for the 57-nm-thick film, large amounts of polymer lie at shortest distances as high as 25 nm from an interface. Looking at the combined effects of charge generation and charge collection, it was concluded that the relatively poor performance of thin P3HT:ZnO hybrid devices was related to

inefficient charge generation as a result of low ZnO content and coarse phase separation into large domains, accompanied by exciton losses at the electrodes. For thicker layers, charge generation was much more efficient, owing to more favorable separation, but lowered percolation pathways to the respective electrodes led to lower charge collection.

BLOCK COPOLYMERS AS THE DONOR COMPONENT FOR HYBRID SOLAR CELLS

Precise control of active layer morphology is one of the critical issues to obtaining high performance in hybrid BHJ solar cells. Conjugated polymers and inorganic nanocrystals are chemically incompatible and tend to form uncontrolled macrophase-separated morphologies, which impedes charge generation and transport, reducing the overall efficiencies that can be achieved.[226,228,232,244,245] Extensive efforts have been devoted to optimizing the morphology of hybrid BHJ solar cells, including surface modification of the inorganic nanocrystals, *in situ* preparation of the inorganic semiconductor within the conjugated polymer from organometallic precursors, and functionalization of the conjugated polymers.[226,232,245–247] While these methods show promise for creating composites with interpenetrating donor-acceptor interfaces, there are still issues with achieving intimate mixing of the inorganic semiconductor in the polymer matrix. Recently, utilization of conjugated block copolymers (BCPs) containing a semiconducting block and a Lewis-basic block as the photoactive donor material in hybrid solar cells has attracted interest as a possible means to overcome these morphology issues. Incorporating a Lewis-basic functionality into one of the blocks of the copolymer should aid in the solubility and dispersion of the Lewis-acidic metal NPs within the polymer matrix. This approach, which uses semiconducting BCPs for improved morphological and stability control, has been well-studied for OPV

applications, but few reports on hybrid BHJ solar cells based on BCP materials have been made.

In 2011, Stefan and coworkers synthesized a BCP composed of P3HT and poly(4-vinylpyridine) (P4VP) (P3HT-*b*-P4VP) and blended it with CdSe quantum dots to fabricate a hybrid BHJ.[248] The P3HT-*b*-P4VP BCP was synthesized by reversible addition-fragmentation chain-transfer (RAFT) polymerization of 4-vinylpyridine with a tricarbonate-terminated P3HT macroinitiator. UV-Vis spectroscopy demonstrated no appreciable change in the absorption spectrum of the BCP, both in solution and thin film, when compared to the P3HT homopolymer spectrum, signifying that incorporation of the P4VP segment did not decrease the effective conjugation length of the P3HT segment or disrupt π-π stacking between P3HT chains. However, the presence of the insulating P4VP segment did result in a decrease in the measured field-effect mobility. The researchers then synthesized CdSe quantum dots capped with pyridine ligands with an approximate diameter of 4 nm, as determined from TEM. Solution UV-Vis spectroscopy of a 50 wt% CdSe in P3HT-*b*-P4VP blend showed absorption maxima at 480 nm, corresponding to the diblock copolymer, and 580 nm, corresponding to the CdSe quantum dots, with no additional absorption peaks. These results indicate that there is no charge transport between the BCP and the quantum dots in the ground state. Furthermore, solution fluorescence spectroscopy measurements showed increasing PL quenching with the addition of increasing amounts of CdSe quantum dots as a result of charge transfer events between the P3HT donor segment in the BCP and the CdSe acceptor. While hybrid devices were fabricated, they demonstrated very low PCEs, likely due to the presence of the insulating pyridine-capping ligands on the CdSe quantum dots.

In the same year, Su and coworkers used blends of a rod-coil BCP composed of P3HT and poly(2-vinylpyridine) (P3HT-*b*-P2VP) and nicotinic acid (NA)-modified TiO_2

as the active layer in hybrid solar cells.[249] To synthesize the rod-coil BCP, P3HT with a weight-average molecular weight (M_w) of 7 kDa was used as a macroinitiator for the anionic polymerization of 2-vinylpyridine.[144] By varying the wt% of P3HT in the resulting BCP, nanoscale morphologies ranging from spherical ($wt\%_{P3HT}$ = 14) to cylindrical ($wt\%_{P3HT}$ = 25) to lamellar ($wt\%_{P3HT}$ = 41) and fibrillar ($wt\%_{P3HT}$ = 60) could be achieved. Using TEM, the researchers observed that the addition of 40 wt% NA-modified TiO_2 to pure P3HT resulted in microscale separation of the polar TiO_2 NPs and the hydrophobic polymer. Conversely, in the P3HT-*b*-P2VP BCP, the TiO_2 nanoparticles were preferentially confined within the P2VP domains. However, the addition of 40 wt% TiO_2 NPs, which was previously shown as the amount of TiO_2 required to form continuous pathways in polymer-nanoparticle hybrid materials,[250] disrupted the nanoscale morphology of the self-assembled block copolymers, with the exception of the spherical copolymer, which exhibited the largest domain size (d = 30 nm). The lamellar copolymer, (d = 15 nm) could accommodate 10 wt% TiO_2 NPs and the cylindrical copolymer (d = 23 nm) could accommodate up to 20 wt% TiO_2 NPs before loss of the self-assembled structure. Hybrid device based on the P3HT-*b*-P2VP BCP exhibited over a 30-fold improvement in PCE compared to the corresponding 30:70 wt% P3HT:P2VP blend, although the PCEs were very low (η = 0.06% for P3HT-*b*-P2VP with 50 wt% TiO_2). Still, this study demonstrates proof-of-concept for utilizing BCPs to improve the morphology of hybrid polymer-inorganic solar cells.

In 2013, Chen and coworkers described the use of a semiconducting rod-coil block copolymer, P3HT-*b*-poly(ethylene glycol) (PEG), to fabricate hybrid solar cells with ZnO nanoparticles.[244] The interest in PEG stems from the compatibility with ZnO NPs *via* interaction between the oxygen atoms in the PEG backbone and the polar ZnO surface. XRD and UV-Vis spectroscopy studies indicated that the PEG segments in the

BCP chain did not impede crystallization and interchain aggregation of P3HT. In fact, thermal annealing of a composite film of P3HT-*b*-PEG:ZnO (1:2 w/w ratio) demonstrated increased polymer aggregation, while a composite film of P3HT:ZnO showed no appreciable change in aggregation. This suggests that the presence of PEG segments leads to higher ordering of the P3HT domain. Compared to pristine films of P3HT and P3HT-*b*-PEO, composite films with the ZnO NPs showed strong PL quenching even before annealing at 120 °C, after which nearly quantitative PL quenching was observed in the hybrid films. In order to gain insight into the morphology of the blend films, the researchers utilized AFM and TEM, both of which demonstrated that, upon annealing, the P3HT-*b*-PEO:ZnO composite film demonstrated improved dispersion and less agglomeration of the ZnO NPs within the polymer matrix, driven by self-assembly of the block copolymer and strong association of the ZnO NPs with the PEG chains. Comparatively, TEM images of the P3HT:ZnO hybrid film showed unfavorably large domains of pure polymer accompanied by clusters of ZnO NPs, which would limit exciton diffusion to a polymer-ZnO interfaces, lowering free charge carrier generation. Fabrication of BHJ hybrid solar cells using the P3HT-*b*-PEO:ZnO as the active layer led to a best PCE of η = 0.21% before annealing, which improved to η = 0.49% upon thermal treatment. Hybrid BHJ devices made from the P3HT:ZnO blend film yield PCEs of η = 0.18% for the unannealed film, and η = 0.24% for the annealed films, demonstrating that self-assembly of the block copolymer, and the resultant formation of well-dispersed ZnO NP domains, led to more efficient device performance.

With all of this in mind, donor-acceptor BCPs containing terthiophene (Ter) donor moieties and PEG-like chains attached to a flexible norbornene-backbone were synthesized and characterized (see **Figure 4.5**). Electrochemical studies were used to determine the frontier molecular orbital energy levels of the donor segment in the block

copolymers. SAXS measurements were used to investigate bulk self-assembly behavior in the semiconducting BCPs, demonstrating the formation of ordered lamellar morphologies in bulk samples and suggesting the ability to make self-assembled nanostructures from the BCP materials. ZnO NPs were synthesized and characterized using TEM and photophysical methods. Solution-based PL studies were used to demonstrate charge transfer from the singlet-excited state of the Ter donor to the ZnO NP acceptors. Hybrid thin film composites of the lamellar-forming Ter-PEG BCPs and the ZnO NPs were spin-cast. Photophysical studies were used to characterize charge transfer in the self-assembled polymer-inorganic composite films, demonstrating the effects of interfacial distance and morphology on charge transfer.

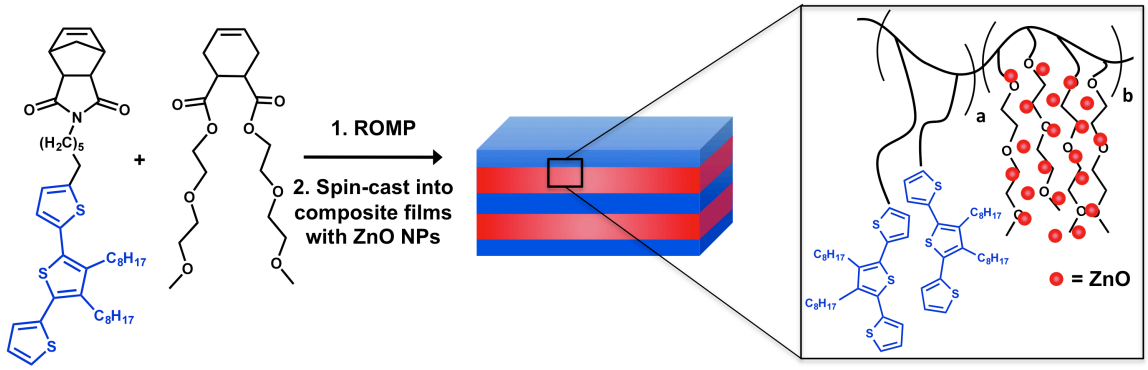

Figure 4.5. Schematic of Ter-PEG block copolymer and ZnO NPs composite films.

EXPERIMENTAL

Instrumentation

Nuclear magnetic resonance (NMR) spectroscopy was carried out on a Varian DirectDrive 400 MHz or 500 MHz spectrometer at ambient temperature and spectra were referenced internally to the residual solvent peaks. All chemical shifts are reported in ppm and coupling constants are given in Hertz (Hz). Absorption spectra were obtained on

a Varian Cary 6000i UV-Vis-NIR spectrophotometer in Starna quartz fluorimeter cells with a 1.0 cm path length. Mass spectroscopy was performed with a Micromass Autospec Ultima HRMS (for CI^+) or an Agilent 6530 Q-TOF system (for ESI^+). Elemental analysis was performed by QTI, Whitehouse, NJ (www.qtionline.com). Gel permeation chromatography (GPC) was done on an Agilent 1100 Series Instrument with Viscoteck Triple Array Detector 302 Series in THF. Thermal gravimetric analysis (TGA) was performed on TA Instruments TGA Q50 under inert N_2 atmosphere with 3.5 °C/min ramp to 500 °C and then 8.0 °C/min ramp to 800 °C. Differential scanning calorimetry (DSC) was performed on a Mettler Toledo DSC-1 instrument model. All DSC samples ranged from 5-8 mg and followed the same run procedure with a N_2 flow rate of 50 mL/min: (1) Isothermal at 30 °C for 2 min; (2) Heating from 30 °C to 100 °C at 10 °C/min to remove water and any residual solvent; (3) Isothermal at 100 °C for 2 min; (4) Cooling from 100 °C to 30 °C at 10 °C/min; (5) Isothermal at 30 °C for 2 min; (6) Heating from 30 °C to 280 °C at 10 °C/min; (7) Isothermal at 280 °C for 2 min; (8) Cooling from 280 °C to 30 °C at 10 °C/min. Fluorimetry experiments were carried out on a Photon Technology International QuantaMaster 4 spectrophotometer equipped with a 6-inch diameter K Sphere-B integrating sphere and using PTI software. All solution measurements were recorded in Starna quartz fluorimeter cells with a path length of 1.0 cm in dicholoromethane (DCM), unless otherwise noted. Small-angle X-ray scattering (SAXS) analysis was performed using Cu Kα radiation (λ = 1.5418 Å) from a Molecular Metrology instrument equipped with a high brilliance rotating copper anode source and a two-dimensional 120 mm gas-filled multiwire detector. Vertical focus was attained with a single-crystal Ge mirror, and horizontal focus and wavelength selection were acquired with an asymmetrically cut Si(111) monochromator. The beam center was calibrated using the primary reflection peak of silver behenate set at 1.076 nm^{-1}. The SAXS holder-

to-holder distance (between the front and back chambers) was 624 nm. Prior to SAXS analysis, samples were annealed at 280 °C under vacuum for 15 hours, unless otherwise noted.

Electrochemistry

Electrochemical experiments were carried out in a dry box under a N_2 atmosphere using a GPES system from Eco. Chemie B. V. All the electrochemical experiments were performed using a three-electrode cell with a $Ag/AgNO_3$ reference electrode (silver wire in a 0.01 M silver nitrate solution with 0.1 M $[(n\text{-}Bu)_4N]^+[PF_6]^-$ ($TBAPF_6$) in acetonitrile), a 1.6 mm Pt button working electrode, and a Pt wire coil counter electrode. All measured potentials were referenced to the ferrocene/ferrocenium redox couple (Fc/Fc^+) as determined by the average $E_{1/2}$ value obtained before and after the experiment. The supporting electrolyte used was 0.1 M tetrabutylammonium hexafluorophosphate ($TBAPF_6$), which was purified by three successive recrystallizations from hot ethanol and dried for three days at 100-150 °C under high vacuum before use. All measurements were carried out in DCM with scan rate of 100 mVs^{-1}. The HOMO and LUMO energy levels were found from the onset of oxidation and reduction using **Equations 2.1**, **2.2** (see **Chapter 2**).

Synthesis

General Considerations

Air- and/or moisture-sensitive reactions were carried out in heat-gun-dried glassware using standard Schlenk techniques under a dry N_2 atmosphere. Dry solvents were collected in solvent bulbs from an Innovative Technology PureSolv 400 solvent purification system and stored over 3Å molecular sieves. All chemicals were used as received from commercial suppliers unless otherwise specified. Thin layer

chromatography (TLC) was performed using Silicycle silica gel 60 F_{254} pre-coated aluminum sheets. Column chromatography was performed using Silicycle Silica Flash® F60.

Synthesis of PEG Monomer [4.1] and ZnO nanoparticles

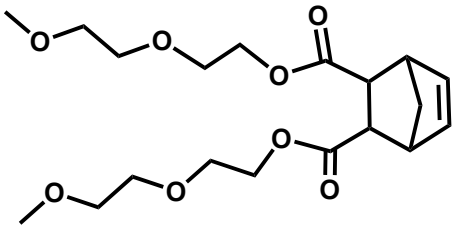

bis(2-(2-methoxyethoxy)ethyl) cyclohex-4-ene-1,2-dicarboxylate [4.1]: 5-norbornene-2,3-dicarboxylic anhydride (compound **2.7**) (1.45 g, 8.86 mmol), Mukaiyama's reagent (2.72 g, 10.6 mmol), and 4-dimethylaminopyridine (DMAP) (0.435 g, 3.5 mmol) were added to a 50-mL round-bottomed flask equipped with a reflux condenser under N_2 and cycled 3x under high vacuum before dissolving in dry DCM (25 mL). Diethylene glycol monomethyl ether (2.3 mL, 2.34 g, 19.5 mmol) and dry Et_3N (3.7 mL, 2.69 g, 26.6 mmol) were added to the reaction vessel. The reaction was heated to 40 °C overnight under a N_2 atmosphere. Upon completion, the reaction mixture had gone from a bright yellow suspension to an orange heterogeneous solution. The reaction mixture was cooled to room temperature, diluted with DCM (20 mL), and poured into DI H_2O (200 mL). The solution was transferred to a separatory funnel and the aqueous phase was extracted with DCM (2 x 100 mL). The combined organic phases were washed with 1M HCl (2 x 50 mL), DI H_2O (2 x 150 mL), and brine (1 x 150 mL), and dried over $MgSO_4$. The filtered solution was concentrated *in vacuo* and the crude product was purified by silica gel column chromatography (2% MeOH/DCM) to afford a light yellow oil (3.18 g, 93%). ^{1}H NMR (400 MHz, $CDCl_3$) δ: 6.23 (t, 2H, J = 1.8), 4.20 (m, 2H), 4.08 (m, 2H), 3.62 (m, 8H), 3.52 (m, 4H), 3.36 (s, 6H), 3.30 (t, 2H, J = 1.6), 3.15 (m, 2H),

1.44 (dt, 1H, J = 8.7, 1.8), 1.34 (d, 1H, J = 8.6). ^{13}C {^{1}H} NMR (100 MHz, $CDCl_3$) δ: 172.34, 134.85, 71.81, 70.31, 69.07, 63.34, 58.99, 48.56, 46.31. HRMS (ESI): calcd for $C_{19}H_{30}O_8$ *m/z* 409.1833, found 409.1837 (M^+ Na).

ZnO nanoparticle synthesis: Zinc acetate dihydrate ($Zn(OAc)_2$•$2H_2O$, 2.95 g, 13.4 mmol) was dissolved in MeOH (125 mL) and heated to 60 °C with vigorous stirring in a three-neck round-bottomed flask equipped with a reflux condenser open to air and a 125-mL addition funnel. KOH (1.49 g, 26.5 mmol) was dissolved in MeOH (70 mL) and added dropwise to the stirring $Zn(OAc)_2$•$2H_2O$ solution over 15 mins at 60 °C, during which the solution went from clear to milky, opaque white. After 30 mins of stirring at 60 °C, the solution had become clear again. Over the next 6 hrs, the reaction solution slowly went from clear, to turbid, to white and opaque, after which the reaction was cooled to room temperature. The solution was transferred to test tubes and centrifuged for 15 mins. The MeOH was decanted off and the white gel-like solid was redissolved in fresh MeOH with stirring and sonication (5 min). This new suspension was centrifuged for 10 mins and then the above procedure was repeated (2x). After the final centrifugation step, the ZnO NPs were redissolved in CB or $CHCl_3$ (11 mL). In order to get the concentration of the sol, a small aliquot of known volume was concentrated to dryness and massed. Assuming homogeneity of the sol, the concentration could be calculated as 70.8 mg/mL.

General Polymerizations Methods:

All polymerizations were carried out in small glass vials with Teflon-lined lids in a glovebox under N_2 atmosphere in dry DCM using Grubbs' 2nd Generation (G2) catalyst. The amount of G2 used was determined by the desired molecular weight of the resultant homopolymer or copolymer materials using **Equation 2.3** (see **Chapter 2**). Homopolymerizations were terminated with ~2 mL ethyl vinyl ether upon removal from

the glovebox. The polymer solutions were then concentrated *in vacuo* and purified *via* precipitation into either Et_2O or hexanes from DCM (3x).

All block copolymers (BCPs) contain equimolar ratios of the donor block (the norbornene polymer with Ter pendant groups) and the Lewis-basic block (the norbornene polymer with PEG pendant groups) unless otherwise noted. BCPs were synthesized starting with polymerization of the Ter block with G2 and monitoring by TLC until complete consumption of the donor monomer (**2.13**). Then, the polyethylene glycol monomer (**4.1**) was added to the stirring polymerization solution. Upon complete consumption of the Lewis-basic monomer, as determined by TLC, the copolymers were removed from the glovebox and terminated with excess ethyl vinyl ether. Random copolymers (RCP) were synthesized for comparison by adding both monomers at the same time and polymerizing with G2 until complete consumption of the monomeric materials, as determined by TLC. The polymer solutions were concentrated *in vacuo* and purified *via* precipitation into hexanes or Et_2O (3x) from small amounts of DCM (~2 mL).

All polymers were characterized by ^{1}H NMR ($CDCl_3$), GPC (THF), DSC, and TGA, unless otherwise noted. Polydispersity ($Đ$) was determined using GPC. ^{1}H NMR indicates inclusion of both monomers into the RCPs and BCPs in close to the theoretical 1:1 molar ratio of the two blocks.

Polymerization of PEG homopolymers and Ter-PEG Copolymers [P4.1 – P4.4]

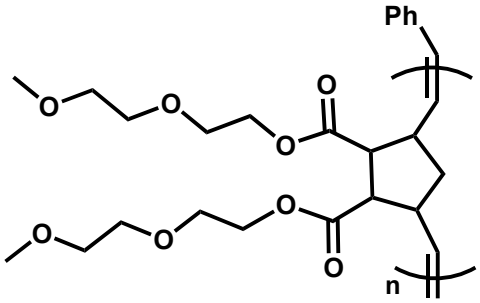

Poly(bis(2-(2-methoxyethoxy)ethyl)cyclohex-4-ene-1,2-dicarboxylate [P4.1]: ^{1}H NMR (representative homopolymer, 400 MHz, $CDCl_3$) all signals broad singlets unless otherwise stated, δ: 5.53-5.30 (broad d, 2H), 4.28 (2H), 4.10 (2H), 3.65-3.59 (broad d, 8H), 3.51 (4H), 3.39 (6H), 3.16 (3H), 2.96 (1H), 1.95 (2H).

Table 4.1. Molecular weight characterization of PEG homopolymers (**P4.1** series).

Polymer	***[M]/[I]*[a]**	**M_n(GPC)[b] (kg/mol)**	**M_n (theoretical)[c] (kg/mol)**	**$Đ$[b]**
P4.1a	25	12.8	9.7	1.22
P4.1b	50	23.6	19.3	1.09
P4.1b-2	50	32.6	19.3	1.23
P4.1c	100	36.1	38.6	1.16
P4.1d	130	79.0	50.2	1.28
P4.1e	200	57.3	77.3	1.06

[a][M]/[I] indicates the initial molar ratio of **4.1** *([M])* to G2 catalyst (*[I]*). Assuming complete conversion, $[M]/[I] = N_n$; [b]Determined from GPC in THF, calibrated with polystyrene standards; [c]Theoretical molecular weights calculated from $M_n = N_n$ x 386.44 g/mol (**4.1** molecular weight), assuming 100% conversion.

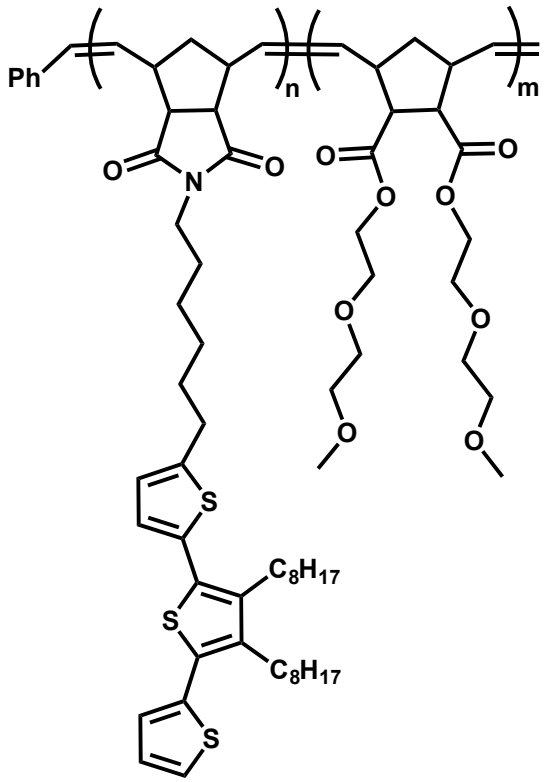

Poly(2-(6-(3',4'-dioctyl-[2,2':5',2''-terthiophen]-5-yl)hexyl)isoindoline-1,3-dione)-*block*-Poly(bis(2-(2-methoxyethoxy)ethyl)cyclohex-4-ene-1,2-dicarboxylate (Ter-*b*-PEG) [P4.2]: ^{1}H NMR (400 MHz, $CDCl_3$) all signals broad singlets, δ: 7.24 (1H), 7.07 (1H), 7.00 (1H), 6.88 (1H), 6.66 (1H), 5.67-5.28 (broad m, 4H), 4.29 (2H), 4.12 (2H), 3.67-3.52 (overlapping signals, 12H), 3.36 (8H), 3.14 (6H), 2.85 (2H), 2.74 (2H), 2.63 (2H), 2.08-1.88 (broad m, 3H), 1.63-1.52 (broad m, 9H), 1.36-1.25 (broad m, 26H), 0.86 (6H).

Poly(2-(6-(3',4'-dioctyl-[2,2':5',2''-terthiophen]-5-yl)hexyl)isoindoline-1,3-dione)-*random*-Poly(bis(2-(2-methoxyethoxy)ethyl)cyclohex-4-ene-1,2-dicarboxylate (Ter-*r*-PEG) [P4.3]: ^{1}H NMR (400 MHz, $CDCl_3$) all signals broad singlets, δ: 7.26 (1H), 7.08 (1H), 7.02 (1H), 6.89 (1H), 6.68 (1H), 5.64-5.28 (broad m, 4H), 4.40-4.00 (4H),

3.67-3.45 (overlapping signals, 18H), 3.35 (6H), 3.16 (6H), 2.76 (2H), 2.64 (2H), 1.64 (3H), 1.52 (7H), 1.36-1.25 (broad m, 26H), 0.85 (6H).

Table 4.2. Symmetric mole ratio Ter-PEG copolymers.

Polymer	***[M]/[I]*[a]**	**N_n[b]**	**M_n(GPC)[c] (kg/mol)**	**M_n (theoretical)[d] (kg/mol)**	**$Đ$[c]**
P4.2a	25	50	61.6	27.6	1.15
P4.2a-2	25	50	59.6	27.6	1.11
P4.2b	50	100	104.3	55.2	1.26
P4.2b-2	50	100	90.1	55.2	1.11
P4.2c	75	150	126.4	82.8	1.18
P4.2d	177	354	273.9	110.4	1.24
P4.3	50	50	78.2	55.2	1.26

[a]*[M]/[I]* indicates the initial molar ratio of **2.13** (*[M]*) to G2 catalyst (*[I]*). Assuming complete conversion, $[M]/[I] = N_n$ (per block); [b]N_n describes the overall degree of polymerization; [c]Determined from GPC in THF, calibrated with polystyrene standards; [d]Theoretical molecular weights calculated using $M_n = N_{n,\,Ter}(MW_{Ter}) + N_{n,\,PEG}\,(MW_{PEG})$ for block copolymers, assuming 100% conversion and living polymerization conditions. For random copolymer, $M_n = N_n(MW_{Ter} + MW_{PEG})/2$; MW_{Ter} = 718.13 g/mol and MW_{PEG} = 386.44 g/mol.

Table 4.3. Asymmetric mole ratio Ter-PEG copolymers.

Polymer	$[M]_{Ter}/[I]$[a]	$[M]_{PEG}/[I]$[a]	N_n[b]	M_n(GPC)[c] (kg/mol)	M_n (theoretical)[d] (kg/mol)	$Đ$[c]	*mol% Ter*[e]	*wt% Ter*[e]
P4.4a	25	12.5	37	37.1	22.7	1.30	60	74
P4.4b	25	8.1	33	69.1	21.0	1.22	70	81
P4.4c[f]	89	25	114	115.8	73.6	1.15	76	85
P4.4d[f]	60	30	90	54.7	69.6	1.15	72	83
P4.4e[f]	45	15	60	38.1	63.6	1.10	64	77

[a]*[M]/[I]* indicates the initial molar ratio of monomer (*[M]*) to G2 catalyst (*[I]*). Assuming complete conversion, $[M]/[I] = N_n$ (of that block); [b]N_n describes the theoretical overall degree of polymerization; [c]Determined from GPC in THF, calibrated with polystyrene standards; [d]Theoretical molecular weights calculated using $M_n = N_{n,\,Ter}(MW_{Ter}) + N_{n,\,PEG}\,(MW_{PEG})$ for block copolymers, assuming 100% conversion and living polymerization conditions. MW_{Ter} = 718.13 g/mol and MW_{PEG} = 386.44 g/mol; [e]Determined from ^{1}H NMR integrations; [f]For these block copolymers, the PEG monomer (**4.1**) was polymerized first. Upon complete consumption of **4.1**, the Ter monomer (**2.13**) was added.

RESULTS AND DISCUSSION

Synthesis

The poly(ethylene glycol) (PEG) monomer (**4.1**) was synthesized following modified literature procedures.[251,252] Compound **4.1** can be made in a one-pot esterification reaction (**Scheme 4.1**). In the first step of the reaction, DMAP activates the anhydride carbonyl towards nucleophilic attack by the weak nucleophilic alcohol, diethylene glycol monomethyl ether (PEG-OH) by activating, to ring open the norbornene dione anhydride (compound **2.7**), forming the intermediate acid-ester derivative. In the subsequent reaction step, Mukaiyama's reagent is utilized to activate the hydroxyl group of the formed carboxylic acid towards nucleophilic attack by a second equivalent of PEG-OH.[253] This reaction sequence results in the desired monomeric compound in high yield.

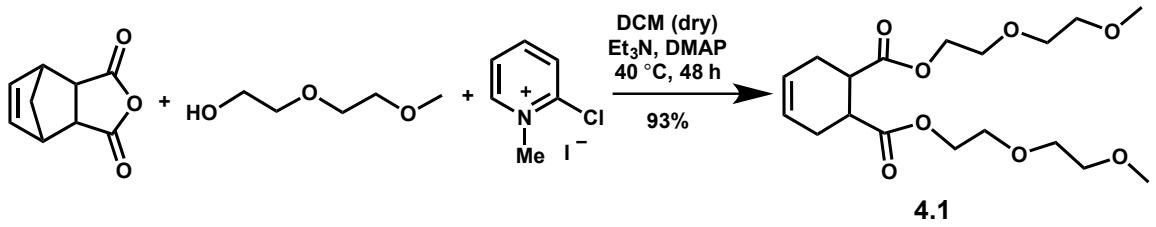

Scheme 4.1. Synthetic route for PEG monomer **4.1**.

Polymerization

The PEG monomer (**4.1**) was polymerized by ROMP using G2 in DCM under N_2 atmosphere to yield a series of corresponding homopolymers with different molecular weights. The good solubility of the monomer and resulting homopolymers in common organic solvents allowed for characterization by ^{1}H NMR and GPC. Molecular weight characterization of the PEG homopolymer series is given in **Table 4.1**. The polymerization of the PEG monomer was shown to be living, with the number-average molecular weight (M_n) of the homopolymer tracking linearly with ratio of monomer to catalyst added, as shown in **Figure 4.6**.

TGA plots of two representative samples of the PEG homopolymers (**P4.1b-2, P4.1d**) are also shown in **Figure 4.6**. Both homopolymer samples show good thermal stability under N_2, with onset degradation temperatures (T_{onset}) above 300 °C. Interestingly, there appears to be an initial loss of approximately 20 wt% for both polymer samples at 110 °C for **P4.1b-2 (50)** and 96 °C for **P4.1d (177)**. This initial mass loss occurs over a temperature range of approximately 200 °C, and is followed by a more significant thermal degradation, corresponding to approximately 60 wt% of the polymer samples, at 325 °C for **P4.1b-2 (50)** and 318 °C for **P4.1d (177)**. The second thermal degradation occurs over a smaller temperature range of approximately 100 °C. It is possible that the first thermal degradation corresponds to trapped water or solvent in the

polymer chains. The high thermal stability of the PEG homopolymers is desirable, not only for thermal annealing purposes, but also for potential metallation and processing techniques that would allow for applications in hybrid optoelectronics.

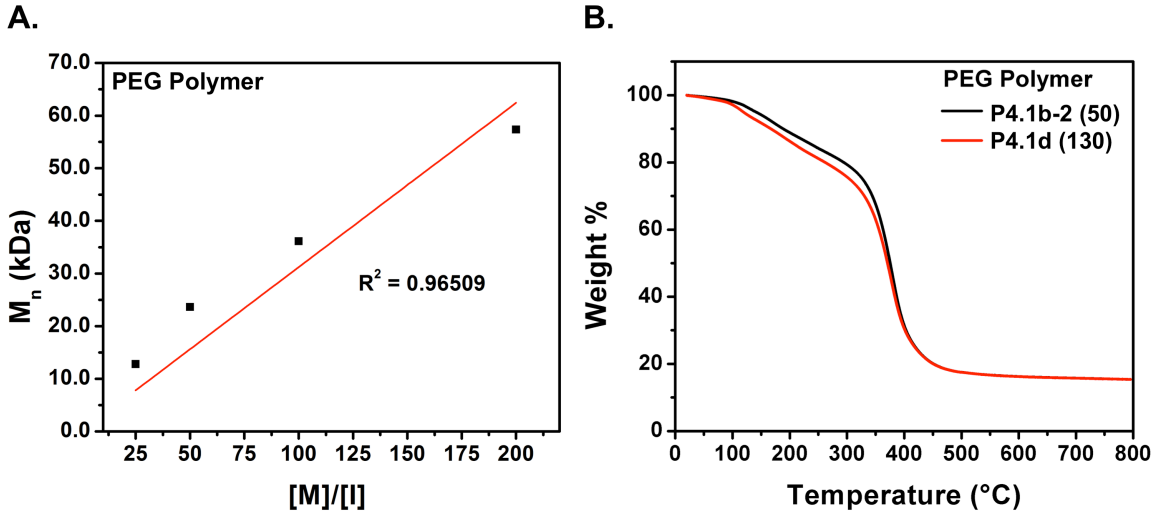

Figure 4.6. (A) Living polymerization plot (M_n vs. *[M]/[I]*) for homopolymerization of PEG monomer **4.1**, where M_n represents the number-average molecular weight as determined by GPC in THF and *[M]/[I]* represents the molar ratio of monomer to G2 catalyst added; (B) TGA plots showing thermal degradation profiles of representative PEG polymers: **P4.1b-2 (50)** (black line), T_{onset} = 325 °C; **P4.1d (177)** (red line), T_{onset} = 318 °C. N_n of PEG homopolymers denoted in parentheses

Copolymerizations were carried out using ROMP with G2 in DCM under an inert atmosphere to synthesize functional BCPs comprised of a Ter donor block with a Lewis-basic PEG block. A random copolymer (RCP) was also synthesized for comparison. These copolymer materials contain equimolar ratios of the two blocks, as verified by ^{1}H NMR, but have different block lengths as a consequence of the *[M]/[I]* ratio used, and thus different overall molecular weights. **Table 4.2** summarizes the molecular weight characterization of the symmetric Ter-PEG copolymer series. For all of copolymers, the calculated theoretical molecular weight is lower than that determined by GPC using

polystyrene standards. This is likely due, in part, to aggregation of the amphiphilic copolymers. It is possible that the copolymers form micellular structures in THF as a result of the covalent tether between the hydrophobic Ter block and the hydrophilic PEG block, leading to an increased hydrodynamic radius and slightly overestimated molecular weights.[167] Interestingly, the BCPs show larger error between the measured M_n value and the calculated theoretical M_n, lending support to micelle formation affecting the hydrodynamic radius in the GPC measurements.

TGA of representative samples of the Ter-PEG RCP and BCPs exhibit high thermal stability ≥ 350 °C for all samples (see **Figure 4.7**). All the copolymer materials show almost complete thermal degradation after approximately 350 °C, with mass losses between 80-85 wt%. The incorporation of the PEG polymer into the copolymer materials improves the thermal stability, increasing the thermal degradation temperature by close to 25 °C. Representative DSC analysis (see **Figure 4.8**) of the Ter-PEG RCP (**P4.3**) shows a small glass transition with onset at T_g = 119 °C. For the Ter-PEG BCP **P4.2b (50)**, the DSC trace shows two T_g's with onsets at 99 °C and 119 °C (see **Figure 4.8**). The presence of two T_g's for the BCP suggests the presence of two distinct domains. Due to the amphiphilic nature of the Ter-PEG copolymer materials, it is likely that the Flory-Huggins interaction parameter is very high, favoring self-segregation in the Ter-PEG block copolymers.[63]

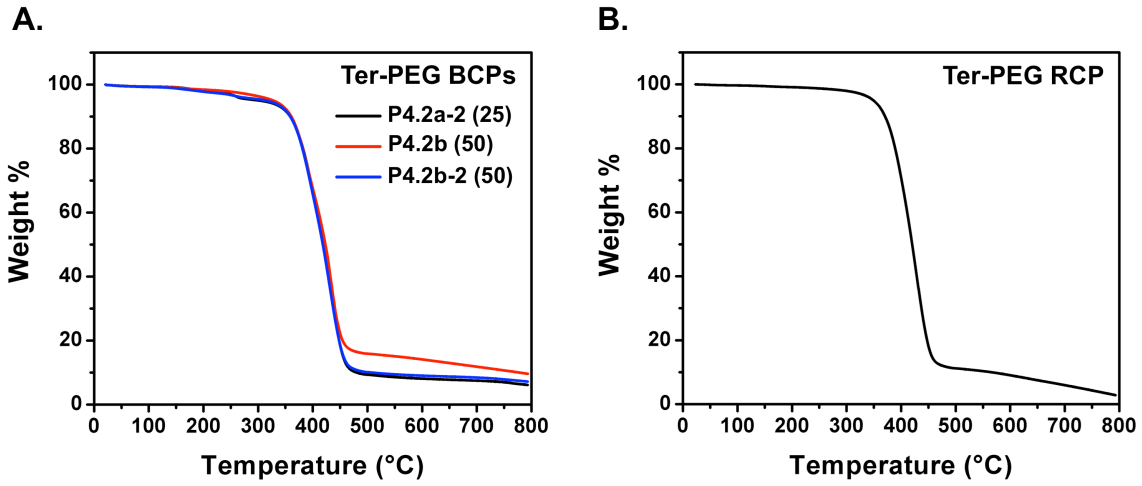

Figure 4.7. TGA plots showing thermal degradation profiles of (A) representative Ter-PEG BCPs: **P4.2a-2 (25)** (black), T_{onset} = 360 °C; **P4.2b (50)** (red), T_{onset} = 350 °C; **P4.2b-2 (50)** (blue), T_{onset} = 360 °C; (B) Ter-PEG RCP **P4.3**, T_{onset} = 358 °C. Block lengths of Ter-PEG BCPs denoted in parentheses.

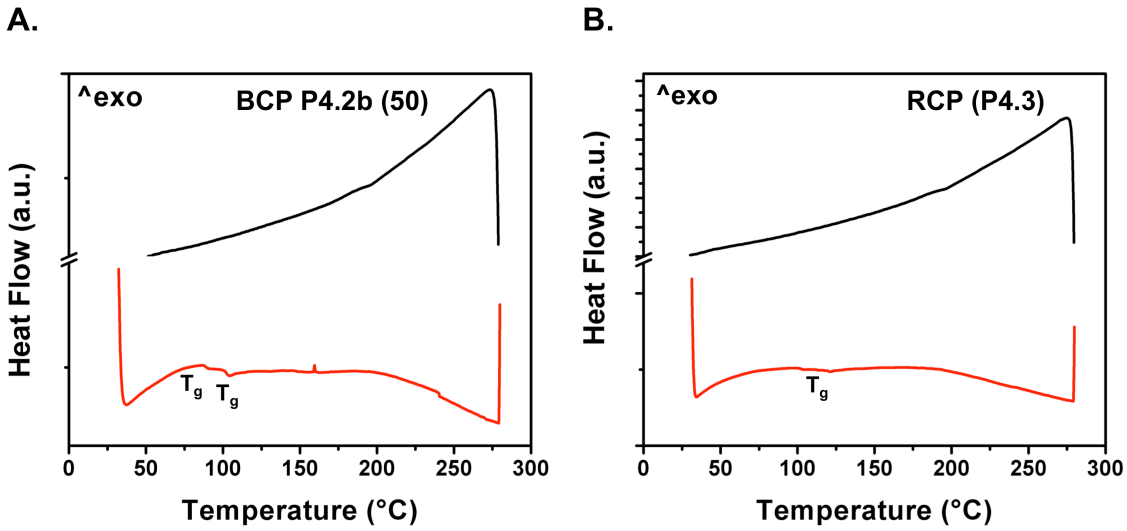

Figure 4.8. DSC traces for Ter-PEG copolymer materials (black line shows heating cycle, red line shows cooling cycle): (A) **P4.2b (50)**; (B) **P4.3**. Block lengths of Ter-PEG BCPs denoted in parentheses.

Photophysical and Electrochemical Characterization

The UV-Vis absorption spectra of the Ter-PEG RCP and BCP materials are shown in **Figure 4.9A**. For both materials, the UV-Vis absorption spectrum mirrors the absorption profile of the Ter homopolymer (**P2.1**), with λ_{max} = 342 nm. The PEG monomer (**4.1**) and polymer (**P4.1**) have no apparent absorption in the visible region of the solar spectrum. In both the RCP and BCP systems, the distinct absorption corresponding to the Ter chromophore suggests that there is minimal interaction between the PEG and Ter units in the ground state. Furthermore, the absorption of the Ter-PEG BCPs is independent of molecular weight (i.e. block length) of the copolymer materials. From the red edge of the absorption profiles (between 414 nm and 416 nm for all the Ter-PEG copolymers studied), the average optical band gap for the Ter-PEG copolymer materials was calculated as 2.98 eV. This matches well with the previously determined band gap for the Ter homopolymers (**P2.1**) of 2.90 eV. The slightly increased band gap for the Ter-PEG copolymer materials is due to the presence of the insulating PEG chains, and similar band gap enlargement was observed for diblock copolymers composed of P3HT and P4VP.[248]

The excitation and emission profiles of the Ter-PEG copolymer series (**P4.2** – **P4.3**) correspond well to the excitation and emission spectra of the Ter homopolymer and demonstrate excitation and emission maxima that are independent of block length, with λ_{ex} = 340 nm and λ_{em} = 442 nm (see **Figure 4.9B**). Again, the PEG monomer and polymer materials have no apparent excitation or emission in the UV-visible region. The excitation profiles of the Ter-PEG copolymers demonstrate the same bathochromic shift as the Ter homopolymer in comparison to the Ter monomer excitation profile. While the Ter polymer emission shows a distinct red shoulder (λ = 475 nm) compared to the Ter monomer emission, the Ter-PEG copolymer materials show varying intensities of this

shoulder in their respective emission profiles. The Ter-PEG RCP (**P4.3**) has an emission profile that most closely mimics that of the Ter monomer, with a blue shoulder appearing at higher wavelengths than the maximum emission and only very slight red-edge broadening. Conversely, the Ter-PEG BCPs (**P4.2a – P4.2d**) have emission profiles that more-closely match that of the Ter homopolymer. While the emission profiles still show a slight blue shoulder compared to the Ter polymer emission, the Ter-PEG BCPs also display clearly enhanced red shoulders compared to the Ter monomer. If the red shoulder indicates aggregation induced by π-π interactions between the conjugated Ter semiconductors in the homopolymer, it is not surprising that the Ter-PEG RCP demonstrates the least aggregation behavior, lending support to the idea that in the RCP the Ter and PEG repeat units are in an alternating or semi-alternating arrangement along the polymer chain. The decreased red shoulder (red-edge) broadening in the Ter-PEG BCP series compared to the Ter homopolymer is not necessarily surprising either, as the PEG chains in the block copolymer may change the solubility of the material and disrupt interactions between adjacent Ter moieties along a polymer chain (*via* intra-chain interactions), as well as those between neighboring chains (inter-chain interactions). It is also possible that the BCP materials adopt a quasi-micellular structure in solution, leading to disruption of the π-π interactions between Ter moieties owing to partial contraction of the polymer backbone. This is very similar to what is observed in the PDI homopolymers when the polymer backbone is poorly solubilized, leading to polymer agglomeration that disrupts H-aggregation. Overall, these effects are small, and it appears that copolymerization with the PEG monomer does not significantly change the Ter fluorophore photophysics.

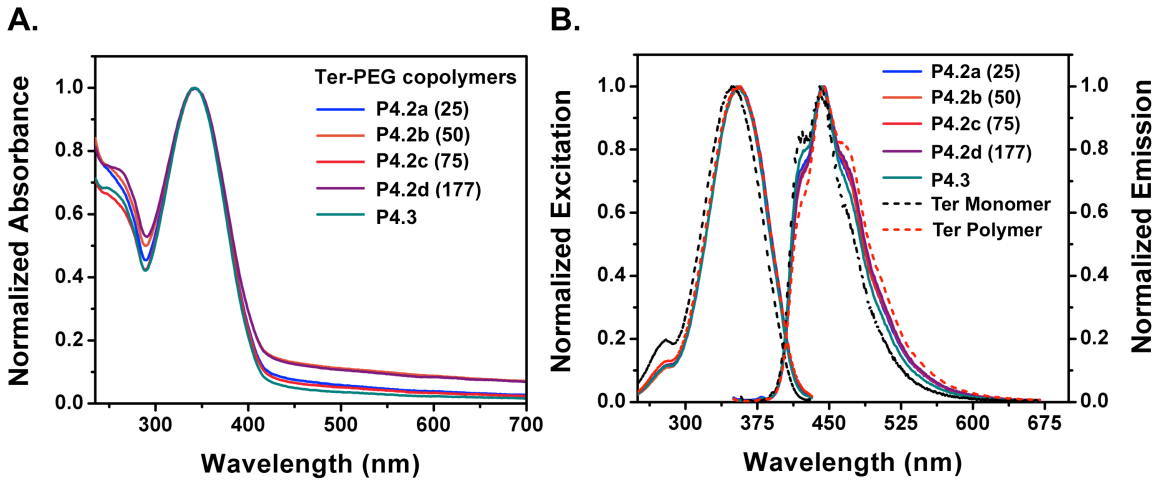

Figure 4.9. (A) Normalized UV-Vis absorption spectra for the symmetric Ter-PEG BCP series (**P4.2a – P4.2d**) and Ter-PEG RCP (**P4.3**), demonstrating that λ_{max} is not affected by the molecular weight (i.e. block length) of the copolymer materials (λ_{max} = 342 nm); (B) Excitation and emission spectra for the Ter-PEG BCPs and RCP, demonstrating that λ_{ex} and λ_{em} are independent of the molecular weight (λ_{ex} = 340 nm, λ_{em} = 442 nm). Ter monomer (**2.13**, black dotted line) and Ter polymer (**P2.1**, red dotted line) are shown for comparison.

The electrochemical behavior of the Ter-PEG copolymers was studied using cyclic voltammetry (CV). The CV curves show distinct oxidation events corresponding to the oxidation of the Ter donor moieties, with onsets of oxidation matching those observed in the Ter homopolymer (see **Figure 4.10** and **Figure 4.11**). The PEG monomer and representative homopolymers show no significant electrochemical behavior (see **Figure 4.12**).

Electrochemical studies of the Ter-PEG BCPs show that the onset of oxidation, and consequently the HOMO energy level, does not change significantly with increasing block length in the copolymers. Representative samples of the Ter-PEG BCP series show oxidation events corresponding to oxidation of the Ter moiety, with onsets at 0.39 V vs. Fc/Fc^+ for **P4.2a-2 (25)** and **P4.2b-2 (50),** and 0.38V vs. Fc/Fc^+ for **P4.2d (177)**. The

electrochemical profile of the Ter-PEG RCP (**P4.3**) is similar, with the onset of the Ter oxidation event occurring at 0.38V vs. Fc/Fc^+. These onsets of oxidation were used to calculate an average HOMO energy level of -5.19 eV for the Ter-PEG BCP materials and -5.18 eV for the Ter-PEG RCP. The LUMO energy level was then calculated from the optical band gap and HOMO energy level to be -2.20 eV. This matches well with the molecular orbital energy levels determined previously for the Ter homopolymers (HOMO = -5.15 eV, LUMO = -2.25 eV) (**P2.1**).

While comparison of the onsets of oxidation show no significant change between the Ter-PEG BCPs and RCP, the oxidation peak potential does change. For the smaller (lower M_n) BCPs (**P4.2a-2** and **P4.2b-2**), the CV scans only show one oxidation potential centered at 0.58V vs. Fc/Fc^+ for **P4.2a-2** and 0.63V vs. Fc/Fc^+ for **P4.2b-2**. In the larger (higher M_n) BCP (**P4.2d**), the peak oxidation potential is centered at 0.82 V vs. Fc/Fc^+, with a small shoulder at 0.64 V vs. Fc/Fc^+. The RCP (**P4.3**) also exhibits two peak oxidation potentials (0.60 V vs. Fc/Fc^+ and 0.82 V vs. Fc/Fc^+). These two oxidation events can be seen in the Ter homopolymer series (see **Figure 2.10**), and Ter polymer **P2.1a-2** (25 repeat units) is shown for comparison in **Figure 4.10**. Interestingly, in the Ter homopolymer series, the intensities of the peak oxidation potentials change with M_n, with the second oxidation event (centered at 0.80 V vs. Fc/Fc^+) increasing in intensity with increasing number of repeat units. It is possible that this second oxidation event is indicative of bipolaron formation, which would be more easily stabilized on the larger polymer materials. The largest Ter-PEG BCP, containing an average of 177 repeat units of Ter per chain, shows a large increase in intensity of the oxidation peak centered at 0.82 V vs. Fc/Fc^+. This indicates that this material may be able to more easily stabilize multiple oxidized charges due to the block length. Also interesting is the fact that the smaller BCPs do not demonstrate this two-peak oxidation profile, while the RCP does to

a lesser extent. The reason for this is still under study. It is possible that the smaller oxidation window used to prevent oxidative decomposition during the CV of **P4.2a-2** and **P4.2b-2** prevents visualization of this second peak oxidation potential.

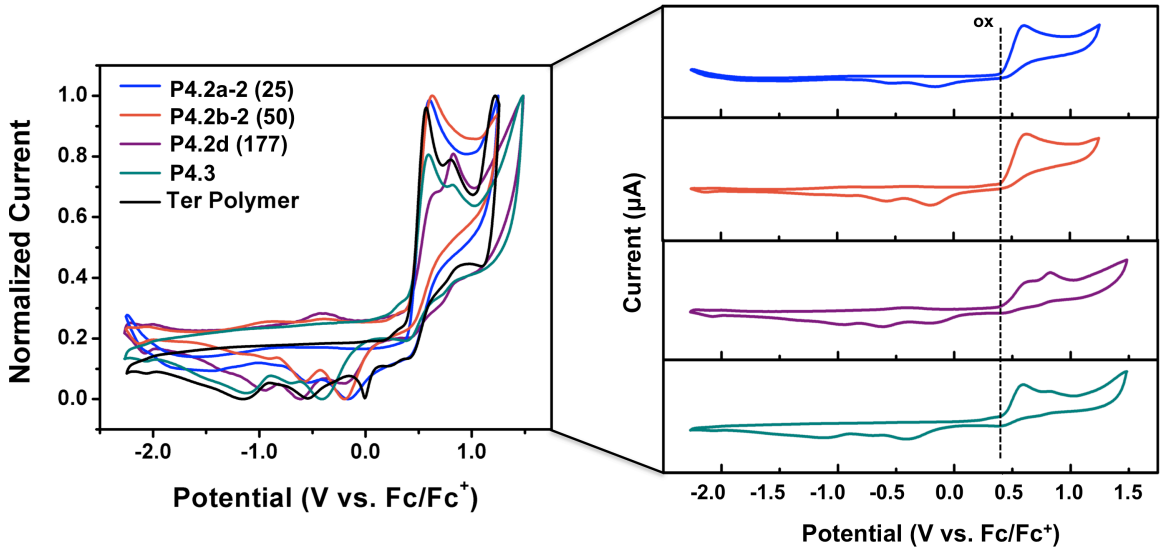

Figure 4.10. Overlay of Ter-PEG copolymer CV scans showing electrochemical behavior of representative polymers from the Ter-PEG BCP series (**P4.2a-2** – **P4.2d**), as well as Ter-PEG RCP (**P4.3**). Onsets of oxidation (shown in parentheses) are reported vs. Fc/Fc^+: **P4.2a-2** (0.39 V), **P4.2b-2** (0.39 V), **P4.2d** (0.38 V), **P4.3** (0.38 V). CV of Ter homopolymer **P2.1a-2** (black line) is shown for comparison.

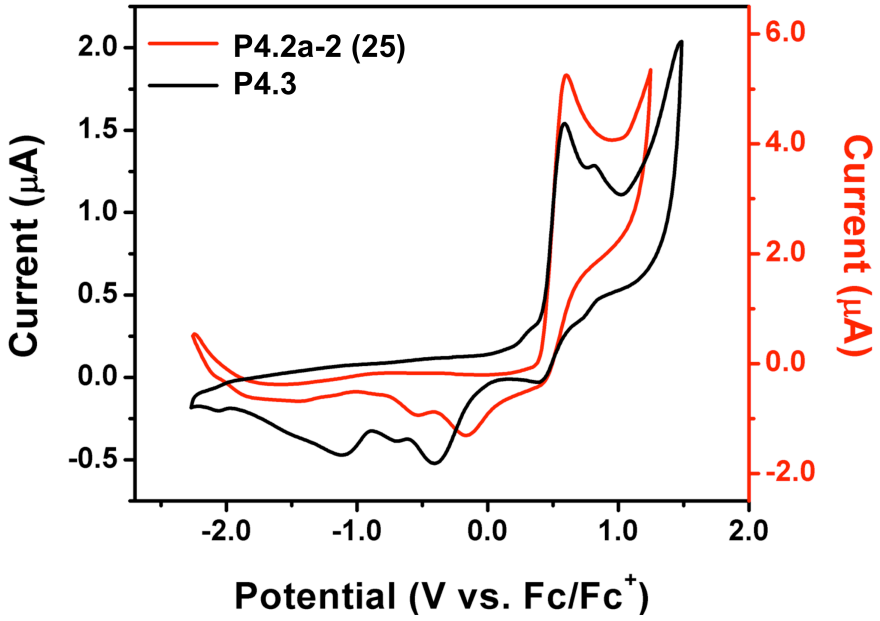

Figure 4.11. CV scans in DCM under inert atmosphere of Ter-PEG BCP **P4.2a-2 (25)** (red) and Ter-PEG RCP **P4.3** (black).

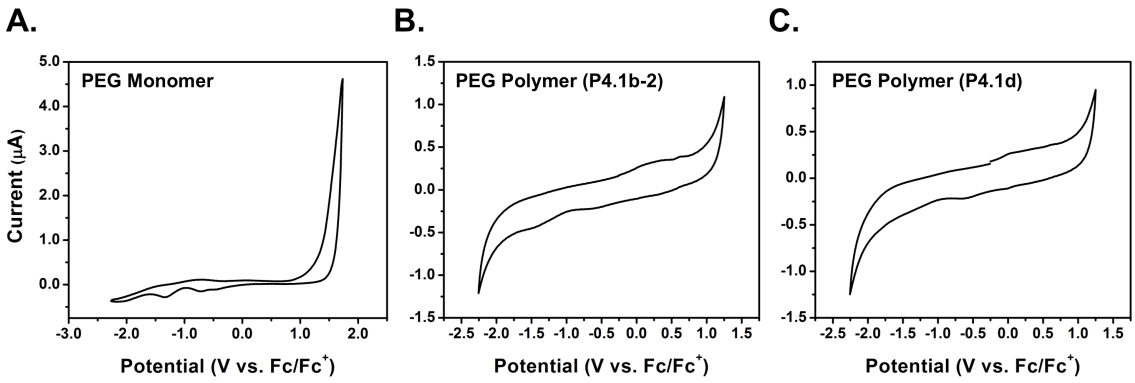

Figure 4.12. CV scans of (A) PEG monomer (**4.1**); (B) PEG homopolymer **P4.1b-2 (50)**; (C) PEG homopolymer **P4.1d (100)**, all showing no significant electrochemical behavior. N_n of the homopolymers shown in parentheses.

Small-Angle X-ray Scattering

SAXS was used to investigate the bulk self-assembly behavior of the Ter-PEG diblock copolymers. These BCPs show excellent bulk self-assembly behavior due to the

dissimilarity between the two blocks in the amphiphilic Ter-PEG BCPs. This dissimilarity increases the Flory-Huggins parameter and allows self-assembly to be achieved at lower molecular weights. It is important to note that, while the molar ratios of the two blocks are equal, it is the volume fraction that determines the resultant morphology of self-assembled BCPs. Lamellar morphologies are generally achieved for $f_A = 0.4 - 0.6$, where f_A represents the volume fraction of block A.[61] In BCPs containing crystalline blocks (or blocks containing crystalline pendant groups), the anisotropy of the crystalline block can influence morphology control. Consequently, lamellar or hexagonally-packed cylinder morphologies are often observed over a larger range of BCP compositions than for traditional amorphous copolymers.[82,83,85,222,224,254,255]

In the case of the symmetric (1:1 mole-ratio) BCPs (Ter-PEG BCP series **P4.2**), the molecular weight of the monomeric units (Ter monomer = 718.13 g/mol; PEG monomer = 386.44 g/mol) leads to a weight percent ratio of approximately 65:35 Ter:PEG. Assuming an estimated density for the PEG block of 1.2 g/mL (as determined for similar hydrophilic PEG polymers[90]) and for the Ter block of 1.1 g/mL (as estimated for other liquid crystalline side chain polymers[90]), the volume fraction of Ter in the copolymers can be estimated as 67% ($f_{Ter} \approx 0.67$). This volume ratio would suggest that, given the traditional coil-coil phase diagram,[62,63] the **P4.2** series should be right on the edge of the lamellar/cylindrical phase transition, depending on the product of the degree of polymerization for a given BCP and the Flory-Huggins parameter (χN_n). The lower molecular weight BCPs (**P4.2a (25)** with overall $N_n = 50$, **P4.2b (50)** with overall $N_n = 100$) show well-defined lamellar ordering, as seen in **Figure 4.13 – Figure 4.15**. A Lorentz correction was used to better resolve the higher angle scattering peaks present in the smaller BCPs, with the observed scattering pattern of q = q*, 2q*, 3q*, etc. indicative of lamellar ordering in the bulk material. For **P4.2c (75)**, the scattering peaks are very

weak, and there is no apparently ordering in the highest molecular weight BCP (**P4.2d (177)**). The domain sizes for the lamellae ordering seen in the smaller Ter-PEG BCPs, calculated using the relationship $d = 2\pi/q^*$, match well with exciton diffusion lengths in organic semiconductors (5–10 nm), with d = 27.3 nm for **P4.2a** (q^* = 0.23 nm^{-1}) and d = 39.2 nm for **P4.2b** (q^* = 0.16 nm^{-1}).

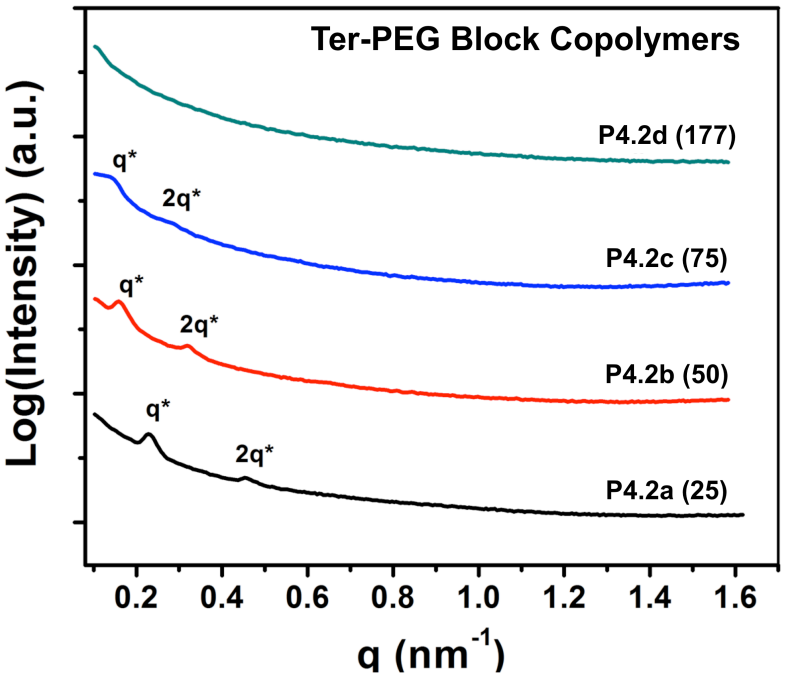

Figure 4.13. SAXS diffraction patterns for Ter-PEG BCP series (**P4.2a – P4.2d**), showing scattering patterns consistent with lamellar ordering in the smaller block copolymers. Block length is denoted in parentheses. For **P4.2a (25)**, q^* = 0.23 nm^{-1} and $2q^*$ = 0.46 nm^{-1}; for **P4.2b (50)**, q^* = 0.16 nm^{-1} and $2q^*$ = 0.32 nm^{-1}.

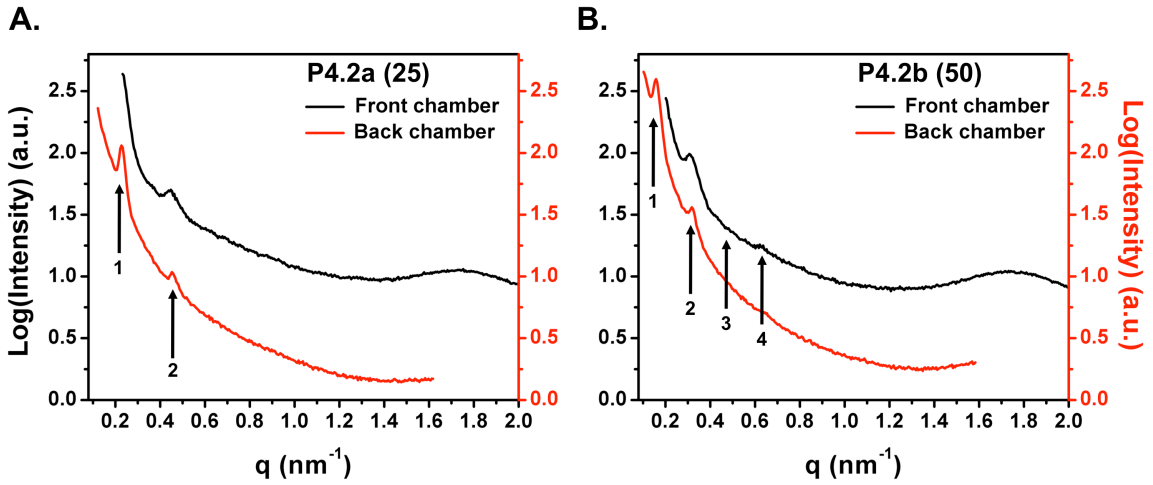

Figure 4.14. Back (red) and front (black) chamber SAXS scattering data for (A) Ter-PEG **P4.2a (25)** and (B) Ter-PEG **P4.2b (50)**, where the block length is denoted in parentheses. The peak labeled 1 indicates q*. The higher angle scattering peaks, labeled 2, 3, and 4, indicate formation of a lamellar morphology in the bulk self-assembled materials. For **P4.2a**, ordering peaks are located at 0.23 nm^{-1} (1) and 0.46 nm^{-1} (2); For **P4.2b**, ordering peaks are located at 0.16 nm^{-1} (1), 0.32 nm^{-1} (2), 0.48 nm^{-1} (3), and 0.64 nm^{-1} (4).

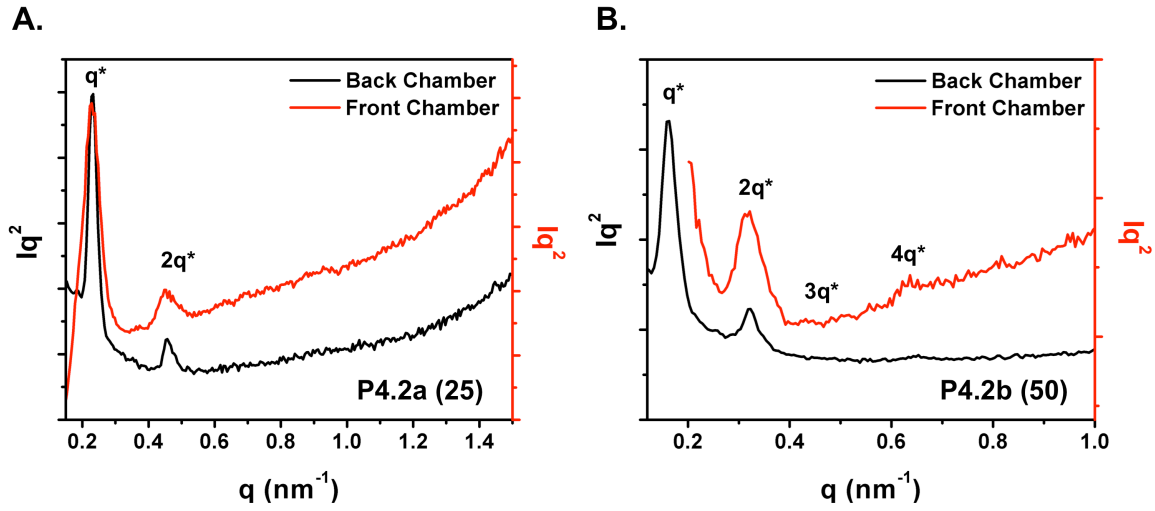

Figure 4.15. Lorentz-corrected SAXS diffraction pattern, used to better resolve the weak higher order scattering peaks for (A) **P4.2a (25)** and (B) **P4.2b (50)**.

In order to see if cylindrical morphologies could be achieved by increasing the asymmetry in the Ter-PEG BCPs, a new series of BCPs (**P4.4a** – **P4.4e)** was synthesized following the same procedure used for the **P4.2** series. The SAXS data is shown in **Figure 4.16**. For **P4.4a** with a Ter composition of 74 wt% ($f_{Ter} \approx 0.76$), SAXS indicates a self-assembled lamellar microphase morphology, with q* = 0.23 nm^{-1} (d = 27.7 nm) and a higher angle scattering peak at 2q* = 0.45 nm^{-1}. While **P4.4b** (wt% Ter = 81, $f_{Ter} \approx 0.82$) and **P4.4e** (wt% Ter = 77, $f_{Ter} \approx 0.78$) show clear primary scattering peaks, indicating microphase separation (**P4.4b**: q* = 0.26 nm^{-1}, d = 24.5 nm; **P4.4e**: q* = 0.25 nm^{-1}, d = 25.3 nm), there are no higher angle scattering peaks to indicate a continuous, well-defined morphology in these bulk materials. It is possible that with the high content of the conjugated Ter pendant groups, a lamellar morphology is favorable as a result of the anisotropic liquid crystalline behavior of the Ter pendant groups. Cylindrical, or other curvaceous, morphologies may be accessible if the PEG block is the majority component in the asymmetric BCPs. This has been seen for other PEG-containing BCPs, where the second block contains liquid crystalline pendant groups.[90]

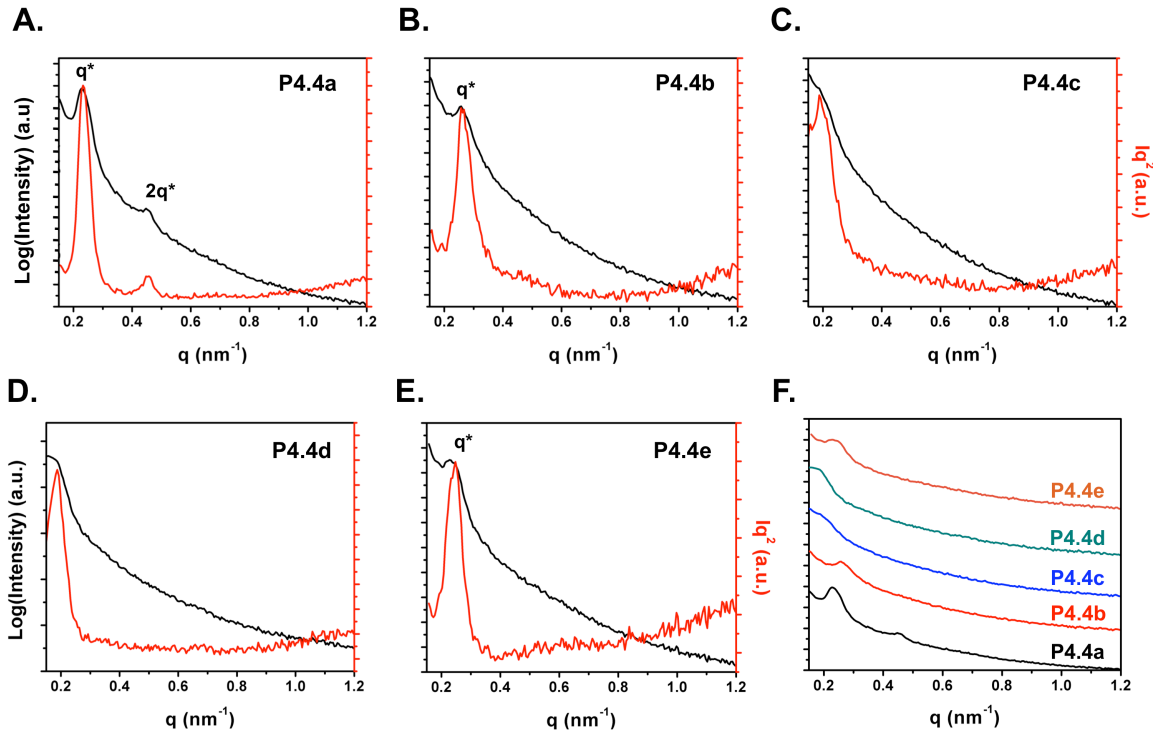

Figure 4.16. SAXS diffraction patterns for asymmetric Ter-PEG BCP series (**P4.4a** – **P4.4e**), black line shows log(Intensity) plot and red line shows the Lorentz-corrected data, used to better resolve the weak scattering peaks: (A) **P4.4a** (wt% Ter = 74, N_n = 37), q* = 0.23 nm^{-1}, 2q* = 0.45 nm^{-1}; (B) **P4.4b** (wt% Ter = 81, N_n = 33), q* = 0.26 nm^{-1}; (C) **P4.4c** (wt% Ter = 85, N_n = 114); (D) **P4.4d** (wt% Ter = 83, N_n = 90); (E) **P4.4e** (wt% Ter = 77, N_n = 60), q* = 0.25 nm^{-1}; (F) Overlay of SAXS diffraction patterns for **P4.4** asymmetric BCP series.

ZnO Nanoparticle Synthesis and Characterization

Synthesis of NPs with uniform size and shape *via* easy synthetic pathways is an important issue for inorganic NP growth. Chemical (liquid) growth methods are most typically utilized due to the low cost, reproducibility, and rigorous control over size and shape.[256] ZnO NPs were synthesized following modified literature procedures *via* the hydrolysis and condensation of $Zn(OAc)_2 \bullet 2H_2O$ by KOH in MeOH.[242–244,257,258] The size of the resultant NPs can be controlled by several factors including the precursor

concentrations in the starting solution, the reaction time, and the Zn^{2+}:OH^- ratio used.[242,257,259] Janssen found that increasing the Zn^{2+}:OH^- ratio from 1:1 to 1:1.75 resulted in larger particles.[242] A further increase of the ratio leads to smaller particles, until the sol becomes unstable at a ratio of 1:2.5.[257]

For the described synthesis of ZnO NPs, a ratio of 1:1.7 was used, which was previously reported by Weller and coworkers to give stable colloidal solutions of particles with approximately 5 nm diameters.[242,257] These NPs were characterized by p-XRD to verify ZnO composition and TEM to determine particle size and distribution (see **Figure 4.17**). The reflections in XRD confirm the formation of a wurtzite-type ZnO crystalline phase. The correct positions (in 2θ) for the peaks are: 31.8 (100), 34.4 (002), 36.2 (101), 47.5 (102), 56.6 (110), 62.9 (103), 66.4 (200), 68.0 (112), and 69.1° (201), which were calculated using the Inorganic Crystal Structure Database (ICSD). These peaks match well with previously reported ZnO NPs.[242,256,257] TEM indicates that the ZnO NPs are relatively monodisperse, with an average NP diameter of 4.1 nm, close to that reported by Weller and coworkers.[242,243]

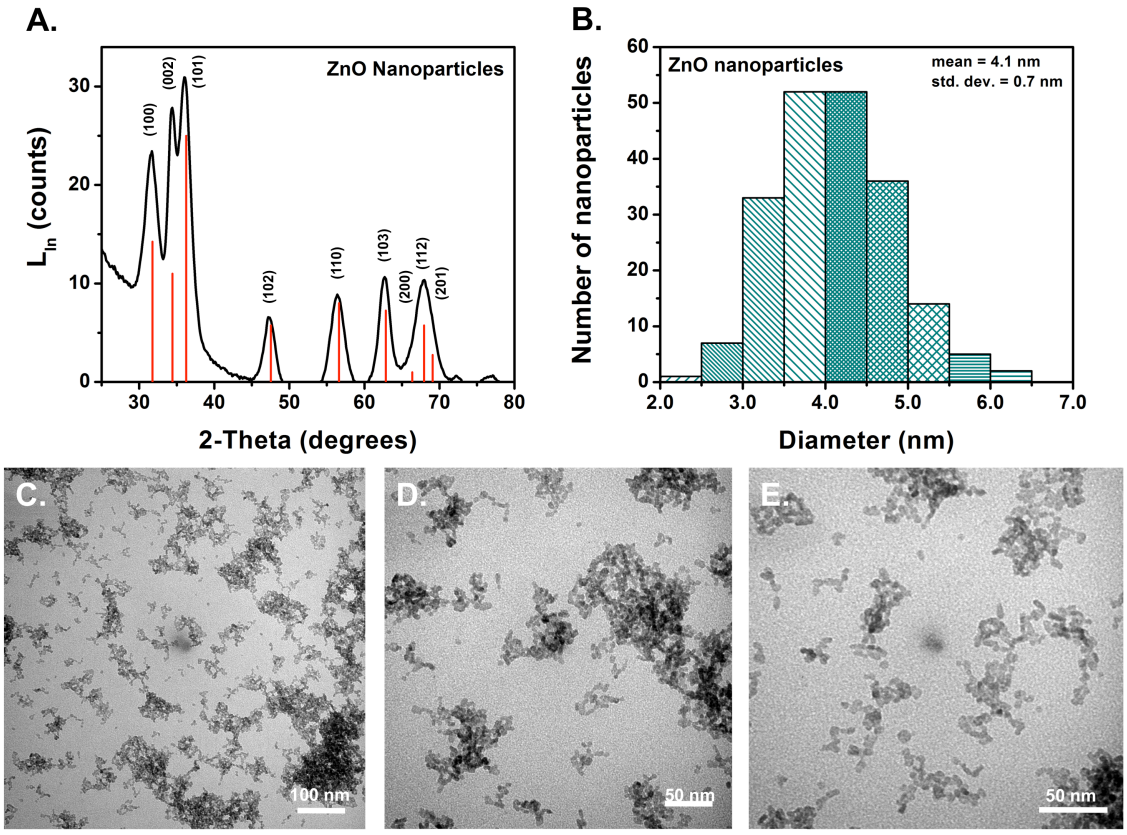

Figure 4.17. ZnO NP characterization: (A) powder XRD pattern; (B) Histogram showing mean NP diameter (4.1 nm), determined from TEM; (C,D,E) TEM images of synthesized ZnO NPs.

Figure 4.18 shows the UV-Vis absorption and fluorescence excitation and emission spectra of the synthesized ZnO NPs. ZnO shows quantum size effects for particles with diameters ≤ 7 nm, hence, UV-Vis absorption can be used as a convenient technique to investigate particle size.[260] The average particle size in a nanocolloid can be calculated from the absorption onset of the UV-Vis spectrum by using the effective mass model, described in **Equation 4.1**, where E_g^{bulk} denotes the bulk semiconductor band gap (~3.30 eV for ZnO); *h* is Plank's constant; r is the particle radius; m_e is the electron effective mass (0.26 for ZnO); m_h is the hole effective mass (0.59 for ZnO); m_0 is the

mass of the free electron (9.1 x 10^{-31} kg); e is the charge on the electron (1.6 x 10^{-19} C); ε describes the relative permittivity; and ε_0 is the permittivity of free space (8.85 x 10^{-12} Fm^{-1}). Due to the relatively small effective masses for ZnO, band gap enlargement is typically seen for particles with radii less than 4 nm ($d \approx 8$ nm).[261–263]

$$E_g^* = E_g^{bulk} + \frac{h^2\pi^2}{2er}\left(\frac{1}{m_e m_0} + \frac{1}{m_h m_0}\right) - \frac{1.8e}{4\pi\varepsilon\varepsilon_0 r} \qquad \textbf{(Equation 4.1)}$$

More recently, Meulenkamp reported a practical method to equate E_g* with the wavelength at which the absorption is 50% of that at the excitonic peak (or shoulder), described by $\lambda_{1/2}$, using a graphical procedure.[259] According to Meulenkamp, the observed $\lambda_{1/2}$ of 356 nm for the synthesized ZnO NPs corresponds to an approximate diameter of 4.1 nm. This value correlates exactly with the mean diameter found from TEM.

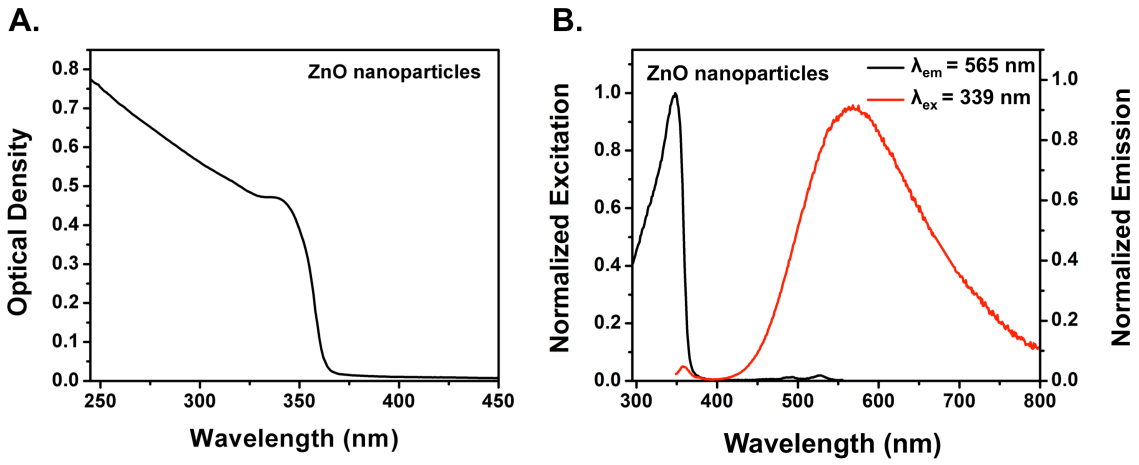

Figure 4.18. (A) UV-Vis absorption profile of ZnO nps in $CHCl_3$; (B) Excitation (λ_{em} = 565 nm) and emission (λ_{ex} = 339 nm) profiles of ZnO NPs in $CHCl_3$.

The fluorescence spectrum of the ZnO NPs shows a broad, featureless emission peak, centered at 565 nm. There is also a very weak emission centered at λ_{em} = 365 nm. It

has been documented that crystalline ZnO exhibits a characteristic fluorescence spectrum with two maxima around 380 and 500 nm. The emission at λ_{em} = 380 nm is attributed to "band gap" fluorescence caused by a transition from the lower edge of the conduction band to the upper edge of the valence band.[262] Interestingly, work by Hoffman and coworkers suggests that smaller ZnO NPs do not exhibit (or show very weak) UV fluorescence, as the lifetimes of electrons and holes in the conduction and valence band seem to increase with increasing particle size.[262] Furthermore, Hoffman and coworkers speculated that for smaller NPs, relaxation into more favorable energy levels could result in increased emission at longer wavelength, and suggested that the longer wavelength fluorescence may be attributed to photogenerated electrons tunneling to pre-existing, trapped holes. In other words, the broad emission in the visible region may be related to defect-induced emission caused by oxygen vacancies or crystal defects.[244]

Incorporation of ZnO Nanoparticles into Ter-PEG Copolymers

In order to investigate the viability of using a diblock copolymer with a Ter semiconductor donor block and a Lewis-basic PEG block as a template material for the fabrication of hybrid inorganic-organic semiconducting materials, the charge transfer behavior in mixtures of Ter-PEG BCPs and ZnO NPs was investigated. Solution-based PL quenching studies using Ter-PEG BCPs **P4.2a-2 (25)** and **P4.2b-2 (50)**, which demonstrate formation of lamellar morphologies upon thermal annealing, were performed. Additionally, ZnO NPs were incorporated into a low molecular weight Ter homopolymer (**P2.1**, N_n = 50) as a control to monitor the effect of the PEG block on ZnO NP incorporation. The incompatibility of ZnO NPs with conjugated semiconducting polymers is one of the key issues in the development of inorganic-organic hybrid materials. Incorporation of the hydrophilic Lewis-basic PEG block into the

semiconducting block copolymer should address this issue by facilitating the dispersion of the ZnO NPs (via the PEG chains) evenly throughout the polymer film.

A solution of ZnO NPs with an average concentration of 117 mg/mL in $CHCl_3$ was used to prepare the blend solutions of a 1:2 w/w ratio of polymer:ZnO NPs. This ratio was chosen to match previously reported studies involving the preparation of BHJ inorganic-organic hybrid materials for solar cell applications.[242–244] Additionally, following literature procedure,[242,243] 5 vol% MeOH was added to the solutions in order to stabilize the NPs in the polymer solution, as samples without added MeOH showed small amounts of precipitated NPs. In order to be able to quantitatively compare the blend solutions, the Ter optical density of each solution was normalized before addition of the ZnO NPs, as shown in **Figure 4.19**. Upon addition of ZnO NPs to the solution, an absorbance corresponding to the ZnO NPs is observed in the UV-Vis absorbance spectrum, similar to what has been observed for other hybrid ZnO NP:conjugated polymer systems utilizing MDMO-PPV or P3HT as the donor material, although these composites show a decreased overlap of the absorptions of the ZnO NPs and the conjugated donor compared to the Ter:ZnO hybrid system.[242,243]

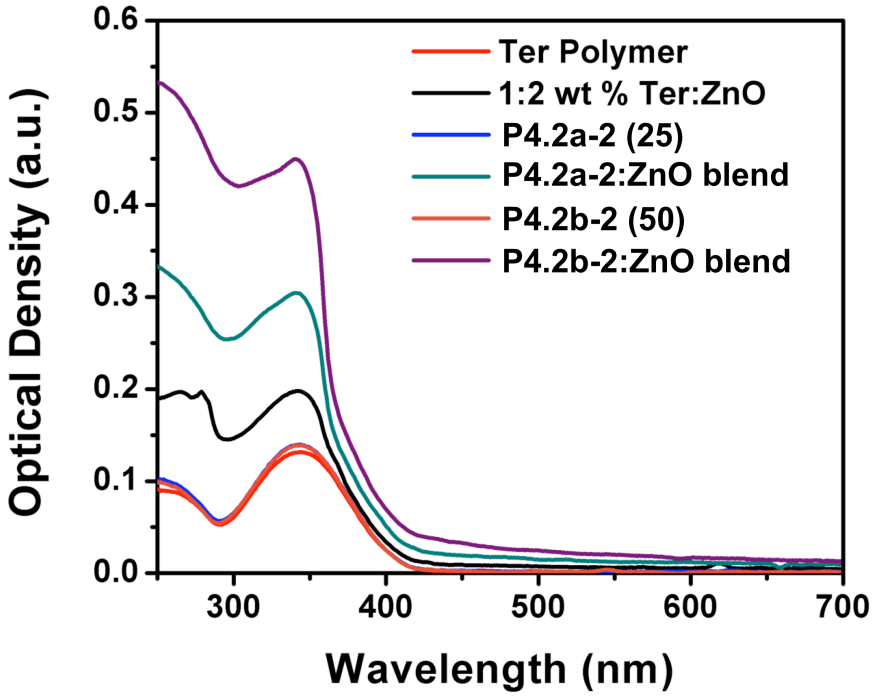

Figure 4.19. UV-Vis spectra showing the normalized Ter optical density of solution blends of Ter-PEG BCPs (**P4.2a-2** and **P4.2b-2**) with ZnO NPs. UV-Vis spectra of the Ter homopolymer and the corresponding ZnO blend solution are shown for comparison.

Fluorescence spectroscopy was used to monitor the degree of Ter emission quenching upon addition of ZnO NPs, using λ_{ex} = 343 nm and λ_{em} = 443 nm, which correspond with the peak absorbance and peak emission of the Ter chromophore, respectively. Upon addition of ZnO NPs, it is expected that fast electron transfer from the Ter donor to the ZnO acceptor will occur, which should result in PL quenching of the Ter emission.[237,242–244] **Figure 4.20** shows the resulting photophysics of the Ter:ZnO donor-acceptor blend solutions. All of the samples show PL quenching in the presence of the ZnO NPs. The Ter homopolymer emission is very slightly quenched (η = 0.10, where η represents the efficiency of energy (exciton) transfer in the system and can be calculated using **Equation 3.3**), which is accompanied by the appearance of a small, red-shoulder

emission around 560 nm (resembling ZnO emission). For both of the Ter-PEG BCPs, PL quenching is increased compared to the Ter polymer, to $\eta = 0.12$ for **P4.2a-2 (25)** and $\eta = 0.25$ for **P4.2b-2 (50)**. This increase in PL quenching with increasing number of repeat units is interesting and may be related to an increased likelihood of collisional quenching in solution with the increasing number of repeat units. It is also possible that, in solution, the increased number of PEG repeat units leads to better sequestration of the ZnO NPs, allowing for closer proximity for charge transfer from the Ter donor to the ZnO NPs. This PL quenching in BCP materials is accompanied by a slight bathochromic shift and narrowing of the excitation profile, leading to a closer resemblance to the ZnO excitation profile. There is also the appearance of a broad red shoulder in the emission profile of the BCP:ZnO solution blends centered around 560 nm. In **P4.2b-2**, this red shoulder emission is more intense than the Ter emission at 443 nm. The ZnO absorbance at $\lambda_{ex} = 340$ nm is not negligible, so it is likely that this emission is from excitation of the ZnO NPs at 340 nm. In this regard, PL quenching as a result of a portion of the incoming photons being absorbed by the ZnO NPs instead of the Ter moieties cannot be discounted.

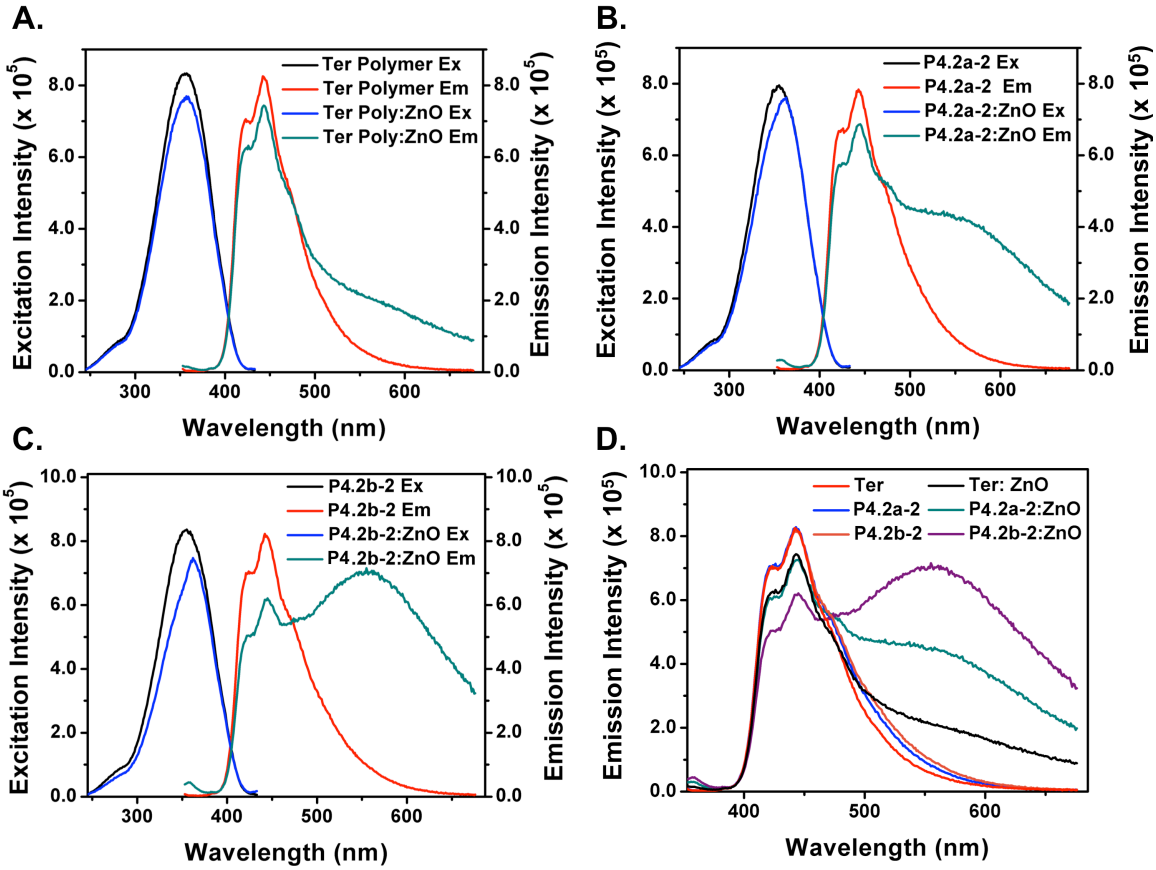

Figure 4.20. Solution-based PL quenching of Ter emission in the presence of ZnO NPs (1:2 w/w polymer:ZnO ratio), λ_{ex} = 343 nm, λ_{em} = 443 nm: (A) Ter homopolymer and Ter:ZnO blend; (B) Ter-PEG BCP **P4.2a-2 (25)** and **P4.2a-2**:ZnO blend; (C) Ter-PEG BCP **P4.2b-2 (50)** and **P4.2b-2**:ZnO blend; (D) Overlay of emission profiles showing relative Ter PL quenching as a result of added ZnO NPs from $\eta = 0.10$ for Ter polymer (black) to $\eta = 0.12$ for **P4.2a-2** (green) and $\eta = 0.25$ for **P4.2b-2** (purple), emission intensity of polymers before addition of ZnO has been normalized for comparison.

It is likely that increasing the amount of ZnO NPs incorporated into the blend solutions would further increase the amount of PL quenching in the BCP materials. In 2006, Janssen and coworkers reported that only after addition of > 26 vol% of ZnO NPs (based on a ZnO NP sol with concentration of 140 mg/mL and ϱ_{ZnO} = 5.6 g/mL) did PL quenching of the P3HT emission occur in thin film blends.[243] Furthermore, it was not

until the addition of > 40 vol% ZnO NPs that the PL quenching of the thin films was significant (i.e. at 26 vol% ZnO NPs, PL quenching was very slight; at 42 vol% ZnO NPs, P3HT PL quenching was approximately 50% of the original emission intensity). Assuming that the polymer materials have an approximate density of 1.0 g/mL[243] the volume percentage of ZnO NPs incorporated into the polymeric material in the solution blends can be calculated as ~35 vol% ZnO in the Ter:ZnO solution, ~37 vol% ZnO in the **P4.2a-2**:ZnO solution, and ~36 vol% in the **P4.2b-2**:ZnO solution.

Given these promising results, ZnO NPs were incorporated into thin films of the Ter-PEG BCPs (**P4.2a-2** and **P4.2b-2**), as well as thin films of the low molecular weight Ter homopolymer (**P2.1**) and Ter-PEG RCP (**P4.3**) for comparison. Theoretically, by annealing the Ter-PEG BCP films above their respective T_g's, well-defined lamellar morphologies should be achieved, with domain sizes (d) between 27 nm and 39 nm. Incorporation of ZnO NPs into the spin-coating solutions, followed by deposition onto glass slides and thermal treatment, should allow for the formation of ZnO NP-containing PEG domains within the BCP thin films. This should lead to high interfacial area throughout the film for efficient photoinduced charge transfer between the Ter donors and the ZnO NP acceptors, which can be visualized by PL quenching of the Ter emission. Theoretically, in the Ter homopolymer and Ter-PEG RCP, annealing should not increase Ter PL quenching significantly, since no microphase self-assembly can occur.

Table 4.4 shows the polymer:ZnO blend formulas used for thin film preparation. In a typical procedure, samples with and without ZnO NPs were made for each polymer material in 95:5 (v/v) CB:MeOH. The concentration of the ZnO NP sol used was 70.8 mg/mL in CB and samples containing ZnO NPs were in a 1:2 w/w polymer:ZnO ratio following previously established procedures, unless otherwise noted.[242,244] These solutions were sonicated to fully dissolve polymer, aiming for a 1.4-1.5 wt% polymer solution. The

solutions were then filtered through a 0.2 μm PTFE filter before spin-casting onto small glass slides at 1000 rpm (depositing 4-5 drops of polymer solution onto the center of the glass slide and then spin-casting for 30 seconds). For samples without ZnO NPs, the final solutions were diluted to the same overall polymer concentration as those samples containing ZnO NPs, since the concentration of the prepared solution can affect the thickness of the resultant thin films. After depositing the thin films, they were heated on a 250 °C hot plate in air for ~2 min to remove residual CB and then stored in labeled petri dishes prior to thermal annealing. Film thicknesses were estimated using profilometry to be approximately 60–70 nm for all films studied.

Table 4.4. Polymer:ZnO NP spin-coating solution formulations.

Sample	Polymer mass (mg)	Vol CB (mL)	Vol MeOH (mL)	Vol ZnO sol (mL)	ZnO mass (mg)	Polymer wt% in solution
Ter Polymer	23.9	1.1 + 0.6	0.06	–	–	1.5
Ter:ZnO	23.9	1.1	0.06	0.67	47.8	1.5
P4.3	13.7	0.6 + 0.4	0.03	–	–	1.4
P4.3:ZnO	13.9	0.6	0.03	0.39	27.8	1.4
P4.2a-2	24.6	1.1 + 0.7	0.06	–	–	1.4
P4.2a-2:ZnO	24.6	1.1	0.06	0.69	49.2	1.4
P4.2a-2:ZnO *(1:6 w/w)*	24.7	1.1	0.06	2.1	148.2	0.8
P4.2b-2	33.0	1.5 + 0.9	0.08	–	–	1.4
P4.2b-2:ZnO	33.1	1.5	0.08	0.94	66.2	1.4

Fluorescence spectroscopy was performed on the unannealed samples using a film holder. The placement of each thin film in the holder was marked in order to standardize post-annealing measurements. Then, the samples were annealed under vacuum at 225 °C

overnight (~16 hrs) and cooled to room temperature before exposing to air. The annealed films were also studied using fluorescence spectroscopy. For all emission studies, a 400-nm filter was used in order to eliminate the second harmonic excitation peak, allowing the emission to be monitored from 353 nm to 800 nm for λ_{ex} = 343 nm. **Figure 4.21** shows the normalized emission data for the thin films. **Figure 4.22** shows the overlay of the normalized emission data for the polymer:ZnO hybrid films. **Figure 4.23** – **Figure 4.28** compare the emission intensities and PL quenching between the unannealed (as-cast) and annealed pristine polymer and polymer-ZnO composite films.

It is important to note that there is still a lot of optimization that needs to be done with these measurements. The emission intensity for each thin film is highly dependent on placement and orientation of the sample in the film holder, so great care was taken to mark the film placement in the sample holder so that the position and alignment of the thin film could be replicated for measurements taken before and after annealing. The placement of the film holder in the fluorimeter was also marked so that it could be consistently positioned between measurements. In addition, the same thin films were used for the emission scans before and after annealing, eliminating possible changes in emission caused by variations in thickness or film imperfections.

In the normalized emission profiles (see **Figure 4.21**), a bathochromic shift of the Ter emission in the as-cast films is observed compared to the Ter materials in solution (from λ_{em} = 443 nm to $\lambda_{em} \approx$ 475 nm). This phenomenon is commonly observed for thin films of conjugated polymer materials typically used in OPVs, and is related to increased π-π interactions in the solid-state films.[239] Upon annealing at 225 °C, all of the pristine polymer films demonstrate a bathochromic shift in the peak emission (from $\lambda_{em} \approx$ 475 nm to $\lambda_{em} \approx$ 520–550 nm), accompanied by red-edge broadening of the normalized emission spectra. This is likely the result of increased Ter pendant group ordering along the

norbornene backbone due to thermal treatment. The polymer:ZnO hybrid films show this same red-edge broadening.

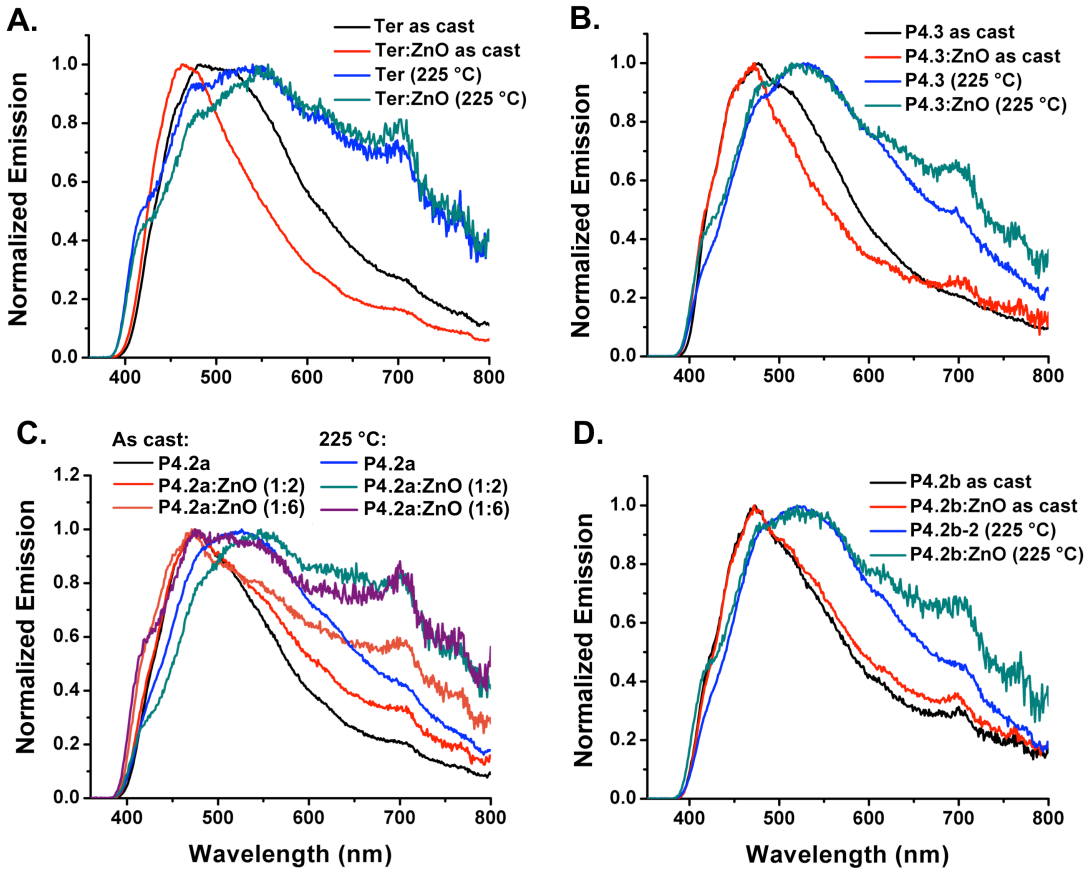

Figure 4.21. Normalized emission profiles for as-cast and annealed thin films on glass slides of (A) Ter polymer (**P2.1**) and Ter:ZnO (1:2 w/w) blend; (B) Ter-PEG RCP (**P4.3**) and **P4.3**:ZnO (1:2 w/w) blend; (C) Ter-PEG BCP **P4.2a-2 (25)**, **P4.2a-2**:ZnO (1:2 w/w) blend, and **P5.2a-2**:ZnO (1:6 w/w) blend; (D) Ter-PEG BCP **P4.2b-2 (50)** and **P4.2b-2**:ZnO (1:2 w/w) blend.

For the thin films of the pristine Ter homopolymer (**P2.1**, see **Figure 4.21A**) and the Ter-PEG RCP (**P4.3**, see **Figure 4.21B**), the unannealed polymer films show a broad emission profile with a large red-edge shoulder. Incorporation of ZnO NPs into the unannealed films leads to a decrease in the red-edge broadening of the emission profiles.

While the emission maxima of the as-cast films is not significantly different between the **P4.3** polymer and **P4.3**:ZnO composite films, the as-cast Ter polymer film shows a 20-nm bathochromic emission shift compared to the Ter:ZnO composite film. It is likely that in the unannealed composite films, the random dispersion of the ZnO NPs within the polymer films leads to interruption of the π-π interactions between the Ter moieties. This increased disorder is observed as a blue shift in the composite film emission. This has been previously seen by Janssen and coworkers in hybrid thin films of P3HT:ZnO.[243] As seen in **Figure 4.21**, this phenomenon is more pronounced in the Ter polymer film, as the PEG moieties in the **P4.3** RCP films should aid in the formation of a more favorable, intermixed (BHJ) morphology, with the ZnO NPs preferentially confined within the PEG chains of the RCP material. After annealing, the normalized emission profiles of the pristine and composite films for the Ter and **P4.3** RCP materials are very similar, with the exception of increased red-edge broadening in the **P4.3**:ZnO composite film.

The normalized emission profiles of the as-cast Ter-PEG BCP thin films (**P4.2a-2 (25)**, see **Figure 4.21C**; **P4.2b-2 (50)**, see **Figure 4.21D**) are very similar to the as-cast composite films. The ZnO NPs preferentially interact with the PEG moieties and the presence of distinct Ter and PEG domains within the block copolymer films, even before annealing, leads to less disruption of the π-π interactions between Ter pendant groups in the BCP films. Therefore, the unannealed emission profiles of both the pristine BCPs and BCP:ZnO composite films should match well, as observed. This data supports that the Lewis-basic PEG chains interact strongly with the Lewis-acidic ZnO NPs, leading to preferential confinement of the ZnO NPs within the PEG domains in the copolymer materials. This interaction aids not only in the formation of favorable donor-acceptor interfaces throughout the active layer, but also improves dispersion of the ZnO NPs within the conjugated polymer. Upon annealing, the emission profiles of all of the films

red-shift and broaden, similar to what is observed for the Ter and RCP thin film series (see **Figure 4.22**).

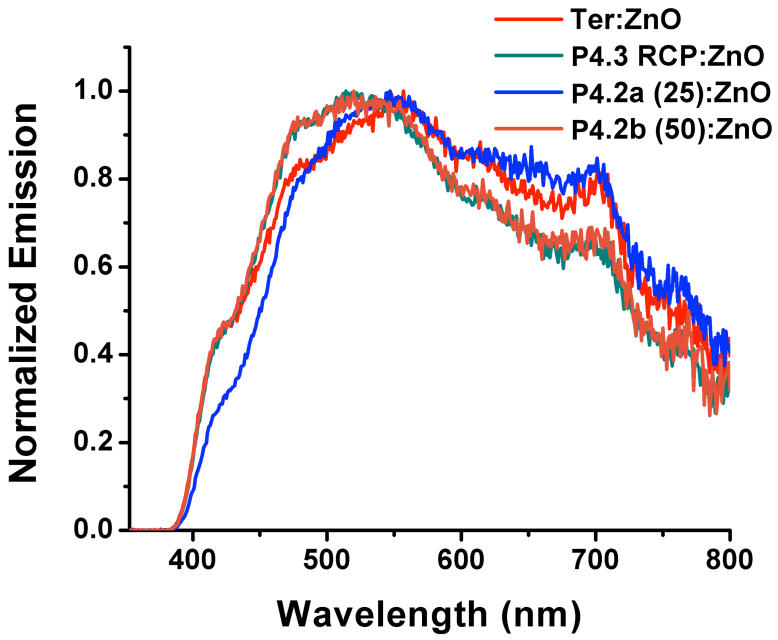

Figure 4.22. Overlay of normalized emission data for the 1:2 w/w polymer:ZnO composite films.

While the normalized emission data provides important insight into the effects of annealing and ZnO incorporation on the conjugated polymer materials, changes in the emission intensity (PL) can provide information about charge transfer in the thin films. Both the pristine Ter polymer film and Ter:ZnO (1:2 w/w ratio) composite film show drastic PL quenching upon annealing (see **Figure 4.23**). Compared to the as-cast Ter polymer film, emission intensity is quenched by approximately 95% upon annealing. The Ter:ZnO composite film also demonstrates almost quantitative emission quenching upon annealing, with a 97% decrease in emission after thermal treatment. This Ter:ZnO composite film most closely resembles a traditional BHJ hybrid inorganic-organic active

layer, so the almost quantitative PL quenching could be very promising. However, since the pristine Ter polymer film also demonstrates high PL quenching upon annealing, and the as-cast Ter film and Ter:ZnO composite film demonstrate similar emission intensities, it is likely that the observed PL quenching is related to the increased orientational ordering of the Ter pendant groups after annealing, which leads to strong aggregation-based emission quenching.

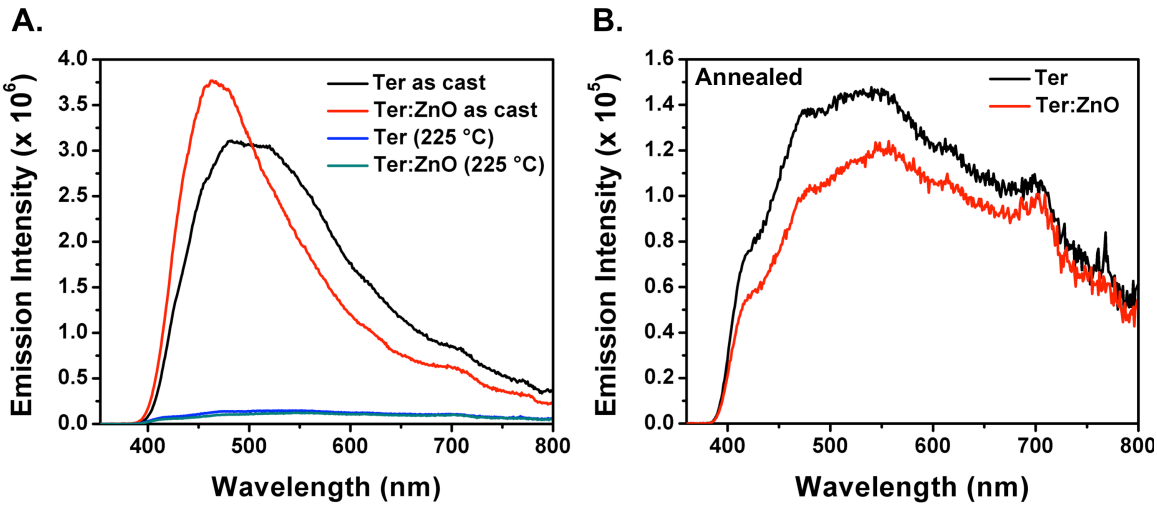

Figure 4.23. Thin film emission intensity data for (A) As cast and annealed (225 °C) Ter polymer film and Ter:ZnO (1:2 w/w) blend film; (B) Zoomed-in view of annealed Ter polymer film and Ter:ZnO blend film.

Since there is little difference in the extent of PL quenching between the Ter polymer film and the Ter:ZnO composite film, it is possible that the ZnO NPs do not form well-dispersed interfaces within the conjugated Ter polymer due to poor solubility caused by low compatibility of the polar ZnO NPs and highly conjugated (and hydrophobic) Ter polymer. This would result in the formation of large aggregates within the film, lowering the donor-acceptor interfacial area and limiting the photoinduced electron transfer. This may explain why the unannealed hybrid Ter:ZnO film shows no

PL quenching compared to the unannealed Ter film, as well as why PL quenching is approximately the same in both films upon annealing.

It is important to note that in all of the studied composite films some of the observed emission intensity may be related to the ZnO NPs, since they demonstrate a strong absorbance around λ = 340 nm and have an emission profile with a broad emission centered around 560 nm in solution measurements. However, excitation at λ_{ex} = 343 nm of a thin film of ZnO NPs deposited on a glass slide resulted in a very weak emission (see **Figure 4.24**). The PL intensity of the annealed ZnO thin film is over a magnitude lower than the PL intensity observed for any of the polymer blend films. Furthermore, the broad visible emission observed in solution measurements of ZnO NPs is not present in the thin film. Interestingly, this may indicate a low number of defect sites on the deposited ZnO NPs, as the emission band at 560 nm is associated with defect-induced emission events.[244]

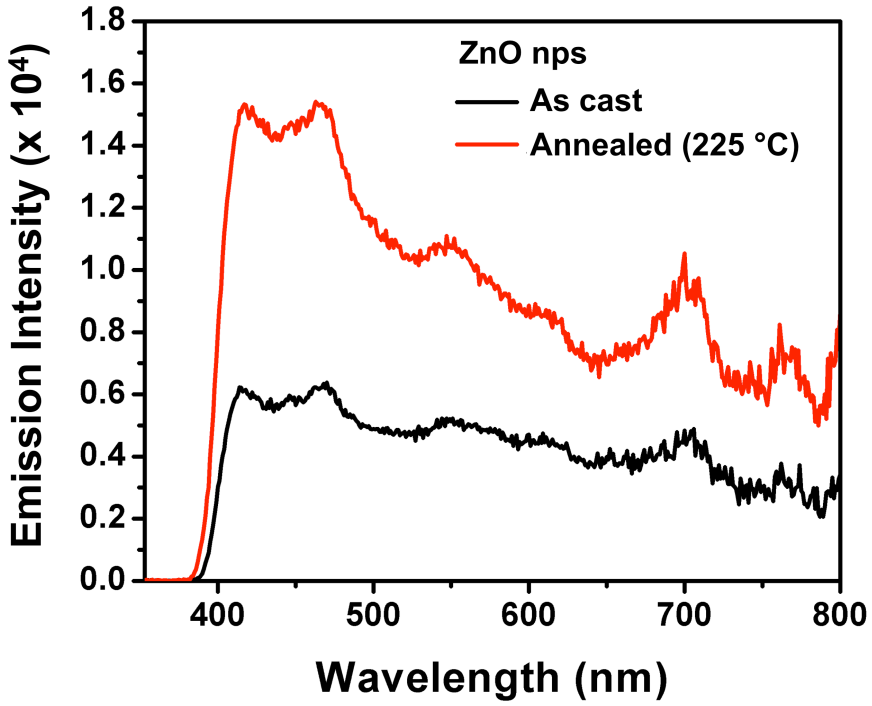

Figure 4.24. Thin film emission intensity data for unannealed (black line) and annealed (red line, 225 °C) ZnO NPs on glass slide, demonstrating low emission intensity upon excitation at λ = 343 nm.

Figure 4.25 shows the emission intensity data for the pristine Ter-PEG RCP (**P4.3**) and Ter-PEG RCP:ZnO composite films before and after annealing. The RCP:ZnO composite film shows almost complete quenching of the Ter emission both before and after annealing compared to the pristine RCP polymer thin film. In fact, the as-cast RCP:ZnO hybrid films demonstrates a 96% decrease in emission compared to the as-cast RCP polymer film. After annealing, the hybrid film shows an 81% decrease in emission compared to the annealed Ter-PEG RCP film. This suggests that efficient charge transfer from the Ter donor to the ZnO NPs occurs in this system as a result of high interfacial area in the film. This high interfacial area results from the covalently-tethered PEG moieties in the Ter-PEG RCP, which leads to close proximity of the ZnO

NP acceptors and the Ter donors throughout the film. The Lewis acid-base interactions between the ZnO NPs and the PEG chains not only aid in solubilizing the polar ZnO NPs within the polymer film, but also ensure distribution of the ZnO NPs throughout the film. Annealing the RCP:ZnO composite film has little effect on the already drastically quenched PL intensity. The pristine Ter-PEG RCP polymer film also demonstrates PL quenching after annealing (79% decrease in emission compared to as-cast), although the PL intensity is still much higher than that observed in either of the composite films. This provides proof-of-concept that incorporation of the PEG chains into the copolymer material can increase charge transfer in the inorganic-organic hybrid films as a result of more favorable mixing.

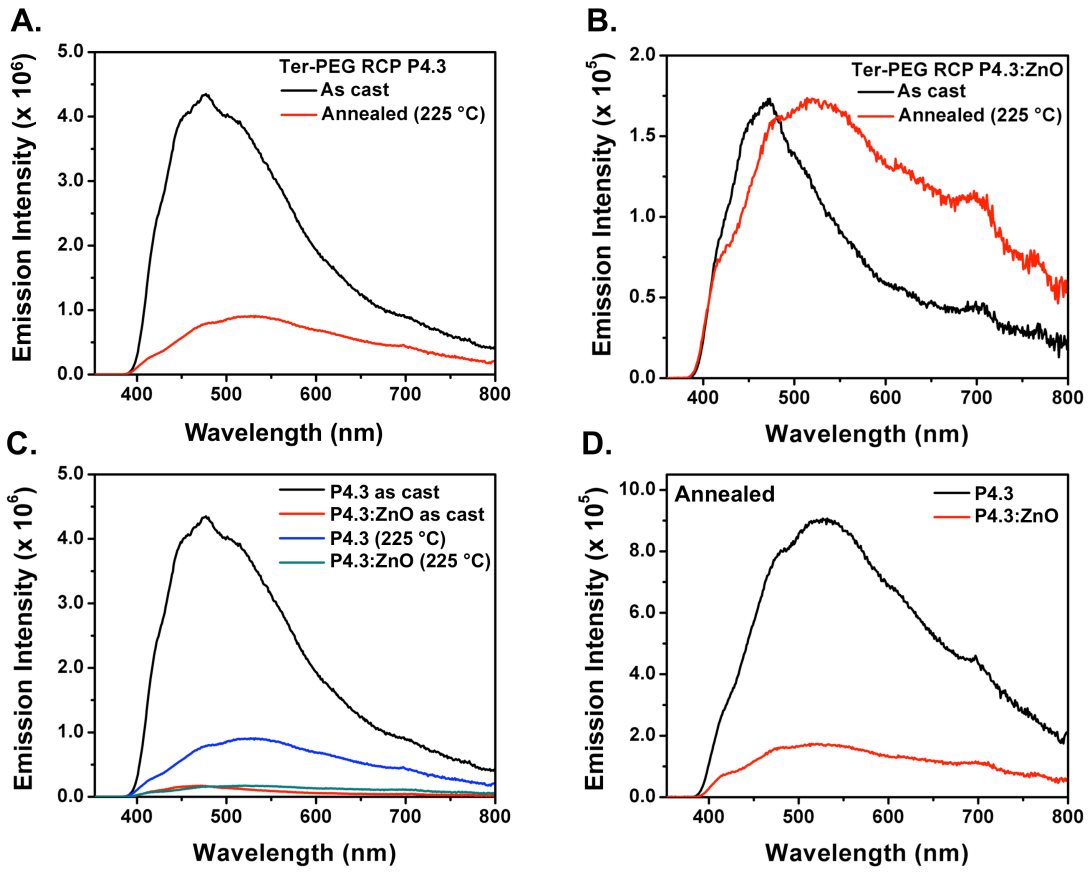

Figure 4.25. Thin film emission intensity data for (A) As cast (black line) and annealed (red line) Ter-PEG RCP (**P4.3**) polymer film; (B) As cast (black line) and annealed (red line) **P4.3**:ZnO (1:2 w/w) composite film; (C) Overlay of thin film emission intensities for the Ter-PEG RCP (**P4.3**) thin film series; (D) Comparison of annealed emission intensities of the **P4.3** polymer film and the **P4.3**:ZnO hybrid film, showing the high PL quenching in the inorganic-organic hybrid film, indicative of efficient charge transfer from the Ter donor to the ZnO NPs.

While the Ter and the Ter-PEG RCP blend films most closely resemble a typical hybrid inorganic-organic BHJ (with the RCP best demonstrating an ideal BHJ morphology, with the NPs well-dispersed throughout the film due to the presence of the PEG chains), the Ter-PEG BCPs (**P4.2a-2 (25)** and **P4.2b-2 (50)**) represent an ideal ordered morphology. Self-assembly of the BCP materials into well-ordered and

continuous nanometer-scale domains, with dimensions well-matched to exciton diffusion lengths, should lead to very high interfacial area and high charge transfer efficiencies. Furthermore, the use of BCPs offers inherent control over the resultant morphology, as well as improved stability due to the covalent tether between polymer blocks, which prevents macroscopic phase separation in the thin film.

The as-cast **P4.2a-2**:ZnO (1:2 w/w ratio, 67 wt% ZnO) composite film shows high PL quenching (66%) compared to the as-cast pristine BCP polymer film. This suggests that charge transfer is an efficient process in the inorganic-organic hybrid film even before self-assembly. Interestingly, the as-cast Ter-PEG RCP composite film shows higher PL quenching than the as-cast Ter-PEG BCP composite film. This is due to closer proximity of ZnO NPs to Ter pendant groups as a result of the alternating (or semi-alternating) arrangement of the blocks in the RCP compared to the continuous blocks of Ter and PEG in the BCP (i.e. less intermixing in the as-cast film). Increasing the ZnO content to 86 wt% in the **P4.2a-2**:ZnO (1:6 w/w ratio) composite film leads to an even larger decrease in the emission intensity, with a quenching efficiency of $\eta = 0.84$ for the unannealed composite film.

In the case of the Ter-PEG BCP (25) (**P4.2a-2)** polymer film, annealing leads to a 40% increase in the emission intensity. This is likely related to the formation of a lamellar morphology upon thermal annealing. For the **P4.2a-2**:ZnO (1:2 w/w ratio, 67 wt% ZnO) composite thin film, annealing results in a drastic increase in PL quenching efficiency ($\eta = 0.92$) compared to the pristine annealed polymer film. The increased amount of ZnO NPs in the **P4.2a-2**:ZnO (1:6 w/w ratio, 86 wt% ZnO) composite film also demonstrates almost complete PL quenching, with $\eta = 0.96$. Furthermore, unlike in the RCP hybrid film, PL quenching in the BCP hybrid films increases by over 60% upon annealing for both composite films (67 wt% ZnO and 86 wt% ZnO), suggesting that BCP

self-assembly has an important role in the charge transfer efficiency. Assuming that the ZnO NPs are preferentially located in the PEG domains in the BCP, annealing leads to the formation of nanometer-sized lamellae, creating donor-acceptor interfaces throughout the composite films. From SAXS, the **P4.2a-2 (25)** BCP thin films should form a lamellar morphology upon annealing, with d = 27 nm. This domain size is well matched to exciton diffusion lengths, which are on the order of ~10 nm. The formation of these well-organized domains leads to increased charge transfer events from the Ter donor to ZnO NPs. This is supported by the fact that in the RCP film, annealing results in no change in the emission intensity, since the RCP cannot undergo microphase separation in the same way as the BCP materials. Furthermore, increasing the weight percent of ZnO in the films from ~67 wt% ZnO to ~86 wt% ZnO increases the overall emission quenching in the BCP composite films.

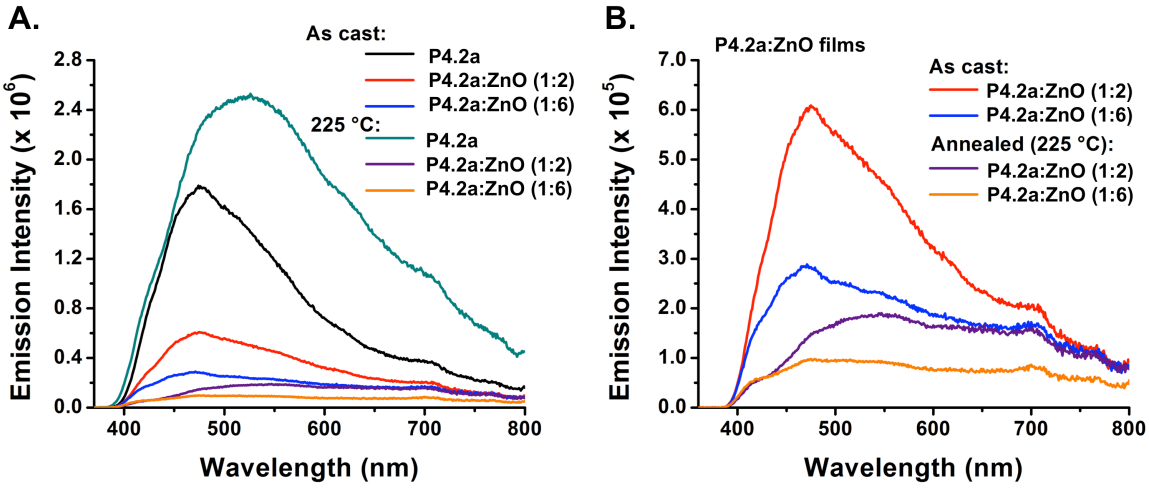

Figure 4.26. Thin film emission intensity data for (A) As-cast and annealed Ter-PEG BCP **P4.2a-2 (25)** polymer film, **P4.2a-2**:ZnO (1:2 w/w) blend film, and **P4.2a-2**:ZnO (1:6 w/w) blend film; (B) Zoomed-in view of the as-cast and annealed PL intensity of the **P4.2a-2**:ZnO composite films, demonstrating the high amount of Ter donor emission quenching.

Figure 4.27 shows the thin film PL quenching data for the Ter-PEG BCP **P4.2b-2 (50)** series with and without ZnO NPs. In the solution quenching studies, **P4.2b-2** demonstrated the highest PL quenching in the presence of ZnO NPs. **P4.2b-2 (50)** self-assembles into a lamellar morphology upon thermal annealing, with d = 39 nm. Similar to the pristine **P4.2a-2 (25)** polymer film, the **P4.2b-2 (50)** polymer film shows a large increase in emission upon annealing, although the increase in the intensity is much greater for the higher M_n BCP. Furthermore, the as-cast **P4.2b-2**:ZnO (1:2 w/w ratio) composite film shows a higher emission intensity than the BCP polymer film. This may be due to the increased block length in **P4.2b-2**, leading to less intermixing of the Ter and PEG domains in BCP film before annealing and thus less charge transfer events.

Upon annealing, the **P4.2b-2**:ZnO composite film demonstrates an 84% decrease in PL intensity compared to the unannealed composite film, and demonstrates a PL quenching efficiency of η = 0.89 compared to the annealed pristine polymer film. This indicates that self-assembly of the BCP material upon thermal annealing leads to an increased interfacial area in the active layer material. The lower charge transfer efficiency compared to the **P4.2a-2**:ZnO (67 wt% ZnO) composite film results from the fact that the domain size of the lamellae formed for the lower M_n BCP are better matched to exciton diffusion lengths. Consequently, a higher number of the absorbed photons are located near a donor-acceptor interface, leading to the increased creation of free charge carriers in the material.

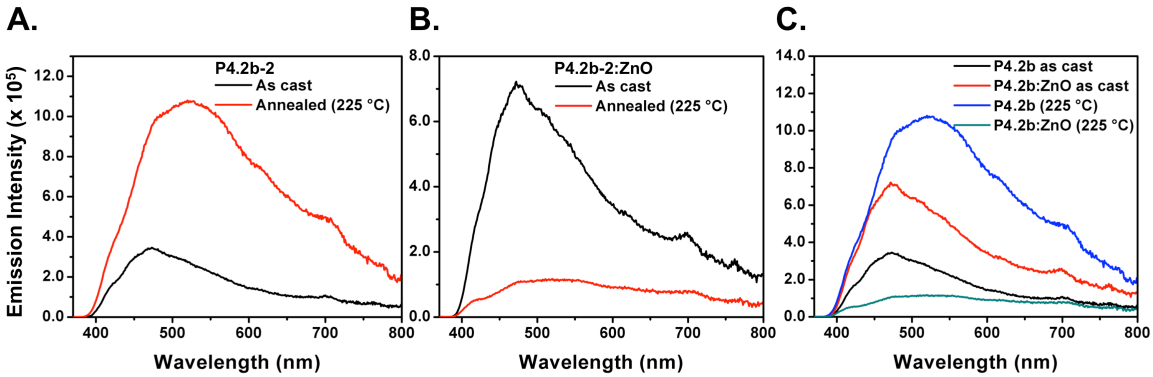

Figure 4.27. Thin film emission intensity data for (A) As-cast and annealed Ter-PEG BCP **P4.2b-2 (50)** polymer film; (B) As-cast and annealed **P4.2b-2**:ZnO (1:2 w/w ratio) composite film; (C) Overlay of emission intensity profiles for the **P4.2b-2** series.

Figure 4.28 shows the combined PL data for all of the pristine polymer and composite polymer:ZnO NP thin films, as well as an overlay of just the composite films. Overall, this proof-of-concept study is promising. The results indicate that the ZnO NPs are preferentially confined in the PEG chains due to the favorable Lewis acid-base interactions between the metal NP and the ethylene glycol chains. This leads to better compatibility between the Ter-PEG copolymers and the synthesized ZnO NPs, resulting in better solubility and dispersion of the hydrophilic ZnO NPs within the semiconducting copolymer films. Furthermore, thermal annealing of the Ter-PEG BCP films with 25 and 50 repeat units per block leads to the formation of nanometer lamellae in the thin films. This self-assembly behavior allows for increased interfacial area between the ZnO-containing PEG domains and the Ter donor domains. The increased interfacial area leads to increased PL quenching as a result of fast electron transfer from the photoexcited Ter donor to the ZnO NP acceptor. All of these results suggest potential for use as an inorganic-organic active layer material for hybrid solar cell applications.

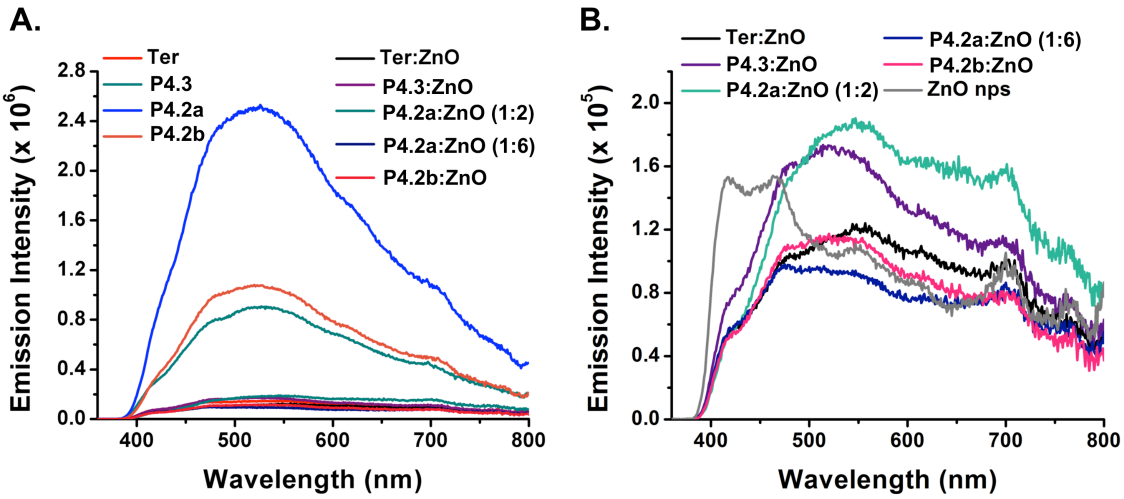

Figure 4.28. Combined thin film emission intensity data for: (A) Annealed thin film samples; (B) Annealed ZnO NP composite thin films.

CONCLUSION

By designing and synthesizing amphiphilic copolymers containing Ter and PEG pendant groups attached to a flexible norbornene-type backbone, coil-coil BCP templates for inorganic-organic hybrid materials were synthesized using ROMP. The incorporation of the PEG chains into the copolymer materials had little effect on the photophysical and electrochemical properties of the Ter donor. SAXS measurements suggest microphase separation in bulk samples of the Ter-PEG BCPs with 25 and 50 repeat units in each block into lamellar structures with domain sizes between 27–39 nm. Despite the synthesis of BCPs with increasing asymmetry, other self-assembled morphologies were not achieved. ZnO NPs with an average particle diameter of 4.1 nm were synthesized and initial solution-based photophysical studies show PL quenching of the Ter donor emission upon addition of the ZnO NP acceptors, indicating fast electron transfer to the metal oxide NP. Further studies, including time-resolved photoluminescence studies, are needed to verify that the observed PL quenching is a result of fast electron transfer from the Ter donor to the ZnO NP acceptors. As-cast composite thin films of the Ter-PEG

RCP, Ter-PEG BCP (25), and Ter-PEG BCP (50) with 67 wt% ZnO demonstrate very high charge transfer efficiencies upon photoexcitation. After thermal annealing to induce microphase self-assembly in the BCP materials, the PL quenching increases significantly in the BCP composite films, but no appreciable change in PL intensity is observed for the RCP. This indicates that the formation of nanoscale lamellar domains in the BCPs upon annealing increases the donor-acceptor interfacial area, allowing for more photoexcitation events to lead to free charge carriers. The PEG chains aid in solubilizing the ZnO NPs during thin film preparation, and, more important, in organizing and dispersing the ZnO NPs throughout the film. All of these results demonstrate the ability to make well-ordered inorganic-organic donor-acceptor BCPs, which have potential applications in hybrid OPV technologies. In addition, these amphiphilic BCPs have potential for use in other hybrid applications, utilizing wet synthesis techniques (as demonstrated here) or sequential infiltration synthesis[264–269] to imbed and grow metal oxide NPs within the Lewis-basic PEG domain. Finally, the synthesis of the Ter-PEG copolymers demonstrates the flexibility and functional group tolerance of the previously reported synthetic route (see **Chapter 2**, **Chapter 3**) for creating functional polymers for a myriad of applications.

Appendix: Toward Hybrid Inorganic-Organic Block Copolymer Materials: Synthesis and Characterization of Polymerizable Dipicolylamine Norbornene Monomer and Ter-DPA Block Copolymers

INTRODUCTION

Hybrid polymer-nanoparticle (NP) composites have a variety of applications, including use in electronic materials and devices such as sensors, light-emitting diodes, and photovoltaics.[270] Polymer-NP composites are currently synthesized by a variety of methods, including post-synthesis mixing of the two materials, impregnating polymers electrochemically with metal centers, and utilizing one-pot syntheses.[271] However, many of these techniques lead to large particle size distributions, uneven dispersion of the NPs within the polymer film, or passivation of the particles by surfactant or oxide layers. Furthermore, it can be difficult to control the homogeneity of the polymer-NP blends, and good intermixing of the organic and inorganic components is crucial to the performance of these hybrid materials in electronic applications.[270] Along the same lines, surfactants or capping agents, often used in the synthesis of the inorganic NPs to aid in stabilization, can act as an inherent barrier to charge transport in the materials.

With these issues in mind, previous group members developed a novel approach to synthesize polymer-NP hybrid materials based on the seeded growth of semiconducting NPs within a conducting metallopolymer.[185,191,272] In this synthetic strategy, an electropolymerizable metal complex is prepared, which can be polymerized to form well-defined conducting metallopolymers with metal centers directly embedded in the polymer backbone. Then, these preorganized metal "seed points" act as nucleation sites to initiate the growth of semiconducting NPs directly in the conducting polymer backbone. This approach ensures direct physical and electrical contact between the two active components in the material. Research in our group has been previously focused on

the use of salen or salch Schiff-base type complexes as a way to incorporate metal centers into a conducting polymer backbone (**Scheme A.1**). These salen and salch ligands can coordinate a variety of metals, are easily synthesized in a one-pot reaction between a diamine and an aldehyde (or benzylic ketone), and are easily derivatized. These characteristics allow for the preparation of a variety of different metal complexes, as well as tuning of the overall performance and application of the material, through choice of ligand and metal center.[185,191,273] While synthesis of the symmetric Schiff base ligands is easily achieved, the preparation of asymmetric ligands from symmetric diamines has proven to be no simple task, and a variety of approaches have been employed.[185,274,275] Of these, salt formation has been the most successful. In this method, first outlined by Nguyen and coworkers[276], reaction of diaminocyclohexane with one equivalent of HCl results in the formation of the mono-quaternary ammonium salt. This mono-protected diamine can then be reacted with one equivalent of a derivatized salicylaldehyde. Deprotection of the protected amine allows for reaction with a second equivalent of a different salicylaldehyde to form the desired asymmetric salch ligand. Despite reported successful synthetic procedures for asymmetric salen and salch ligands[275277], synthesis of a norbornene-type monomer with a salch pendant group was unsuccessful, so attention was turned to a different ligand system.

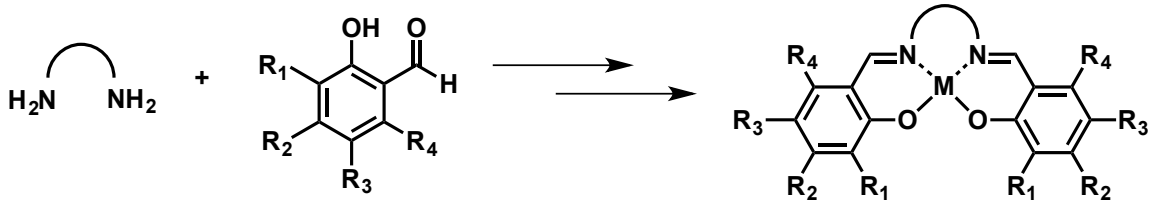

Scheme A.1. General synthetic scheme for the preparation of symmetric salen-type ligands and their corresponding metal complexes.

With the goal of developing a norbornene-type monomer with a pendant ligand capable of acting as a seed point for the directed growth of ZnO NPs for hybrid photovoltaic applications, attention was turned to the dipicolylamine (DPA) ligand (**Figure A.1**). The DPA ligand is well-known in the literature to bind Zn^{2+} metal centers selectively over other divalent metal cations, and is used extensively in sensing applications, especially in biologically relevant systems.[278–281] The DPA ligand provides a tridentate binding site with three nitrogen donors that affords good selectivity for Zn^{2+} over other biologically relevant metals such as Na^{+}, K^{+}, Mg^{2+}, and Ca^{2+}. Furthermore, it is easily synthesized and readily appended to a variety of scaffolds, leading to its widespread use. With this in mind, a DPA monomer was synthesized, copolymerized with the previously described Ter monomer (compound **2.13**), and metallated with various zinc salts. This material was characterized by photophysical and electrochemical methods, with the ultimate goal of developing a hybrid organic polymer-inorganic NP semiconducting material using a seeded growth approach to form ZnO NPs within the ordered BCP film.

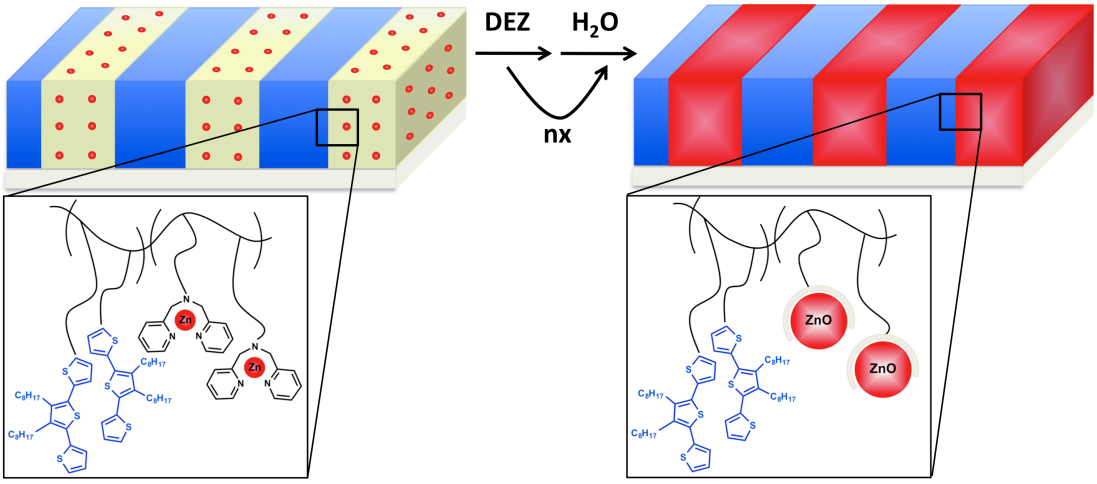

Figure A.1. Schematic representation of seeded ZnO nanoparticle growth within a self-assembled Ter-DPA BCP thin film as a method for the development of ordered hybrid organic-inorganic materials.

EXPERIMENTAL

Instrumentation

Nuclear magnetic resonance (NMR) spectroscopy was recorded with a Varian DirectDrive 400 MHz or 500 MHz spectrometer at ambient temperature and NMR spectra were referenced internally to the residual solvent peaks. All chemical shifts are reported in ppm and coupling constants are given in Hertz (Hz). Absorption spectra were obtained on a Varian Cary 6000i UV-Vis-NIR spectrophotometer in Starna quartz fluorimeter cells with a 1.0 cm path length. Mass spectroscopy was performed with a Micromass Autospec Ultima HRMS (for CI^+) or an Agilent 6530 Q-TOF system (for ESI^+). Elemental analysis was performed by QTI, Whitehouse, NJ (www.qtionline.com). Gel permeation chromatography (GPC) was done on an Agilent 1100 Series Instrument with Viscoteck Triple Array Detector 302 Series in THF. Thermal gravimetric analysis (TGA) was performed on TA Instruments TGA Q50 under inert N_2 atmosphere with 3.5 °C/min ramp to 500 °C and then 8.0 °C/min ramp to 800 °C. Differential scanning

calorimetry (DSC) was performed on a Mettler Toledo DSC-1 instrument model. All DSC samples ranged from 5-8 mg and followed the same run procedure with a N_2 flow rate of 50 mL/min: (1) Isothermal at 30 °C for 2 min; (2) Heating from 30 °C to 100 °C at 10 °C/min to remove water and any residual solvent; (3) Isothermal at 100 °C for 2 min; (4) Cooling from 100 °C to 30 °C at 10 °C/min; (5) Isothermal at 30 °C for 2 min; (6) Heating from 30 °C to 280 °C at 10 °C/min; (7) Isothermal at 280 °C for 2 min; (8) Cooling from 280 °C to 30 °C at 10 °C/min. Fluorimetry experiments were carried out on a Photon Technology International QuantaMaster 4 spectrophotometer equipped with a 6-inch diameter K Sphere-B integrating sphere and using PTI software. All solution measurements were recorded in Starna quartz fluorimeter cells with a path length of 1.0 cm in dicholoromethane (DCM), unless otherwise noted.

Electrochemistry

Electrochemical experiments were carried out in a dry box under a N_2 atmosphere using a GPES system from Eco. Chemie B. V. All the electrochemical experiments were performed using a three-electrode cell with a $Ag/AgNO_3$ reference electrode (silver wire in a 0.01 M silver nitrate solution with 0.1 M $[(n\text{-}Bu)_4N]^+[PF_6]^-$ ($TBAPF_6$) in acetonitrile), a 1.6 mm Pt button working electrode, and a Pt wire coil counter electrode. All measured potentials were referenced to the ferrocene/ferrocenium redox couple (Fc/Fc^+) as determined by the average $E_{1/2}$ value obtained before and after the experiment. The supporting electrolyte used was 0.1 M tetrabutylammonium hexafluorophosphate ($TBAPF_6$), which was purified by three successive recrystallizations from hot ethanol and dried for three days at 100-150 °C under high vacuum before use. All measurements were carried out in DCM with scan rate of 100 mVs^{-1}.

Synthesis

General Considerations

Air- and/or moisture-sensitive reactions were carried out in heat-gun-dried glassware using standard Schlenk techniques under a dry N_2 atmosphere. Dry solvents were collected in solvent bulbs from an Innovative Technology PureSolv 400 solvent purification system and stored over 3Å molecular sieves. All chemicals were used as received from commercial suppliers unless otherwise specified. Thin layer chromatography (TLC) was performed using Silicycle silica gel 60 F_{254} pre-coated aluminum sheets. Column chromatography was performed using Silicycle Silica Flash® F60.

Synthesis of DPA Monomer [A.1 – A.4]

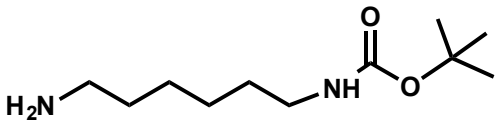

***tert*-butyl(6-aminohexyl)carbamate [A.1]:** 1,6-diaminohexane (11.28 g, 97.1 mmol) was dissolved in $CHCl_3$ (370 mL) in a 1-L round-bottomed flask equipped with a 125-mL addition funnel. The solution was cooled to 0 °C in an ice bath. Di-*tert*-butyldicarbonate (4.59 g, 20.9 mmol) was dissolved in $CHCl_3$ (100 mL), transferred to the addition funnel, and added dropwise to the stirring diamine solution at 0 °C over approximately 2 hrs. After complete addition, the ice bath was removed and the reaction was stirred overnight at room temperature. Upon completion, the reaction mixture was filtered over celite to remove the white solid precipitate, rinsed with $CHCl_3$, and concentrated *in vacuo*. The crude clear oil was redissolved in EtOAc (250 mL) and transferred to a separatory funnel. The organic phase was washed with DI H_2O (3 x 150 mL) and brine (1 x 150 mL), dried over Na_2SO_4, and concentrated *in vacuo* to yield the

desired product as a clear oil (3.89 g, 86%). ^{1}H NMR (400 MHz, $CDCl_3$) δ: 4.74 (s, broad, 1H), 3.01 (m, 3H), 2.59 (t, 2H, *J* = 7), 1.39 (m, 4H), 1.35 (s, 9H), 1.24 (m, 4H), 1.12 (s, 2H).

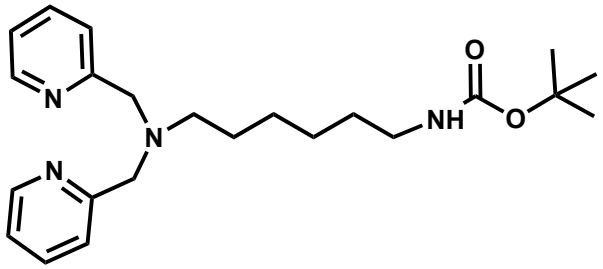

***tert*-butyl(6-(bis(pyridin-2-ylmethyl)amino)hexyl)carbamate [A.2]:** Na_2CO_3 (20.13 g, 189.9 mmol) and 2-chloromethylpyridine hydrochloride (3.12 g, 19.0 mmol) were suspended in dry ACN (100 mL) in a 200-mL Schlenk flask equipped with a 60-mL addition funnel. **A.1** (2.05 g, 9.5 mmol) was cycled 3x under high vacuum and dissolved in dry ACN (40 mL). This solution was cannula-transferred to the addition funnel and added dropwise to the stirring reaction mixture over 1 hr. Upon complete addition, the Schlenk flask was fitted with a reflux condenser under N_2 and heated to 86 °C overnight. During this time, the reaction went from a heterogeneous but mostly colorless solution to a pink solution with suspended white solid. Upon completion, the reaction was cooled to room temperature and the white solid was removed *via* vacuum filtration. The resultant solution was concentrated *in vacuo*. The crude product was purified by silica gel column chromatography (95:5 v/v DCM:MeOH) to afford an amber oil (3.56 g, 94%). ^{1}H NMR (400 MHz, $CDCl_3$) δ: 8.49 (d with hyperfine coupling, 2H, *J* = 4.9), 7.62 (td, 2H, *J* = 13.2, 7.4, 2), 7.51 (d, 2H, *J* = 7.6), 7.11 (t with hyperfine coupling, 2H, *J* = 2.4), 4.53 (s, broad, 1 H), 3.77 (s, 4H), 3.04 (m, 2H), 2.50 (t, 2H, *J* = 6.2), 2.27 (s, 1H), 1.51 (m, 2H), 1.39 (m, 11H), 1.24 (m, 4H). ^{13}C {^{1}H} NMR (100 MHz, $CDCl_3$) δ: 160.01, 155.91,

148.88, 136.30, 122.79, 121.81, 78.93, 60.45, 54.23, 40.45, 29.94, 28.38, 26.92, 26.88, 26.54.

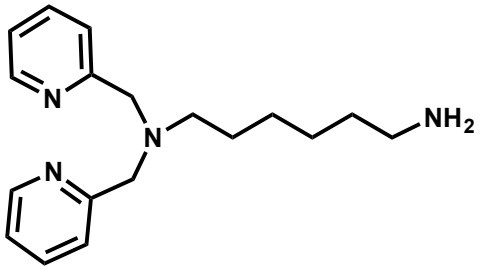

***N,N*-bis(pyridin-2-ylmethyl)hexane-1,6-diamine [A.3]: A.2** (3.56 g, 8.9 mmol) was dissolved in DCM (120 mL) and cooled to 0 °C in an ice bath. Trifluoroacetic acid (6.6 mL, 10.2 g, 89.3 mmol) was added and the reaction was stirred for 20 mins at 0 °C before removing the ice bath and stirring at room temperature for 7 hrs. Upon completion, the reaction was concentrated *in vacuo* and the crude product mixture was redissolved in DCM (50 mL) and DI H_2O (50 mL). This solution was transferred to a separatory funnel and 1 M NaOH was added slowly to pH ~ 9. The layers were separated, and the aqueous phase was extracted with DCM (2 x 50 mL). The combined organic phases were washed with DI H_2O (1 x 50 mL) and brine (1 x 50 mL), dried over Na_2SO_4, and concentrated *in vacuo* to yield the desired product as an amber oil (1.86 g, 70%). ^{1}H NMR (400 MHz, CH_3OD) δ: 8.69 (d, 2H, *J* = 5.2), 8.00 (td, 2H, *J* = 15.6, 7.8, 1.6), 7.62 (d, 2H, *J* = 7.6), 7.54 (dd, 2H, *J* = 7.4, 2.2), 4.56 (s, 4H), 3.18 (m, 2H), 2.90 (m, 2H), 1.80 (m, 2H), 1.64 (m, 2H), 1.38 (m, 4H). ^{13}C {^{1}H} NMR (100 MHz, CH_3OD) δ: 152.21, 149.34, 140.63, 125.90, 125.77, 58.28, 56.17, 40.45, 28.24, 27.04, 26.88, 25.32. HRMS (ESI^+): calcd for $C_{18}H_{26}N_4$ *m/z* 299.2230, found 299.2235.

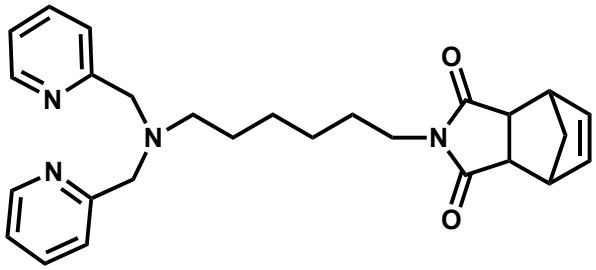

2-(6-(bis(pyridin-2-ylmethyl)amino)hexyl)-3a,4,7,7a-tetrahydro-1*H*-4,7-methanoisoindole-1,3(2*H*)-dione [A.4]: A.3 (3.09 g, 10.4 mmol) and 5-norbornene-2,3-dicarboxylic anhydride (compound **2.7**) (1.87 g, 11.4 mmol) were dissolved in toluene (50 mL) in a small round-bottomed flask equipped with a reflux condenser. The reaction was heated to 115 °C overnight, open to air. Upon cooling, the reaction was concentrated *in vacuo* and the crude product was purified by silica gel column chromatography (95:4:1 v/v/v DCM:MeOH:Et_3N) to yield the product as an amber oil (4.20 g, 91%). ^{1}H NMR (400 MHz, $CDCl_3$) δ: 8.47 (d with hyperfine coupling, 2H, J = 4.8), 7.62 (td, 2H, J = 15.2, 7.6, 1.6), 7.49 (d, 2H, J = 7.6), 7.10 (t with hyperfine coupling, 2H, J = 6.2), 6.03 (t, 2H, J = 1.8), 3.75 (s, 4H), 3.33 (m, 2H), 3.23 (t, 2H, J = 7.4), 3.18 (m, 2H), 2.47 (t, 2H, J = 7.2), 1.68 (dt, 1H, J = 8.8, 1.6), 1.48 (m, 3H), 1.34 (m, 2H), 1.21 (m, 2H), 1.12 (m, 2H). ^{13}C {^{1}H} NMR (100 MHz, $CDCl_3$) δ: 177.68, 160.04, 148.90, 136.31, 134.34, 122.77, 121.81, 60.45, 54.23, 52.16, 45.66, 44.84, 38.30, 27.72, 26.96, 26.80, 26.67. HRMS (ESI^+): calcd for $C_{27}H_{32}N_4O_2$ *m/z* 467.2417 $(M+Na)^+$, found 467.2422. Elemental analysis: theoretical: C, 72.94; H, 7.26; N, 12.6; found: C, 72.82; H, 7.18; N, 12.59.

Synthesis of Metallated DPA-Zn Monomers [A.5—A.8]

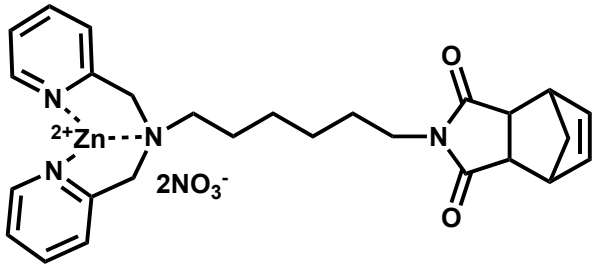

2-(6-(bis(pyridin-2-ylmethyl)amino)hexyl)-3a,4,7,7a-tetrahydro-1*H*-4,7-methanoisoindole-1,3(2*H*)-dione—$Zn(NO_3)_2$ complex [A.5]: A.4 (0.43 g, 1.0 mmol) was dissolved in MeOH (4 mL) in a small round-bottomed flask. $Zn(NO_3)_2 \bullet 6H_2O$ (0.29 g, 1.0 mmol) was dissolved in MeOH (4 mL) and added to the round-bottomed flask dropwise. The reaction was stirred at room temperature for 1 hr before concentrating *in vacuo* to yield the desired product as a white-tan solid (0.59 g, 98%). ^{1}H NMR (400 MHz, $CDCl_3$) δ: 8.78 (d, 2H, *J* = 5.6), 7.97 (td, 2H, *J* = 15.4, 7.8, 1.6), 7.52 (t, 2H, *J* = 5.2), 7.41 (d, 2H, *J* = 7.6), 6.02 (s, 2H), 4.24 (m, 4H), 3.34 (s, 2H), 3.21 (m, 4H), 2.55 (t, 2H, *J* = 8.4), 1.71 (d, 1H, *J* = 8.8), 1.52 (d, 1H, *J* = 8.8), 1.41-1.25 (m, 4H), 1.08 (m, 4H). ^{13}C {^{1}H} NMR (100 MHz, $CDCl_3$) δ: 177.72, 154.17, 148.87, 140.62, 134.34, 125.15, 123.52, 57.55, 53.42, 52.19, 45.68, 44.81, 37.82, 27.20, 26.40, 26.12, 22.75. HRMS (ESI^+): calcd for $C_{27}H_{32}N_4O_2Zn$ *m/z* 254.0903, found 254.0906.

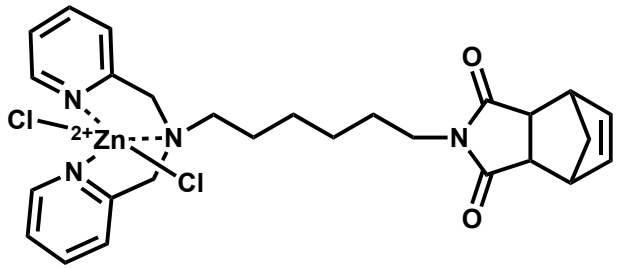

2-(6-(bis(pyridin-2-ylmethyl)amino)hexyl)-3a,4,7,7a-tetrahydro-1*H*-4,7-methanoisoindole-1,3(2*H*)-dione—$ZnCl_2$ complex [A.6]: A.4 (0.51 g, 1.1 mmol) was dissolved in DCM (8 mL) in a small glass vial. $ZnCl_2$ (0.16 g, 1.2 mmol) was dissolved in ACN (8 mL) and added to the stirring ligand solution. The reaction was loosely capped and stirred overnight at room temperature. Upon completion, the reaction solution was concentrated *in vacuo* to yield the desired product as a brown viscous oil that slowly crystallized upon sitting (0.66 g, quantitative). ^{1}H NMR (400 MHz, $CDCl_3$) δ: 9.04 (d, 2H, *J* = 5.2), 7.83 (td, 2H, *J* = 15.2, 7.6, 1.6), 7.38 (t, 2H, *J* = 6.4), 7.33 (d, 2H, *J* = 1.9), 5.91 (t, 2H, *J* = 1.8), 4.10 (s, 4H), 3.23 (m, 2H), 3.14 (m, 2H), 3.08 (t, 2H, *J* = 7.4), 2.49 (t, 2H, *J* = 8.4), 1.59 (d, 1H, *J* = 8.8), 1.43 (d, 1H, *J* = 8.8), 1.24-1.16 (m, 4H), 0.95 (m, 4H). HRMS (ESI^+): calcd for $C_{27}H_{32}ClN_4O_2Zn$ *m/z* 543.1500, found 543.1498.

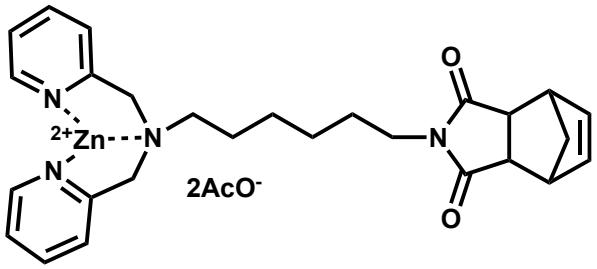

2-(6-(bis(pyridin-2-ylmethyl)amino)hexyl)-3a,4,7,7a-tetrahydro-1*H*-4,7-methanoisoindole-1,3(2*H*)-dione—$Zn(OAc)_2$ complex [A.7]: A.4 (0.48 g, 1.1 mmol) was dissolved in MeOH (4 mL) in a small glass vial. $Zn(OAc)_2$•$2H_2O$ (0.23, 1.1 mmol) was dissolved in MeOH (3 mL) and added to the stirring ligand solution. The reaction

was stirred at room temperature for 1.5 hrs before concentrating *in vacuo* to yield the desired product as a viscous oil that crystallized upon sitting (0.64 g, 96%). ^{1}H NMR (400 MHz, CD_2Cl_2) δ: 8.79 (d, 2H, *J* = 5.2), 7.86 (td, 2H, *J* = 15.4, 7.8, 1.6), 7.42 (t, 2H, *J* = 6.3), 7.32 (d, 2H, *J* = 8), 6.00 (t, 2H, *J* = 1.8), 4.20 (d, broad, 4H, *J* = 40.0), 3.29 (m, 2H), 3.20-3.16 (m, 4H), 2.52 (m, 2H), 1.86 (s, 6H), 1.66 (dt, 1H, *J* = 8.8, 1.8), 1.50 (d, 1H, *J* = 8.8), 1.37-1.24 (m, 4H), 1.12-1.03 (m, 4H). HRMS (ESI$^+$): calcd for $C_{29}H_{35}N_4O_4Zn$ *m/z* 567.1944, found 567.1941.

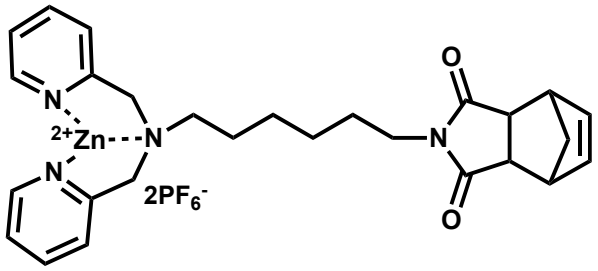

2-(6-(bis(pyridin-2-ylmethyl)amino)hexyl)-3a,4,7,7a-tetrahydro-1*H*-4,7-methanoisoindole-1,3(2*H*)-dione—Zn(PF$_6$)$_2$ complex [A.8]: A.6 (0.48 g, 0.8 mmol) was dissolved in DCM (5 mL) in a small glass vial. $AgPF_6$ (0.21 g, 0.8 mmol) was added to reaction and the reaction vessel was loosely capped and stirred for 2 hrs, during which the solution when from dark brown to mauve in color. Upon completion, the reaction was filtered to remove the suspended grey solid (AgCl) and the resultant solution was concentrated *in vacuo* to yield the desired product as a brown oil (0.52 g, 77%). ^{1}H NMR (400 MHz, CD_2Cl_2) δ: 8.87 (d, 2H, *J* = 5.6), 8.06 (td, 2H, *J* = 15.2, 7.6, 1.6), 7.58 (m, 4H), 6.03 (t, 2H, *J* = 1.8), 4.26 (d, 2H, *J* = 15.6), 4.08 (d, 2H, *J* = 16), 3.31 (m, 2H), 3.23 (m, 4H), 2.91 (m, 2H), (dt, 1H, *J* = 8.8, 1.6), 1.53 (d, 2H, 8.8), 1.44 (m, 2H), 1.35 (m, 2H), 1.20 (m, 4H). ^{19}F NMR (376 MHz, CD_2Cl_2): -71.82, -73.71. HRMS (ESI$^+$): calcd for $C_{27}H_{32}ClN_4O_2Zn$ *m/z* 543.1500, found 543.1498.

Polymerization of DPA homopolymer and Ter-DPA block copolymer [PA.1 – PA.4]

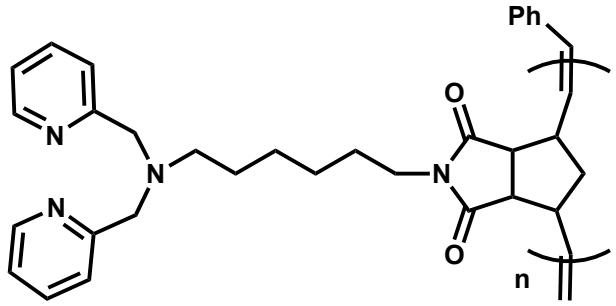

Poly(2-(6-(bis(pyridin-2-ylmethyl)amino)hexyl)-3a,4,7,7a-tetrahydro-1*H*-4,7-methanoisoindole-1,3(2*H*)-dione) [PA.1]: ^{1}H NMR (representative homopolymer, 400 MHz, CD_2Cl_2) all signals broad singlets unless otherwise stated, δ: 8.45 (2H), 7.63 (2H), 7.52 (2H), 7.11 (2H), 5.65-5.45 (broad d, 2H), 3.74 (4H), 3.36 (2H), 3.16 (2H), 2.87 (1H), 2.48 (2H), 1.79 (1H), 1.49 (4H), 1.24 (6H).

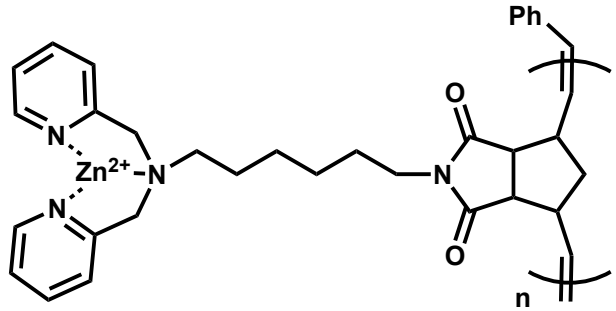

Poly(2-(6-(bis(pyridin-2-ylmethyl)amino)hexyl)-3a,4,7,7a-tetrahydro-1*H*-4,7-methanoisoindole-1,3(2*H*)-dione)—Zn(NO_3)$_2$ complex [PA.2]: ^{1}H NMR (400 MHz, D_2O) all signals broad singlets unless otherwise stated, δ: 8.45 (2H), 7.85 (2H), 7.39 (4H), 5.35 (2H), 4.13–3.92 (broad doublet, 4H), 3.28–3.00 (6H), 2.46 (2H), 1.29–0.90 (10H).

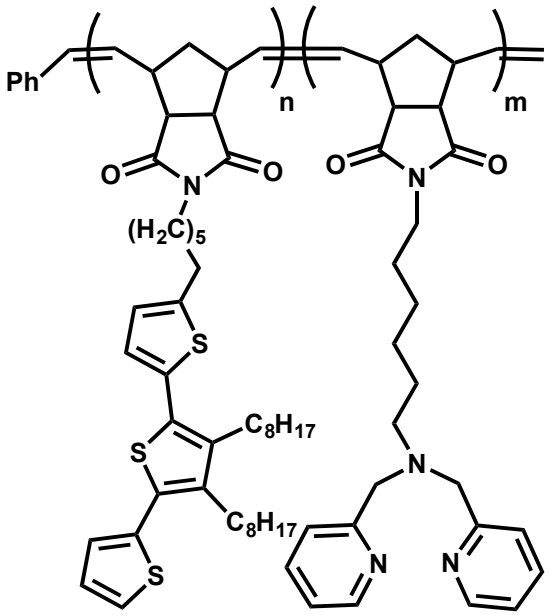

Poly(2-(6-(3',4'-dioctyl-[2,2':5',2''-terthiophen]-5-yl)hexyl)isoindoline-1,3-dione)-*block*-poly(2-(6-(bis(pyridin-2-ylmethyl)amino)hexyl)-3a,4,7,7a-tetrahydro-1*H*-4,7-methanoisoindole-1,3(2*H*)-dione) (Ter-*b*-DPA) [PA.3]: ^{1}H NMR (400 MHz, CD_2Cl_2) all signals broad singlets unless otherwise stated, δ: 8.46 (2H), 7.64 (2H), 7.52 (2H), 7.29 (1H), 7.11 (3H), 7.04 (1H), 6.91 (1H), 6.70 (1H), 5.66-5.51 (broad d, 4H), 3.75 (4H), 3.42 (4H), 3.18 (6H), 2.78 (3H), 2.66 (4H), 2.49 (2H), 1.85 (2H), 1.67–1.19 (multiple overlapping broad singlets, 43H), 0.88 (6H).

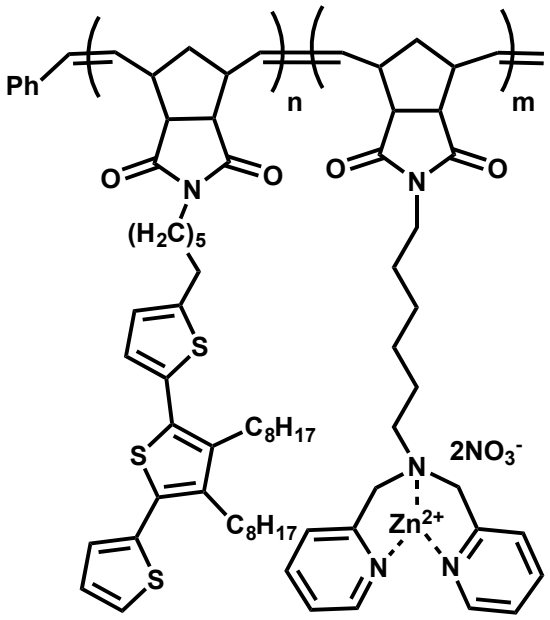

Poly(2-(6-(3',4'-dioctyl-[2,2':5',2''-terthiophen]-5-yl)hexyl)isoindoline-1,3-dione)-*block*-poly(2-(6-(bis(pyridin-2-ylmethyl)amino)hexyl)-3a,4,7,7a-tetrahydro-1*H*-4,7-methanoisoindole-1,3(2*H*)-dione)–$Zn(NO_3)_2$ complex (Ter-*b*-DPA-$Zn(NO_3)_2$) [PA.4]: ^{1}H NMR (400 MHz, CD_2Cl_2) all signals broad singlets unless otherwise stated, δ: 8.68 (2H), 8.02 (2H), 7.54 (4H), 7.26 (1H), 7.08 (1H), 7.01 (1H), 6.88 (1H), 6.72 (1H), 5.62-5.41 (broad d, 4H), 4.29–4.08 (weak dd, 4H, *J* = 52.8, 14.8), 3.41–3.16 (broad overlapping signals, 10H), 2.90 (2H), 2.74 (2H), 2.63 (6H), 1.85 (2H), 1.64–1.11 (multiple overlapping broad singlets, 43H), 0.85 (6H).

RESULTS AND DISCUSSION

DPA Monomer Synthesis and Metallation

The DPA monomer was synthesized following modified literature procedures (**Scheme A.2**).[278,282] The first step of the synthesis involved the asymmetric Boc-protection of 1,6-diaminohexane to yield compound **A.1** in good yield. Reaction of compound **A.1** with two equivalents of 2-chloromethylpyridine hydrochloride under

basic conditions provided the DPA end group (**A.2**) in one step. Deprotection of the Boc-protected amine with trifluoroacetic acid yielded compound **A.3**, which was then condensed with the norbornene dione anhydride (compound **2.7**) to afford the desired DPA monomer in 51% overall yield over the 4 steps. This monomer could be easily metallated with a variety of zinc salts, including zinc nitrate hexahydrate ($Zn(NO_3)_2 \bullet 6H_2O$) (**A.5**), zinc acetate dihydrate ($Zn(OAc)_2 \bullet 2H_2O$) (**A.6**), and anhydrous $ZnCl_2$ (**A.7**). The DPA-$Zn(PF_6)_2$ complex (**A.8**) could also be accessed through anion exchange of the DPA-$ZnCl_2$ with $AgPF_6$. Upon complexation, the benzylic-like protons alpha to the amine demonstrated a large downfield shift in ^1H NMR from ~3.7 ppm to ~4.2 ppm as a result of decreased shielding (electron density) due to electron donation by the nitrogen atoms of the DPA ligand onto the Zn metal center.

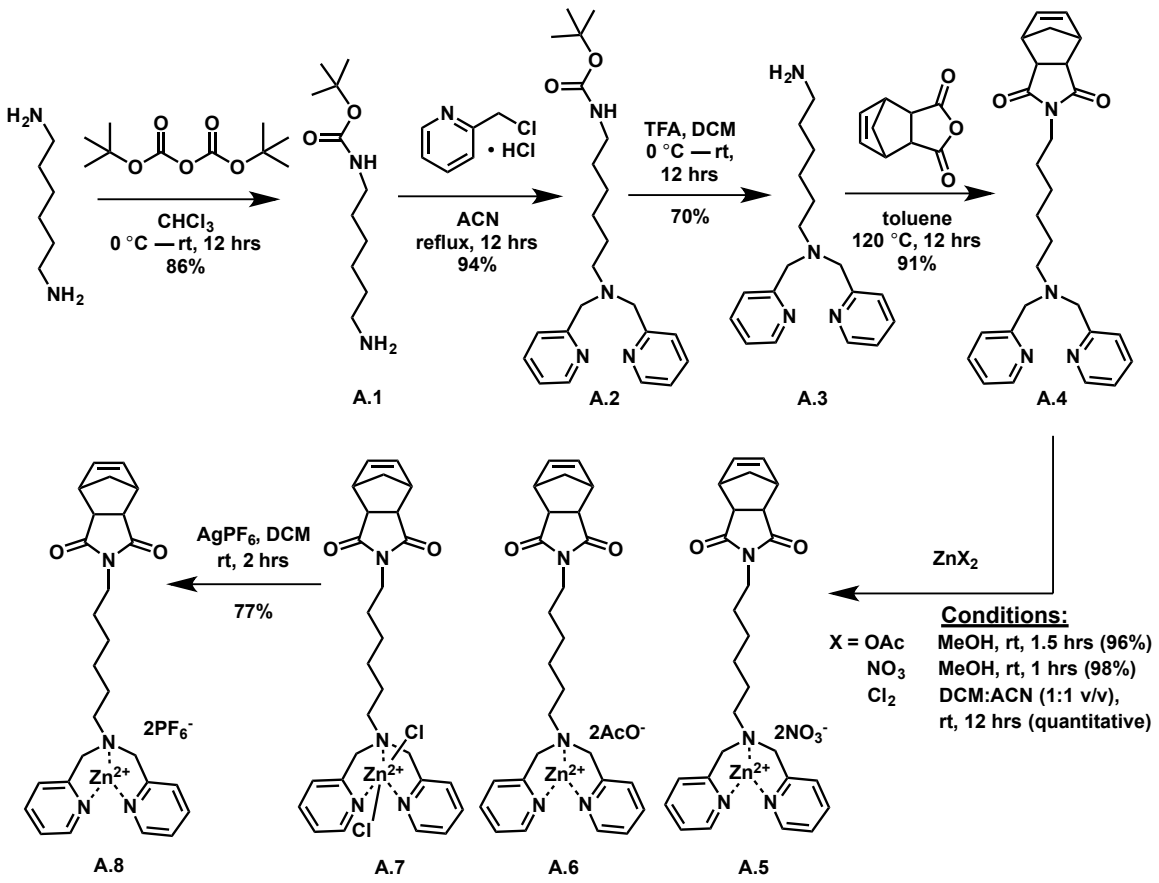

Scheme A.2. Synthetic route for DPA monomer **A.4** and DPA-ZnX_2 complexes **A.5 – A.8**.

Polymerization of DPA Monomer and DPA-ZnX_2 Monomers

Polymerization of the DPA monomer (**A.4**) was carried out using Grubbs' 2nd generation catalyst (G2) and Grubbs' 3rd generation catalyst (G3) under inert atmosphere with *[M]/[I]* = 50 for all polymerization trials (M_n^{theo} = 22.2 kDa). Due to the coordinating nature of the DPA pendant group, homopolymerization attempts of **A.4** were carried out in several different solvents, including acetone, DCM, and dimethylformamide (DMF). Polymerizations were run for 12 hrs, after which TLC showed complete consumption of the monomeric species. Upon completion, polymerizations were removed from the glovebox and terminated with excess ethyl vinyl

ether, concentrated to approximate dryness *in vacuo*, and purified by precipitation from small amount of DCM into hexanes (3x). Hexanes was used as the precipitation solvent for the purification step due to the good solubility of the DPA homopolymers (**PA.1**) in MeOH as a result of the polar pendant group. Successful polymerization in all three solvents were confirmed by ^{1}H NMR, with characteristic broadening of the proton signals in the polymeric material compared to the monomer, as well an upfield shift and splitting of the norbornene alkene protons from a triplet at ~6.0 ppm in the monomer to two peaks at ~5.6 ppm and ~5.5 ppm in the polymer, observed for all of the synthesized DPA homopolymers. Unfortunately, molecular weight characterization by GPC in THF was unsuccessful despite good solubility of the polymer, possibly due to unfavorable interactions between the DPA pendant ligand and the GPC column material. End-group analysis using ^{1}H NMR could not be utilized due to overlapping aromatic signals from the DPA pyridine protons with the phenyl endgroup. One possible solution to this characterization issue would be to quench the polymerization with vinylene carbonate or molecular oxygen instead of ethyl vinyl ether, which would provide an aldehyde endgroup handle to use for ^{1}H NMR molecular weight analysis.

All polymerization attempts of the DPA-$Zn(NO_3)_2$ monomer complex (**A.5**) were unsuccessful, as evidenced by the lack of signal broadening, as well as the lack of shift in the norbornene alkene proton signal in ^{1}H NMR. Grubbs 1st (G1), G2, and G3 were all unsuccessful, as was changing the *[M]/[I]* ratio. Furthermore, using DMF instead of DCM proved futile. Using a solvent mixture of 1:1 (v/v) DCM:MeOH, thinking that the addition of MeOH would improve solubility of the polar DPA-$Zn(NO_3)_2$ monomer and the growing polymer chain, was also unsuccessful. In order to determine if the nitrate anions were affecting polymerization, polymerization attempts of the DPA-$Zn(OAc)_2$ monomer (**A.6**) and DPA-$ZnCl_2$ (**A.7**) utilizing G1, G2, and G3 in DCM were carried out

under inert conditions. However, all of these polymerizations were unsuccessful as well based on ^{1}H NMR. The DPA-Zn(PF_6)$_2$ monomer (**A.8**) was synthesized due to the weakly-coordinating nature of the PF_6 anion, under the premise that the highly-coordinating nitrate, acetate, and chloride anions may be inhibiting polymerization, either by preventing oxidative addition of the DPA monomer to the Ru-metal center or by inhibiting monomer addition to the growing polymer chain. However, polymerization attempts with **A.8** in DCM or DMF using either G2 or G3 were unsuccessful. The desire to polymerize the metallated DPA monomer stemmed from the fact that metallation prior to polymerization is more facile due to the discrete nature of the monomeric species. Furthermore, it ensures quantitative coordination and allows for removal of excess ZnX_2 and purification of the metallated monomer prior to polymerization. However, since none of the polymerization attempts using the metallated monomers were successful, post-polymerization zinc metallation was attempted with the previously synthesized DPA homopolymer.

Metallation of the DPA homopolymer **PA.1** (0.20 g, M_n^{theo} = 22.2 kDa, N_n^{theo} = 50, ~0.45 mmol) was carried out using Zn(NO_3)$_2$•6H_2O (0.16 g, 0.54 mmol). To perform the metallation, Zn(NO_3)$_2$•6H_2O was dissolved in MeOH (3 mL) and added to the stirring solution of **PA.1** in DCM (6 mL) at room temperature. Upon addition of the zinc salt, the polymer solution went from amber to maroon in color. The metallation reaction was loosely capped and run overnight at room temperature. Upon completion, ^{1}H NMR in D_2O indicated quantitative metallation, as evidenced by a downfield shift of the benzylic-like protons from ~3.8 ppm to ~4.2 ppm. The metallated DPA-Zn(NO_3)$_2$ homopolymer (**PA.2**) was insoluble in both pure MeOH and pure DCM, but was soluble in water, likely due to the presence of the nitrate anions. Anion exchange using KPF_6 to improve solubility in organic solvents was unsuccessful.

Once post-polymerization metallation of the DPA homopolymer **PA.1** had been successfully carried out, a Ter-DPA BCP (**PA.3)** was synthesized using G2 in DCM under inert conditions, first polymerizing the Ter monomer (**2.13**) with $[M]_{Ter}/[I]$ = 28, and monitoring by TLC until complete consumption of the monomer was confirmed. Then, an equimolar amount of DPA monomer (**A.4)** was added and the polymerization was continued overnight, after which complete consumption of the DPA monomer was confirmed by TLC. The BCP was removed from the glovebox, terminated with ethyl vinyl ether, concentrated *in vacuo*, and purified by precipitation from DCM into hexanes (3x). ^{1}H NMR was used to confirm copolymerization and to verify incorporation of the Ter and DPA segments in an equimolar ratio in the final diblock copolymer (M_n^{theo} = 32.6 kDa). Again, GPC characterization of the diblock copolymer could not be carried out, despite the incorporation of the Ter block.

A sample of the Ter-DPA BCP was metallated following a similar procedure as for the DPA homopolymer using excess $Zn(NO_3)_2 \bullet 6H_2O$ to give the Ter-DPA-$Zn(NO_3)_2$ BCP complex (**PA.4**). To perform the metallation, **PA.3** (0.15 g, M_n^{theo} = 32.6 kDa, N_n^{DPA} = 28, ~0.13 mmol DPA) was dissolved in DCM (12 mL) and $Zn(NO_3)_2 \bullet 6H_2O$ (0.056 g, 0.19 mmol) in MeOH:DCM (3:1 v/v, 8 mL) was added dropwise to the stirring BCP solution. The metallation was stirred at room temperature overnight before concentrating *in vacuo*. The resulting sticky solid was soluble in a 2:1 (v/v) DCM:MeOH mixture, although it was insoluble in both pure MeOH and pure DCM. ^{1}H NMR shows quantitative metallation based on the downfield shift, and splitting into a weak doublet of doublets, of the benzylic-like protons of the DPA pendant group from ~3.7 ppm to ~4.3 ppm. There are also shifts in the pyridine protons.

Photophysical and Electrochemical Characterization

UV-Vis spectroscopy shows a high-energy absorption for the DPA monomer **A.1** and DPA homopolymer **PA.1** at 262 nm (see **Figure A.2A**). This is likely related to an n-π^* transition in the DPA pendant group. **PA.1** shows slight red-edge broadening in the absorption profile compared to **A.1**. Metallation of the DPA homopolymer does not significantly change the absorption maxima of the DPA material, although the red-edge broadening is no longer present in **PA.2**. This suggests that the observed broadening in the DPA homopolymer is related to intrachain interactions between the pyridine rings of the DPA moieties, which are disrupted upon metallation with $Zn(NO_3)_2$. The molar absorptivity of the DPA monomer was determined to be ε = 6,265 $M^{-1}cm^{-1}$, consistent with an n-π^* transition.

UV-Vis spectroscopy of the Ter-DPA BCP (**PA.3**) shows absorption peaks corresponding to the individual DPA chromophore (λ = 263 nm) and the Ter chromophore (λ = 339 nm) (see **Figure A.2B**). The retention of the individual absorptions, as well as the lack of new peaks, indicates that the DPA and Ter pendant groups groups do not interact in the ground state.

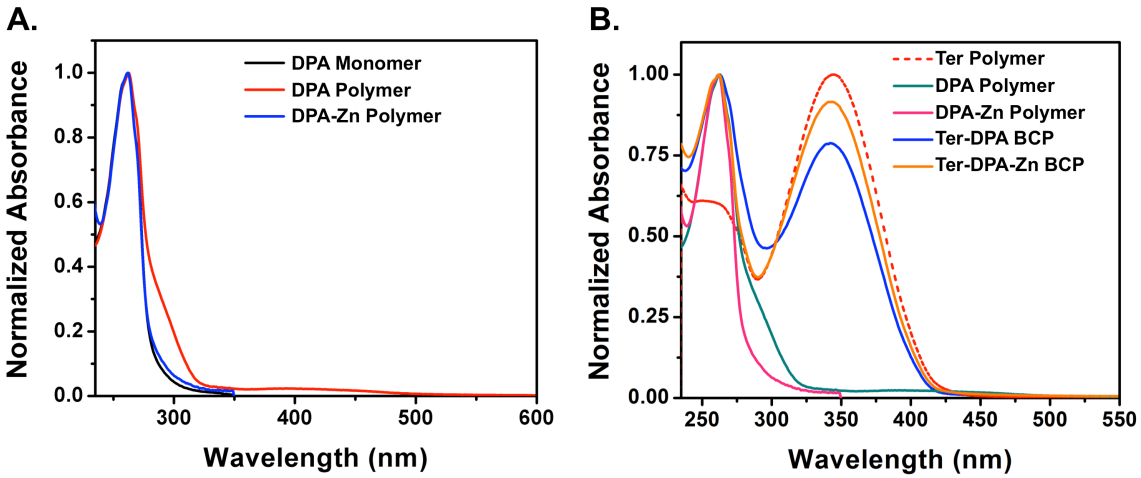

Figure A.2. UV-Vis spectra in DCM of the DPA materials: (A) DPA monomer (**A.4**), DPA homopolymer (**PA.1**), and DPA-Zn$(NO_3)_2$ polymer (**PA.2**); (B) Ter Polymer (**P2.1**), DPA polymer (**PA.1**), DPA-Zn$(NO_3)_2$ polymer (**PA.2**), Ter-DPA BCP (**PA.3**), and Ter-DPA-Zn$(NO_3)_2$ BCP (**PA.4**); λ_{DPA} = 262 nm and λ_{Ter} = 339 nm.

The DPA monomer and DPA homopolymer show no emission upon excitation at 262 nm. For the Ter-DPA BCP **PA.3**, the excitation of the copolymer matches that of the previously synthesized Ter homopolymer (**P2.1**), with λ_{ex} = 354 nm (**Figure A.3**). However, the emission profile of the diblock copolymer more closely matches that of the Ter monomer (**2.13**), demonstrating a blue shoulder similar to what was observed with the Ter-PEG BCPs (see **P4.2** series). This is likely related to disruption of Ter aggregation due to the presence of the polar DPA pendant groups.

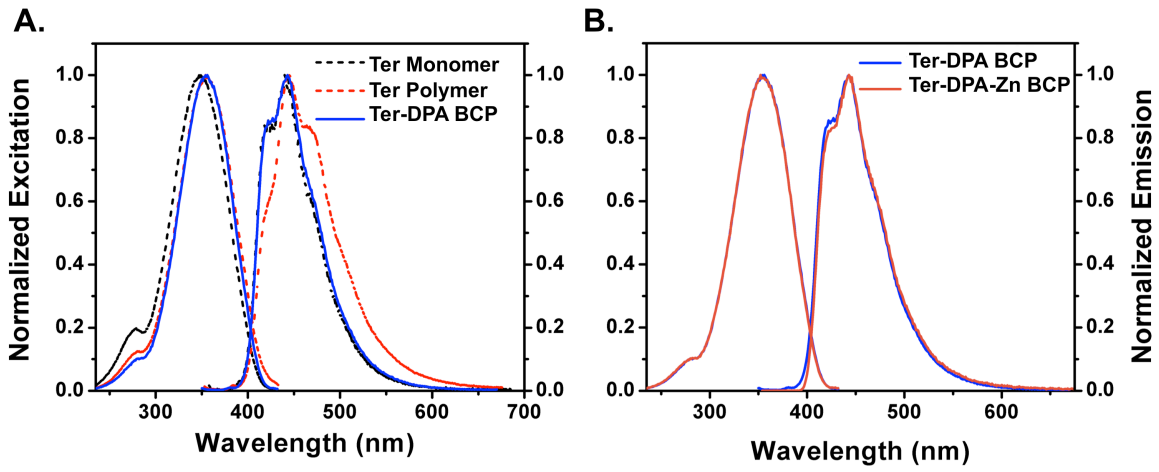

Figure A.3. (A) Excitation and emission profile of Ter-DPA BCP (**PA.3**, blue line), with Ter monomer (**2.13**, black line) and Ter polymer (**P2.1**, red line) shown for comparison; (B) Excitation and emission profiles of Ter-DPA BCP (**PA.3**) and Ter-DPA-Zn$(NO_3)_2$ BCP (**PA.4**).

Figure A.4 shows the cyclic voltammetry (CV) of the DPA monomer (**A.4**) and DPA homopolymer (**PA.1**). The DPA monomer shows a clear reductive event with onset at -0.91 V vs. Fc/Fc^+. The DPA homopolymer also shows a reductive event with onset at -1.19 V vs. Fc/Fc+. **Figure A.5** shows an overlay of the CV scans for the Ter-DPA BCP (**PA.3**) and metallated Ter-DPA-Zn$(NO_3)_2$ BCP (**PA.4**). The Ter-DPA BCP has a reductive event that looks very similar to that of the DPA homopolymer, with onset at -1.22 V vs. Fc/Fc^+. There is also a small oxidation event with onset at 0.42 V vs. Fc/Fc^+, which could correspond to oxidation of the Ter pendant groups, since Ter polymer exhibits an oxidation event with onset at approximately 0.35 V vs. Fc/Fc^+.

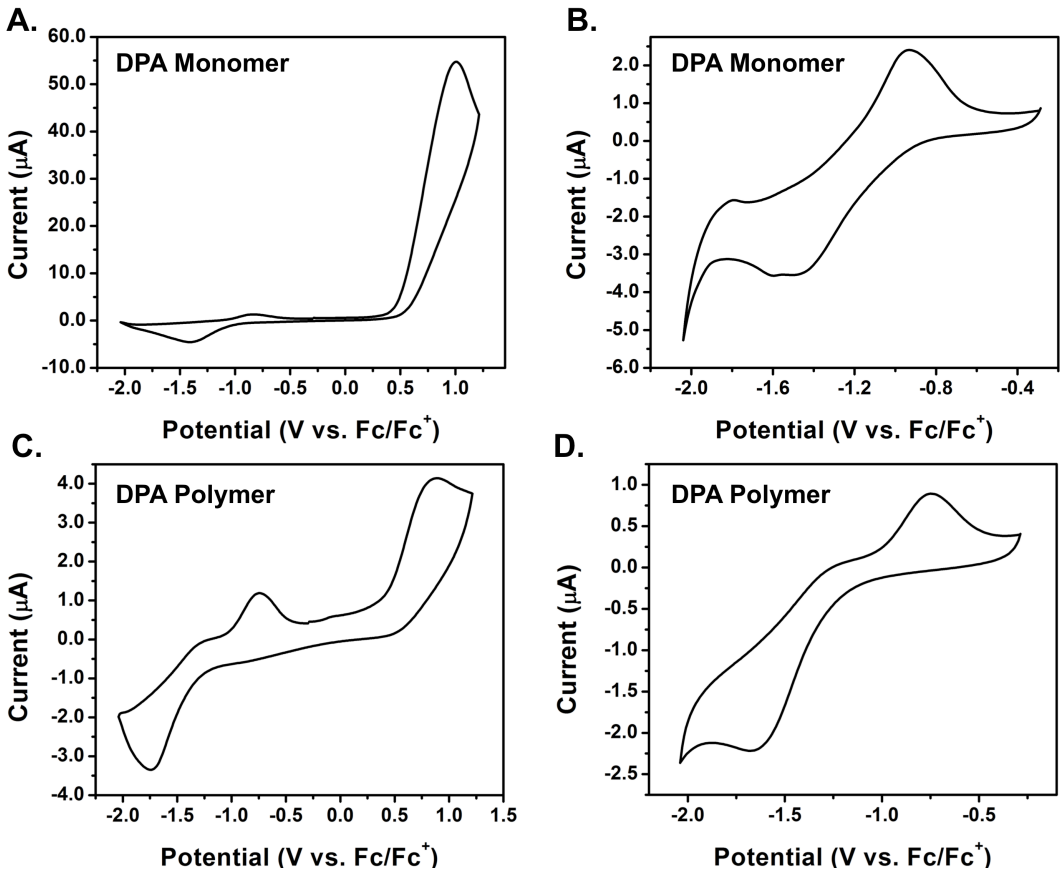

Figure A.4. CV scans in DCM under inert atmosphere of (A,B) DPA monomer (**A.4**), onset of reduction = -0.91 V vs. Fc/Fc^+; (C,D) DPA homopolymer (**PA.1**), onset of reduction = -1.19 V vs. Fc/Fc^+.

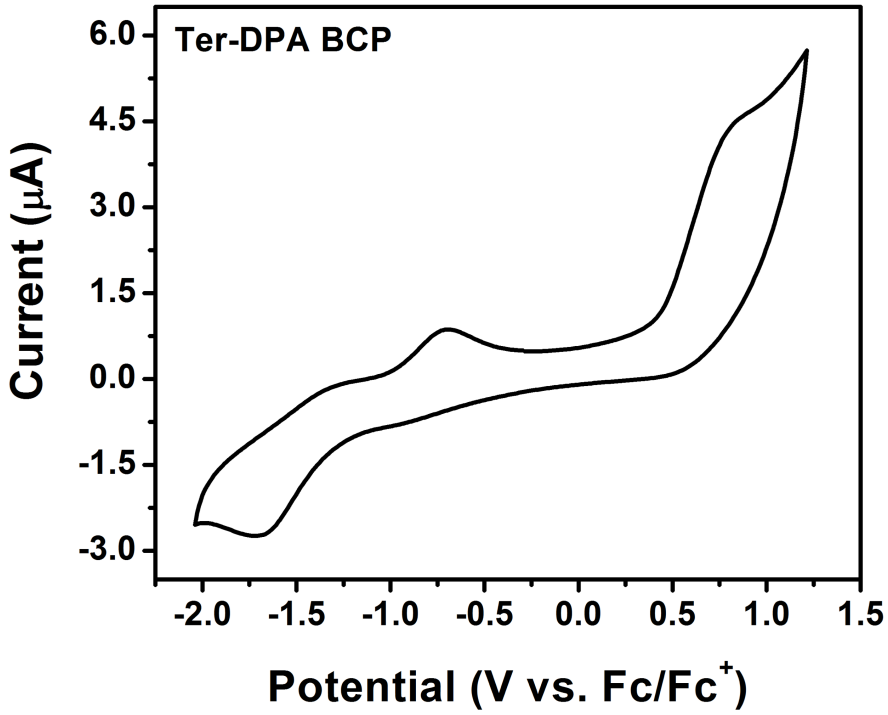

Figure A.5. CV scan in DCM under inert atmosphere of Ter-DPA BCP (**PA.3**). Onsets of oxidation and reduction shown in parentheses and reported vs. Fc/Fc^+ for **PA.3** (0.42 V, –1.22 V).

CONCLUSION

A novel norbornene type monomer with DPA pendant groups was synthesized. Homopolymerizations of the DPA monomer using either G2 or G3 in acetone, DCM, or DMF were successful, however limited molecular weight characterization could be performed. Polymerization attempts of the metallated DPA-ZnX_2 monomer were unsuccessful, but post-polymerization metallation using $Zn(NO_3)_2 \bullet 6H_2O$ provided the desired polymer with Zn-coordinated DPA pendant groups in quantitative yield. Block copolymers compromised of a semiconducting Ter segment and the Lewis-basic DPA segment were synthesized and the Ter-DPA BCP was successfully metallated post-polymerization. Photophysical and electrochemical characterization was carried out on

the DPA and Ter-DPA copolymer materials. Future directions for this project include changing the termination method for the polymerizations in order to introduce an endgroup handle that can be used for ^{1}H NMR molecular weight analysis of the polymers. Further investigation is needed into the electrochemical behavior of the metallated Ter-DPA BCP. From there, the DPA-Zn complex pendant groups should facilitate the seeded growth of ZnO NPs as a method to achieve directed growth of semiconducting nanoparticles.

References

(1) International Energy Outlook 2014 - Energy Information Administration http://www.eia.gov (accessed Jun 11, 2015).

(2) Darling, S. B.; You, F. The Case for Organic Photovoltaics. *RSC Adv*. **2013**, *3*, 17633–17648.

(3) Servaites, J. D.; Ratner, M. A.; Marks, T. J. Organic Solar Cells: A New Look at Traditional Models. *Energy Environ. Sci*. **2011**, *4*, 4410–4422.

(4) Topham, P. D.; Parnell, A. J.; Hiorns, R. C. Block Copolymer Strategies for Solar Cell Technology. *J. Polym. Sci. Part B Polym. Phys*. **2011**, *49*, 1131–1156.

(5) Chapin, D. M.; Fuller, C. S.; Pearson, G. L. A New Silicon P-N Junction Photocell for Converting Solar Radiation into Electrical Power. *J. Appl. Phys*. **1954**, *25*, 676.

(6) Perlin, J. The Silicon Solar Cell Turns 50. http://www.nrel.gov/education/pdfs/educational_resources/high_school/solar_cell_history.pdf (accessed Jun 11, 2015).

(7) Perlin, J. The Story of Solar Cells. In *Organic Photovoltaics: Mechanisms, Materials, and Devices*; Sun, S.-S., Sariciftci, N. S., Eds.; CRC Press, Taylor & Francis Group: Boca Rouge, FL, 2005; pp 3–18.

(8) Hepp, A. F.; Bailey, S. G. Forward 2. In *Organic Photovoltaics: Mechanisms, Materials, and Devices*; Sun, S.-S., Sariciftci, N. S., Eds.; CRC Press, Taylor & Francis Group: Boca Rouge, FL, 2005.

(9) Cao, W.; Xue, J. Recent Progress in Organic Photovoltaics: Device Architecture and Optical Design. *Energy Environ. Sci*. **2014**, *7*, 2123–2144.

(10) Green, M. A.; Emery, K.; Hishikawa, Y.; Warta, W.; Dunlop, E. D. Solar Cell Efficiency Tables. *Prog. Photovoltaics Res. Appl*. **2015**, *23*, 1–9.

(11) Annual Energy Outlook 2015 - Energy Information Administration http://www.eia.gov (accessed Jun 11, 2015).

(12) Service, R. F. Outlook Brightens for Plastic Solar Cells. *Science* **2011**, *332*, 293.

(13) Brabec, C.; Sariciftci, N. S.; Hummelen, J. C. Plastic Solar Cells. *Adv. Funct. Mater*. **2001**, *11*, 15–26.

(14) Coakley, K. M.; Mcgehee, M. D. Conjugated Polymer Photovoltaic Cells. *Chem. Mater*. **2004**, *16*, 4533–4542.

(15) Forrest, S. R. Electronic Appliances on Plastic. *Nature* **2004**, *428*, 911–918.

(16) Thompson, B. C.; Fréchet, J. M. J. Polymer-Fullerene Composite Solar Cells. *Angew. Chemie - Int. Ed*. **2008**, *47*, 58–77.

(17) Andersen, T. R.; Dam, H. F.; Hösel, M.; Helgesen, M.; Carle, J. E.; Larsen-Olsen, T. T.; Gevorgyan, S. a; Andreasen, J. W.; Adams, J.; Li, N.; Machui, F.;

Spyropoulos, G. D.; Ameri, T.; Lemaitre, N.; Legros, M.; Scheel, A.; Gaiser, D.; Kreul, K.; Berny, S.; Lozman, O. R.; Nordman, S.; Valimaki, M.; Vilkman, M.; Sondergaard, R. R.; Jorgensen, M.; Brabec, C. J.; Krebs, F. C. Scalable, Ambient Atmosphere Roll-to-Roll Manufacture of Encapsulated Large Area, Flexible Organic Tandem Solar Cell Modules. *Energy Environ. Sci.* **2014**, 2925–2933.

(18) Tang, C. W. Two-Layer Organic Photovoltaic Cell. *Appl. Phys. Lett.* **1986**, *48*, 183–185.

(19) Heliatek Consolidates Its Technology Leadership by Establishing a New World Record for Organic Solar Technology with a Cell Efficiency of 12%. *Heliatek* **2013**.

(20) Liu, Y.; Zhao, J.; Li, Z.; Mu, C.; Ma, W.; Hu, H.; Jiang, K.; Lin, H.; Ade, H.; Yan, H. Multiple Cases of High-Efficiency Polymer Solar Cells. *Nat. Commun.* **2014**, *5*, 5293–5301.

(21) Li, N.; Baran, D.; Forberich, K.; Machui, F.; Ameri, T.; Turbiez, M.; Carrasco-Orozco, M.; Drees, M.; Facchetti, A.; Krebs, F. C.; Brabec, C. J. Towards 15% Energy Conversion Efficiency: A Systematic Study of the Solution-Processed Organic Tandem Solar Cells Based on Commercially Available Materials. *Energy Environ. Sci.* **2013**, *6*, 3407–3413.

(22) Bundgaard, E.; Helgesen, M.; Carlé, J. E.; Krebs, F. C.; Jørgensen, M. Advanced Functional Polymers for Increasing the Stability of Organic Photovoltaics. *Macromol. Chem. Phys.* **2013**, *214*, 1546–1558.

(23) Su, Y.; Lan, S.; Wei, K. Organic Photovoltaics. *Materialstoday* **2012**, *15*, 554–562.

(24) Azzopardi, B.; Emmott, C. J. M.; Urbina, A.; Krebs, F. C.; Mutale, J.; Nelson, J. Economic Assessment of Solar Electricity Production from Organic-Based Photovoltaic Modules in a Domestic Environment. *Energy Environ. Sci.* **2011**, *4*, 3741–3753.

(25) de Boer, B.; Stalmach, U.; van Hutten, P. F.; Melzer, C.; Krasnikov, V. V.; Hadziioannou, G. Supramolecular Self-Assembly and Opto-Electronic Properties of Semiconducting Block Copolymers. *Polymer* **2001**, *42*, 9097–9109.

(26) Knupfer, M. Exciton Binding Energies in Organic Semiconductors. *Appl. Phys. A Mater. Sci. Process.* **2003**, *77*, 623–626.

(27) Brédas, J. L.; Cornil, J.; Heeger, A. J. The Exciton Binding Energy in Luminescent Conjugated Polymers. *Adv. Mater.* **1996**, *8*, 447–452.

(28) Darling, S. B. Block Copolymers for Photovoltaics. *Energy Environ. Sci.* **2009**, *2*, 1266–1273.

(29) Tao, Y.; McCulloch, B.; Kim, S.; Segalman, R. A. The Relationship between Morphology and Performance of Donor–acceptor Rod–coil Block Copolymer Solar Cells. *Soft Matter* **2009**, *5*, 4219–4230.

(30) Sommer, M.; Huettner, S.; Thelakkat, M. Donor–acceptor Block Copolymers for Photovoltaic Applications. *J. Mater. Chem.* **2010**, *20*, 10788–10797.

(31) Segalman, R. A.; McCulloch, B.; Kirmayer, S.; Urban, J. J. Block Copolymers for Organic Optoelectronics. *Macromolecules* **2009**, *42*, 9205–9216.

(32) Kippelen, B.; Bredas, J. L. Organic Photovoltaics. *Energy Environ. Sci.* **2009**, *2*, 251–261.

(33) Dimitrov, S. D.; Durrant, J. R. Materials Design Considerations for Charge Generation in Organic Solar Cells. *Chem. Mater.* **2014**, *26*, 616–630.

(34) Dennler, G.; Scharber, M. C.; Brabec, C. J. Polymer-Fullerene Bulk-Heterojunction Solar Cells. *Adv. Mater.* **2009**, *21*, 1323–1338.

(35) Park, S. H.; Roy, A.; Beaupré, S.; Cho, S.; Coates, N.; Moon, J. S.; Moses, D.; Leclerc, M.; Lee, K.; Heeger, A. J. Bulk Heterojunction Solar Cells with Internal Quantum Efficiency Approaching 100%. *Nat. Photonics* **2009**, *3*, 297–302.

(36) Zhang, M.; Wang, H.; Tang, C. W. Effect of the Highest Occupied Molecular Orbital Energy Level Offset on Organic Heterojunction Photovoltaic Cells. *Appl. Phys. Lett.* **2010**, *97*, 4–7.

(37) Coropceanu, V.; Cornil, J.; da Silva Filho, D. A.; Olivier, Y.; Silbey, R.; Bredas, J. L. Charge Transport in Organic Semiconductors. *Chem. Rev.* **2007**, *107*, 926–952.

(38) Yassar, A.; Miozzo, L.; Gironda, R.; Horowitz, G. Rod–coil and All-Conjugated Block Copolymers for Photovoltaic Applications. *Prog. Polym. Sci.* **2013**, *38*, 791–844.

(39) Scharber, M. C.; Mühlbacher, D.; Koppe, M.; Denk, P.; Waldauf, C.; Heeger, A. J.; Brabec, C. J. Design Rules for Donors in Bulk-Heterojunction Solar Cells—Towards 10 % Energy-Conversion Efficiency. *Adv. Mater.* **2006**, *18*, 789–794.

(40) Qi, B.; Wang, J. Fill Factor in Organic Solar Cells. *Phys. Chem. Chem. Phys.* **2013**, *15*, 8972–8982.

(41) Dibb, G. F. A.; Jamieson, F. C.; Maurano, A.; Nelson, J.; Durrant, J. R. Limits on the Fill Factor in Organic Photovoltaics: Distinguishing Nongeminate and Geminate Recombination Mechanisms. *J. Phys. Chem. Lett.* **2013**, *4*, 803–808.

(42) Watkins, P. K.; Walker, A. B.; Verschoor, G. L. B. Dynamical Monte Carlo Modelling of Organic Solar Cells: The Dependence of Internal Quantum Efficiency on Morphology. *Nano Lett.* **2005**, *5*, 1814–1818.

(43) Yu, G.; Gao, J.; Hummelen, J. C.; Wudl, F.; Heeger, A. J. Polymer Photovoltaic Cells: Enhanced Efficiencies via a Network of Internal Donor-Acceptor Heterojunctions. *Science* **1995**, *270*, 1789–1791.

(44) Halls, J. J. M.; Walsh, C. A.; Greenham, N. C.; Marseglia, E. A.; Friend, R. H.; Moratti, S. C.; Holmes, A. B. Efficient Photodiodes from Interpenetrating Polymer Networks. *Nature* **1995**, *376*, 498–500.

(45) Brabec, C. J.; Gowrisanker, S.; Halls, J. J. M.; Laird, D.; Jia, S.; Williams, S. P. Polymer-Fullerene Bulk-Heterojunction Solar Cells. *Adv. Mater.* **2010**, *22*, 3839–3856.

(46) Urien, M.; Wantz, G.; Cloutet, E.; Hirsch, L.; Tardy, P.; Vignau, L.; Cramail, H.; Parneix, J.-P. Field-Effect Transistors Based on Poly(3-Hexylthiophene): Effect of Impurities. *Org. Electron.* **2007**, *8*, 727–734.

(47) Zhao, J.; Swinnen, A.; Van Assche, G.; Manca, J.; Vanderzande, D.; Van Mele, B. Phase Diagram of P3HT/PCBM Blends and Its Implication for the Stability of Morphology. *J. Phys. Chem. B* **2009**, *113*, 1587–1591.

(48) Virkar, A. A.; Mannsfeld, S.; Bao, Z.; Stingelin, N. Organic Semiconductor Growth and Morphology Considerations for Organic Thin-Film Transistors. *Adv. Mater.* **2010**, *22*, 3857–3875.

(49) Hiorns, R. C.; de Bettignies, R.; Leroy, J.; Bailly, S.; Firon, M.; Sentein, C.; Khoukh, A.; Preud'homme, H.; Dagron-Lartigau, C. High Molecular Weights, Polydispersities, and Annealing Temperatures in the Optimization of Bulk-Heterojunction Photovoltaic Cells Based on Poly(3-Hexylthiophene) or Poly(3-Butylthiophene). *Adv. Funct. Mater.* **2006**, *16*, 2263–2273.

(50) Erb, T.; Zhokhavets, U.; Gobsch, G.; Raleva, S.; Stühn, B.; Schilinsky, P.; Waldauf, C.; Brabec, C. J. Correlation Between Structural and Optical Properties of Composite Polymer/Fullerene Films for Organic Solar Cells. *Adv. Funct. Mater.* **2005**, *15*, 1193–1196.

(51) Schilinsky, P.; Asawapirom, U.; Scherf, U.; Biele, M.; Brabec, C. J. Influence of the Molecular Weight of Poly(3-Hexylthiophene) on the Performance of Bulk Heterojunction Solar Cells. *Chem. Mater.* **2005**, *17*, 2175–2180.

(52) Kim, Y.; Cook, S.; Tuladhar, S. M.; Choulis, S. A.; Nelson, J.; Durrant, J. R.; Bradley, D. D. C.; Giles, M.; McCulloch, I.; Ha, C.-S.; Ree, M. A Strong Regioregularity Effect in Self-Organizing Conjugated Polymer Films and High-Efficiency Polythiophene:fullerene Solar Cells. *Nat. Mater.* **2006**, *5*, 197–203.

(53) Ballantyne, A. M.; Chen, L.; Dane, J.; Hammant, T.; Braun, F. M.; Heeney, M.; Duffy, W.; McCulloch, I.; Bradley, D. D. C.; Nelson, J. The Effect of Poly(3-Hexylthiophene) Molecular Weight on Charge Transport and the Performance of Polymer:Fullerene Solar Cells. *Adv. Funct. Mater.* **2008**, *18*, 2373–2380.

(54) van Bavel, S. S.; Bärenklau, M.; de With, G.; Hoppe, H.; Loos, J. P3HT/PCBM Bulk Heterojunction Solar Cells: Impact of Blend Composition and 3D Morphology on Device Performance. *Adv. Funct. Mater.* **2010**, *20*, 1458–1463.

(55) Berson, S.; De Bettignies, R.; Bailly, S.; Guillerez, S. Poly(3-Hexylthiophene) Fibers for Photovoltaic Applications. *Adv. Funct. Mater.* **2007**, *17*, 1377–1384.

(56) Müller, C.; Ferenczi, T. A. M.; Campoy-Quiles, M.; Frost, J. M.; Bradley, D. D. C.; Smith, P.; Stingelin-Stutzmann, N.; Nelson, J. Binary Organic Photovoltaic

Blends: A Simple Rationale for Optimum Compositions. *Adv. Mater.* **2008**, *20*, 3510–3515.

(57) Clarke, T. M.; Ballantyne, A. M.; Nelson, J.; Bradley, D. D. C.; Durrant, J. R. Free Energy Control of Charge Photogeneration in Polythiophene/Fullerene Solar Cells: The Influence of Thermal Annealing on P3HT/PCBM Blends. *Adv. Funct. Mater.* **2008**, *18*, 4029–4035.

(58) Marsh, R. A.; Hodgkiss, J. M.; Albert-Seifried, S.; Friend, R. H. Effect of Annealing on P3HT:PCBM Charge Transfer and Nanoscale Morphology Probed by Ultrafast Spectroscopy. *Nano Lett.* **2010**, *10*, 923–930.

(59) Linda Chen, X.; Jenekhe, a. Block Conjugated Copolymers: Toward Quantum-Well Nanostructures for Exploring Spatial Confinement Effects on Electronic, Optoelectronic, and Optical Phenomena. *Macromolecules* **1996**, *29*, 6189–6192.

(60) Botiz, I.; Darling, S. B. Optoelectronics Using Block Copolymers. *Mater. Today* **2010**, *13*, 42–51.

(61) Bates, F. S.; Fredrickson, G. H. Block Copolymers-Designer Soft Materials. *Phys. Today* **1999**, *52*, 32–38.

(62) Bates, F. S.; Fredrickson, G. H. Block Copolymer Thermodynamics: Theory and Experiment. *Annu. Rev. Phys. Chem.* **1990**, *41*, 525–557.

(63) Bates, F. S. Polymer-Polymer Phase Behavior. *Science* **1991**, *251*, 898–905.

(64) Matsen, M. W.; Bates, F. S. Conformationally Asymmetric Block Copolymers. *J. Polym. Sci. Part B Polym. Phys.* **1997**, *35*, 945–952.

(65) Leibler, L. Theory of Microphase Separation in Block Copolymers. *Macromolecules* **1980**, *13*, 1602–1617.

(66) Zalusky, A. S.; Olayo-Valles, R.; Wolf, J. H.; Hillmyer, M. A. Ordered Nanoporous Polymers from Polystyrene–Polylactide Block Copolymers. *J. Am. Chem. Soc.* **2002**, *124*, 12761–12773.

(67) Matsen, M. W.; Bates, F. S. Unifying Weak- and Strong-Segregation Block Copolymer Theories. *Macromolecules* **1996**, *29*, 1091–1098.

(68) De Cuendias, A.; Hiorns, R. C.; Cloutet, E.; Vignau, L.; Cramail, H. Conjugated Rod-Coil Block Copolymers and Optoelectronic Applications. *Polym. Int.* **2010**, *59*, 1452–1476.

(69) Matsen, M. W.; Schick, M. Stable and Unstable Phases of a Diblock Copolymer Melt. *Phys. Rev. Lett.* **1994**, *72*, 2660–2663.

(70) Cochran, E. W.; Garcia-Cervera, C. J.; Fredrickson, G. H. Stability of the Gyroid Phase in Diblock Copolymers at Strong Segregation. *Macromolecules* **2006**, *39*, 2449–2451.

(71) Thurn-Albrecht, T.; Derouchey, J.; Russell, T. P.; Jaeger, H. M. Overcoming Interfacial Interactions with Electric Fields. *Macromolecules* **2000**, *33*, 3250–3253.

(72) Angelescu, D. E.; Waller, J. H.; Register, R. a.; Chaikin, P. M. Shear-Induced Alignment in Thin Films of Spherical Nanodomains. *Adv. Mater.* **2005**, *17*, 1878–1881.

(73) Bates, C. M.; Seshimo, T.; Maher, M. J.; Durand, W. J.; Cushen, J. D.; Dean, L. M.; Blachut, G.; Ellison, C. J.; Willson, C. G. Polarity-Switching Top Coats Enable Orientation of Sub-10-Nm Block Copolymer Domains. *Science* **2012**, *338*, 775–779.

(74) Hu, H.; Gopinadhan, M.; Osuji, C. O. Directed Self-Assembly of Block Copolymers: A Tutorial Review of Strategies for Enabling Nanotechnology with Soft Matter. *Soft Matter* **2014**, *10*, 3867–3889.

(75) Tseng, Y. C.; Darling, S. B. Block Copolymer Nanostructures for Technology. *Polymers* **2010**, *2*, 470–489.

(76) Darling, S. B. Directing the Self-Assembly of Block Copolymers. *Prog. Polym. Sci.* **2007**, *32*, 1152–1204.

(77) Reenders, M.; ten Brinke, G. Compositional and Orientational Ordering in Rod−Coil Diblock Copolymer Melts. *Macromolecules* **2002**, *35*, 3266–3280.

(78) Olsen, B. D.; Segalman, R. A. Structure and Thermodynamics of Weakly Segregated Rod−Coil Block Copolymers. *Macromolecules* **2005**, *38*, 10127–10137.

(79) Olsen, B. D.; Segalman, R. A. Nonlamellar Phases in Asymmetric Rod−Coil Block Copolymers at Increased Segregation Strengths. *Macromolecules* **2007**, *40*, 6922–6929.

(80) Olsen, B. D.; Segalman, R. a. Self-Assembly of Rod-Coil Block Copolymers. *Mater. Sci. Eng. R Reportsence* **2008**, *62*, 37–66.

(81) Lee, M.; Cho, B.-K.; Zin, W.-C. Supramolecular Structures from Rod−Coil Block Copolymers. *Chem. Rev.* **2001**, *101*, 3869–3892.

(82) Pryamitsyn, V.; Ganesan, V. Self-Assembly of Rod-Coil Block Copolymers. *J. Chem. Phys.* **2004**, *120*, 5824–5838.

(83) Ho, V.; Boudouris, B. W.; McCulloch, B. L.; Shuttle, C. G.; Burkhardt, M.; Chabinyc, M. L.; Segalman, R. A. Poly(3-Alkylthiophene) Diblock Copolymers with Ordered Microstructures and Continuous Semiconducting Pathways. *J. Am. Chem. Soc.* **2011**, *133*, 9270–9273.

(84) Lee, Y.-H.; Yen, W.-C.; Su, W.-F.; Dai, C.-A. Self-Assembly and Phase Transformations of π-Conjugated Block Copolymers That Bend and Twist: From Rigid-Rod Nanowires to Highly Curvaceous Gyroids. *Soft Matter* **2011**, *7*, 10429.

(85) Shah, M.; Pryamitsyn, V.; Ganesan, V. A Model for Self-Assembly in Side Chain Liquid Crystalline Block Copolymers. *Macromolecules* **2008**, *41*, 218–229.

(86) Wu, P.-T.; Ren, G.; Kim, F. S.; Li, C.; Mezzenga, R.; Jenekhe, S. A. Poly(3-

Hexylthiophene)- B -poly(3-Cyclohexylthiophene): Synthesis, Microphase Separation, Thin Film Transistors, and Photovoltaic Applications. *J. Polym. Sci. Part A Polym. Chem.* **2010**, *48*, 614–626.

(87) Verduzco, R.; Botiz, I.; Pickel, D. L.; Kilbey, S. M.; Hong, K.; Dimasi, E.; Darling, S. B. Polythiophene-block-Polyfluorene and Polythiophene-block-Poly(fluorene-Co- Benzothiadiazole): Insights into the Self-Assembly of All-Conjugated Block Copolymers. *Macromolecules* **2011**, *44*, 530–539.

(88) Deshmukh, P.; Ahn, S.; Geelhand de Merxem, L.; Kasi, R. M. Interplay between Liquid Crystalline Order and Microphase Segregation on the Self-Assembly of Side-Chain Liquid Crystalline Brush Block Copolymers. *Macromolecules* **2013**, *46*, 8245–8252.

(89) Hamley, I. W.; Castelletto, V.; Parras, P.; Lu, Z. B.; Imrie, C. T.; Itoh, T. Ordering on Multiple Lengthscales in a Series of Side Group Liquid Crystal Block Copolymers Containing a Cholesteryl-Based Mesogen. *Soft Matter* **2005**, *1*, 355–363.

(90) Komiyama, H.; Sakai, R.; Hadano, S.; Asaoka, S.; Kamata, K.; Iyoda, T.; Komura, M.; Yamada, T.; Yoshida, H. Enormously Wide Range Cylinder Phase of Liquid Crystalline PEO- B -PMA(Az) Block Copolymer. *Macromolecules* **2014**, *47*, 1777–1782.

(91) Osuji, C. O.; Chen, J. T.; Mao, G.; Ober, C. K.; Thomas, E. L. Understanding and Controlling the Morphology of Styrene–isoprene Side-Group Liquid Crystalline Diblock Copolymers. *Polymer* **2000**, *41*, 8897–8907.

(92) Hamley, I. W.; Castelletto, V.; Lu, Z. B.; Imrie, C. T.; Itoh, T.; Al-Hussein, M. Interplay between Smectic Ordering and Microphase Separation in a Series of Side-Group Liquid-Crystal Block Copolymers. *Macromolecules* **2004**, *37*, 4798–4807.

(93) Zhou, Y.; Ahn, S.; Lakhman, R. K.; Gopinadhan, M.; Osuji, C. O.; Kasi, R. M. Tailoring Crystallization Behavior of PEO-Based Liquid Crystalline Block Copolymers through Variation in Liquid Crystalline Content. *Macromolecules* **2011**, *44*, 3924–3934.

(94) Zhao, Y.; Qi, B.; Tong, X.; Zhao, Y. Synthesis of Double Side-Chain Liquid Crystalline Block Copolymers Using RAFT Polymerization and the Orientational Cooperative Effect. *Macromolecules* **2008**, *41*, 3823–3831.

(95) Lindner, S. M.; Hüttner, S.; Chiche, A.; Thelakkat, M.; Krausch, G. Charge Separation at Self-Assembled Nanostructured Bulk Interface in Block Copolymers. *Angew. Chemie Int. Ed.* **2006**, *45*, 3364–3368.

(96) Popere, B. C.; Pelle, A. M. Della; Poe, A.; Thayumanavan, S. Macromolecular Architectures for Organic Photovoltaics. *Phys. Chem. Chem. Phys.* **2012**, *14*, 4043–4057.

(97) Zhou, H.; Yang, L.; You, W. Rational Design of High Performance Conjugated Polymers for Organic Solar Cells. *Macromolecules* **2012**, *45*, 607–632.

(98) Shirakawa, H.; Louis, E. J.; MacDiarmid, A. G.; Chiang, C. K.; Heeger, A. J. Synthesis of Electrically Conducting Organic Polymers: Halogen Derivatives of Polyacetylene, $(CH)_x$. *J. Chem. Soc. Chem. Commun.* **1977**, 578–580.

(99) Bredas, J.; Street, G. Polarons, Bipolarons, and Solitons in Conducting Polymers. *Acc. Chem. Res.* **1985**, *1305*, 309–315.

(100) Heeger, A. J. Semiconducting and Metallic Polymers : The Fourth Generation of Polymeric Materials (Nobel Lecture) **2001**.

(101) Marrocchi, A.; Lanari, D.; Facchetti, A.; Vaccaro, L. Poly(3-Hexylthiophene): Synthetic Methodologies and Properties in Bulk Heterojunction Solar Cells. *Energy Environ. Sci.* **2012**, *5*, 8457–8474.

(102) Kularatne, R. S.; Magurudeniya, H. D.; Sista, P.; Biewer, M. C.; Stefan, M. C. Donor-Acceptor Semiconducting Polymers for Organic Solar Cells. *J. Polym. Sci. Part A Polym. Chem.* **2013**, *51*, 743–768.

(103) Mühlbacher, D.; Scharber, M.; Morana, M.; Zhu, Z.; Waller, D.; Gaudiana, R.; Brabec, C. High Photovoltaic Performance of a Low-Bandgap Polymer. *Adv. Mater.* **2006**, *18* (21), 2884–2889.

(104) Xu, T.; Yu, L. How to Design Low Bandgap Polymers for Highly Efficient Organic Solar Cells. *Mater. Today* **2014**, *17*, 11–15.

(105) Soci, C.; Hwang, I.-W.; Moses, D.; Zhu, Z.; Waller, D.; Gaudiana, R.; Brabec, C. J.; Heeger, A. J. Photoconductivity of a Low-Bandgap Conjugated Polymer. *Adv. Funct. Mater.* **2007**, *17*, 632–636.

(106) Bian, L.; Zhu, E.; Tang, J.; Tang, W.; Zhang, F. Recent Progress in the Design of Narrow Bandgap Conjugated Polymers for High-Efficiency Organic Solar Cells. *Prog. Polym. Sci.* **2012**, *37*, 1292–1331.

(107) Boudreault, P. L. T.; Najari, A.; Leclerc, M. Processable Low-Bandgap Polymers for Photovoltaic Applications. *Chem. Mater.* **2011**, *23*, 456–469.

(108) Van Mullekom, H. a M.; Vekemans, J. a J. M.; Havinga, E. E.; Meijer, E. W. Developments in the Chemistry and Band Gap Engineering of Donor-Acceptor Substituted Conjugated Polymers. *Mater. Sci. Eng. R Reports* **2001**, *32*, 1–40.

(109) Duan, C.; Huang, F.; Cao, Y. Recent Development of Push–pull Conjugated Polymers for Bulk-Heterojunction Photovoltaics: Rational Design and Fine Tailoring of Molecular Structures. *J. Mater. Chem.* **2012**, *22*, 10416–10434.

(110) Liang, Y.; Yu, L. Development of Semiconducting Polymers for Solar Energy Harvesting. *Polym. Rev.* **2010**, *50*, 454–473.

(111) Dou, L.; You, J.; Yang, J.; Chen, C.-C.; He, Y.; Murase, S.; Moriarty, T.; Emery, K.; Li, G.; Yang, Y. Tandem Polymer Solar Cells Featuring a Spectrally Matched

Low-Bandgap Polymer. *Nat. Photonics* **2012**, *6*, 180–185.

(112) Liang, Y.; Xu, Z.; Xia, J.; Tsai, S.-T.; Wu, Y.; Li, G.; Ray, C.; Yu, L. For the Bright Future-Bulk Heterojunction Polymer Solar Cells with Power Conversion Efficiency of 7.4%. *Adv. Mater.* **2010**, *22*, E135–E138.

(113) He, M.; Qiu, F.; Lin, Z. Conjugated Rod–coil and Rod–rod Block Copolymers for Photovoltaic Applications. *J. Mater. Chem.* **2011**, *21*, 17039–17048.

(114) Kozma, E.; Catellani, M. Perylene Diimides Based Materials for Organic Solar Cells. *Dye. Pigment.* **2013**, *98*, 160–179.

(115) Würthner, F. Perylene Bisimide Dyes as Versatile Building Blocks for Functional Supramolecular Architectures. *Chem. Commun.* **2004**, 1564–1579.

(116) Sonar, P.; Lim, J. P. F. L.; Chan, K. L. Organic Non-Fullerene Acceptors for Organic Photovoltaics. *Energy Environ. Sci.* **2011**, *4*, 1558–1574.

(117) Meyers, F.; Heeger, A. J.; Brédas, J. L. Fine Tuning of the Band Gap in Conjugated Polymers via Control of Block Copolymer Sequences. *J. Chem. Phys.* **1992**, *97*, 2750–2758.

(118) Guo, C.; Lin, Y.; Witman, M. D.; Smith, K. a; Wang, C.; Hexemer, A.; Strzalka, J.; Gomez, E. D.; Verduzco, R. Conjugated Block Copolymer Photovoltaics with near 3% E Ffi Ciency through Microphase Separation. *Nano Lett.* **2013**, *13*, 2957–2963.

(119) Hillmyer, M. A.; Lodge, T. P. Synthesis and Self-Assembly of Fluorinated Block Copolymers. *J. Polym. Sci. Part A Polym. Chem.* **2002**, *40*, 1–8.

(120) Wang, B.; Watt, S.; Hong, M.; Domercq, B.; Sun, R.; Kippelen, B.; Collard, D. M. Synthesis, Properties, and Tunable Supramolecular Architecture of Regioregular Poly(3-Alkylthiophene)s with Alternating Alkyl and Semifluoroalkyl Substituents. *Macromolecules* **2008**, *41*, 5156–5165.

(121) Lombeck, F.; Komber, H.; Sepe, A.; Friend, R. H.; Sommer, M. Enhancing Phase Separation and Photovoltaic Performance of All-Conjugated Donor–Acceptor Block Copolymers with Semifluorinated Alkyl Side Chains. *Macromolecules* **2015**, *48*, 7851–7860.

(122) Mulherin, R. C.; Jung, S.; Huettner, S.; Johnson, K.; Kohn, P.; Sommer, M.; Allard, S.; Scherf, U.; Greenham, N. C. Ternary Photovoltaic Blends Incorporating an All-Conjugated Donor–Acceptor Diblock Copolymer. *Nano Lett.* **2011**, *11*, 4846–4851.

(123) Ku, S.-Y.; Brady, M. A.; Treat, N. D.; Cochran, J. E.; Robb, M. J.; Kramer, E. J.; Chabinyc, M. L.; Hawker, C. J. A Modular Strategy for Fully Conjugated Donor–Acceptor Block Copolymers. *J. Am. Chem. Soc.* **2012**, *134*, 16040–16046.

(124) Scherf, U.; Gutacker, A.; Koenen, N.; Copolymers, A. B.; Scherf, U.; Gutacker, A.; Koenen, N. All-Conjugated Block Copolymers. *Acc. Chem. Res.* **2008**, *41*,

1086–1097.

(125) Izuhara, D.; Swager, T. M. Poly(3-Hexylthiophene)-Block-Poly(pyridinium Phenylene)s: Block Polymers of P- and N-Type Semiconductors. *Macromolecules* **2011**, *44*, 2678–2684.

(126) Wang, J.; Ueda, M.; Higashihara, T. Synthesis of All-Conjugated Donor–Acceptor–Donor ABA-Type Triblock Copolymers via Kumada Catalyst-Transfer Polycondensation. *ACS Macro Lett*. **2013**, *2*, 506–510.

(127) Sommer, M.; Komber, H.; Huettner, S.; Mulherin, R.; Kohn, P.; Greenham, N. C.; Huck, W. T. S. Synthesis, Purification, and Characterization of Well-Defined All-Conjugated Diblock Copolymers PF8TBT-B-P3HT. *Macromolecules* **2012**, *45*, 4142–4151.

(128) Urien, M.; Erothu, H.; Cloutet, E.; Hiorns, R. C.; Vignau, L.; Cramail, H. Poly(3-Hexylthiophene) Based Block Copolymers Prepared by "Click" Chemistry. *Macromolecules* **2008**, *41*, 7033–7040.

(129) Pang, X.; Zhao, L.; Feng, C.; Lin, Z. Novel Amphiphilic Multiarm, Starlike Coil–Rod Diblock Copolymers via a Combination of Click Chemistry with Living Polymerization. *Macromolecules* **2011**, *44*, 7176–7183.

(130) Ho, C.-C.; Lee, Y.-H.; Dai, C.-A.; Segalman, R. A.; Su, W.-F. Synthesis and Self-Assembly of Poly(diethylhexyloxy- P -Phenylenevinylene)- B -Poly(methyl Methacrylate) Rod–Coil Block Copolymers. *Macromolecules* **2009**, *42*, 4208–4219.

(131) Brochon, C.; Sary, N.; Mezzenga, R.; Ngov, C.; Richard, F.; May, M.; Hadziioannou, G. Synthesis of Poly(paraphenylene Vinylene)-Polystyrene-Based Rod-Coil Block Copolymer by Atom Transfer Radical Polymerization: Toward a Self-Organized Lamellar Semiconducting Material. *J. Appl. Polym. Sci*. **2008**, *110*, 3664–3670.

(132) Lee, J. U.; Cirpan, A.; Emrick, T.; Russell, T. P.; Jo, W. H. Synthesis and Photophysical Property of Well-Defined Donor–acceptor Diblock Copolymer Based on Regioregular poly(3-Hexylthiophene) and Fullerene. *J. Mater. Chem*. **2009**, *19*, 1483–1489.

(133) de Cuendias, A.; Le Hellaye, M.; Lecommandoux, S.; Cloutet, E.; Cramail, H. Synthesis and Self-Assembly of Polythiophene-Based Rod–Coil and Coil–Rod–Coil Block Copolymers. *J. Mater. Chem*. **2005**, *15*, 3264–3267.

(134) Liu, J.; Sheina, E.; Kowalewski, T.; McCullough, R. D. Tuning the Electrical Conductivity and Self-Assembly of Regioregular Polythiophene by Block Copolymerization: Nanowire Morphologies in New Di- and Triblock Copolymers. *Angew. Chem. Int. Ed*. **2002**, *41*, 329–332.

(135) Fang, Y.-K.; Liu, C.-L.; Li, C.; Lin, C.-J.; Mezzenga, R.; Chen, W.-C. Synthesis, Morphology, and Properties of Poly(3-Hexylthiophene)-Block-Poly(vinylphenyl

Oxadiazole) Donor-Acceptor Rod-Coil Block Copolymers and Their Memory Device Applications. *Adv. Funct. Mater.* **2010**, *20*, 3012–3024.

(136) Matyjaszewski, K.; Tsarevsky, N. V. Macromolecular Engineering by Atom Transfer Radical Polymerization. *J. Am. Chem. Soc.* **2014**, *136*, 6513–6533.

(137) Iovu, M. C.; Zhang, R.; Cooper, J. R.; Smilgies, D. M.; Javier, A. E.; Sheina, E. E.; Kowalewski, T.; McCullough, R. D. Conducting Block Copolymers of Regioregular Poly(3-Hexylthiophene) and Poly(methacrylates): Electronic Materials with Variable Conductivities and Degrees of Interfibrillar Order. *Macromol. Rapid Commun.* **2007**, *28*, 1816–1824.

(138) Moad, G.; Chen, M.; Häussler, M.; Postma, A.; Rizzardo, E.; Thang, S. H. Functional Polymers for Optoelectronic Applications by RAFT Polymerization. *Polym. Chem.* **2011**, *2*, 492–519.

(139) Iovu, M. C.; Craley, C. R.; Jeffries-EL, M.; Krankowski, A. B.; Zhang, R.; Kowalewski, T.; McCullough, R. D. Conducting Regioregular Polythiophene Block Copolymer Nanofibrils Synthesized by Reversible Addition Fragmentation Chain Transfer Polymerization (RAFT) and Nitroxide Mediated Polymerization (NMP). *Macromolecules* **2007**, *40*, 4733–4735.

(140) Heiser, T.; Adamopoulos, G.; Brinkmann, M.; Giovanella, U.; Ould-Saad, S.; Brochon, C.; van de Wetering, K.; Hadziioannou, G. Nanostructure of Self-Assembled Rod-Coil Block Copolymer Films for Photovoltaic Applications. *Thin Solid Films* **2006**, *511-512*, 219–223.

(141) Van De Wetering, K.; Brochon, C.; Ngov, C.; Hadziioannou, G. Design and Synthesis of a Low Band Gap Conjugated Macroinitiator: Toward Rod–Coil Donor–Acceptor Block Copolymers. *Macromolecules* **2006**, *39*, 4289–4297.

(142) Stalmach, U.; de Boer, B.; Videlot, C.; van Hutten, P. F.; Hadziioannou, G. Semiconducting Diblock Copolymers Synthesized by Means of Controlled Radical Polymerization Techniques. *J. Am. Chem. Soc.* **2000**, *122*, 5464–5472.

(143) Grubbs, R. B. Nitroxide-Mediated Radical Polymerization: Limitations and Versatility. *Polym. Rev.* **2011**, *51*, 104–137.

(144) Dai, C.-A.; Yen, W.-C.; Lee, Y.-H.; Ho, C.-C.; Su, W.-F. Facile Synthesis of Well-Defined Block Copolymers Containing Regioregular poly(3-Hexyl Thiophene) via Anionic Macroinitiation Method and Their Self-Assembly Behavior. *J. Am. Chem. Soc.* **2007**, *129*, 11036–11038.

(145) Hirao, A.; Goseki, R.; Ishizone, T. Advances in Living Anionic Polymerization: From Functional Monomers, Polymerization Systems, to Macromolecular Architectures. *Macromolecules* **2014**, *47*, 1883–1905.

(146) Boudouris, B. W.; Frisbie, C. D.; Hillmyer, M. A. Nanoporous Poly(3-Alkylthiophene) Thin Films Generated from Block Copolymer Templates. *Macromolecules* **2008**, *41*, 67–75.

(147) Radano, C. P.; Scherman, O. A.; Stingelin-Stutzmann, N.; Müller, C.; Breiby, D. W.; Smith, P.; Janssen, R. A. J.; Meijer, E. W. Crystalline-Crystalline Block Copolymers of Regioregular Poly(3-Hexylthiophene) and Polyethylene by Ring-Opening Metathesis Polymerization. *J. Am. Chem. Soc.* **2005**, *127*, 12502–12503.

(148) Botiz, I.; Darling, S. B. Self-Assembly of Poly(3-Hexylthiophene)- Block - Polylactide Block Copolymer and Subsequent Incorporation of Electron Acceptor Material. *Macromolecules* **2009**, *42*, 8211–8217.

(149) Sivula, K.; Ball, Z. T.; Watanabe, N.; Fréchet, J. M. J. Amphiphilic Diblock Copolymer Compatibilizers and Their Effect on the Morphology and Performance of Polythiophene:Fullerene Solar Cells. *Adv. Mater.* **2006**, *18*, 206–210.

(150) Rajaram, S.; Armstrong, P. B.; Kim, B. J.; Frechet, J. M. J. Effect of Addition of a Diblock Copolymer on Blend Morphology and Performance of Poly(3-Hexylthiophene):Perylene Diimide Solar Cells. *Chem. Mater.* **2009**, *21*, 1775–1777.

(151) Yang, C.; Lee, J. K.; Heeger, A. J.; Wudl, F. Well-Defined Donor–acceptor Rod–coil Diblock Copolymers Based on P3HT Containing C60: The Morphology and Role as a Surfactant in Bulk-Heterojunction Solar Cells. *J. Mater. Chem.* **2009**, *19*, 5416–5423.

(152) Bicciocchi, E.; Haeussler, M.; Rizzardo, E.; Scully, A. D.; Ghiggino, K. P. Donor-Acceptor Rod-Coil Block Copolymers Comprising Poly[2,7-(9,9-Dihexylfluorene)- Alt -Bithiophene] and Fullerene as Compatibilizers for Organic Photovoltaic Devices. *J. Polym. Sci. Part A Polym. Chem.* **2015**, *53*, 888–903.

(153) Renaud, C.; Mougnier, S.-J.; Pavlopoulou, E.; Brochon, C.; Fleury, G.; Deribew, D.; Portale, G.; Cloutet, E.; Chambon, S.; Vignau, L.; Hadziioannou, G. Block Copolymer as a Nanostructuring Agent for High-Efficiency and Annealing-Free Bulk Heterojunction Organic Solar Cells. *Adv. Mater.* **2012**, *24*, 2196–2201.

(154) Lee, J. U.; Jung, J. W.; Emrick, T.; Russell, T. P.; Jo, W. H. Morphology Control of a Polythiophene-Fullerene Bulk Heterojunction for Enhancement of the High-Temperature Stability of Solar Cell Performance by a New Donor-Acceptor Diblock Copolymer. *Nanotechnology* **2010**, *21*, 105201.

(155) Sun, Z.; Xiao, K.; Keum, J. K.; Yu, X.; Hong, K.; Browning, J.; Ivanov, I. N.; Chen, J.; Alonzo, J.; Li, D.; Sumpter, B. G.; Payzant, E. A.; Rouleau, C. M.; Geohegan, D. B. PS-B-P3HT Copolymers as P3HT/PCBM Interfacial Compatibilizers for High Efficiency Photovoltaics. *Adv. Mater.* **2011**, *23*, 5529–5535.

(156) Stalmach, U.; Boer, B. De; Post, A. D.; Hutten, P. F. Van; Hadziioannou, G. Synthesis of a Conjugated Macromolecular Initiator for Nitroxide- Mediated Free Radical Polymerization. *Angew. Chemie Int. Ed.* **2001**, *40*, 428–430.

(157) Van Der Veen, M. H.; De Boer, B.; Stalmach, U.; Van De Wetering, K. I.;

Hadziioannou, G. Donor-Acceptor Diblock Copolymers Based on PPV and C60: Synthesis, Thermal Properties, and Morphology. *Macromolecules* **2004**, *37*, 3673–3684.

(158) Adamopoulos, G.; Heiser, T.; Giovanella, U.; Ould-Saad, S.; van de Wetering, K. I.; Brochon, C.; Zorba, T.; Paraskevopoulos, K. M.; Hadziioannou, G. Electronic Transport Properties Aspects and Structure of Polymer-Fullerene Based Organic Semiconductors for Photovoltaic Devices. *Thin Solid Films* **2006**, *511-512*, 371–376.

(159) Barrau, S.; Heiser, T.; Richard, F.; Brochon, C.; Ngov, C.; van de Wetering, K.; Hadziioannou, G.; Anokhin, D. V; Ivanov, D. A. Self-Assembling of Novel Fullerene-Grafted Donor–Acceptor Rod-Coil Block Copolymers. *Macromolecules* **2008**, *41*, 2701–2710.

(160) Sary, N.; Richard, F.; Brochon, C.; Leclerc, N.; Lévêque, P.; Audinot, J. N.; Berson, S.; Heiser, T.; Hadziioannou, G.; Mezzenga, R. A New Supramolecular Route for Using Rod-Coil Block Copolymers in Photovoltaic Applications. *Adv. Mater.* **2010**, *22*, 763–768.

(161) Hufnagel, M.; Fischer, M.; Thurn-Albrecht, T.; Thelakkat, M. Donor–Acceptor Block Copolymers Carrying Pendant PC 71 BM Fullerenes with an Ordered Nanoscale Morphology. *Polym. Chem.* **2015**, *6*, 813–826.

(162) Zhang, X.; Lu, Z.; Ye, L.; Zhan, C.; Hou, J.; Zhang, S.; Jiang, B.; Zhao, Y.; Huang, J.; Zhang, S.; Liu, Y.; Shi, Q.; Liu, Y.; Yao, J. A Potential Perylene Diimide Dimer-Based Acceptor Material for Highly Efficient Solution-Processed Non-Fullerene Organic Solar Cells with 4.03% Efficiency. *Adv. Mater.* **2013**, *25*, 5791–5797.

(163) Lv, A.; Puniredd, S. R.; Zhang, J.; Li, Z.; Zhu, H.; Jiang, W.; Dong, H.; He, Y.; Jiang, L.; Li, Y.; Pisula, W.; Meng, Q.; Hu, W.; Wang, Z. High Mobility, Air Stable, Organic Single Crystal Transistors of an N-Type Diperylene Bisimide. *Adv. Mater.* **2012**, *24*, 2626–2630.

(164) Delgado, M. C. R.; Kim, E.-G.; Filho, D. A. da S.; Bredas, J.-L. Tuning the Charge-Transport Parameters of Perylene Diimide Single Crystals via End and/or Core Functionalization: A Density Functional Theory Investigation. *J. Am. Chem. Soc.* **2010**, *132*, 3375–3387.

(165) Schmidt, R.; Oh, J. H.; Sun, Y.-S.; Deppisch, M.; Krause, A.-M.; Radacki, K.; Braunschweig, H.; Könemann, M.; Erk, P.; Bao, Z.; Würthner, F. High-Performance Air-Stable N-Channel Organic Thin Film Transistors Based on Halogenated Perylene Bisimide Semiconductors. *J. Am. Chem. Soc.* **2009**, *131*, 6215–6228.

(166) Jones, B. A.; Ahrens, M. J.; Yoon, M.-H.; Facchetti, A.; Marks, T. J.; Wasielewski, M. R. High-Mobility Air-Stable N-Type Semiconductors with Processing Versatility: Dicyanoperylene-3,4:9,10-Bis(dicarboximides). *Angew.*

Chem. Int. Ed. **2004**, *43*, 6363–6366.

(167) Lang, A. S.; Muth, M.-A.; Heinrich, C. D.; Carassco-Orozco, M.; Thelakkat, M. Pendant Perylene Polymers with High Electron Mobility. *J. Polym. Sci. Part B Polym. Phys.* **2013**, *51*, 1480–1486.

(168) Sommer, M.; Lang, A. S.; Thelakkat, M. Crystalline-Crystalline Donor-Acceptor Block Copolymers. *Angew. Chemie Int. Ed.* **2008**, *47*, 7901–7904.

(169) Zhang, Q.; Cirpan, A.; Russell, T. P.; Emrick, T. Donor–Acceptor Poly(thiophene-Block-Perylene Diimide) Copolymers: Synthesis and Solar Cell Fabrication. *Macromolecules* **2009**, *42*, 1079–1082.

(170) Lohwasser, R. H.; Gupta, G.; Kohn, P.; Sommer, M.; Lang, A. S.; Thurn-albrecht, T.; Thelakkat, M. Phase Separation in the Melt and Confined Crystallization as the Key to Well-Ordered Microphase Separated Donor–Acceptor Block Copolymers. *Macromolecules* **2013**, *46*, 4403–4410.

(171) Gupta, G.; Singh, C. R.; Lohwasser, R. H.; Himmerlich, M.; Krischok, S.; Mu, P.; Thelakkat, M.; Hoppe, H.; Thurn-Albrecht, T. Morphology , Crystal Structure and Charge Transport in Donor – Acceptor Block Copolymer Thin Films. *ACS Appl. Mater. Interfaces* **2015**, *7*, 12309–12318.

(172) Koyuncu, S.; Wang, H.-W.; Liu, F.; Toga, K. B.; Gu, W.; Russell, T. P. A Novel Complementary Absorbing Donor–acceptor Pair in Block Copolymers Based on Single Material Organic Photovoltaics. *J. Mater. Chem. A* **2014**, *2*, 2993–2998.

(173) Sommer, M.; Lindner, S. M.; Thelakkat, M. Microphase-Separated Donor-Acceptor Diblock Copolymers: Influence of HOMO Energy Levels and Morphology on Polymer Solar Cells. *Adv. Funct. Mater.* **2007**, *17*, 1493–1500.

(174) Lindner, S. M.; Thelakkat, M. Nanostructures of N-Type Organic Semiconductor in a p-Type Matrix via Self-Assembly of Block Copolymers. *Macromolecules* **2004**, *37*, 8832–8835.

(175) King, S.; Sommer, M.; Huettner, S.; Thelakkat, M.; Haque, S. A. Charge Separation and Recombination in Self-Organizing Nanostructured Donor–Acceptor Block Copolymer Films. *J. Mater. Chem.* **2009**, *19*, 5436.

(176) Bielawski, C. W.; Grubbs, R. H. Living Ring-Opening Metathesis Polymerization. *Prog. Polym. Sci.* **2007**, *32*, 1–29.

(177) Grubbs, R. H. Olefin Metathesis. *Tetrahedron* **2004**, *60*, 7117–7140.

(178) Nomura, K.; Abdellatif, M. M. Precise Synthesis of Polymers Containing Functional End Groups by Living Ring-Opening Metathesis Polymerization (ROMP): Efficient Tools for Synthesis of Block/graft Copolymers. *Polymer* **2010**, *51* (9), 1861–1881.

(179) Hollauf, M.; Trimmel, G.; Knall, A.-C. Dye-Functionalized Polymers via Ring Opening Metathesis Polymerization: Principal Routes and Applications.

Monatshefte für Chemie - Chem. Mon. **2015**, *146*, 1063–1080.

(180) Leitgeb, A.; Wappel, J.; Slugovc, C. The ROMP Toolbox Upgraded. *Polymer* **2010**, *51*, 2927–2946.

(181) Elacqua, E.; Lye, D. S.; Weck, M. Engineering Orthogonality in Supramolecular Polymers: From Simple Scaffolds to Complex Materials. *Acc. Chem. Res.* **2014**, *47*, 2405–2416.

(182) Bunz, U. H. F.; Mäker, D.; Porz, M. Alkene Metathesis - A Tool for the Synthesis of Conjugated Polymers. *Macromol. Rapid Commun.* **2012**, *33*, 886–910.

(183) Hilf, S.; Klos, J.; Char, K.; Woo, H.; Kilbinger, A. F. M. Polymerizable Well-Defined Oligo(thiophene Amide)s and Their ROMP Block Copolymers. *Macromol. Rapid Commun.* **2009**, *30*, 1249–1257.

(184) Huang, C.; Potscavage, W. J.; Tiwari, S. P.; Sutcu, S.; Barlow, S.; Kippelen, B.; Marder, S. R. Polynorbornenes with Pendant Perylene Diimides for Organic Electronic Applications. *Polym. Chem.* **2012**, *3*, 2996–3006.

(185) Milum, K. M. Functional Materials Based on Redox-Active Components. *Univ. Texas PhD Thesis* **2010**.

(186) Loewe, R. S.; Ewbank, P. C.; Liu, J.; Zhai, L.; McCullough, R. D. Regioregular, Head-to-Tail Coupled Poly(3-Alkylthiophenes) Made Easy by the GRIM Method: Investigation of the Reaction and the Origin of Regioselectivity. *Macromolecules* **2001**, *34*, 4324–4333.

(187) McCullough, R.; Tristram-Nagle, S.; Williams, S.; Lowe, R. D.; Jayarman, M. Self-Orienting Head-to-Tail Poly(3-Alkylthiophenes): New Insights on Structure-Property Relationship in Conducting Polymers. *J. Am. Chem. Soc.* **1993**, *115*, 4910–4911.

(188) Stefan, M. C.; Bhatt, M. P.; Sista, P.; Magurudeniya, H. D. Grignard Metathesis (GRIM) Polymerization for the Synthesis of Conjugated Block Copolymers Containing Regioregular Poly(3-Hexylthiophene). *Polym. Chem.* **2012**, *3*, 1693–1701.

(189) Stefan, M. C.; Javier, A. E.; Osaka, I.; McCullough, R. D. Grignard Metathesis Method (GRIM): Toward a Universal Method for the Synthesis of Conjugated Polymers. *Macromolecules* **2009**, *42*, 30–32.

(190) Zhang, F.; Wu, D.; Xu, Y.; Feng, X. Thiophene-Based Conjugated Oligomers for Organic Solar Cells. *J. Mater. Chem.* **2011**, *21*, 17590–17600.

(191) Mejía, M. L. Synthesis and Characterization of Electronic Materials for Photovoltaic Applications. *Univ. Texas PhD Thesis* **2010**.

(192) Brown, A. H.; Sheares, V. V. Amorphous Unsaturated Aliphatic Polyesters Derived from Dicarboxylic Monomers Synthesized by Diels-Alder Chemistry. *Macromolecules* **2007**, *40*, 4848–4853.

(193) Pappenfus, T. M.; Mann, K. R. Synthesis, Spectroscopy, and Electrochemical Studies of Binuclear Tris-Bipyridine Ruthenium(II) Complexes with Oligothiophene Bridges. *Inorg. Chem.* **2001**, *40*, 6301–6307.

(194) Sahu, D.; Padhy, H.; Patra, D.; Yin, J.-F.; Hsu, Y.-C.; Lin, J.-T.; Lu, K.-L.; Wei, K.-H.; Lin, H.-C. Synthesis and Applications of Novel Acceptor–Donor–Acceptor Organic Dyes with Dithienopyrrole- and Fluorene-Cores for Dye-Sensitized Solar Cells. *Tetrahedron* **2011**, *67*, 303–311.

(195) Huang, Y.; Hu, J.; Kuang, W.; Wei, Z.; Faul, C. F. J. Modulating Helicity through Amphiphilicity-Tuning Supramolecular Interactions for the Controlled Assembly of Perylenes. *Chem. Commun.* **2011**, *47*, 5554–5556.

(196) Tauber, M. J.; Kelley, R. F.; Giaimo, J. M.; Rybtchinski, B.; Wasielewski, M. R. Electron Hopping in π-Stacked Covalent and Self-Assembled Perylene Diimides Observed by ENDOR Spectroscopy. *J. Am. Chem. Soc.* **2006**, *128*, 1782–1783.

(197) Wicklein, A.; Lang, A.; Muth, M.; Thelakkat, M. Swallow-Tail Substituted Liquid Crystalline Perylene Bisimides: Synthesis and Thermotropic Properties. *J. Am. Chem. Soc.* **2009**, *131*, 14442–14453.

(198) Lang, A. S.; Thelakkat, M. Modular Synthesis of Poly(Perylene Bisimides) Using Click Chemistry: A Comparative Study. *Polym. Chem.* **2011**, *2*, 2213–2221.

(199) Glaz, M. S.; Biberdorf, J. D.; Nguyen, M. T.; Travis, J. J.; Holliday, B. J.; Vanden Bout, D. a. Perylene Diimide Functionalized Polynorbornene: A Macromolecular Scaffold for Supramolecular Self-Assembly. *J. Mater. Chem. C* **2013**, *1*, 8060–8065.

(200) Gomez, R.; Veldman, D.; Blanco, R.; Seoane, C.; Segura, J. L.; Janssen, R. A. J.; Segura, L.; Janssen, a J.; Würthner, F. Energy and Electron Transfer in a Poly (Fluorene-Alt-Phenylene) Bearing Perylenediimides as Pendant Electron Acceptor Groups. *Macromolecules* **2007**, *40*, 2760–2772.

(201) Wang, W.; Li, L. S.; Helms, G.; Zhou, H. H.; Li, A. D. Q. To Fold or to Assemble? *J. Am. Chem. Soc.* **2003**, *125*, 1120–1121.

(202) Ahrens, M. J.; Sinks, L. E.; Rybtchinski, B.; Liu, W.; Jones, B. a.; Giaimo, J. M.; Gusev, A. V.; Goshe, A. J.; Tiede, D. M.; Wasielewski, M. R. Self-Assembly of Supramolecular Light-Harvesting Arrays from Covalent Multi-Chromophore Perylene-3,4,9,10-bis(dicarboximide) Building Blocks. *J. Am. Chem. Soc.* **2004**, *126*, 8284–8294.

(203) Spano, F. C. The Spectral Signatures of Frenkel Polarons in H-and J-Aggregates. *Acc. Chem. Res.* **2009**, *43*, 429–439.

(204) van der Boom, T.; Hayes, R. T.; Zhao, Y. Y.; Bushard, P. J.; Weiss, E. A.; Wasielewski, M. R. Charge Transport in Photofunctional Nanoparticles Self-Assembled from Zinc 5,10,15,20-Tetrakis(Perylene-Diimide)porphyrin Building Blocks. *J. Am. Chem. Soc.* **2002**, *124*, 9582–95900.

(205) Camaioni, N.; Po, R. Pushing the Envelope of the Intrinsic Limitation of Organic Solar Cells. *J. Phys. Chem. Lett.* **2013**, *4*, 1821–1828.

(206) Scholes, G. D. Long-Range Resonance Energy Transfer in Molecular Systems. *Annu. Rev. Phys. Chem.* **2003**, *54*, 57–87.

(207) Xu, G.; Lu, N.; Wang, W.; Gao, N.; Ji, Z.; Li, L.; Liu, M. Universal Description of Exciton Diffusion Length in Organic Photovoltaic Cell. *Org. Electron.* **2015**, *23*, 53–56.

(208) Brendel, J. C.; Liu, F.; Lang, A. S.; Russell, T. P.; Thelakkat, M. Macroscopic Vertical Alignment of Nanodomains in Thin Films of Semiconductor Amphiphilic Block Copolymers. *ACS Nano* **2013**, *7*, 6069–6078.

(209) Brendel, J. C.; Burchardt, H.; Thelakkat, M. Semiconductor Amphiphilic Block Copolymers for Hybrid Donor–acceptor Nanocomposites. *J. Mater. Chem.* **2012**, *22*, 24386–24393.

(210) Jung, H.; Hwang, D.; Kim, E.; Kim, B. J.; Lee, W. B.; Poelma, J. E.; Kim, J.; Hawker, C. J.; Huh, J.; Ryu, D. Y.; Bang, J. Three-Dimensional Multilayered Nanostructures with Controlled Orientation of Microdomains from Cross-Linkable Block Copolymers. *ACS Nano* **2011**, *5*, 6164–6173.

(211) Chang, J. B.; Son, J. G.; Hannon, A. F.; Alexander-Katz, A.; Ross, C. A.; Berggren, K. K. Aligned Sub-10-Nm Block Copolymer Patterns Templated by Post Arrays. *ACS Nano* **2012**, *6*, 2071–2077.

(212) Rockford, L.; Liu, Y.; Mansky, P.; Russell, T.; Yoon, M.; Mochrie, S. Polymers on Nanoperiodic, Heterogeneous Surfaces. *Phys. Rev. Lett.* **1999**, *82*, 2602–2605.

(213) Morkved, T. L.; Lu, M.; Urbas, a. M.; Ehrichs, E. E.; Jaeger, H. M.; Mansky, P.; Russell, T. P. Local Control of Microdomain Orientation in Diblock Copolymer Thin Films with Electric Fields. *Science* **1996**, *273*, 931–933.

(214) Goldberg-Oppenheimer, P.; Kabra, D.; Vignolini, S.; Sommer, M.; Neumann, K.; Thelakkat, M.; Steiner, U.; Hüttner, S. Hierarchical Orientation of Crystallinity by Block-Copolymer Patterning and Alignment in an Electric Field. *Chem. Mater.* **2013**, *25*, 1063–1070.

(215) Huettner, S.; Hodgkiss, J. M.; Sommer, M.; Friend, R. H.; Steiner, U.; Thelakkat, M. Morphology-Dependent Charge Photogeneration in Donor-Acceptor Block Copolymer Films Based on pPoly(3-Hexylthiophene)-block-Poly(Perylene Bisimide Acrylate). *J. Phys. Chem. B* **2012**, *116*, 10070–10078.

(216) Hofmann, C. C.; Bauer, P.; Haque, S. a.; Thelakkat, M.; Köhler, J. Energy- and Charge-Transfer Processes in Flexible Organic Donor-Acceptor Dyads. *J. Chem. Phys.* **2009**, *131*, 1–11.

(217) Niklas, J.; Beaupré, S.; Leclerc, M.; Xu, T.; Yu, L.; Sperlich, A.; Dyakonov, V.; Poluektov, O. G. Photoinduced Dynamics of Charge Separation: From Photosynthesis to Polymer–Fullerene Bulk Heterojunctions. *J. Phys. Chem. B*

2015, *119*, 7407–7416.

(218) Marchanka, A.; Maier, S. K.; Höger, S.; Van Gastel, M. Photoinduced Charge Separation in an Organic Donor-Acceptor Hybrid Molecule. *J. Phys. Chem. B* **2011**, *115*, 13526–13533.

(219) Kraffert, F.; Steyrleuthner, R.; Albrecht, S.; Neher, D.; Scharber, M. C.; Bittl, R.; Behrends, J. Charge Separation in PCPDTBT:PCBM Blends from an EPR Perspective. *J. Phys. Chem. C* **2014**, *118*, 28482–28493.

(220) Kohn, P.; Ghazaryan, L.; Gupta, G.; Sommer, M.; Wicklein, A.; Thelakkat, M.; Thurn-Albrecht, T. Thermotropic Behavior, Packing, and Thin Film Structure of an Electron Accepting Side-Chain Polymer. *Macromolecules* **2012**, *45*, 5676–5683.

(221) Wu, Z.; Petzold, A.; Henze, T.; Thurn-Albrecht, T.; Lohwasser, R. H.; Sommer, M.; Thelakkat, M. Temperature and Molecular Weight Dependent Hierarchical Equilibrium Structures in Semiconducting Poly(3-Hexylthiophene). *Macromolecules* **2010**, *43*, 4646–4653.

(222) Lee, Y.-H.; Yang, Y.-L.; Yen, W.-C.; Su, W.-F.; Dai, C.-A. Solution Self-Assembly and Phase Transformations of Form II Crystals in Nanoconfined Poly(3-Hexylthiophene) Based Rod-Coil Block Copolymers. *Nanoscale* **2014**, *6*, 2194–2200.

(223) Laity, P. R.; Taylor, J. E.; Wong, S. S.; Khunkamchoo, P.; Norris, K.; Cable, M.; Andrews, G. T.; Johnson, A. F.; Cameron, R. E. A Review of Small-Angle Scattering Models for Random Segmented Poly(ether-Urethane) Copolymers. *Polymer* **2004**, *45*, 7273–7291.

(224) Muthukumar, M.; Ober, C. K.; Thomas, E. L. Competing Interactions and Levels of Ordering in Self-Organizing Polymeric Materials. *Science* **1997**, *277*, 1225–1232.

(225) Singh, C. R.; Gupta, G.; Lohwasser, R.; Engmann, S.; Balko, J.; Thelakkat, M.; Thurn-Albrecht, T.; Hoppe, H. Correlation of Charge Transport with Structural Order in Highly Ordered Melt-Crystallized Poly(3-Hexylthiophene) Thin Films. *J. Polym. Sci. Part B Polym. Phys.* **2013**, *51*, 943–951.

(226) Zhou, R.; Xue, J. Hybrid Polymer-Nanocrystal Materials for Photovoltaic Applications. *ChemPhysChem* **2012**, *13*, 2471–2480.

(227) Huynh, W. U.; Dittmer, J. J.; Alivisatos, A. P. Hybrid Nanorod-Polymer Solar Cells. *Science* **2002**, *295*, 2425–2427.

(228) Hsu, J. W. P.; Lloyd, M. T. M. Organic / Inorganic Hybrids for Solar Energy Generation. *MRS Bull.* **2010**, *35*, 422–428.

(229) Huang, J.; Yin, Z.; Zheng, Q. Applications of ZnO in Organic and Hybrid Solar Cells. *Energy Environ. Sci.* **2011**, *4*, 3861–3877.

(230) Li, S.-S.; Chen, C.-W. Polymer–metal-Oxide Hybrid Solar Cells. *J. Mater. Chem. A* **2013**, *1*, 10574–10591.

(231) Günes, S.; Sariciftci, N. S. Hybrid Solar Cells. *Inorganica Chim. Acta* **2008**, *361*, 581–588.

(232) Martínez-Ferrero, E.; Albero, J.; Palomares, E. Materials, Nanomorphology, and Interfacial Charge Transfer Reactions in Quantum Dot/polymer Solar Cell Devices. *J. Phys. Chem. Lett.* **2010**, *1*, 3039–3045.

(233) Xu, T.; Qiao, Q. Conjugated Polymer–Inorganic Semiconductor Hybrid Solar Cells. *Energy Environ. Sci.* **2011**, *4*, 2700.

(234) Qian, L.; Yang, J.; Zhou, R.; Tang, A.; Zheng, Y.; Tseng, T.-K.; Bera, D.; Xue, J.; Holloway, P. H. Hybrid Polymer-CdSe Solar Cells with a ZnO Nanoparticle Buffer Layer for Improved Efficiency and Lifetime. *J. Mater. Chem.* **2011**, *21*, 3814–3817.

(235) Zhou, Y.; Eck, M.; Kruger, M. Bulk-Heterojunction Hybrid Solar Cells Based on Colloidal Nanocrystals and Conjugated Polymers. *Energy Environ. Sci.* **2010**, *3*, 1851–1864.

(236) Oosterhout, S. D.; Wienk, M. M.; van Bavel, S. S.; Thiedmann, R.; Koster, L. J. A.; Gilot, J.; Loos, J.; Schmidt, V.; Janssen, R. A. J. The Effect of Three-Dimensional Morphology on the Efficiency of Hybrid Polymer Solar Cells. *Nat. Mater.* **2009**, *8*, 818–824.

(237) Beek, W. J. E.; Wienk, M. M.; Kroon, J. M.; Slooff, L. H.; Janssen, R. A. J. Hybrid Solar Cells Using a Zinc Oxide Precursor and a Conjugated Polymer. *Adv. Funct. Mater.* **2005**, *15*, 1703–1707.

(238) Moet, D. J. D.; Koster, L. J. A.; Boer, B. De; Blom, P. W. M. Hybrid Polymer Solar Cells from Highly Reactive Diethylzinc: MDMO–PPV versus P3HT. *Chem. Mater.* **2007**, *19*, 5856–5861.

(239) Dayal, S.; Kopidakis, N.; Olson, D. C.; Ginley, D. S.; Rumbles, G. Photovoltaic Devices with a Low Band Gap Polymer and CdSe Nanostructures Exceeding 3% Efficiency. *Nano Lett.* **2010**, *10*, 239–242.

(240) Lin, Y.; Chu, T.; Li, S.; Chuang, C.; Su, W.; Chang, C.; Chu, M.; Chen, C. Interfacial Nanostructuring on the Performance of Polymer / TiO Nanor. *J. Am. Chem. Soc.* **2009**, *131*, 3644–3649.

(241) Beek, W. J. E.; Wienk, M. M.; Janssen, R. A. J. Efficient Hybrid Solar Cells from Zinc Oxide Nanoparticles and a Conjugated Polymer. *Adv. Mater.* **2004**, *16*, 1009–1013.

(242) Beek, W. J. E.; Wienk, M. M.; Kemerink, M.; Yang, X.; Janssen, R. A. J. Hybrid Zinc Oxide Conjugated Polymer Bulk Heterojunction Solar Cells. *J. Phys. Chem. B* **2005**, *109*, 9505–9516.

(243) Beek, W. J. E.; Wienk, M. M.; Janssen, R. A. J. Hybrid Solar Cells from Regioregular Polythiophene and ZnO Nanoparticles. *Adv. Funct. Mater.* **2006**, *16*, 1112–1116.

(244) Li, F.; Shi, Y.; Yuan, K.; Chen, Y. Fine Dispersion and Self-Assembly of ZnO Nanoparticles Driven by P3HT-B-PEO Diblocks for Improvement of Hybrid Solar Cells Performance. *New J. Chem.* **2013**, *37*, 195–203.

(245) Borchert, H. Elementary Processes and Limiting Factors in Hybrid Polymer/nanoparticle Solar Cells. *Energy Environ. Sci.* **2010**, *3*, 1682.

(246) Moulé, A. J.; Chang, L.; Thambidurai, C.; Vidu, R.; Stroeve, P. Hybrid Solar Cells: Basic Principles and the Role of Ligands. *J. Mater. Chem.* **2012**, *22*, 2351–2368.

(247) Palaniappan, K.; Murphy, J. W.; Khanam, N.; Horvath, J.; Alshareef, H.; Quevedo-Lopez, M.; Biewer, M. C.; Park, S. Y.; Kim, M. J.; Gnade, B. E.; Stefan, M. C. Poly(3-Hexylthiophene)–CdSe Quantum Dot Bulk Heterojunction Solar Cells: Influence of the Functional End-Group of the Polymer. *Macromolecules* **2009**, *42*, 3845–3848.

(248) Palaniappan, K.; Hundt, N.; Sista, P.; Nguyen, H.; Hao, J.; Bhatt, M. P.; Han, Y. Y.; Schmiedel, E. A.; Sheina, E. E.; Biewer, M. C.; Stefan, M. C. Block Copolymer Containing Poly(3-Hexylthiophene) and Poly(4-Vinylpyridine) : Synthesis and Its Interaction with CdSe Quantum Dots for Hybrid Organic Applications. *J. Polym. Sci. Part A Polym. Chem.* **2011**, *49*, 1802–1808.

(249) Yen, W.-C.; Lee, Y.-H.; Lin, J.-F.; Dai, C.-A.; Jeng, U.-S.; Su, W.-F. Effect of TiO2 Nanoparticles on Self-Assembly Behaviors and Optical and Photovoltaic Properties of the P3HT-b-P2VP Block Copolymer. *Langmuir* **2011**, *27*, 109–115.

(250) Zeng, T.; Lin, Y.; Lo, H.-H.; Chen, C. C.-H.; Chen, C. C.-H.; Liou, S.-C.; Huang, H.-Y.; Su, W.-F. A Large Interconnecting Network within Hybrid MEH-PPV/TiO2 Nanorod Photovoltaic Devices. *Nanotechnology* **2006**, *17*, 5387–5392.

(251) Mitchell, L. A. Functional Polymers : Polyoxanorbornene-Based Block Copolymers for the Separation of F-Elements and Luminescent Conducting Metallopolymers. *Univ. Texas PhD Thesis* **2014**.

(252) Sankaran, N. B.; Rys, A. Z.; Nassif, R.; Nayak, M. K.; Metera, K.; Chen, B.; Bazzi, H. S.; Sleiman, H. F. Ring-Opening Metathesis Polymers for Biodetection and Signal Amplification: Synthesis and Self-Assembly. *Macromolecules* **2010**, *43*, 5530–5537.

(253) Novosjolova, I. The Mukaiyama Reagent: An Efficient Condensation Agent. *Synlett* **2013**, *24*, 135–136.

(254) Olsen, B.; Segalman, R. A. Self-Assembly of Rod–coil Block Copolymers. *Mater. Sci. Eng. R Reports* **2008**, *62*, 37–66.

(255) Patel, S. N.; Javier, A. E.; Beers, K. M.; Pople, J. a.; Ho, V.; Segalman, R. A.;

Balsara, N. P. Morphology and Thermodynamic Properties of a Copolymer with an Electronically Conducting Block: Poly(3-Ethylhexylthiophene)-Block-Poly(ethylene Oxide). *Nano Lett.* **2012**, *12*, 4901–4906.

(256) Vaseem, M.; Umar, A.; Hahn, Y. ZnO Nanoparticles: Growth , Properties , and Applications. In *Metal Oxide Nanostructures and Their Applications*; Umar, A., Hahn, Y. B., Eds.; American Scientific Publishers, 2010; Vol. 5, pp 1–36.

(257) Pacholski, C.; Kornowski, A.; Weller, H. Self-Assembly of ZnO: From Nanodots, to Nanorods. *Angew. Chemie-International Ed.* **2002**, *41*, 1188–1191.

(258) Shao, S.; Zheng, K.; Pullerits, T.; Zhang, F. Enhanced Performance of Inverted Polymer Solar Cells by Using Poly(Ethylene Oxide)-Modified ZnO as an Electron Transport Layer. *ACS Appl. Mater. Interfaces* **2013**, *5*, 380–385.

(259) Meulenkamp, E. a. Synthesis and Growth of ZnO Nanoparticles. *J. Phys. Chem. B* **1998**, *102*, 5566–5572.

(260) Kukreja, L. M.; Misra, P. Photoluminescence Processes in ZnO Thin Films and Quantum Structures. In *ZnO Nanocrystals and Allied Materials*; Ramachandra Rao, M. S., Okada, T., Eds.; Springer India, 2014; Vol. 180, pp 49–89.

(261) Brus, L. Electronic Wave Functions in Semiconductor Clusters: Experiment and Theory. *J. Phys. Chem.* **1986**, *90*, 2555–2560.

(262) Bahnemann, D. W.; Kormann, C.; Hoffmann, M. R. Preparation and Characterization of Quantum Size Zinc Oxide: A Detailed Spectroscopic Study. *J. Phys. Chem.* **1987**, *91*, 3789–3798.

(263) Haase, M.; Weller, H.; Henglein, A. Photochemistry and Radiation Chemistry of Colloidal Semiconductors. 23. Electron Storage on Zinc Oxide Particles and Size Quantization. *J. Phys. Chem.* **1988**, *92*, 482–487.

(264) Peng, Q.; Tseng, Y. C.; Darling, S. B.; Elam, J. W. Nanoscopic Patterned Materials with Tunable Dimensions via Atomic Layer Deposition on Block Copolymers. *Adv. Mater.* **2010**, *22*, 5129–5133.

(265) Peng, Q.; Tseng, Y.-C.; Darling, S. B.; Elam, J. W. A Route to Nanoscopic Materials via Sequential Infiltration Synthesis on Block Copolymer Templates. *ACS Nano* **2011**, *5*, 4600–4606.

(266) Yin, J.; Xu, Q.; Wang, Z.; Yao, X.; Wang, Y. Highly Ordered TiO2 Nanostructures by Sequential Vapour Infiltration of Block Copolymer Micellar Films in an Atomic Layer Deposition Reactor. *J. Mater. Chem. C* **2013**, *1*, 1029.

(267) Biswas, M.; Libera, J. A.; Darling, S. B. New Insight into the Mechanism of Sequential Infiltration Synthesis from Infrared Spectroscopy. *Chem. Mater.* **2014**, *26*, 6135–6141.

(268) Kamcev, J.; Germack, D. S.; Nykypanchuk, D.; Grubbs, R. B.; Nam, C. Y.; Black, C. T. Chemically Enhancing Block Copolymers for Block-Selective Synthesis of

Self-Assembled Metal Oxide Nanostructures. *ACS Nano* **2013**, *7*, 339–346.

(269) Ramanathan, M.; Tseng, Y.-C.; Ariga, K.; Darling, S. B. Emerging Trends in Metal-Containing Block Copolymers: Synthesis, Self-Assembly, and Nanomanufacturing Applications. *J. Mater. Chem. C* **2013**, *1*, 2080.

(270) Basché, T.; Bottin, A.; Li, C.; Müllen, K.; Kim, J.-H.; Sohn, B.-H.; Prabhakaran, P.; Lee, K.-S. Energy and Charge Transfer in Nanoscale Hybrid Materials. *Macromol Rapid Commun* **2015**, *36*, 1026–1046.

(271) Janáky, C.; Rajeshwar, K. The Role of (photo)electrochemistry in the Rational Design of Hybrid Conducting Polymer/semiconductor Assemblies: From Fundamental Concepts to Practical Applications. *Prog. Polym. Sci.* **2015**, *43*, 96–135.

(272) Holliday, B. J.; Swager, T. M. Conducting Metallopolymers: The Roles of Molecular Architecture and Redox Matching. *Chem. Commun.* **2005**, 23–36.

(273) Madhavan, N.; Jones, C. W.; Weck, M. Rational Approach to Polymer-Supported Catalysts: Synergy between Catalytic Reaction Mechanism and Polymer Design. *Acc. Chem. Res.* **2008**, *41*, 1153–1165.

(274) Weck, M. A Practical One-Pot Synthesis of Enantiopure Unsymmetrical Salen Ligands. *J. Org. Chem.* **2006**, *71*, 2903–2906.

(275) Kleij, A. W. Nonsymmetrical Salen Ligands and Their Complexes: Synthesis and Applications. *Eur. J. Inorg. Chem.* **2009**, No. 2, 193–205.

(276) Campbell, E. J.; Nguyen, S. T. Unsymmetrical Salen-Type Ligands: High Yield Synthesis of Salen-Type Schiff Bases Containing Two Different Benzaldehyde Moieties. *Tetrahedron Lett.* **2001**, *42*, 1221–1225.

(277) Wen, Y. Q.; Ren, W. M.; Lu, X. B. Unsymmetric Salen Ligands Bearing a Lewis Base: Intramolecularly Cooperative Catalysis for Cyanosilylation of Aldehydes. *Org. Biomol. Chem.* **2011**, *9*, 6323–6330.

(278) Xiao, S.; Turkyilmaz, S.; Smith, B. D. Convenient Synthesis of Multivalent zinc(II)-Dipicolylamine Complexes for Molecular Recognition. *Tetrahedron Lett.* **2013**, *54*, 861–864.

(279) Ngo, H. T.; Liu, X.; Jolliffe, K. a. Anion Recognition and Sensing with Zn(II)-Dipicolylamine Complexes. *Chem. Soc. Rev.* **2012**, *41*, 4928–4965.

(280) Hu, Y.; Yin, J.; Yoon, J. A Multi-Responsive Cyanine-Based Colorimetric Chemosensor Containing Dipicolylamine Moieties for the Detection of Zn(II) and Cu(II) Ions. *Sensors Actuators B Chem.* **2016**, *230*, 40–45.

(281) Minamiki, T.; Minami, T.; Koutnik, P.; Anzenbacher, P.; Tokito, S. Antibody- and Label-Free Phosphoprotein Sensor Device Based on an Organic Transistor. *Anal. Chem.* **2016**, *88*, 1092–1095.

(282) Afrasiabi, R.; Kraatz, H. B. Stimuli-Responsive Supramolecular Gelation in

Ferrocene-Peptide Conjugates. *Chem. A Eur. J.* **2013**, *19*, 17296–17300.